

**Electronic Structure and Electronic-Vibrational  
Energy Exchange in Rydberg States of  
Calcium Monofluoride**

by

Christopher M. Gittins  
B.A., Oberlin College (1987)

Submitted to the Department of Chemistry  
in Partial Fulfillment of the Requirements  
for the Degree of

DOCTOR OF PHILOSOPHY IN CHEMISTRY

at the

MASSACHUSETTS INSTITUTE OF TECHNOLOGY

February 1995

© Massachusetts Institute of Technology  
All rights reserved.

Signature of Author

*C. M. Gittins*

Department of Chemistry  
February 7, 1995

Certified by

*Robert W. Field*

Robert W. Field  
Thesis Supervisor

Accepted by

*Dietmar Seyferth*

Dietmar Seyferth, Chairman  
Departmental Committee on  
Graduate Students

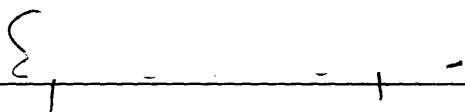
Science


MAR 01 1995

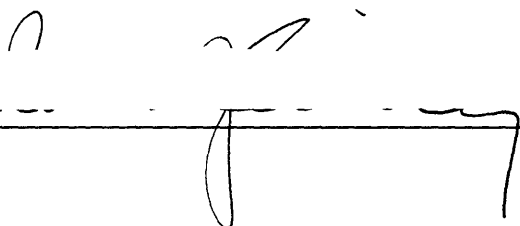
MAR 01 1995

1995

This doctoral thesis has been examined by a Committee of the Department of Chemistry as follows:

Professor Sylvia T. Ceyer  \_\_\_\_\_  
Chairman

Professor Robert W. Field  \_\_\_\_\_  
Thesis Supervisor

Professor Robert J. Silbey  \_\_\_\_\_

**Electronic Structure and Electronic-Vibrational  
Energy Exchange in Rydberg States of  
Calcium Monofluoride**

by

Christopher M. Gittins

Submitted to the Department of Chemistry on February 7, 1995 in partial fulfillment of the requirements for the degree of Doctor of Philosophy in Chemistry.

**Abstract**

The alkaline earth monohalides (MX) are well described as simple three-particle systems consisting of two closed shell atomic ions ( $M^{2+}$ , X) and a single unpaired electron. Because of the simplicity of their composition, MX molecules serve as a prototype for the electronic structure and electron-nuclei energy exchange processes of more complex dipolar core molecules. This thesis presents the results of an experimental study of Rydberg states of Calcium Monofluoride (CaF) with effective principal quantum number,  $n^*$ , between 12.6 and 14.6 and one quantum of vibration in the  $CaF^+$  ion-core. The vibronic energy of  $n^* > 12.6$ ,  $v=1$  CaF Rydberg states exceeds the lowest ionization threshold for neutral CaF. The Rydberg states analyzed here were probed using ionization detected optical-optical double resonance (ID-OODR) spectroscopy.

In addition to observing "core-penetrating" Rydberg states (primarily derived from one-electron atomic orbitals with electron orbital angular momentum quantum number  $\ell \leq 2$ ), "core-non-penetrating" states,  $\ell \geq 3$ , have also been observed. The quantum number  $\ell$  is not a good label for core-penetrating states. Core non-penetrating states retain nearly pure  $\ell$  character, but have their  $2\ell + 1$  degeneracy lifted by the extremely large  $CaF^+$  multipole moments. The problem of a core non-penetrating Rydberg orbital in the field of a highly dipolar cation is equivalent to that of a hydrogen atom with a point dipole located at its nucleus. This problem has been treated theoretically, but there exist few experimental tests of model predictions, particularly for dipoles as large as that of  $CaF^+$ . A finite effective Hamiltonian matrix model for the experimental data yields the atomic  $\ell$ -parentage of molecular states as well as an estimate of the dipole moment of  $CaF^+$ .

In addition, the observation of lifetime broadening of rotational levels in the 13.36  $\Pi$  and 14.36  $\Pi$ ,  $v=1$  states allows for determination of the rate of exchange of energy between the Rydberg electron and the molecular cation to which it is bound.

Thesis Supervisor: Dr. Robert W. Field

Title: Professor of Chemistry

For three professors who encouraged my interest in physics and chemistry long before I considered graduate school:

George Mandeville,  
Diane Richardson,  
Terry Carlton.



"Hoaxes! Don't speak to me of hoaxes, sir! I was part of the worst that was ever dreamt up in all history, and not free of it yet. Two old gnomes from Nantucket, some years ago... Gnomes. Hah! Cracked checkerplayers, that's nearer the mark! Beelzebub and Jaweh! Never mind... interminable damned... Hoaxes. Hah."

He hunches up, cunning, a crafty old loon with his left eye cocked to the northwest corner of the universe. He is teased toward some barest possibility. He purses his lips. He looks both sly and apprehensive. His long, lean nose is the cutting edge of outlandishness.

"I could tell you a tale, if ye'd understand from the outset it has no purpose to it, no shape or form or discipline but the tucket and boom of its highflown language and whatever dim flickers that noise stirs in yer cerebrum, sir - the boom and the bottle we chase it with - fierce rum of everlasting sleep, ha ha! - for I won't be called a liar, no sir! not when I speak of such matters as devils and angels and the making of man, which is my subject, sir."

With dignity, an angel enters, golden-winged, and places spirits on the table between the mariner and his guest (apparently a city fellow). The guest uncomfortably picks his lip. Except for the angel, the mariner's voice, and the guest's self-conscious ear, the room is empty; yellow. The guest is as yet only half-aware of the angel's wings. Blushing slightly, uncertain over who is supposed to pay, the guest glances over his shoulder, adjusts his tie.

"Tell on, old loon! yer supposed to say."

"Tell on," says the guest.

"God bless yer generous soul, sir, that I will!"

from "The King's Indian" by John Gardner

## Table of Contents

<b>Electronic Structure and Electronic-Vibrational Energy Exchange in Rydberg States of Calcium Monofluoride</b>	<b>1</b>
Abstract	3
Dedication	4
Prologue	5
Introduction	8
<b>Chapter 1 - Experimental Apparatus</b>	<b>17</b>
1.1. Timing of Events	17
1.2. Pulsed Nozzle Source and Molecule Production	18
1.3. REMPI-TOFMS System	23
1.3.1. Source Chamber	23
1.3.2. Time-of-Flight Mass Spectrometer	25
1.4. Lasers and Wavelength Calibration	34
References	37
Figures	38
<b>Chapter 2 - Experimental Strategies</b>	<b>57</b>
2.1. Fluorescence Excitation	58
2.2. Fluorescence Dip	63
2.3. 1+1 REMPI	70
2.4. Ionization Detected Optical-Optical Double Resonance	85
References	89
<b>Chapter 3 - Background for Data Analysis: Effective Hamiltonian Matrix Models and Assigning ID-OODR Spectra</b>	<b>90</b>
3.1. Effective Hamiltonian for Rydberg States	90
3.1.1. The Vibrational Hamiltonian	91
3.1.2. The Electronic Hamiltonian	92
3.1.3. The Spin-Orbit Hamiltonian	101
3.1.4. The Rotational Hamiltonian	104
3.2. Interpretation of CaF ID-OODR Spectra	111
3.3. Identification of Core-Non-Penetrating States	123
References	130
<b>Chapter 4 - Analysis of <math>n^*=13</math> and <math>n^*=14</math> Data</b>	<b>131</b>
4.1. Construction of $s\sim p\sim d$ "Supercomplex" Hamiltonians	131
4.2. Fit of Experimental Data to the $3 \times 3$ $p\sim d$ (-) symmetry Hamiltonian	139
4.3. $13.14 \Delta, v=1 \sim 9.14 \Delta, v=2$ Intrachannel Perturbation	144
4.4. Core-Penetrating~Core-Non-Penetrating Perturbations: $n.14 \Delta, v=1 \sim nf, \ell=-2, v=1$ Perturbation	153
4.5. Fit of Experimental Data to $6 \times 6$ $s\sim p\sim d$ and $10 \times 10$ $s\sim p\sim d\sim f$ (+) Symmetry Hamiltonian Models	161
4.6. Analysis and Discussion of $14f$ and $14g$ (Core-Non-Penetrating) States	172
References	188
<b>Chapter 5 - Vibrational Autoionization Rates of the <math>13.36 \Pi, v=1</math> and <math>14.36 \Pi, v=1</math> States</b>	<b>189</b>

Tables	201
References	203
Appendix I - Timing Diagram of ID-OODR Experiment	204
Appendix II - Vacuum Equipment Price List	206
Acknowledgments	209

## INTRODUCTION

This thesis concerns moderate energy Rydberg states (effective principal quantum number,  $n^*$ , between 12.5 and 14.6) of Calcium Monofluoride, CaF, which possess one quantum of vibrational excitation. These states were probed using rotationally resolved Ionization Detected Optical-Optical Double Resonance (ID-OODR) laser spectroscopy. The goal of this work is to accurately model the interaction of the Rydberg electron with the CaF<sup>+</sup> ion-core.

CaF is a member of the alkaline earth monohalide family of molecules. The alkaline earth monohalides (MX) are well described as simple three-particle systems consisting of two closed shell atomic ions (M<sup>2+</sup>, X<sup>-</sup>) and a single unpaired electron. Because of the simplicity of their composition, MX molecules serve as a prototype for the electronic structure and electron-nuclei energy and angular momentum exchange processes of more complex molecules. Below ~3 eV of excitation and near its equilibrium internuclear separation, the CaF electronic states are understood in terms of an unpaired Ca<sup>+</sup> electron perturbed by the field of an F<sup>-</sup> anion [1]. At higher electronic energies, the system may be treated as a single electron weakly bound to a highly polar molecular cation, CaF<sup>+</sup>, consisting of two closed shell atomic ions, Ca<sup>2+</sup> and F<sup>-</sup>.

Previous workers observed and analyzed low energy Rydberg states of CaF (primarily  $n^* < 10$ ,  $v = 0$  and  $n^* < 7.5$ ,  $v = 1$ ) and assigned nominal  $n\ell\Lambda$  quantum numbers<sup>1</sup> to each state[2, 3]. While  $\ell$  is not a rigorously good quantum number in a molecule, it is an approximately good quantum number for Rydberg states of non-polar molecules such as H<sub>2</sub>, O<sub>2</sub>, and N<sub>2</sub>. It was apparent however that pure- $\ell$  labels would not suffice for describing the Rydberg states of CaF. The highly polar CaF<sup>+</sup> ion-core strongly mixes atomic  $n\ell$  basis states having  $\ell \leq 2$ .

All of the observed low energy electronic states of CaF were assigned to one of six Rydberg series[2, 3]. The electronic term values of these states are accurately calculated by the Rydberg formula:

$$E_{n,i,\Lambda} = \text{IP}(\text{CaF}) - \frac{\mathfrak{R}}{(n - \delta_{i,\Lambda})^2},$$

---

<sup>1</sup> The quantum number  $\ell$  is electron orbital angular momentum and  $\Lambda$  is the projection of  $\ell$  on the molecular axis.

where  $\mathfrak{R}$  is the Rydberg constant ( $109736.3 \text{ cm}^{-1}$  for CaF),  $n$  is an integer equivalent to a hydrogenic principal quantum number,  $\delta_{i,\Lambda}$  is the quantum defect for the Rydberg series, and  $\text{IP}(\text{CaF})$  is the ionization potential of the molecule,  $46998 \pm 5 \text{ cm}^{-1}$  [4]. The effective principal quantum number,  $n^*$ , of a Rydberg state is defined as  $n - \delta_{i,\Lambda}$ . CaF Rydberg series may be classified according to the value of their quantum defects and  $\Lambda$ .

The atomic quantum number  $\ell$  is not a good quantum number in the molecule, and the  $\Sigma^+$  and  $\Pi$  ( $\Lambda = 0, 1$ ) electronic states derived from  $\ell \leq 2$  basis states do not even approximately retain pure- $\ell$  character. Earlier analyses [5,6] met with considerable success in modeling CaF Rydberg states in terms of strongly mixed  $\ell \leq 2$  (s, p, and d) atomic orbitals, where the  $\ell$ -mixing arises from the strong interaction between the Rydberg electron and the  $\text{CaF}^+$  ion-core. However these analyses were not able to provide a completely accurate description of spectroscopic data. One of the goals of this work is to determine whether the Rydberg electron-cation interaction may be more accurately described by allowing  $\ell = 3, f$ , basis states to mix with the  $\ell \leq 2$  atomic basis states which are already known to be mixed by the ion-core. The group Rydberg states derived from nominal s, p, and d atomic orbitals and clustered about an integer value of  $n^*$  are referred to as an  $n^*$ -supercomplex. (The details of assigning a state to a particular  $n^*$ -supercomplex are discussed in Chapter 4.)

While low- $\ell$  states are strongly mixed, the situation is quite different for states with higher values of electron orbital angular momentum. This may be understood from the Schrödinger equation for the hydrogen atom. In the Hamiltonian for the hydrogen atom, the potential energy of the electron-proton interaction is  $r^{-1}$  (in atomic units). If one writes out the full Schrödinger equation and simplifies the expression with the intent of determining the radial wavefunction for the electron, the electron could equivalently be viewed as moving in an effective potential which depends on  $\ell$ . The Schrödinger equation for the hydrogen atom is:

$$\left[ -\frac{1}{2} \nabla^2 - \frac{1}{r} \right] \Psi_{n\ell m} = E \Psi_{n\ell m},$$

the radial portion of which is expressed as,

$$\left[ -\frac{1}{2} \frac{d^2}{dr^2} - \frac{1}{r} + \frac{\ell(\ell+1)}{2r^2} \right] P_{n\ell} = E P_{n\ell},$$

where  $P_{n\ell}(r) = rR_{n\ell}(r)$ , and the *effective potential* experienced by the electron is,

$$V_{\text{eff}}(r) = -\frac{1}{r} + \frac{\ell(\ell+1)}{2r^2}.$$

The repulsive term in  $V_{\text{eff}}(r)$  is a centrifugal barrier arising from the orbital angular momentum of the electron. The  $\ell$ -dependent  $V_{\text{eff}}(r)$ 's are shown in Fig. I.1. The effective potential has a minimum at  $r = \ell(\ell+1)$  and an inner turning point at  $r_c$ , where  $V_{\text{eff}}(r_c) = -(2n^2)^{-1}$ . (In the limit of high  $n$ ,  $r_c = \frac{1}{2}\ell(\ell+1)$ . In the low  $n$  limit, i.e.,  $n = \ell+1$ ,  $r_c = (\ell+1)^2 - (\ell+1)^{3/2}$ .) The centrifugal barrier keeps the electron away from the proton. While the unpaired electron in CaF is not hydrogenic, one might suspect that for sufficiently high values of  $\ell$ , the electron would be kept sufficiently far from the region near the  $\text{CaF}^+$  ion-core that the distinction between the pure Coulomb potential of  $\text{H}^+$  and the  $\text{CaF}^+$  potential could be accurately expressed as a small perturbation on the  $\text{H}^+$  potential. States with large enough  $\ell$ , which experience the highly polar nature of the  $\text{CaF}^+$  ion-core only at long-range, are referred to as *core-non-penetrating* states. For these states, the perturbation on the  $\text{H}^+$  potential is:

$$V'(r) = V_{\text{CaF}^+}(r) - V_{\text{H}^+}(r) \approx \frac{\mu^+ P_{10}(\cos\theta)}{r^2} + \frac{Q^+ P_{20}(\cos\theta)}{r^3} + \dots,$$

where  $\mu^+$  and  $Q^+$  are the electric dipole and quadrupole moments of  $\text{CaF}^+$  and the  $P_{n0}$  functions are spherical harmonics with  $\theta$  being the angle between the Rydberg electron and the molecular axis (as measured from the center-of-mass). Additional terms could be included to account for the polarizability of  $\text{CaF}^+$ , but  $\text{CaF}^+$  is essentially two closed shell atomic ions and is not very polarizable, so the electric multipole moments will provide the dominant correction.

One of the questions addressed in this thesis is, "At what value of  $\ell$  do the CaF Rydberg states behave as weakly perturbed atomic states? What is the lowest- $\ell$  core-non-penetrating state?" The answer appears to be  $\ell = 3$  if the state is not a  $^2\Sigma^+$  state, i.e., if the Rydberg orbital has at least one nodal plane which contains the molecular axis. If the state is a  $^2\Sigma^+$  state, then the identity of the lowest non-penetrating  $\ell$  is not quite as clear, but for  $\ell = 4$ , the CaF electronic states definitely appear to behave as weakly perturbed atomic states. This makes sense intuitively if one considers the spatial extent of the ion-core,  $r_{\text{core}} = r_{\text{cm,x}} + r_x$ , where  $r_{\text{cm,x}}$  is the distance from the molecular center of mass to the most distant atom, and  $r_x$  is the ionic or covalent radius of that atom [4]. The inner turning point of  $V_{\text{eff}}(r)$  for

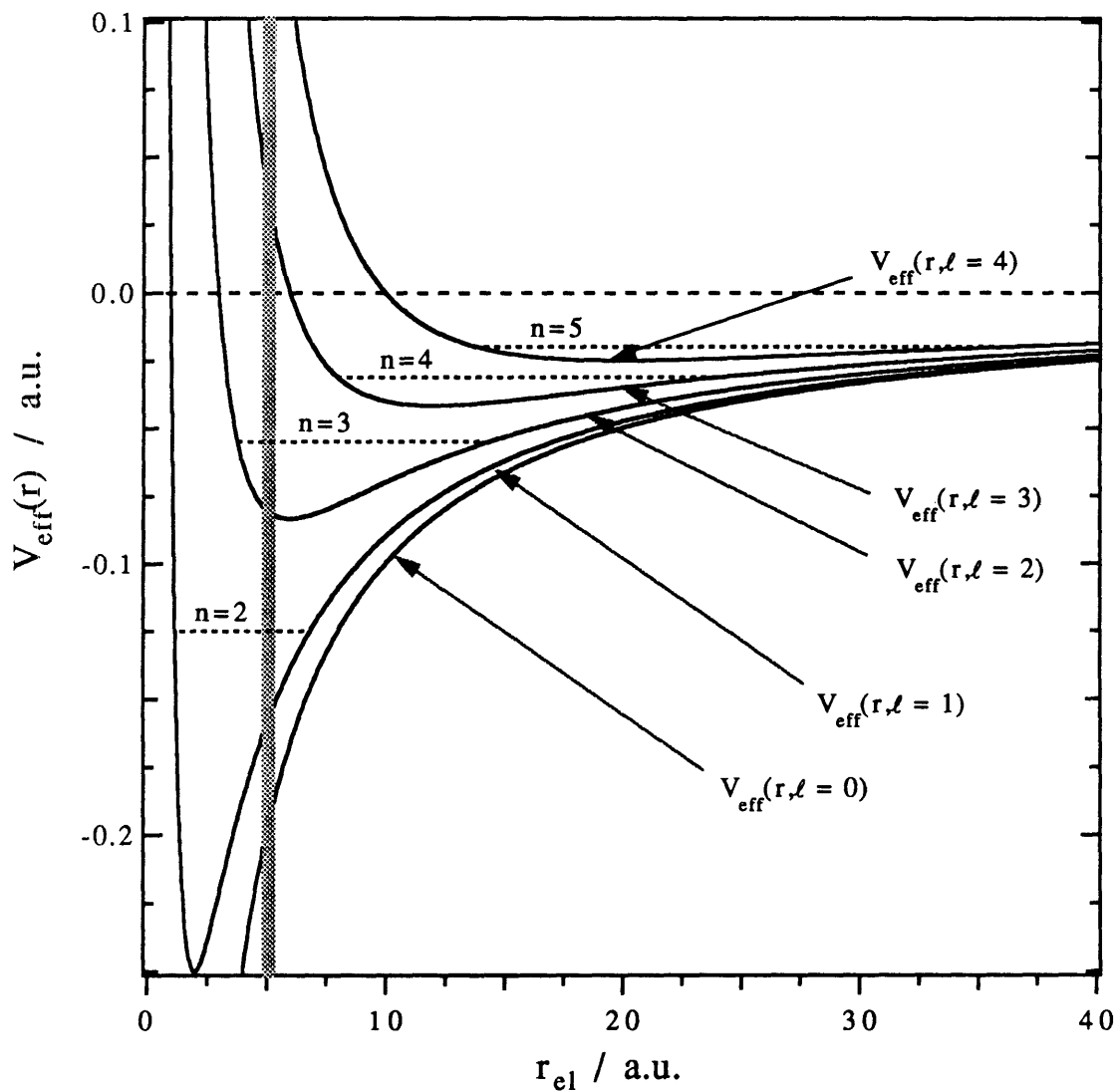


Figure I.1. Effective potentials for a hydrogen electron. Only the lowest- $n$   $V_{\text{eff}}$  is shown for each successively higher  $l$ -value,  $0 \leq l \leq 4$ . The thick gray vertical line indicates the effective radius of the  $\text{CaF}^+$  ion core.

$n = 5, \ell = 4$  occurs at  $r \sim 13.8$  a.u., which is much greater than  $r_{\text{core}}, 5.1$  a.u. The inner turning point of  $V_{\text{eff}}(r)$  for  $n = 4, \ell = 3$  occurs at  $r = 8$  a.u., just slightly greater than  $r_{\text{core}}$ . The inner turning point of  $V_{\text{eff}}(r)$  for  $n = 3, \ell = 2$  occurs at short-range relative to  $r_{\text{core}}, 3.8$  a.u.  $\ll 5.1$  a.u.

The  $\ell \geq 3$  states sample the  $\text{CaF}^+$  cation only at long range and are characterized by quantum defects near zero. Core-non-penetrating states retain their nearly pure  $n\ell$  character, but have their  $2\ell + 1$  degeneracy lifted by the extremely large  $\text{CaF}^+$  electric multipole moments. The problem of a core-non-penetrating Rydberg orbital in the field of a highly dipolar cation is equivalent to that of a hydrogen atom with a point dipole located at its nucleus. The problem has been treated theoretically, but there exist few experimental tests of model predictions, particularly for dipoles as large as that of  $\text{CaF}^+$ . The splitting of the  $\Lambda$  components of  $\ell = 3$  and 4 in the  $n^*=14$  supercomplex are analyzed to estimate the  $\text{CaF}^+$  dipole moment,  $\sim 9$  Debye.

Previous workers on  $\text{CaF}$  identified and analyzed core-penetrating Rydberg series, but were frustrated in their efforts to detect  $\ell \geq 3$  states because of unexpectedly restrictive selection rules associated with the specific intermediate state used in their double resonance experiments. Those experiments utilized the  $A^2\Pi_{3/2}$  state as an intermediate. The  $A^2\Pi$  state is the lowest energy  $^2\Pi$  state and lies  $\sim 2$  eV above  $\text{CaF}$ 's electronic ground state. The  $A^2\Pi$  state has predominantly  $\text{Ca}^+$  4p and 3d character, whereas the  $X^2\Sigma^+$  ground state is predominantly  $\text{Ca}^+$  4s[1,7]. It was expected that the  $\text{Ca}^+$  3d character in the A state would facilitate access to f-states, however no f-states were clearly identified. The key to accessing f-states appears to be the use of the  $C^2\Pi$  state as the intermediate in the double resonance experiment. The  $C^2\Pi$  state is the second  $^2\Pi$  state in  $\text{CaF}$ . It lies  $\sim 4$  eV above the ground state, about  $2/3$  of the way to the ionization threshold. The choice of the  $C^2\Pi$  state was not accidental. It was expected that the spectroscopic data recorded through the  $C^2\Pi$  state would complement that recorded from the  $A^2\Pi$  state. The extent to which the  $A^2\Pi$  and  $C^2\Pi$  data sets are complementary was unexpected, however. The strongest transitions to  $12.5 \leq n^* \leq 14.6, v = 1$  Rydberg states from the  $C^2\Pi_{3/2}$  state terminate on  $nf$  states! Figure I.2 shows the potential energy curves of the  $\text{CaF}$  electronic states involved in these double resonance experiments. Approximate excitation wavelengths are included on the figure.

All six core-penetrating states in both the  $n^*=13$  and 14 supercomplexes, as well as the seven components of each f-state and all higher- $\ell$  core-non-penetrating states belonging to each supercomplex, are found within a very narrow energy region. The electronic term values of states belonging to the  $n^*=14, v=1$  supercomplex span a range of  $\sim 80$   $\text{cm}^{-1}$ . (The energy spanned by an  $n^*$ -supercomplex scales as  $(n^*)^{-3}$ .) The separation between



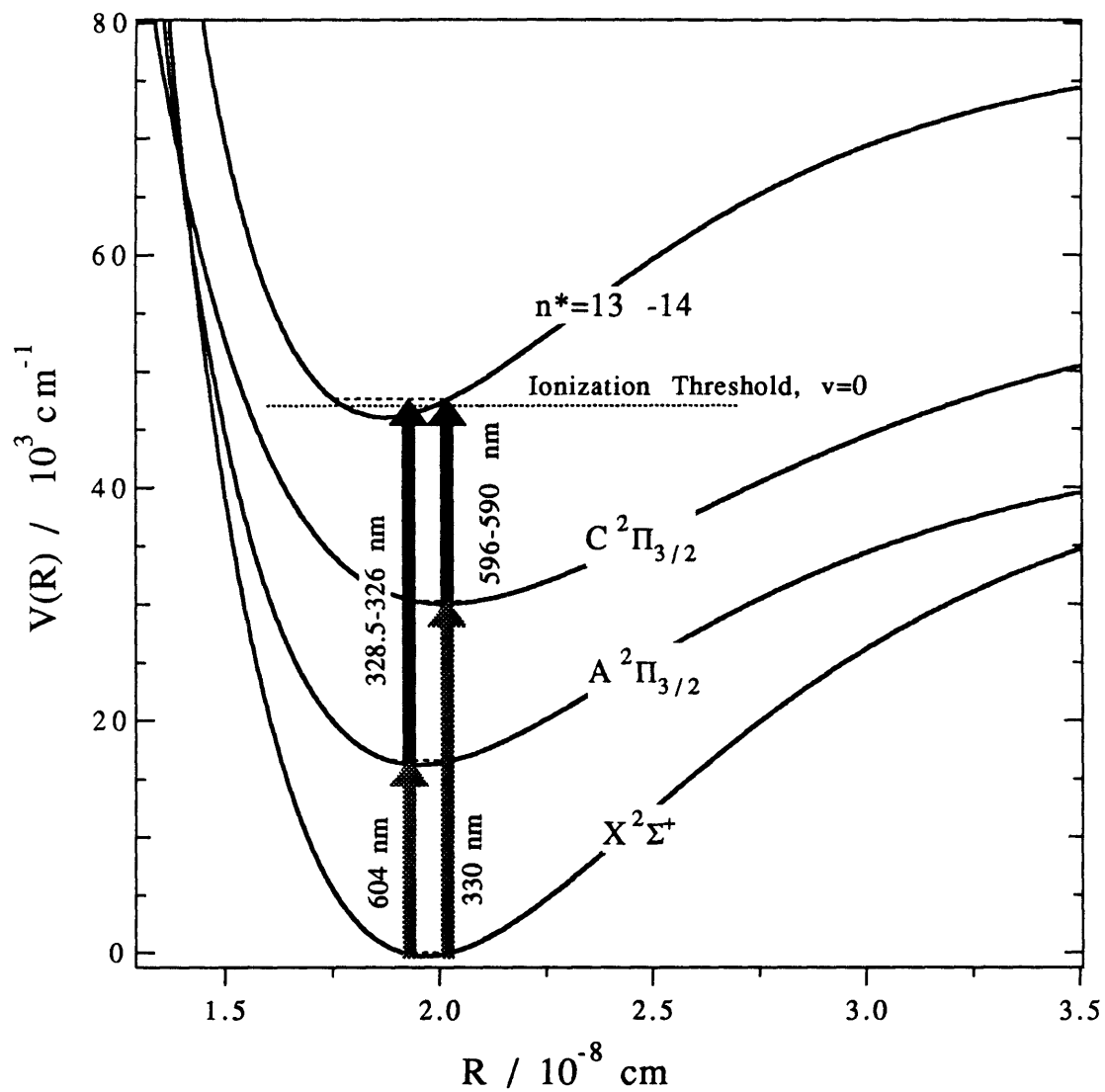


Figure I.2. CaF electronic states involved in ID-OODR experiments. The CaF "n\*=13-14" potential energy curve is the CaF<sup>+</sup> curve shifted to ~600 cm<sup>-1</sup> lower energy. The horizontal dotted line at 46998 cm<sup>-1</sup> indicates the threshold for creation of CaF<sup>+</sup> in its vibrational ground state.

electronic states in the supercomplex is  $O(10 \text{ cm}^{-1})$ . One property of core-non-penetrating states is that many of them possess anomalously large or small, but predictable, rotational constants in comparison to the rotational constants of the core-penetrating states in the same energy region. At sufficiently large values of rotational quantum number,  $O(10^1)$ , the difference in rotational energies of adjacent core-penetrating and core non-penetrating states may be equal in magnitude, but opposite in sign of the difference in their electronic energies. As the rotational quantum number increases, the states tune into and then tune through resonance. As core-penetrating and core-non-penetrating states tune through resonance, they may undergo an avoided crossing. The observation of avoided crossings between core-penetrating and core-non-penetrating states proved to be the key to merging the data recorded from the  $A^2\Pi_{3/2}$  and  $C^2\Pi_{3/2}$  intermediates. While the strongest transitions from  $A^2\Pi_{3/2}$  terminated on core-penetrating states and the strongest transitions from  $C^2\Pi_{3/2}$  terminated on core-non-penetrating f-states, levels located nearest the avoided crossings were observed from both intermediates. These local interactions also provided a qualitative measure of the dominant  $\ell$ -character of the states involved.

The detection scheme previously used for low Rydberg states, UV fluorescence detected Optical-Optical Double Resonance spectroscopy, failed above  $n^* \approx 10$  due to the poor fluorescence quantum yield of these Rydberg states and/or the states to which they initially relax. It was necessary to develop a different detection scheme. Chapter 1 describes a laser-ablation molecular beam source and time-of-flight mass spectrometer designed and constructed for the purpose of investigating molecules which do not readily yield to fluorescence-based probes. In the experiments reported here, UV fluorescence detection is replaced by mass-selected ion detection. It should be noted that in addition to the data analyzed here, the apparatus described in Chapter 1 was used to record ID-OODR spectra of CaF  $n^*=17$  and 18 supercomplexes from the  $A^2\Pi_{3/2}$ ,  $v=0$  state, as well as ID-OODR spectra of CaCl  $n^*=16-19$  supercomplexes from its  $A^2\Pi_{3/2}$ ,  $v=0$  state. ID-OODR of CaF spectra have also been recorded up to the  $\text{CaF}^+$ ,  $v^+=1$  threshold from the lowest rotational levels of the  $A^2\Pi_{3/2}$ ,  $v=0$  state.

Chapter 2 outlines the various laser spectroscopic techniques applicable to probing Rydberg states and provides a general overview of the calculations necessary to evaluate the advantages and disadvantages of each technique.

The Hamiltonian model used to determine the extent of  $\ell$ -mixing is developed is the first topic of Chapter 3. The second topic is a discussion of the Rydberg -  $A/C^2\Pi_{3/2}$  transition selection rules and guidelines for assigning ID-OODR spectra. Considerable processing of the raw spectroscopic data was performed before it could be simulated using an effective Hamiltonian model. Line assignments in the ID-OODR spectrum had to be

tested to exclude possible series misidentification. In order for the effective Hamiltonian fit model to produce meaningful results, all members of the  $n^*$ -supercomplex, even the states which were not observed in the ID-OODR spectrum, must be correctly ranked according to their energy. The data input into the effective Hamiltonian fit model had to be tested to insure that observed levels were properly ranked.

Chapter 4 is an analysis and discussion of the  $n^*=13$  and  $n^*=14$  Rydberg state data. The extent of  $\ell$ -mixing is determined by a non-linear least squares fit of experimental data to the model Hamiltonian(s) developed in Chapter 3. The effective Hamiltonian fits were used to determine electrostatic matrix elements between nominally pure- $\ell$  basis states. While the model Hamiltonian matrix cannot describe all of the data to within the accuracy of the experimental measurements, certain subsets of the data are accounted for by the pure- $\ell$  basis state model with  $\ell \leq 3$ . Explanations are provided in cases where the Hamiltonian model falls short. It is now clear that the finite matrix effective Hamiltonian approach has limitations and that Multichannel Quantum Defect Theory (MQDT) provides a more robust treatment of the interaction between the Rydberg electron and the ion-core. Effective Hamiltonian models can provide a platform from which to embark upon an MQDT analysis. The effective Hamiltonian approach appears to be quite satisfactory for modeling extremely strongly core-non-penetrating,  $\ell \geq 4$ , states.

Chapter 5 is an analysis of the linewidths of the 13.36  $\Pi$  and 14.36  $\Pi$ ,  $v=1$  states. Both of these states display an observable line broadening,  $\sim 0.5 \text{ cm}^{-1}$ . The lifetimes of these states deduced from the linewidths are used to determine the derivative of the quantum defect of the 0.36  $\Pi$  series with respect to internuclear separation,  $d\delta/dR$ . The quantum defect derivative of the 0.36  $\Pi$  series determined from lifetime broadening is in excellent agreement with the value calculated by deperturbing a local interaction between the 7.36  $\Pi$ ,  $v=0$  and 6.36  $\Pi$ ,  $v=1$  states [5]. The quantum defect derivatives govern the exchange of energy between the Rydberg electron and the vibration of the molecular cation.

## References

1. S.F. Rice, H. Martin, and R.W. Field, *J. Chem. Phys.*, v.82 (1985), p. 5023.
2. J.E. Murphy, J.M. Berg, A.J. Merer, N.A. Harris, and R.W. Field, *Phys. Rev. Lett.*, v.65 (1990), p.1861.
- 3.. J.M. Berg, J.E. Murphy, N.A. Harris, and R.W. Field, *Phys. Rev. A*, v.48 (1993), p.3012.
4. Z.J. Jakubek, N.A. Harris, R.W. Field, J.A. Gardner, and E. Murad, *J. Chem. Phys.*, v. 100 (1994), p. 622.
5. J.E. Murphy, Ph.D. Thesis, MIT, 1992.
6. N.A. Harris and Ch. Jungen, *Phys. Rev. Lett.*, v.70 (1993), p.2549.
7. P. Bündgen, B. Engels, and S.D. Peyerimhoff, *Chem. Phys. Lett.*, v.176 (1991), p.407.

# CHAPTER 1

## Experimental Apparatus

There are three stages to the CaF Ionization Detected Optical-Optical Double Resonance experiment:

- 1) Production of molecules.
- 2) Preparation of (autoionizing) Rydberg states.
- 3) Detection of CaF<sup>+</sup> ions.

The laser systems used in these experiments are standard equipment for a laser spectroscopy laboratory and their operating characteristics are described at the end of this chapter. The CaF molecules were produced in a laser ablation-supersonic molecular beam source and the CaF<sup>+</sup> ions were detected in a Time-of-Flight Mass Spectrometer. The laser ablation source and Time-of-Flight Mass Spectrometer were new additions to the laboratory. Considerable time was spent developing, constructing, and testing both of these devices and they are described here in reasonable detail. The description is intended as a user's manual for future generations of graduate students and postdocs who will have to work with the equipment.

A schematic of the ablation source and TOF-MS is shown in Fig. 1.1a (Model numbers and additional specifications are given in the following sections.) Figure 1.1b is a photograph of the apparatus. System operating parameters listed in this section are for CaF Ionization Detected Optical-Optical Double Resonance experiments unless otherwise noted. Throughout this chapter, tables of operating parameters list values for additional molecules, in order to quantify the capabilities of the source.

### 1.1 Timing of Events

A timing diagram for the is provided in Appendix I. The description which follows is qualitative. It is intended to help the reader understand the diagram in Appendix I.

The CaF molecules are produced by a reaction of CHF<sub>3</sub> (fluoroform) with a Ca plasma. The ablation laser which generates the Ca plasma must be synchronized with the pulsed valve which provides the fluoroform. It takes the CaF molecules ~65 μs to travel 11 cm in a molecular beam from the point at which they are created to the point at which the Rydberg states are prepared and the CaF<sup>+</sup> ions are extracted into the mass separating region of the mass spectrometer. The two lasers necessary to prepare the Rydberg states must be synchronized to each other and to the arrival of CaF in the probe region. Once the Rydberg states are prepared, they autoionize very rapidly, ~ 1 ns or less. The electric field pulse which extracts the ions into the mass spectrometer is delayed 100-300 ns relative to the laser pulses which prepare the Rydberg states. Once the CaF<sup>+</sup> ions are drawn into the mass spectrometer by the pulsed electric field, it takes them ~17 μs to reach the detector. The detection electronics must be synchronized to the ion extraction pulse.

## 1.2 Pulsed Nozzle Source and Molecule Production

The current ablation source is a second generation device based on an original design by Smalley *et al.* [1]. The ablation source is shown schematically in Fig. 1.2a. Figure 1.2b is a photograph of the source. An expanded view of the pulsed nozzle and the aluminum block which holds the target rod is shown in Fig. 1.2c. While numerous groups have developed more elegant ablation sources [2-6], the present design remains the most economical, least technically complex, and most reliable. Molecules are produced in this source by focusing the 532 nm output of a Q-switched Nd:YAG laser [Spectra Physics DCR-2] to a 1-2 mm diameter spot on a metal target (see Fig. 1.3). The laser generated metal plasma is entrained in a flow of high pressure inert gas which is seeded with a reactant. As the carrier gas mixes with and cools the metal plasma, reactant molecules are fragmented by the hot plasma and react with the metal atoms, resulting in the production of metal containing molecular species. (In the absence of a reactant, the carrier gas collisionally cools the plasma and facilitates the production of the metal clusters.) The high pressure gas mix then undergoes supersonic expansion into high vacuum. The supersonic jet expansion cools translational, rotational, vibrational, and electronic degrees of freedom in the molecules. The molecules are interrogated with one of a variety of spectroscopic techniques after they have undergone jet cooling.

There are several advantages to performing experiments on supersonic jet cooled molecular species and these advantages have been discussed at great length in the literature[7,8]. The principal advantages to the experiments discussed in this document are:

1. Spectral simplification by lowering of rotational temperature so that only  $O(10^1)$  rovibronic levels are populated, as opposed to  $O(10^2-10^3)$  levels in a room temperature source or high temperature oven.
2. Absence of collisions on the time scale of spectroscopic probes.

If its path is uninterrupted, the molecular beam will undergo supersonic expansion into the vacuum chamber for a distance,  $\ell$ :

$$\ell = 0.67d \sqrt{\frac{P_{\text{nozzle}}}{P_{\text{chamber}}}},$$

where  $d$  is nozzle diameter. Carrier gas pressures range from 2-10 atm and the source chamber pressure is typically  $10^{-5}$  Torr. For a nozzle diameter of 0.05 cm, the diameter of the nozzle used in these experiments,  $\ell = O(3 \text{ m})$ . The geometry of the source chamber results in the supersonic expansion being interrupted by the vacuum chamber walls long before it would undergo a shock with the source chamber background gas.

The photoablation source consists of a pulsed valve [General Valve, Series 900], an aluminum block which holds the target rod, and the target rod drive assembly. The target rod drive is made from a 1/4"-80 micrometer screw [Newport Corp. #AJS-2], a telescoping universal joint [Small Parts #UJT-10], and a simple circuit consisting of two microswitches and a relay to periodically reverse the direction of the target rod rotation. An o-ring sealed rotary motion feedthrough [Kurt J. Lesker Co. #FMH-25B] allows the target drive motor to be mounted externally. (The prototype version of the target drive used speedometer cable in place of the telescoping universal-joint. Unfortunately, the cable could not withstand even modest torques and would bind up on itself when the target drive screw offered any resistance.)

The pulsed valve requires  $50 \mu\text{s}$  to open fully (limited by the magnetic field risetime in the solenoid) and  $150 \mu\text{s}$  to close fully. The close time is determined by the mechanical spring used to keep the nozzle in a normally sealed state [9]. Also according to General Valve engineers, 'Open Time' dial settings of  $<150 \mu\text{s}$  on the valve driver control panel will not reliably open the valve. Nominal valve open times in the CaF experiments ranged from 260-320  $\mu\text{s}$  depending upon the nozzle backing pressure. The pulsed valve opens  $\sim 300 \mu\text{s}$  after leading edge of the 'open' pulse. The value of 300  $\mu\text{s}$  was determined by seeding He carrier gas with  $I_2$  and then monitoring  $I_2$  fluorescence excited by a pulsed laser at a fixed point downstream from the nozzle. The velocity of He in a supersonic jet is well determined, 0.177 cm/ $\mu\text{s}$ , so the nozzle open time was measured by observing the

fluorescence intensity as function of the time delay between the nozzle open pulse and the probe laser pulse.

With 50 psig of He backing pressure, optimum CaF production was obtained with an open time of 300  $\mu$ s. The nozzle trigger pulse could be observed as electrical pick-up on the amplified output of the TOF-MS microchannel plate detector. When the source was operating near peak CaF production conditions, the nozzle trigger pulse appeared 5-10  $\mu$ s before the ablation pulse was fired [signal level O(10 mV) w/20 dB pre-amp gain on the MCP's; MCP's operate at  $\sim$ 750 V each]. The timing scheme required to optimize CaF production implies that the Ca plasma plume must be given sufficient time to expand away from the target surface before it is entrained in the flow of high pressure carrier gas-reagent mix. This is somewhat at variance with prevailing wisdom regarding the generation of larger metal clusters ( $>2$  atoms), but consistent with the observation that the use of Ar instead of He markedly reduces the production of CaF. (Metal cluster generation is rumored to be most efficient when ablation occurs while the carrier gas is at its peak density over the metal target.) While the decrease in CaF production with the use of Ar was not quantified, it is estimated to be about an order of magnitude. Several afternoons were devoted to adjusting ablation conditions to improve CaF production using Ar as a carrier gas. Signal levels were so much poorer with Ar than with He, that it did not merit devoting the time to quantify the difference.

The target rod holder depicted in Fig.1.2b is an aluminum block in which three channels are drilled. A 1 mm channel meets the 0.5 mm orifice of the pulsed nozzle and allows the carrier gas to travel to the point of ablation. The channel expands to 2 mm diameter at the three-way with the 0.257" dia. target rod channel. Expanding the carrier gas channel at the point of ablation reduces the rate at which ablated material clogs the channel [10]. The carrier gas channel extends approximately 7 mm past the point of ablation and serves as the reaction region for the metal plasma and oxidant entrained in the carrier gas. The target rod channel has Teflon inserts to prevent galling of the target rod on the metal target holder block. Galling did not prove to be a problem when using Ca, but was an issue for more refractory metals such as V and Mo with a stainless steel, rather than Al, target block. The target rod is rotated at 15 RPM by a high torque motor (Bodine Electric, Type KYC-24T5, 1 $\Phi$ , 48 oz.-in.). Slowing the rotation increases production of molecules, however the shot-to-shot fluctuations in production are also increased.

The ablation laser beam is focused with a 1.0 m focal length lens to a spot 1.0-2.0 mm in diameter. A considerable amount of ablation light scatters off of the target holding block, so it is difficult to determine precisely how much ablation laser energy is input to the target surface. CaF production was most efficient with 5-8 mJ focussed on the target. The



ablation pulse energy was measured (unfocussed) prior to entering the source chamber. The ablation spot size was determined by placing a piece of black paper in the source chamber at the position of the target rod and measuring the diameter of the burn spot.

The target rod was placed well before the laser focus. Placing the target rod at the beam focus results in enormous shot-to-shot fluctuations in CaF production. Ablating a larger surface area reduces shot-to-shot fluctuations because the surface area on a 1-2 mm length scale is much more homogeneous than the area on a 0.1 mm length scale. CaF production does not increase monotonically with ablation laser power. There is an abrupt onset of signal corresponding the ablation threshold ( $\sim 1/2$  of the optimum laser power), a steady rise in signal with increasing ablation laser power, and then a monotonic decrease in signal with increasing power. There is essentially zero signal when ablating with more than twice the optimum laser flux ( $\text{J cm}^{-2} \text{ s}^{-1}$ ). The optimum flux for CaF production varies  $\sim 20\%$  from day-to-day due to degradation and annealing of the target surface. The optimum flux is also weakly dependent on the carrier gas pressure behind the pulsed nozzle. The CaF number density and Boltzmann temperature does not vary significantly over the range of 40-80 psig He. Increasing the nozzle pressure from 40 to 50 psig improves signal levels slightly,  $\sim 10\%$ . Increasing the nozzle backing pressure from 50 to 80 psig of decreases the CaF signal level by 20-30%. When generating metal dimers, higher backing pressures, 80-120 psig, are necessary (see Table 1.1). Operating at the lowest possible ablation pulse energy prevents surface annealing (a laser annealed surface ablates poorly) and clogging of the reaction channel. These advantages must be balanced against the fact that lower pulse energies give rise to larger shot-to-shot fluctuations in molecule number density. Using too much laser power results in the production of ions and hot atoms which do not react efficiently to form the desired molecules.

The alignment of the ablation laser may be checked in several ways. The simplest method is to strategically place a mirror so that the experimenter has a direct line of sight down the molecular beam path. The experimenter can approximately align the ablation beam by observing ablation laser scatter or plasma emission down the beam axis. The ablation laser scatter may be blocked entirely by an appropriate pair of laser safety goggles, OD 5-6 @ 532 nm. [The goggles must however transmit a visible atomic emission line, *e.g.* Ca (422 nm).] Ablation beam alignment is optimized by maximizing observed plasma emission. This procedure is NOT necessarily equivalent to maximizing ablation laser scatter down the molecular beam axis. The scattered light viewed down the beam axis is typically quite weak and is often difficult to observe in a brightly lit room.

A more sophisticated way to optimize photoablation beam alignment is to observe the Resonance Enhanced Multiphoton Ionization generated mass spectrum of the products in the

molecular beam. When the ablation beam is misaligned, water and calcium based detritus is ablated from the wall of the ablation channel resulting in the creation of  $\text{Ca}_x(\text{Ca}_2\text{O})_m(\text{OH})_n$  clusters. These clusters are easily ionized by multiphoton (most probably two photon) absorption of UV light. Figure 1.4 shows REMPI generated mass spectra recorded using a Ca target rod and He carrier gas. The mass spectra in Fig.1.4 were generated using He carrier gas seeded with  $\text{CHCl}_3$  for the purpose of producing CaCl. The REMPI scheme using UV light is preferentially sensitive to larger clusters. Larger clusters have a more continuous absorption spectrum than smaller molecules. Smaller molecules have sharp absorption lines which, in order to be ionized, must fall within linewidth of the ionizing laser.

The two carrier gases used in photoablation molecule production were He or Ar. Ar is closer in mass to the metal and is therefore more efficient at collisionally cooling the metal plasma. Unfortunately, the fact that Ar is heavier than He also appears to make it quite efficient at returning atoms in the metal plasma back onto the target surface via collisions. The conditions for production of several different species in the photoablation source are listed in Table 1.1.

Figure 1.5 depicts the ionization detected  $\text{A}^2\Pi_{3/2} - \text{X}^2\Sigma^+(0,0)$  laser absorption spectrum. Resonances in the A-X(0,0) band are detected by ionizing the excited levels with a fixed frequency UV laser. The spectrum is equivalent to a fluorescence excitation spectrum. The effective rotational temperature in the molecular beam is determined by analysis of the intensity of the lines in the  $\text{P}_2$  branch. The lines in the the  $\text{Q}_2 + \text{P}_{21}$  braches are not used because the transitions are not baseline resolved and therefore it is more difficult to obtain an accurate intensity measurement. To an excellent approximation, the intensity of a  $\text{P}_2(\text{J})$  line is proportional to the population of the level J in the ground state:

$$I[\text{P}_2(\text{J})] = \text{A}(2\text{J}+1) \exp\left(-\frac{\text{E}_{\text{rot}}(\text{J})}{\text{kT}_{\text{rot}}}\right), \quad (1.1)$$

where k is the Boltzmann constant and  $\text{T}_{\text{rot}}$  is the effective rotational temperature. The rotational temperature may be determined by inverting Eq(1.1) and making the substitution  $\text{E}_{\text{rot}}(\text{J}) = \text{B}(\text{J} + \frac{1}{2})(\text{J} + \frac{3}{2})$ , where B is the rotational constant of  $\text{X}^2\Sigma^+$ ,  $\text{v}=0$ :<sup>1</sup>

$$\ln \frac{I[\text{P}_2(\text{J})]}{2\text{J}+1} = -\frac{\text{B}(\text{J} + \frac{1}{2})(\text{J} + \frac{3}{2})}{\text{k}} \frac{1}{\text{T}_{\text{rot}}} + \ln(\text{A}) \quad (1.2)$$

<sup>1</sup> The J quantum number dependence of rotational energy levels in  $^2\Sigma^+$  states is well established. Interested readers are referred to Ref.[11], [12], or Chapter 3 of this text.

The quantity on the RHS of Eq.(1.2),  $y$ , is plotted versus  $B(J+\frac{1}{2})(J+\frac{3}{2})/k$ ,  $x$ , and fit to a line,  $y = mx + b$ . The slope of the line is the negative reciprocal of  $T_{rot}$ . Determination of  $T_{rot}$  from the data obtained from Fig.1.5 is displayed in Fig.1.6. The effective rotational temperature of CaF generated in 50 psig He is  $130 \pm 5$  K.

Table 1.1 Ablation Source Operating Parameters for Various Molecules\*

	CaF	CaCl	Al <sub>2</sub>	Cu <sub>2</sub>	Mo <sub>2</sub>
Ablation $\lambda$ / nm	532	532	532	532	532
Pulse Energy / mJ	5-8	5-25/35	8	(18/15/9)	26
Carrier Gas	He(Ar)	He	He(Ar)	(Ar)	He
Gas Pressure / psig	42-65(33)	48/90	80(60)	(42/56/56)	80-120
Lowest Observed $T_{rot}$ / K	130(25)	-	10-15	5	-
Reactant	CHF <sub>3</sub> (SF <sub>6</sub> )	CHCl <sub>3</sub>	-	-	-
Reactant Pressure	$p_{He}/20(**)$	~200 torr	-	-	-
Rxn. Channel Length / mm	5-7	5-7	17(17)	(8/17/8)	-
Rxn. Channel Dia. / mm	2	2	2	2	2
Nozzle Open Setting / $\mu$ s	280-360	300- 320/260	450 (300)	(300-400)	260-360

\* Quantities in parentheses are for Ar as carrier gas.

\*\* The optimum SF<sub>6</sub> concentration was determined by monitoring Ca 4p <sup>1</sup>P - 4s <sup>1</sup>S emission and 'titrating' the fluorescence excitation signal by adding SF<sub>6</sub> to the Ar carrier gas. The CaF number density was nearly maximized at the titration point.

### 1.3. REMPI-TOFMS System

An equipment list with vendors and 1992 purchase prices may be found in Appendix II.

#### 1.3.1. Source Chamber

The REMPI-TOFMS vacuum system was constructed entirely from commercially available equipment. The source chamber is a modified MDC 14" six-way cross (MDC Part# L1200-6) with "LF"-style flanges. ("LF" is the MDC brand name, identical flanges are manufactured by competing manufacturers.) The source chamber is pumped by a Varian VHS-10 diffusion pump, which has a pumping speed of 5700  $\ell/s$  for air, 6600  $\ell/s$  for He, and a maximum throughput of 7.7 Torr  $\ell s^{-1}$ . The effective pumping speed is somewhat reduced by the aluminum gate valve used to separate the source chamber from the pump[13].

The maximum permissible backing pressure in the pulsed nozzle is calculated using the diffusion pump throughput specified by Varian [13] and the known velocity of He in a free jet expansion. In a supersonic jet expansion, gas leaves the nozzle orifice at the local speed of sound, which for a monatomic gas is:

$$v_s = \sqrt{\frac{C_p RT}{C_v M}} = \sqrt{\frac{5 RT}{3 M}} \quad (1.3)$$

At 300 K, the nozzle exit velocity is 1.019 mm/ $\mu s$  for He and 0.322 mm/ $\mu s$  for Ar. The gas flux into the chamber is the product of the gas pressure behind the nozzle orifice, the gas velocity out of the orifice, the orifice area, the pulse duration, and the pulse repetition rate:

$$Q_{\text{nozzle}} = P_{\text{nozzle}} v A \tau R \quad (1.4)$$

The flux into the source chamber may not exceed the maximum throughput of the diffusion pump. The calculated maximum permissible nozzle pressure is:

$$P_{\text{nozzle}}^{\text{MAX}} = \frac{Q_{\text{MAX}}}{v A \tau R} = \frac{7.7 \text{ torr } \ell s^{-1}}{(1.0 \cdot 10^5 \text{ cm s}^{-1})(2.0 \cdot 10^{-3} \text{ cm}^2)(5 \cdot 10^{-4} \text{ s})10 \text{ Hz}} \cdot \frac{10^3 \text{ cm}^3 / \ell}{760 \text{ torr / atm}} \approx 10 \text{ atm He}, \quad (1.5)$$

for 500  $\mu s$  duration pulses of He occurring at 10 Hz. Readers interested in calculating vacuum system performance characteristics are advised to consult Refs.[14] and [15].

The source chamber may be isolated from the diffusion pump by a 10" ASA flanged electro-pneumatic gate valve (VRC LP Series, Part#94578-101). The gate valve is wired as "normally closed", meaning that it is sealed when it is not energized. The valve is operated in the normally closed configuration so that it will automatically seal in the event

of a power failure. The valve seals completely only when it is provided with at least 70 psig to the sealing piston. Care must be taken to insure that the supply of compressed air to the electro-pneumatic valve is maintained at  $\geq 70$  psig.

### 1.3.2. Time-of-Flight Mass Spectrometer

The Time-of-Flight Mass Spectrometer (TOF-MS) was manufactured by R.M. Jordan Co. (Grass Valley, CA) and is very similar to one of their standard production instruments, Model#C-677. The instrument was custom modified to operate in conjunction with the laser ablation source. Many of the comments in this section apply specifically to the R.M. Jordan Co. mass spectrometer and related electronics. These comments are intended to augment the literature provided by R.M. Jordan Co. The mass spectrometer consists of an ion extraction region, an ion acceleration region, an ion flight tube, and a dual microchannel plate (MCP) detector. The spectrometer is represented schematically in Fig.1.7. The extraction region is defined as the space between the extraction and acceleration grids. The acceleration region is the space between the acceleration and ground grids.

The two modifications of the present instrument relative to the R.M. Jordan Co. Model C-677 are: 1) extension of the flight tube and ion extraction region past the normal flange mounting point so that the extraction region is located in the geometric center of the ablation chamber and 2) the use of an oversize diameter ion flight tube so that the instrument may be upgraded to a "reflectron" mass spectrometer [16] at a later date. The reflectron upgrade will require remounting the flight tube, welding a new MCP mounting flange, and mounting reflection grids at the current position of the MCP detector [17].

The dual MCP detector was supplied with the TOF. Each MCP was manufactured by Galileo Electro-Optics [Part# 1330-1820] and has an active area of  $\sim 5.0$  cm<sup>2</sup>. The gain of each plate is +200 at -700 V and +4300 at -1000 V. The overall gain of the detector is the product of the gain of the individual plates. The TOF-MS is pumped by a liquid nitrogen (LN<sub>2</sub>) trapped 5-1/4" throat diffusion pump (NRC Model # UNKNOWN, first three digits are 018; 120 VAC, 1450W) operating with DC-704 or DC-705 silicone oil. (DC-705 oil is rated as having a lower ultimate pressure, however the o-ring seals on the mass spec chamber are sufficiently permeable to air that the chamber never reaches the limiting pressure of either the DC-704 or 705 oils.) The LN<sub>2</sub> trap was manufactured by Cook Vacuum Products and purchased from Kurt J. Lesker Co., Part# LNT-4201LL. The LN<sub>2</sub> trap and diffusion pump are mounted to the flight tube on 4" ASA flanges. The effective

pumping speed of the LN2 trap-diffusion pump combination is  $\sim 350$  l/s [11]. The diffusion pump is backed by a 26.8 CFM mechanical pump (Leybold-Heraeus D-30A). The base pressure in the flight tube is  $\sim 2 \cdot 10^{-7}$  Torr with no gas load and  $\sim 7 \cdot 10^{-6}$  Torr under normal operating conditions (4 atm He @ 10 Hz, 300-400  $\mu$ s per pulse from pulsed nozzle) as measured with a nude ionization gauge (Duniway Stockroom Model I-075-P w/Granville-Phillips 271-004 gauge controller). The ionization gauge reading listed here has been corrected for gauge sensitivity to He [14].

The power supplies which provide all high voltages to the mass spectrometer are interlocked to the ionization gauge controller. The ionization gauge controller operates a relay which provides power to the HV power supplies. The controller is set so that when the pressure in the ion flight tube rises above  $1 \cdot 10^{-5}$  Torr, all voltages in the mass spec are turned off. The interlock circuit is described in the Granville-Phillips operating manual. (The high voltages are not immediately grounded, but decay to ground with the time constant of the particular circuit to which they are attached.) Interlocking the HV power supplies to ionization gauge controller helps to protect the MCP detector from accidental exposure to atmosphere. The MCPs will arc over (self-destruct) when exposed to pressures  $O(10^{-4}$  Torr) [18].

The molecular beam is skimmed by 0.5 mm dia. molecular beam skimmer (Beam Dynamics, Inc., St. Paul, MN)  $\sim 10$  mm after it leaves the ablation channel. The skimmed beam of neutral enters the ion extraction region of the TOF-MS. The species are interrogated in the center of the extraction region, halfway between the extraction and acceleration grids. Figure 1.8s depicts the photoablation source in relation to the ion extraction region of the TOF-MS. The ion extraction region is shown in a cut-away view. The scale of Fig.1.8a is approximately 2:1. Figure 1.8b is a photograph of the ion extraction region and photoablation source in the source chamber. Figure 1.9 is a scale drawing of the ion extraction region. The separation between the extraction and acceleration grids, as well as the acceleration and ground grids is 1.27 cm.

The extraction (a.k.a. repeller) and acceleration grids are normally held at a DC voltage  $\sim 1500$  V. After ions are created by REMPI or double resonance excitation, a brief DC pulse applied to the repeller plate sweeps the ions into the acceleration region. The extraction pulse exceeds the DC bias of the extraction and acceleration grids by  $\sim 165$  V. (The particular extraction voltage used will be discussed later in this section.) The extraction pulse has rise and fall-times of  $\sim 20$  ns and an adjustable duration which is usually kept at  $\sim 5$   $\mu$ s. It takes the ions  $\sim 1$   $\mu$ s to move from their point of formation to the acceleration region with the above mentioned operating parameters. R.M. Jordan Co.

claims that operating their high voltage pulser<sup>2</sup> biased at >1500 V increases the risk of pulser FETs and internal power supply shorting out. Higher voltages increase the risk of electrical discharge between the repeller and acceleration grids or between the HV lead wire external to the ion extraction assembly shroud, but internal to the vacuum chamber. The high voltage pulser is designed to drive a high impedance, O(100 M $\Omega$ ), load. Electrical discharge reduces the impedance to near zero, causing the Pulser to attempt to maintain its output voltage at an extremely high current and subsequently short itself out. This claim was validated in the autumn of 1993 when operating with pulser biased at +2500 V, the extraction pulse voltage at +270 V, and photoablating Mo with He carrier gas to produce Mo<sub>2</sub>. Residual Mo<sup>+</sup> from the photoablation process initiated arcing between the lead wires to the repeller and ground grids, resulting in the shorting out of ALL semiconductors inside the Remote Pulser. This problem was solved coating the exposed lead wires to the ion extraction region with RTV silicone sealant.

The ion extraction assembly (repeller, extractor, and ground grids) is covered in a Ni-plated shroud. An Au-plated shroud is also available for use and may be interchanged by disconnecting the lead wires to the ion extraction assembly and removing the appropriate mounting screws. The process requires essentially complete dismantling of the portion of the mass spectrometer residing in the Source Chamber. The change-over process is time consuming, but not technically difficult. Extra care must be taken not to break the electrical lead insulating tubes. The tubes are made of Alumina and are fairly brittle. If a tube should break, it may be replaced with a thermocouple wire insulating tube (available in standard diameters, but custom lengths from Omega Engineering). The Au-plated shroud was the shroud originally installed in the mass spec. It was replaced when using Hg in the molecular beam, as Hg is known to contaminate Au.

The molecular beam axis is normal to TOF-MS axis. When neutral species travelling in the beam are ionized, they must be accelerated in the direction of the MCP detector. The ions gain virtually all of their detector-directed kinetic energy between the acceleration and ground grids. After leaving the acceleration region, the ions travel at a constant velocity down the 1.2 m flight tube to the dual microchannel plate detector. The point of ion formation and the center of the MCP detector (should) define a line parallel to the floor of the laboratory. The ions have an initial velocity in the direction of the molecular beam, i.e. normal to line defined by the point of formation and the detector center. The extraction and acceleration fields are oriented normal to the molecular beam direction. The application of

---

<sup>2</sup> The high voltage pulser is referred to as the "Remote Pulser" in the R.M. Jordan Co. product literature. It is a 5" x 4" x 1" black box with 3 SHV and 2 BNC connectors as is placed in series between the repeller grid and HV power supply.

these fields will turn the ion flight path by  $<90^\circ$ . In order to direct the ions into the detector (and to simulate a  $90^\circ$  turn) the ions' residual translational velocity in the direction of the molecular beam is compensated for by deflection grids located immediately after the acceleration region. The velocity of the molecules in the molecular beam is nearly that of a beam of the pure carrier gas,  $0.177 \text{ cm}/\mu\text{s}$ . Ion flight times are  $O(10 \mu\text{s})$ , so the application of extraction and acceleration fields without xy-compensation beam could easily result in the ion packet missing the detector: distance traveled in the direction of the molecular beam during transit to the detector =  $10 \mu\text{s} \cdot 0.177 \text{ cm}/\mu\text{s} \approx 2 \text{ cm} \approx$  diameter of MCP detector.

The mass spectrometer is based on the design of Wiley and McLaren [17]. Wiley-McLaren mass spectrometers are "space focused" instruments. A space focused TOF-MS has its operating voltages set so that ion flight times are as insensitive as possible to the point of ion-formation, and hence kinetic energy acquired, in the extraction region. The advantages of this design are high mass resolution and simplicity of construction (no magnetic fields, pulsed electric field optional). Ions produced in the extraction region of the mass spectrometer are identified by their time of flight from their point of origin to the detector. Wiley and McLaren derived a formula for the ion flight time as a function of spectrometer dimensions and electric fields (The instrument dimensions listed subsequent to Eq.(1.6) are those of the R.M. Jordan Co. mass spectrometer and are included for the purpose of quantifying its operating characteristics.):

$$t = 1.018 \sqrt{\frac{M}{2U_{\text{ex}}}} \left[ 2\sqrt{k}x_e + \frac{2\sqrt{k}}{\sqrt{k}+1}x_a + x_d \right], \quad (1.6)$$

$t$  = ion flight time [ $\mu\text{s}$ ],

$M$  = ion mass [amu],

$U_{\text{ex}}$  = ion kinetic energy [eV],

$x_e$  = distance traveled in extraction region  $\approx \frac{1}{2} \cdot 1.27 \text{ cm}$ ,

$x_a$  = distance traveled in acceleration region =  $1.27 \text{ cm}$ ,

$x_d$  = length of drift region =  $117 \text{ cm}$ ,

$$U_{\text{ex}} = q[x_e E_e + x_a E_a], \quad (1.7)$$

$$k \equiv \frac{x_e E_e + x_a E_a}{x_e E_e}, \quad (1.8)$$

$E_e$  = Extraction Field [V/cm],



$E_a =$  Acceleration Field [V/cm].

The space-focusing criterion is determined by differentiating Eq.(1.6) and setting the derivative equal to zero:

$$\frac{\partial t}{\partial x_e} = 0. \quad (1.9)$$

In order for Eq.(1.9) to be a minimum, the second derivative of  $t(x_e)$  must be greater than zero:

$$\frac{\partial^2 t}{\partial x_e^2} > 0. \quad (1.10)$$

Equation (1.9) may be used to determine the optimum drift tube length for a particular set of extraction and acceleration voltages and separations between the extraction, acceleration, and ground grids:

$$x_d(\text{optimum}) = 2x_e \sqrt{k^3} \left[ 1 - \frac{1}{k + \sqrt{k}} \frac{x_a}{x_e} \right]. \quad (1.11)$$

Equation (1.11) may also be inverted to determine the parameter  $k$ , where  $k$  is defined by Eq.(1.8). It is convenient to express  $k$  in terms of the ratio of acceleration to extraction voltages. The ratio of acceleration to extraction voltages is defined here as  $p$ . For the extraction-acceleration configuration pictured in Fig.(1.7) with  $x_a = 2x_e$ ,  $k = 1 + 2p$ . When  $p \gg 1$ ,

$$x_d(\text{optimum}) \cong x_a \sqrt{8p^3} \left[ 1 - \frac{2}{2p + \sqrt{2p}} \right] \cong \sqrt{8p^3} \cdot x_a = \left( \frac{8E_a}{E_e} \right)^{3/2} x_a. \quad (1.12)$$

For an acceleration-to-extraction field ratio of 10 and an acceleration-ground grid separation of 1 cm, the optimum flight tube length is approximately 90 cm. The question arises, "Why not more evenly match the acceleration and extraction fields and keep both fields low to lengthen the ion flight time, thereby shortening the optimum length of the flight tube?" The answer to this question lies in Eq.(1.10). Equation (1.9) is a minimum only when Eq.(1.10) is satisfied. Space-focussing [19] requires:

$$x_a < \left[ \frac{k-3}{k} \right] \frac{x_d}{2}. \quad (1.13)$$

or, in terms of the parameter, p,

$$x_a < \left[ \frac{p-1}{1+2p} \right] x_d. \quad (1.14)$$

When the extraction and acceleration voltages are equal,  $p = 1$  and the space focussing criterion can never be met. Similarly, the space focussing criterion can never be met when the extraction voltage exceeds the acceleration voltage. Numerous researchers have sought to improve mass resolution by incorporating a time dependence of spatial gradient to the extraction or acceleration fields [20 and refs. therein]. Improvements in mass resolution can be significant, such would probably not be noticable in the present experiments because they do not push the performance limits of the existing system.

The length of the flight tube could be shortened by choosing a slightly larger extraction to acceleration field ratio. For an acceleration voltage twice the extraction voltage,  $p = 2$ , the flight tube length need only be 5 times the separation of the acceleration and ground grids to satisfy the space focussing condition. The consideration turns now from space-focussing to mass resolution. Wiley and McLaren also show that the maximum  $m/z$  for which adjacent mass peaks are resolvable is

$$M_{\max} / \text{amu} \approx 16k \left( \frac{x_e}{\delta x_e} \right)^2 \leq 16[1+2p]. \quad (1.15)$$

For the case of  $p = 2$ , Eq.(1.15) shows the maximum  $m/z$  is  $\sim 80$ . The R.M. Jordan Co. instrument is designed for resolution of  $m/z \leq 300$ . Such resolution requires  $p \sim 10$  and, from Eq.(1.12), a longer flight tube. Since the geometry of the mass spectrometer is fixed,  $p$  is adjuxted by varying the voltage applied to the acceleration and extraction grids. The manufacturer did not provide an optimum value of  $p$  in the instrument operating manual, so  $p$  must be determined by plotting the LHS and RHS of Eq.(1.11) versus  $p$  and finding the point of intersection, as shown in Fig.(1.20). For this mass spectrometer, the optimum acceleration to extraction field ratio is 10.24:1. A variety of molecular species that have been generated in the ablation source. The flight times of those molecules under standard

operating conditions (see Table 1.2, operating parameters for CaF production) is depicted in Fig.1.11.

The variation in ion arrival time with distance traveled in the extraction region can be determined by differentiating Eq.(1.5) with respect to  $x_e$ . The variation in arrival time with distance travelled in the ion extraction region is important for two reasons:

- 1) Quantifying the loss of mass resolution due to the inevitable creation of a physically large,  $\geq 1$  mm dia., ion packet in the extraction region.
- 2) Quantifying the change in arrival time of a particular mass due to changes in position of the ionizing laser. What happens when the ionizing laser beam is misaligned by 0.5 mm?

The term in brackets on the RHS of Eq.(1.6) is:

$$2\sqrt{k}x_e + \frac{2\sqrt{k}}{\sqrt{k}+1}x_a + x_d \approx x_d. \quad (1.16)$$

Equation (1.6) is therefore well approximated as:

$$t = 1.018 \sqrt{\frac{M}{2U_{\text{tr}}}} x_d. \quad (1.17)$$

The dependence of arrival time on  $x_e$  may be expressed in terms of partial derivatives,

$$\frac{\partial t}{\partial x_e} \approx \left( \frac{\partial t}{\partial U_{\text{tr}}} \right) \left( \frac{\partial U_{\text{tr}}}{\partial x_e} \right). \quad (1.18)$$

The partial derivatives in Eq.(1.18) may be determined from Eq.(1.17):

$$\frac{\partial t}{\partial U_{\text{tr}}} = -\frac{t}{U_{\text{tr}}}, \quad (1.19)$$

and,

$$\frac{\partial U_{\text{tr}}}{\partial x_e} = qE_e. \quad (1.20)$$

Substitution of Eqs.(1.19) and (1.20) into Eq.(1.18) yields:

$$\frac{\partial t}{\partial x_e} \approx -\frac{qE_e}{U_r} t = \frac{-E_e}{x_e E_e + x_s E_s} t. \quad (1.21)$$

The change in ion arrival time due to changes in the point of formation of the ion packet is then:

$$\Delta t = \frac{-E_e}{x_e E_e + x_s E_s} t \Delta x_e. \quad (1.22)$$

After consulting Table 1.2 to determine values of  $E_e$  and  $E_s$  to use in Eq.(1.22), one discovers that moving the point of ionization 0.5 mm closer to the acceleration grid would cause  $\text{CaF}^+$  ions to arrive at the detector ~40 ns later than if they had been created precisely half way between the extraction and acceleration grids. Fortunately, 40 ns corresponds to only 0.3 amu at  $M = 59$  amu.

Differentiating Eq.(1.11) with respect to  $M$  yields,

$$\frac{\partial t}{\partial M} = \frac{t}{2M}. \quad (1.23)$$

Equations(1.21) and (1.23) may be combined and expressed in differential form to see how the width of a mass peak,  $\delta M$ , is dependent upon the spatial width of the initial ion packet,  $\delta x_e$ :

$$\delta M = 2M \left| \frac{E_e}{x_e E_e + x_s E_s} \right| \delta x_e. \quad (1.24)$$

Mass resolution is lost when  $\delta M \geq 1$  amu. Assuming an unfocussed ionization laser beam intersecting the molecular beam,  $\delta x_e \approx 0.05$  cm, and the typical operating voltages listed in Table 1.2,  $\delta M = 1$  amu when  $M \approx 200$  amu. Figures 1.12a and 1.12b depict the 1+1 REMPI generated mass spectrum of  $\text{Mo}_2^+$ . The spectrum was recorded using a focussed laser beam, i.e.  $\delta x_e \ll 0.05$  cm. Figure 1.12a shows ion signal as a function of arrival time. In Fig.1.12b, ion arrival time has been converted to mass-to-charge ratio. The intensity of the mass peaks in Figs.1.12a and b do not mirror the natural abundance of  $\text{Mo}_2$  isotopomers because those isotopomers having absorption transitions resonant with the PROBE laser wavelength are preferentially ionized.

Table 1.2 Operating Voltages for Time-of-Flight Mass Spectrometer

PARAMETER	CaF	CaCl
Mass[amu]/Charge[Z]	59	75, 77
Repellor Voltage	+1500 V *	+1500 V*
Extraction Pulse Voltage	+165 V *	+185 V *
Extraction Pulse Duration	1.5 $\mu$ s	
x-y Deflector Voltage	+50 V *	+65 V*
Flight Tube Liner Voltage	+100 V	
MCP Bias Voltage	-1400V~-1750V	-1450V~-1700V

\* Relative to flight tube liner voltage. The flight tube liner voltage and MCP bias voltages are relative to laboratory ground.

The gain of the dual microchannel plate detector biased at -660 V/plate is  $\sim 8 \cdot 10^4$ . The detector has an output impedance of 50  $\Omega$ . The detector output is sent directly into a Hewlett-Packard 461A preamplifier (50  $\Omega$  input impedance, 0-150 MHz frequency response) operating with +20 dB gain. The amplified signal is sent to a boxcar signal averager (SRS Model 250) and is simultaneously monitored on a 150 MHz analog oscilloscope (Tektronix Model 2450). With MCP detector biased at -660 V/plate, the preamplifier produces a 1.5 V peak signal at MCP saturation. Useful signal levels, as monitored on the oscilloscope, are in the range of 0.1-1.0 V under these conditions. Care must be taken not to saturate the detector by exposing it to unnecessarily high ion fluxes. The microchannels will eventually become clogged by the deposition of ions on the detector surface. The microchannel plates cost O(\$1000) each to replace, so it is wise to extend the detector lifetime as much as possible.

The temporal profile of the ion peaks appears pseudo-Gaussian with a FWHM of 20-100 ns when the intensity of the ionization laser is uniform over the width of the molecular beam. Spatial inhomogeneities in the ionization beam profile produce temporal inhomogeneities (rising edges or tails) in the ion signal at the detector. This is a result of the space focussing condition of the Wiley-McLaren design, Eqs.(1.6) and (1.21). The boxcar averaged signal is sent to a 12 bit A/D converter and then recorded on a personal computer (Quantex 386, 40 MHz w/ a Data Translation data acquisition board).

## 1.4. Lasers and Wavelength Calibration

Two different tunable dye lasers have been used for ID-OODR spectroscopy of CaF: a Lumonics HyperDye 300 and a Lumonics HyperDye 550. Both dye lasers were pumped by a Spectra Physics DCR-1A Nd:YAG. A block diagram of the laser table with the HyperDye 300 and 550 arrangement is shown in Figure 1.13. The diagram is approximately to scale with 1" approximately equal 3'. The Spectra Physics YAG lasers were operated without any custom modifications and operated within the parameter space specified by Spectra Physics. The DCR-1A was manufactured in 1980 and because of its age required considerably more maintainance than the other lasers in the lab. Specific repairs and maintainance procedures are described in its logbook.

The Lumonics dye lasers have Littman-design oscillators [21] and are also run in the oscillator-amplifier configuration. The oscillator cavity mode spacing is  $0.018 \text{ cm}^{-1}$  (6 GHz) [22]. Typically three longitudinal cavity modes survive in the HyperDye oscillators, although these modes are not fully developed due to the fact that the dye gain is extracted for the dye after only several cavity round trips. Appendix 4.A of Ref.[22] includes a single-shot linewidth measurement of a HD-300 using a Fabry-Perot etalon . The HyperDye oscillator behaves as a hybrid between a grating spectrometer and a stable laser resonator.

Both the HyperDye 550 (HD550) and HyperDye 300 (HD300) were run with the oscillator and amplifier dye circulation separated so that the oscillator and amplifier dye concentrations could be varied separately. (Lumonics ships those lasers with a single dye circulator for the oscillator and the amplifier.) When using a line in the  $A^2\Pi_{3/2}-X^2\Sigma^+(0,0)$  band as a PUMP transition, the HD550 was used as the PUMP laser. The wavelength of the PUMP transition is A-X(0,0) PUMP is  $\sim 603.9 \text{ nm}$ . Kiton Red 620 (Exciton, Dayton OH) was used in the oscillator ( $\sim 2.0 \cdot 10^{-4} \text{ M}$  in methanol) and amplifier ( $\sim 1.5 \cdot 10^{-4} \text{ M}$  in methanol). The longest wavelength which could one-photon ionize the  $A^2\Pi_{3/2}$  level excited by the PUMP was  $\sim 328.5 \text{ nm}$ . The PROBE laser used in conjunction with the  $A^2\Pi_{3/2}$  PUMP is the HyperDye 300. The HD300 was operated with 200 mg/l DCM (Exciton, Dayton OH) in 4:1 Methanol/Propylene Carbonate in the oscillator and 150 mg/l DCM in 4:1 Methanol/Propylene Carbonate in the amplifier. In order to generate the UV PROBE wavelength, the output of the HD300 was frequency doubled by an angle tuned  $\beta$ -BBO crystal. The doubling range of the crystal is approximately 540-700 nm. The conversion of red to UV was found to be fairly efficient near the peak of the DCM gain curve. It was found that with 73 mJ of 532 nm pump excitation from the YAG ( $\sim 10\%$  to the oscillator), the HD300 would produce 6-7 mJ of red and 700-800  $\mu\text{J}$  of UV. The UV power used in

the ID-ODR experiment was typically  $<100 \mu\text{J}$ . As the HyperDye wavelength was scanned, the UV output power was maximized with an active feedback 'autotracker' circuit based on a design of Ref.[23].

When a line in the  $\text{C}^2\Pi_{3/2}-\text{X}^2\Sigma^+(0,0)$  band was used for the PUMP transition, the HD300 became the PUMP laser and the HD550 was used as the PROBE. The PUMP wavelength was  $\sim 330.9 \text{ nm}$ , which meant that DCM was still used in the HD300. The longest wavelength which could one-photon ionize the  $\text{C}^2\Pi_{3/2}$  level excited by the PUMP is  $\sim 596.3 \text{ nm}$ . The HD550 was run with Rhodamine 610 in the oscillator ( $\sim 2.0 \cdot 10^{-4} \text{ M}$  in methanol) and amplifier ( $1.0\text{-}1.5 \cdot 10^{-4} \text{ M}$  in methanol).

Absolute wavelength calibration of the dye lasers was accomplished by recording fluorescence excitation spectra of  $\text{I}_2$  or optogalvanic spectra of Ne. The iodine fluorescence excitation spectrum was recorded by observing emission well to the red of the excitation wavelength. The absolute  $\text{I}_2$  linepositions were taken from Ref.[24]. Laser scatter was greatly reduced by place a 'red-pass' filter before the photomultiplier tube. The output of the PMT (typically a Hamamatsu R928 biased at  $\sim 700 \text{ V}$ ) was sent directly to an SRS 250 boxcar and was conditioned in the same manner as the signal from the microchannel plate detector.

The optogalvanic spectra of Ne were recorded by focussing  $O(10 \mu\text{J})$  of PROBE laser light into the discharge region of a Ne hollow cathode lamp. It was necessary to focus the beam in order to observe two-photon absorptions in Ne. Low powers were essential because higher powers ablated the cathode, resulting in electrical noise which swamped the optogalvanic signal. A electronic circuit for use with Ne optogalvanic detection may be found in Ref.[22]. Relative wavelength calibration was accomplished with a  $0.67 \text{ cm}^{-1}$  free spectral range etalon (Optics for Research, Stock#IE-5.0-R4; 1" dia., VIR coating  $\geq 90\%$  reflective from 550-780 nm, finesse=10). The atomic lamp used for optogalvanic spectroscopy is a Photron P863 U/Ne lamp sold by Starna Cells, Inc. of Atascadero, CA. The technique was found to work quite satisfactorily for modest laser powers. One-photon transitions in Ne are well documented [25]. The optimum discharge current depends upon which Ne metastable level the optogalvanic transition originates from. The higher energy the level, the higher the requisite discharge current. Increasing the power dissipated in the lamp increases the temperature of the plasma and the population in higher energy levels increases. The lamp monitor signal is not  $50 \Omega$  terminated, but is input directly into a boxcar signal averager. The peak optogalvanic signal arrives 2-5  $\mu\text{s}$  after the laser pulse. The optimum boxcar gate width is in the range of 2-5  $\mu\text{s}$  with a sensitivity of 5-10 mV.

A number of two-photon optogalvanic transitions in Ne were observed between 725 and 737 nm by focussing a fraction of the dye laser output,  $O(10^1 \mu\text{J})$ , in the center of the Ne plasma. These lines were particularly useful in calibrating the dye laser in this wavelength region, as  $I_2$  fluorescence excitation is difficult at these wavelengths. Table 1.3 lists the calculated wavelengths of the transitions as well as the originating,  $E''$ , and terminating,  $E'$ , states. The term values are taken from Ref.[26]. In general, the best signal-to-noise ratios were obtained with the lowest discharge currents,  $< 5 \text{ mA}$ , which corresponds to a discharge voltage of  $\sim 200 \text{ V}$ .

Table 1.3 Two-Photon Absorption Transitions Observed in the Optogalvanic Spectrum of Ne Between 725 nm and 736 nm.

$2\lambda_{\text{vac}} / \text{nm}$	$E' / \text{cm}^{-1}$	$E'' / \text{cm}^{-1}$
736.7032	161 607.26	134 459.29
735.9075	161 636.62	134 459.29
734.2043	161 699.66	134 459.29
734.1561	161 701.45	134 459.29
728.1256	161 509.63	134 041.84
727.7402	161 524.17	134 041.84
725.9922	161 590.35	134 041.84
725.5467	161 607.26	134 041.84



## References

1. (a) T. G. Dietz, M. A. Duncan, D. E. Powers, and R. E. Smalley, *J. Chem. Phys.*, v.74 (1981), p.6511. (b) R.E.Smalley, *Laser Chem.*, v. 2 (1983), p. 167.
2. P. Milani and W. A. deHeer, *Rev. Sci. Instrum.*, v. 61 (1990), p. 1835.
3. G. Ganteför, H. K. Siekmann, H. O. Lutz, and K. H. Meiwes-Broer, *Chem. Phys. Lett.*, v. 165 (1990), p. 293.
4. S. Maruyama, L. A. Anderson, and R. E. Smalley, *Rev. Sci. Instrum.* v. 61 (1990), p. 3686.
5. S. Nosone, Y. Sone, K. Onodera, S. Sudo, K. Kaya, *J. Phys. Chem.*, v. 94 (1990), p. 2744.
6. T.C.Steimle, D.A.Fletcher, K.Y.Jung, and C.T.Scurlock, *Chem. Phys. Lett.*, v.184 (1991), p.379.
7. M. D. Morse, in "Methods of Experimental Physics, vol.II. Atoms and Molecules", F.B. Dunning and R.Hulet, eds., to be published.
8. R. E. Smalley, B. L. Ramakrishna, D. H. Levy, and L. Wharton, *J. Chem. Phys.*, v.61 (1974), p.4363; R. E. Smalley, D. H. Levy, and L. Wharton, *J. Chem. Phys.*, v.63 (1975), p.4977.
9. Private communication from General Valve Co., Fairfield NJ.
10. M.F. Cai, T.P. Dzugan, and V.E. Bondebey, *Chem. Phys. Lett.*, v.155 (1989), p.430.
11. G. Herzberg, "Molecular Spectra and Molecular Structure. Vol. I. - Spectra of Diatomic Molecules", Krieger Publishing Co., Malabar FL, 1989.
12. H. Lefebvre-Brion and R.W. Field, "Perturbations in the Spectra of Diatomic Molecules", Academic Press, Orlando FL, 1985.
13. Varian Vacuum Products 1993-4 Catalog, Varian Inc., Lexington MA, p.21.
14. J.H. Moore, C.C. Davis, M.A. Coplan, "Building Scientific Apparatus", Addison-Wesley, Reading MA, 1989.
15. J.F. O'Hanlon, "A User's Guide to Vacuum Technology", Wiley, NY, 1980.
16. (a) B. A. Mamyryn, Dokt. diss., Physico-Technical Institute, Academy of Sciences, USSR, Leningrad, (1966); Avt. svid. (Inventors Certificate No. 198034, 1966; Byull. isobr. No. 12 (1967), p.148. (b) V.I.Karatev, B.A.Mamyryn, and D.V.Shmikk, *Zh. Tekh. Fiz.*, v.14 (1971), p.1498 [*Sov. Phys.-Tech. Phys.*, v.16 (1972), p.1177] (c)

- B.A.Mamyrin, V.I.Karataev, D.V.Shmikk, and V.A.Zagulin, *Zh. Eexp. Theor. Fiz.*, v.64 (1973) , p.82. [Sov. Phys. JETP, v.37 (1973), p.45]
17. Private communication from R.M.Jordan Co., Grass Valley CA (FAX transmission date 7/29/92).
  18. Private communication from Galileo Electro-Optics, Sturbridge MA.
  19. W.C.Wiley and I.H.McLaren, *Rev. Sci. Instrum.*, v.26 (1955), p.1150.
  20. R.S. Opsal, S.M. Colby, C.W. Wilkerson, JR., J.P. Reilly, Ch.22 in "Lasers and Mass Spectrometry", D.M. Lubman, ed., Oxford Univ. Press, 1990.
  21. M. Littman and H. Metcalf, *Appl. Opt.*, v.17 (1978), p. 2224.
  22. Lumonics Spectrum Master Pulsed Dye Laser Service Manual, Lumonics Inc. Kanata, Ontario CANADA, 1992.
  23. R.H. Storz and G.C. Bjorklund, unpublished.
  24. S. Gerstenkorn and P. Luc, Atlas du Spectre D'absorption de laMolecule D'iode, CNRS, Paris, 1978. A systematic correction to the linepositions is given in S.Gerstenkorn and P.Luc, *Rev. Phys. Appl*, v.14, p.791.
  25. N. J. Dovichi, D. S. Moore, and R.A.Keller, *Applied Optics*, v.21 (1982), p.1468.
  26. S.Bashkin and J.O.Stoner, Jr., "Atomic Energy Levels and Grotrian Diagrams 1. Hydrogen I - Phosphorus XV", 1975.

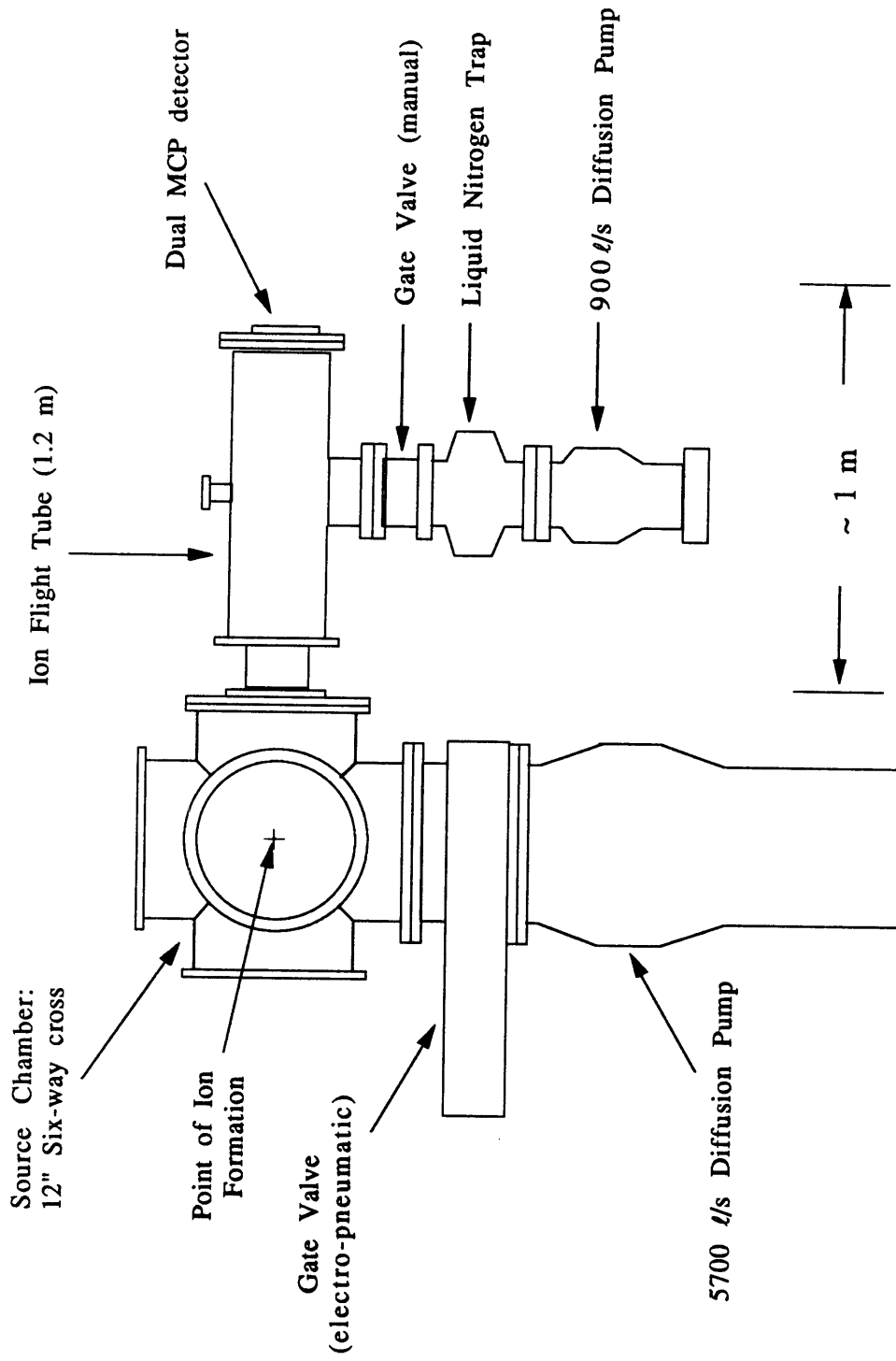


Figure 1.1a. Photoablation Source Chamber with Time-of-Flight Mass Spectrometer. Part numbers and vendors are listed in the text.

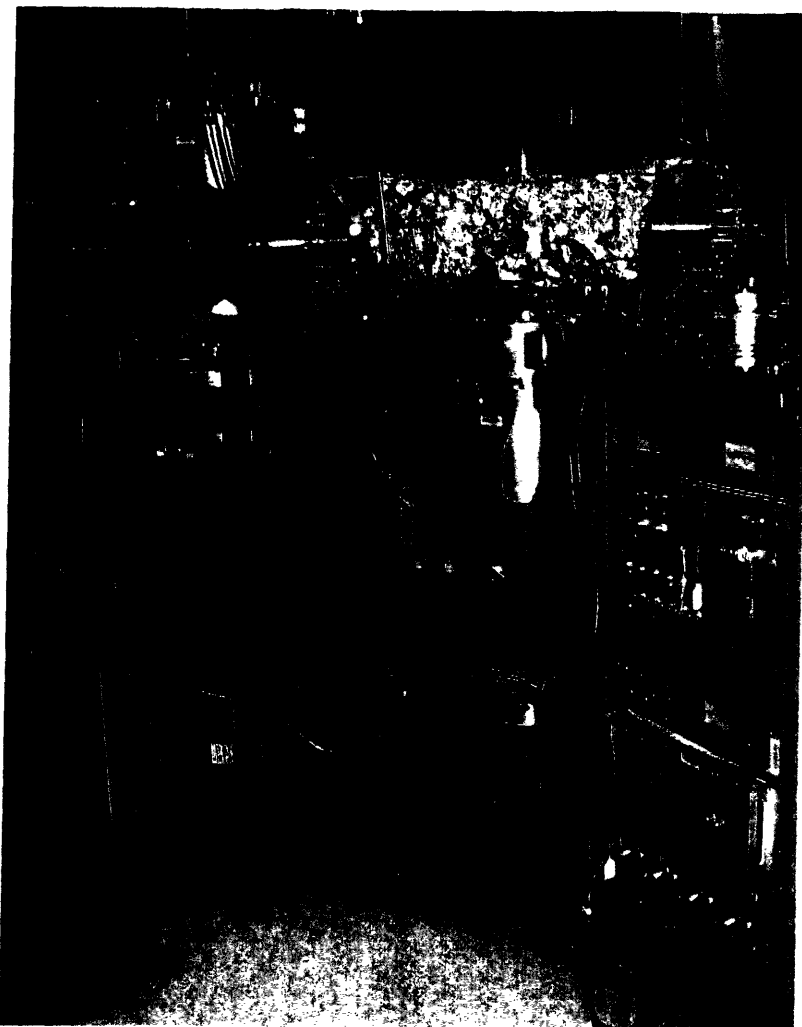


Figure 1.1b. Photograph of Laser Ablation-Supersonic Molecular Beam Source with Time-of-Flight Mass Spectrometer.

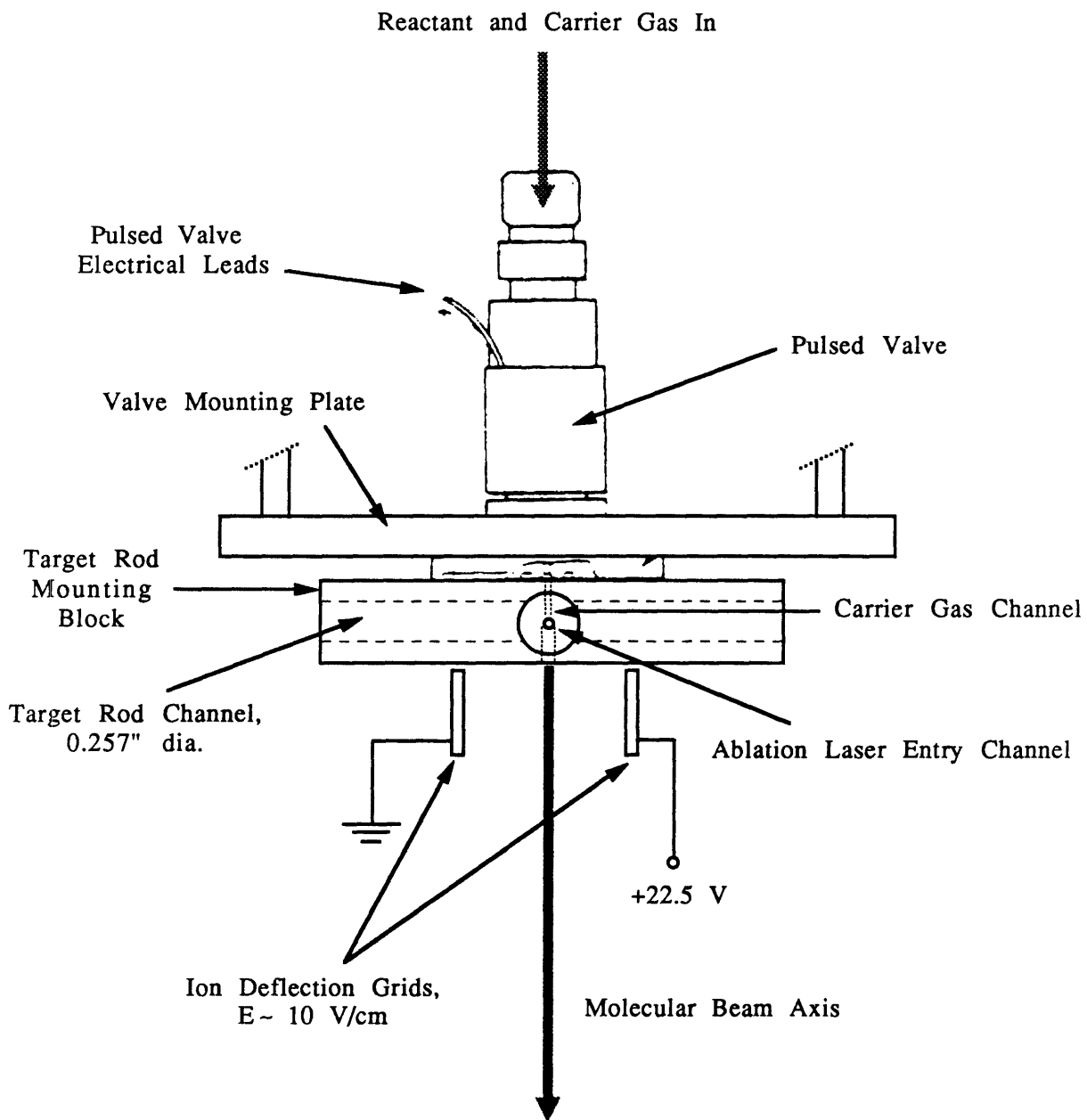


Figure 1.2a. Puzzle nozzle and Ca target mount. An expanded view of the target rod holder is shown in Fig. 2.3b.

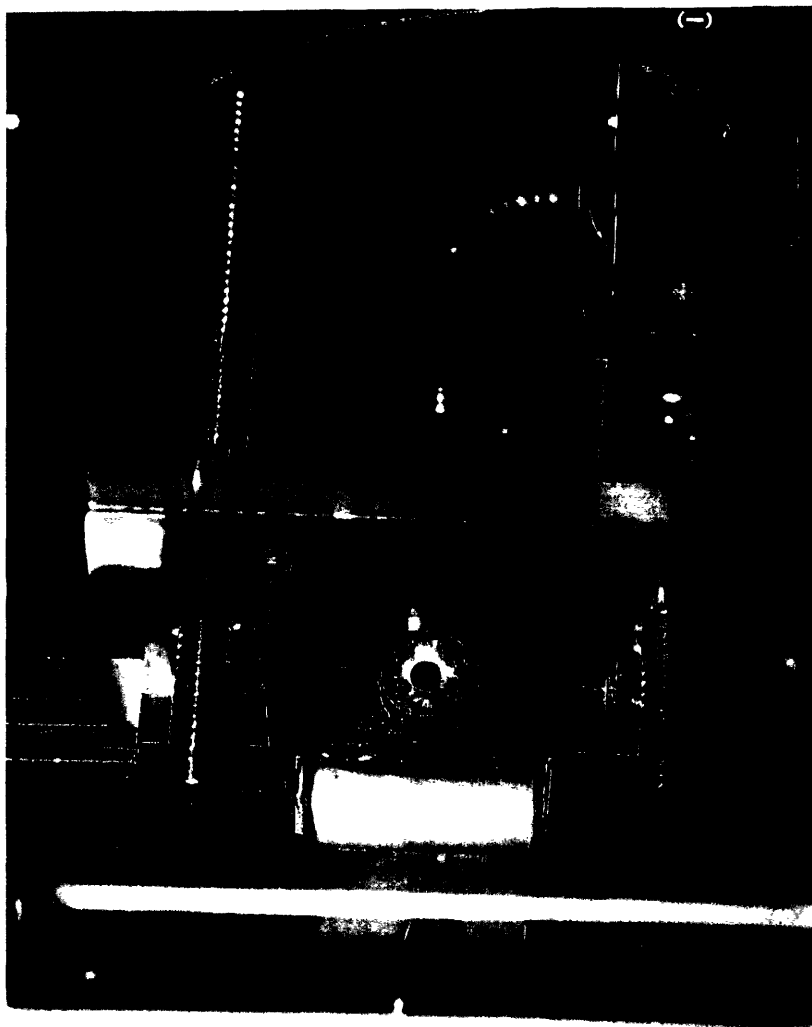


Figure 1.2b. Close-up view of pulsed nozzle and target rod holder depicted in Figure 1.2a. The battery in the upper right corner provides voltage across the ion deflection electrodes. The ion deflection electrodes are the two pieces of copper separated by the white ceramic stand-offs at the bottom center of the photo. (The electrodes are separated by 1".) The ablation laser pulse enters the target block through the hole seen just below the geometric center of the photo.

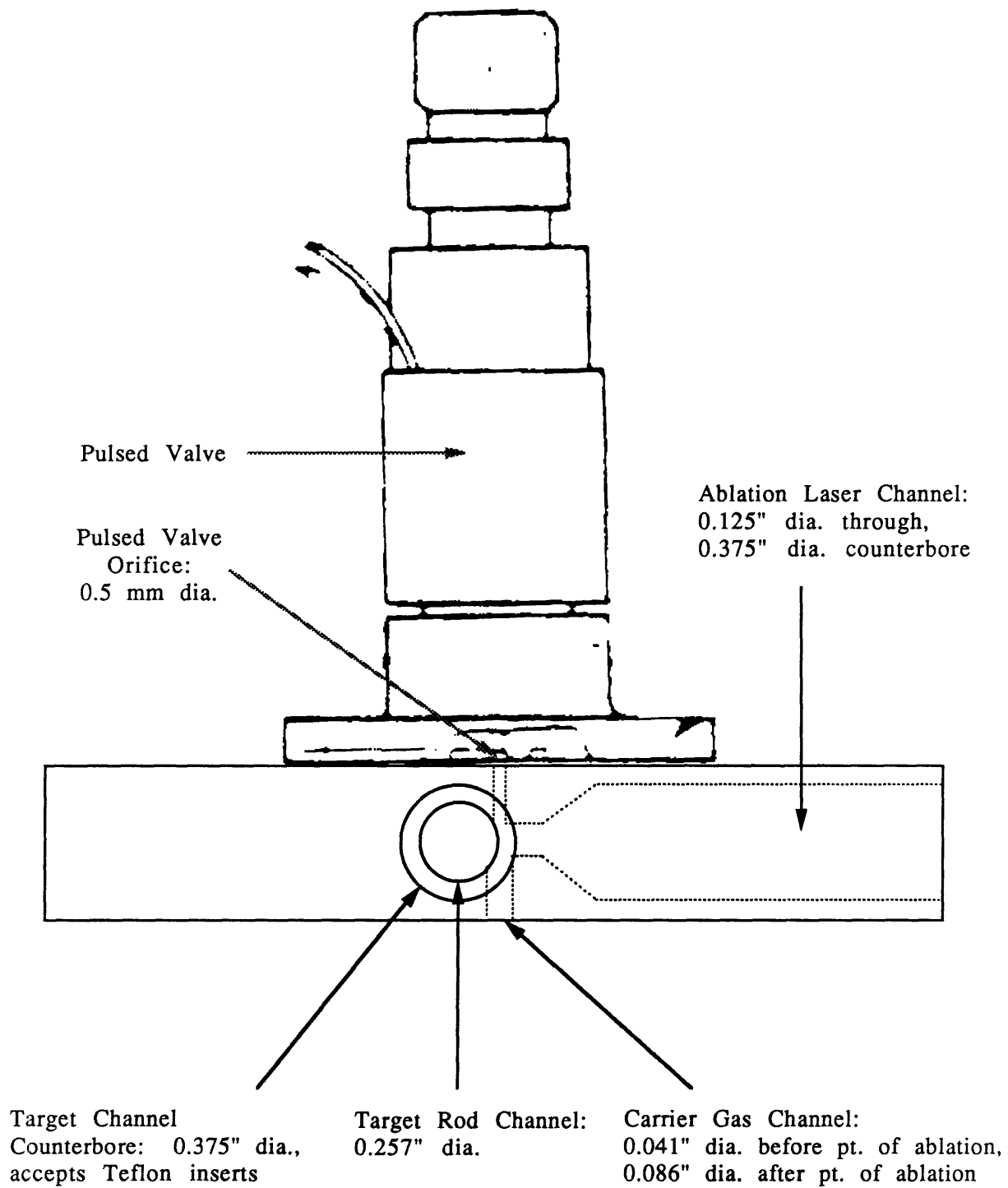


Figure 1.2c Cross-sectional view of target rod holder. Pulsed nozzle image shown to scale as scanned from General Valve product literature.

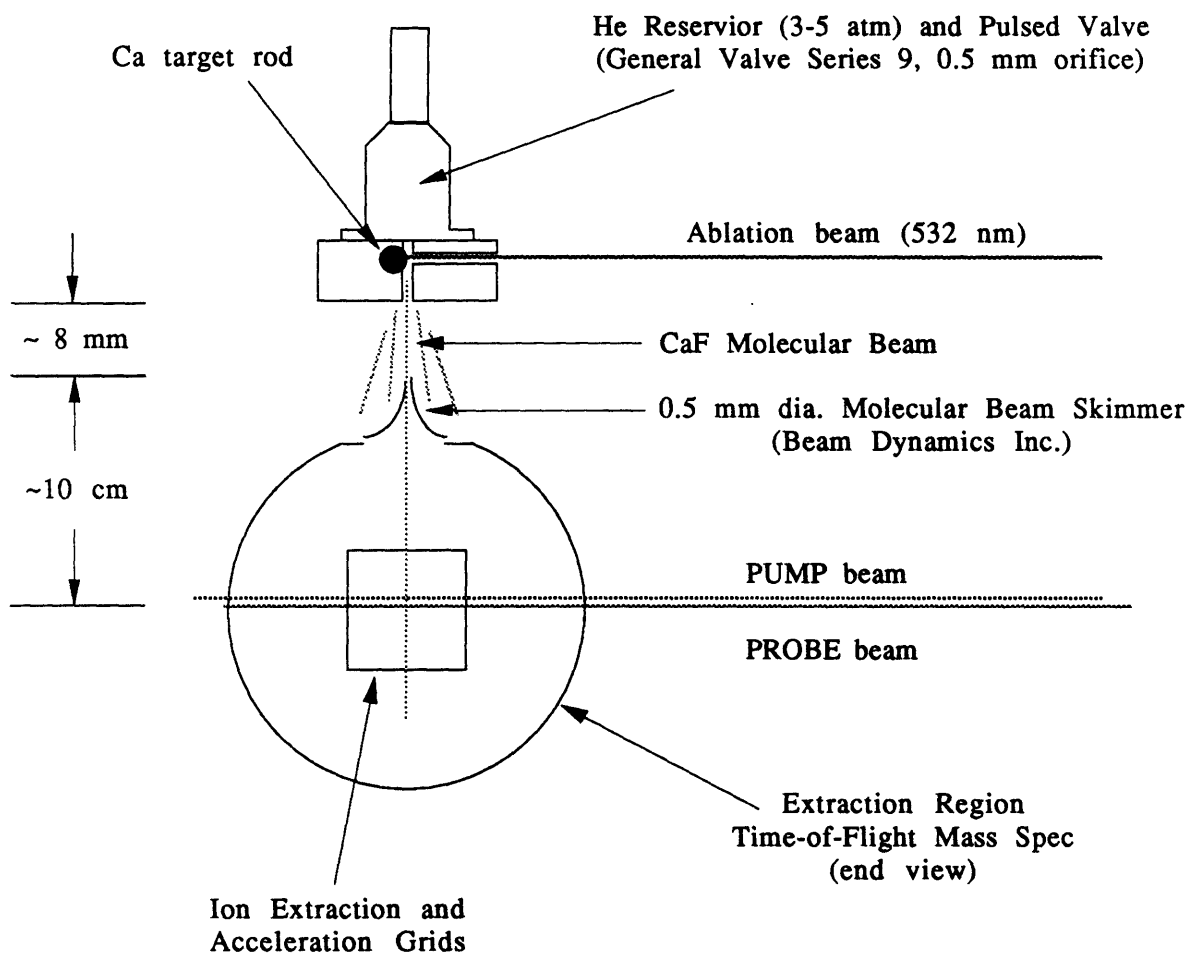


Figure 1.3. Photoablation-Molecular Source with TOF-MS Ion Extraction Assembly.



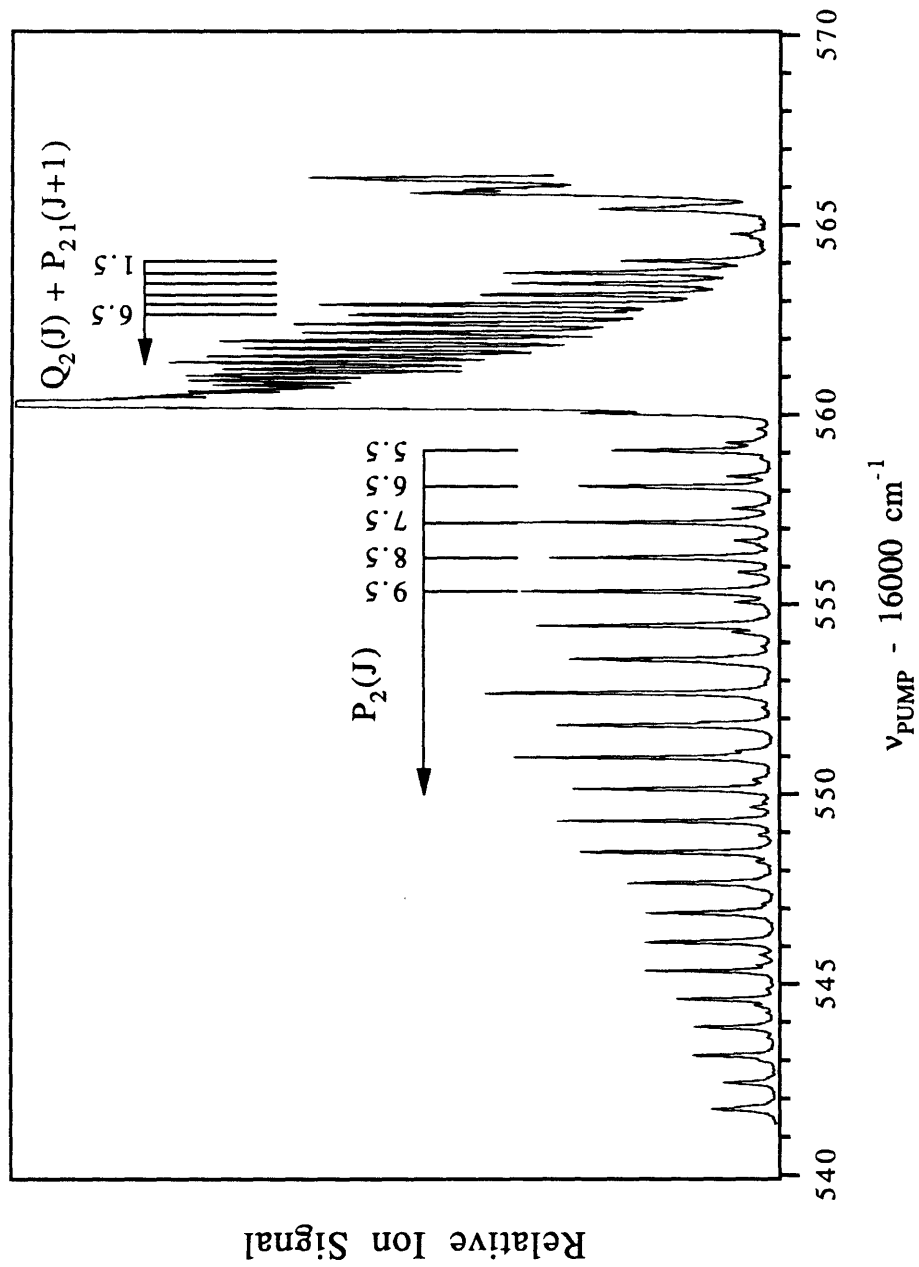


Figure 1.5. Ionization detected  $A^2\Pi_{3/2} - X^2\Sigma^+(0,0)$  absorption spectrum.  $A^2\Pi_{3/2}$  levels were non-resonantly ionized by 328 nm laser light.

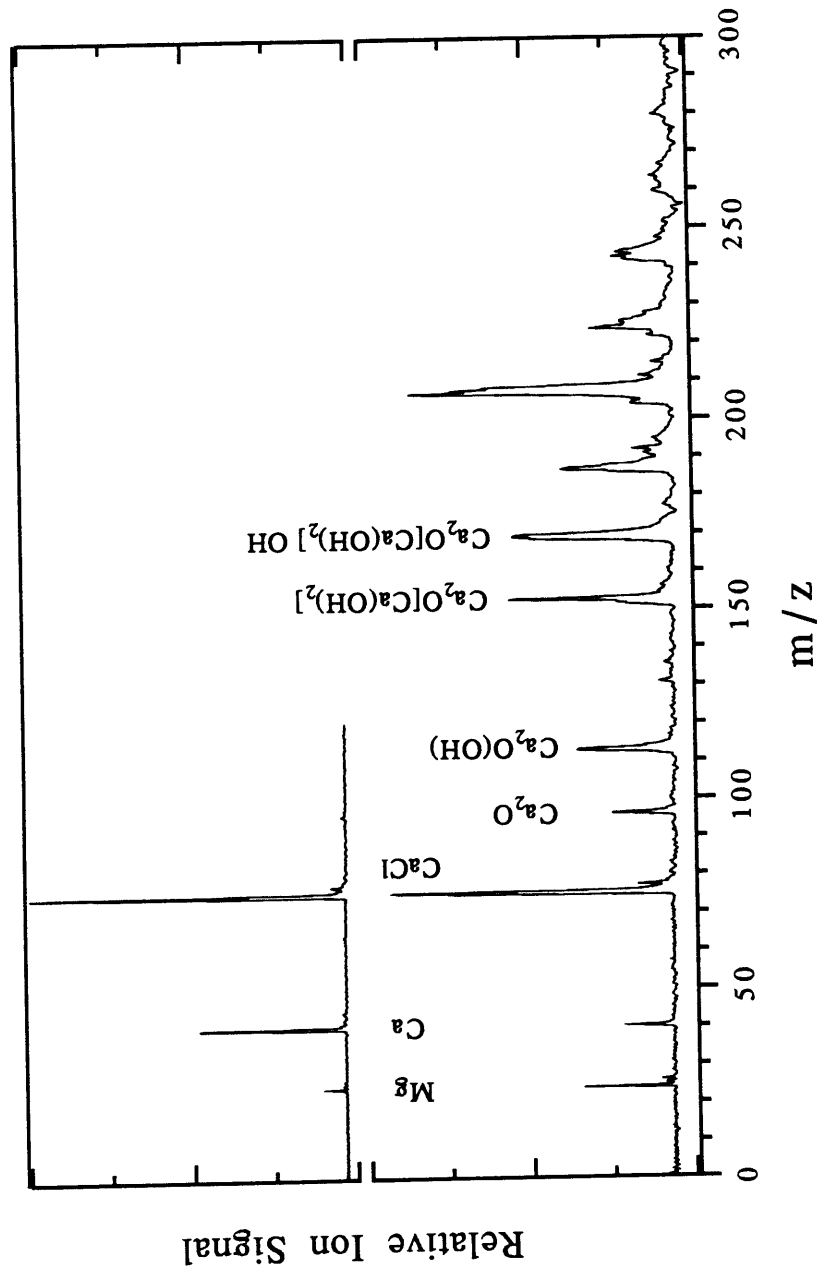


Figure 1.4. Laser ionization generated mass spectrum of Ca/He/CHCl<sub>3</sub> plasma. Ablation with 15-20 mJ @ 532 nm and 90 psig He. Ionization wavelength = 284.4 nm; 1+1 REMPI of Ca <sup>35</sup>Cl through E-X(2,0) P-branch head. Top trace is with ablation laser carefully aligned on Ca target. Bottom trace is with laser misaligned.

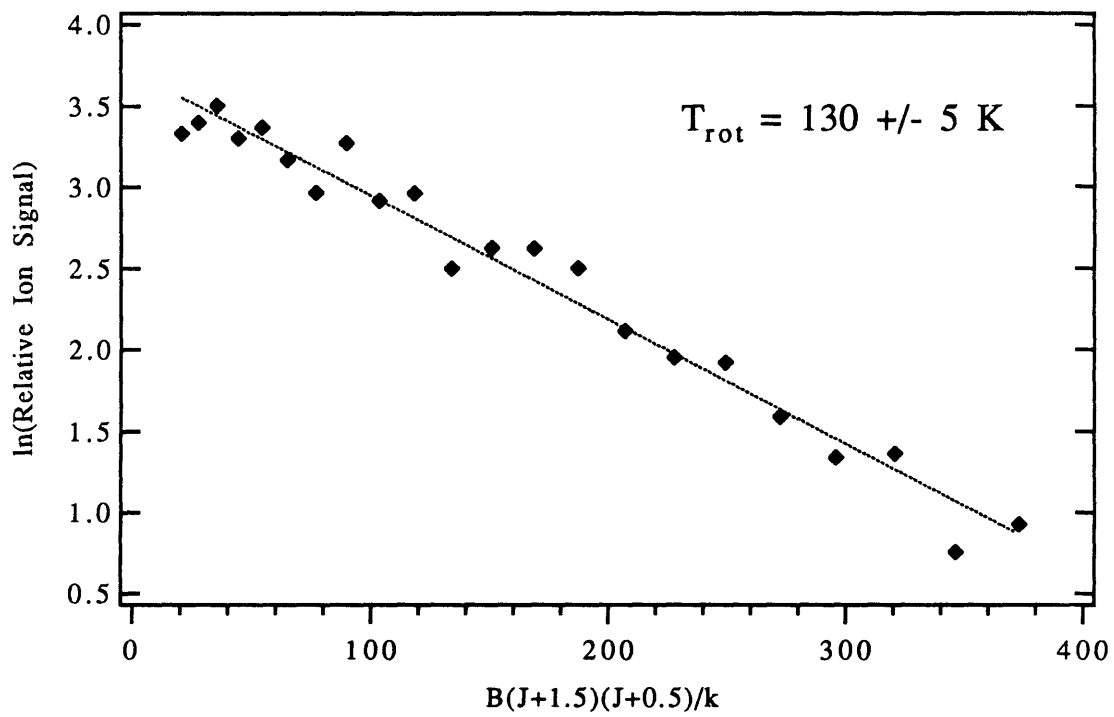


Figure 1.6. Rotational temperature of photoablation produced CaF. Carrier gas is 50 psig He.

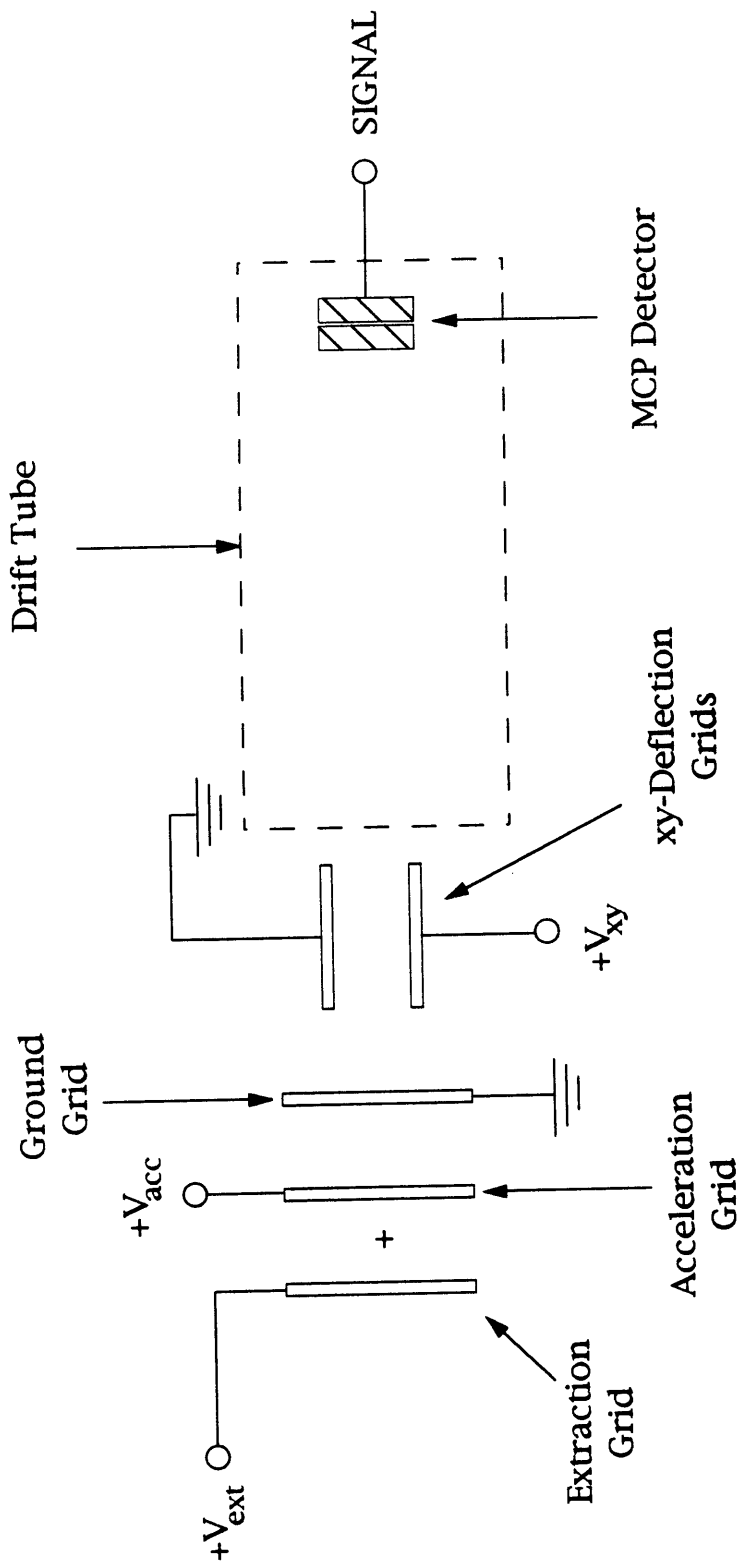


Figure 1.7. Schematic of TOF-MS. Figure is not to scale. The molecular beam travels parallel to and halfway between the Extraction and Acceleration Grids. Ions are generated at the "+" between the Extraction and Acceleration Grids. The Extraction-Acceleration and Acceleration-Ground spacings are 1.27 cm. The xy-Deflection Grid spacing is 2.5 cm. The spacing between the Ground Grid and MCP detector is 1.20 m. The extraction voltage is typically +1650 V and the acceleration voltage +1500 V, making the extraction field 120 V/cm and the acceleration field 1200 V/cm.

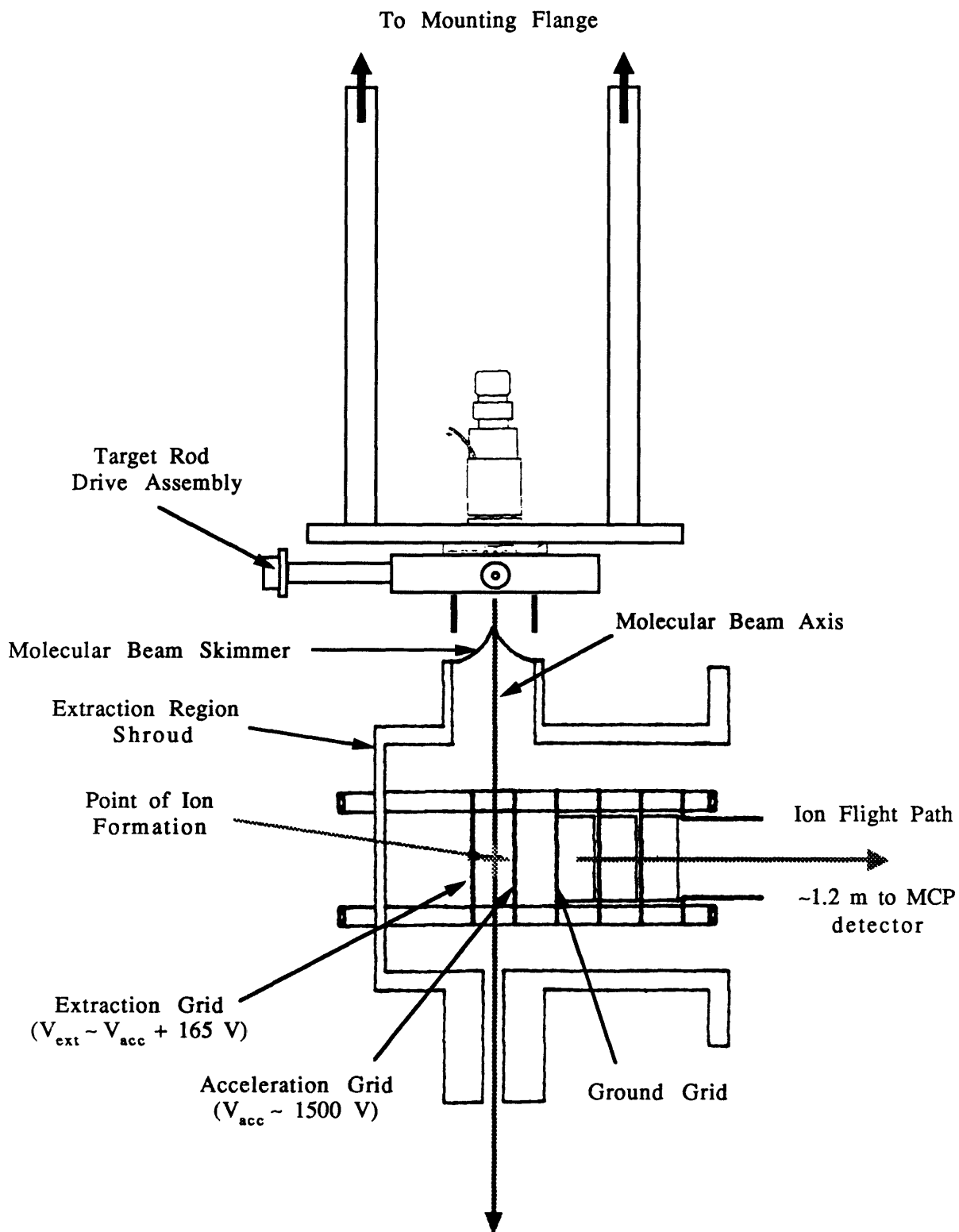


Figure 1.8a. Laser ablation-molecular beam source with extraction region of time-of-flight mass spectrometer.

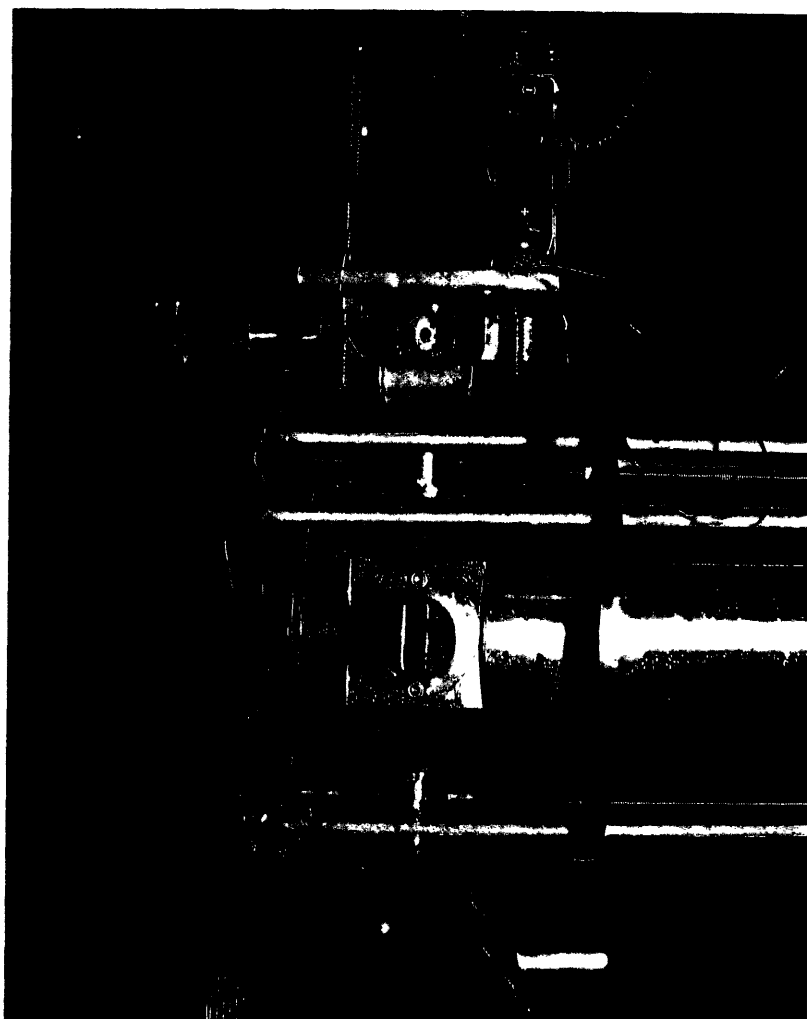


Figure 1.8b. Laser ablation-Molecular Beam Source (top) with extraction region of Time-of-Flight Mass Spectrometer.

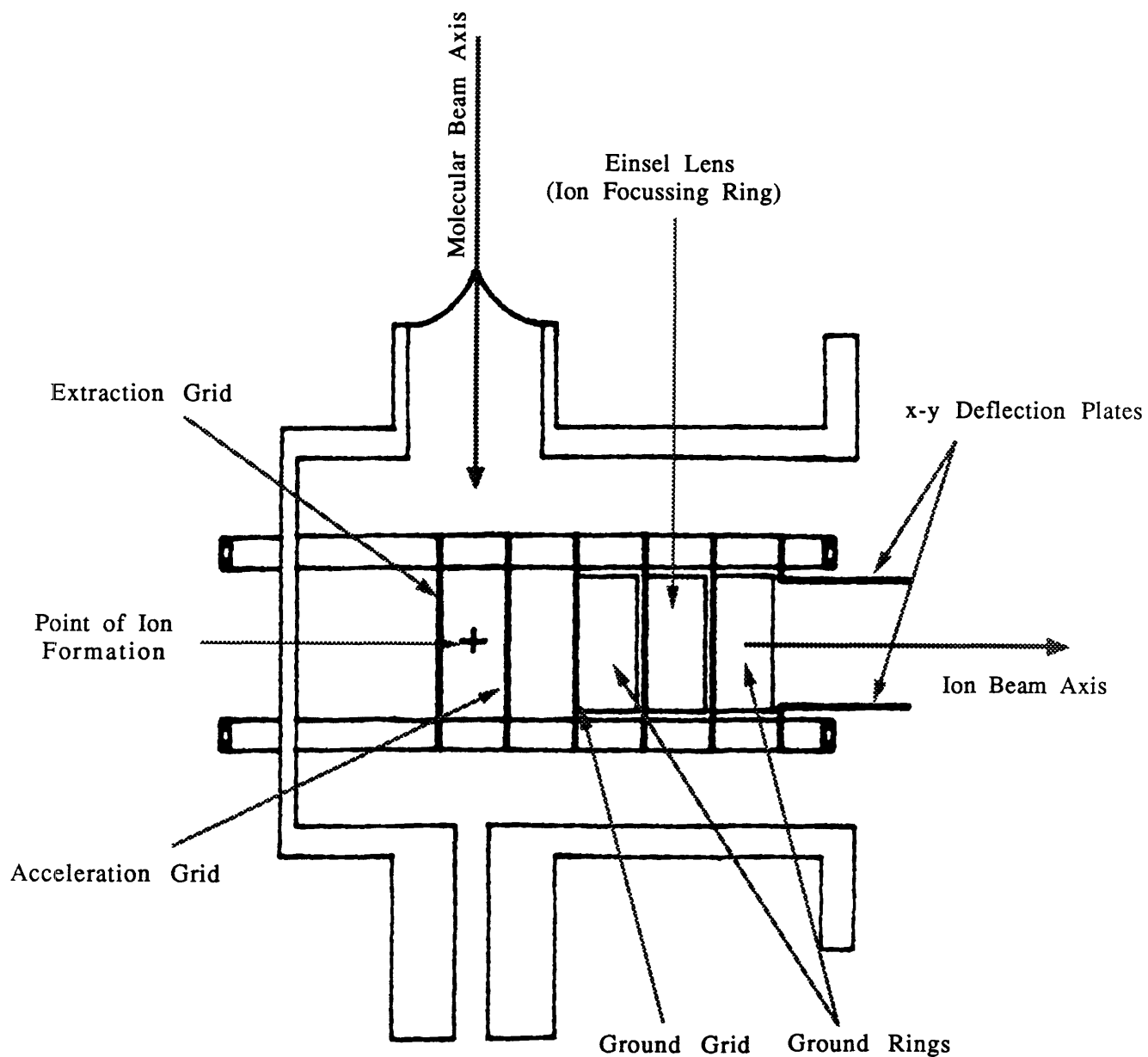


Figure 1.9. Mass spectrometer head. Approximate scale is 4:3. The image was scanned from R.M.Jordan Co. product literature. The mass spec head and flight tube are pumped by the same liquid nitrogen trapped diffusion pump.

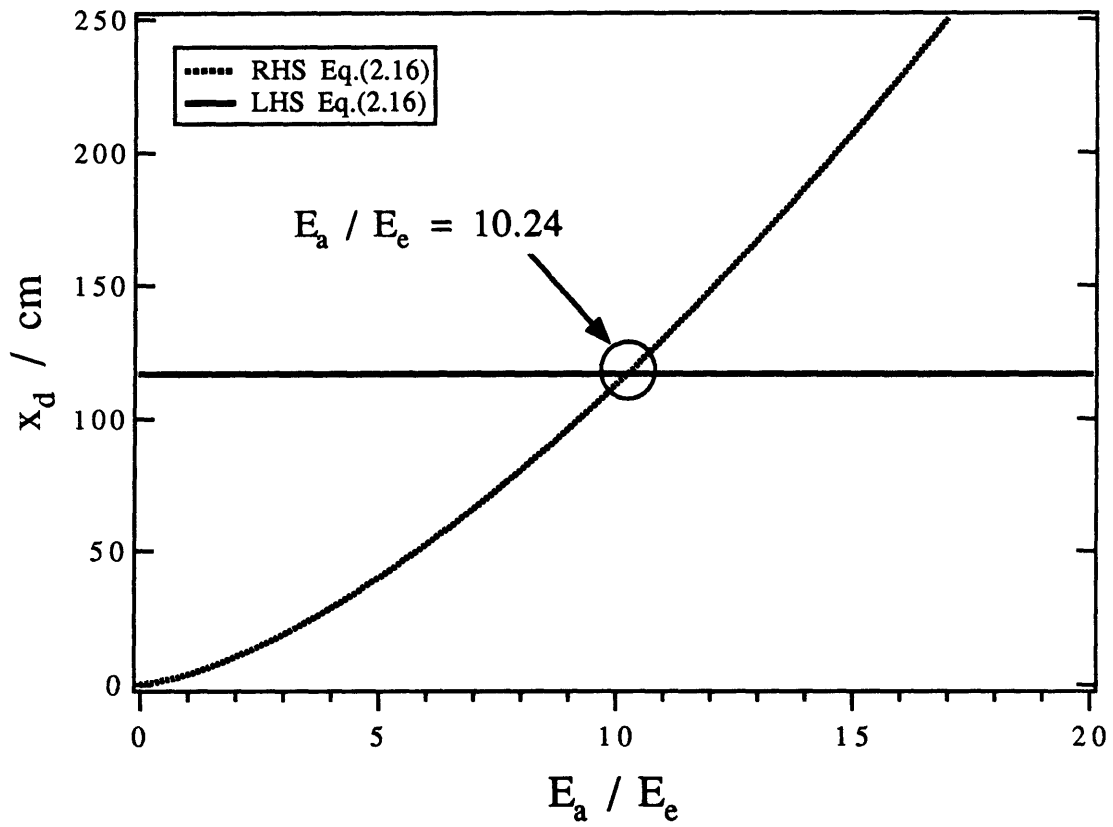


Figure 1.10 Wiley-McLaren Space Focussing Criterion



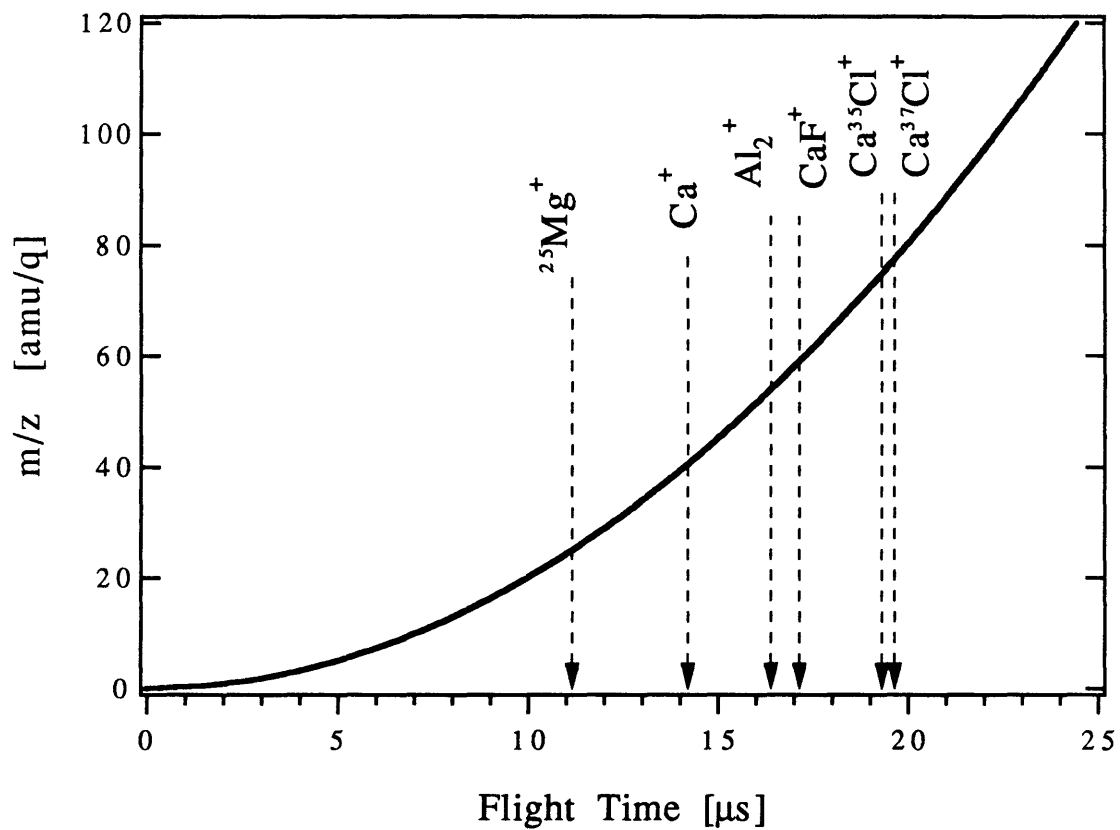


Figure 1.11. Ion flight time vs. mass at standard operating conditions:  $V_{\text{ext}} = +160 \text{ V}$ ,  $V_{\text{accel}} = +1500 \text{ V}$ , 1.2 m flight tube.

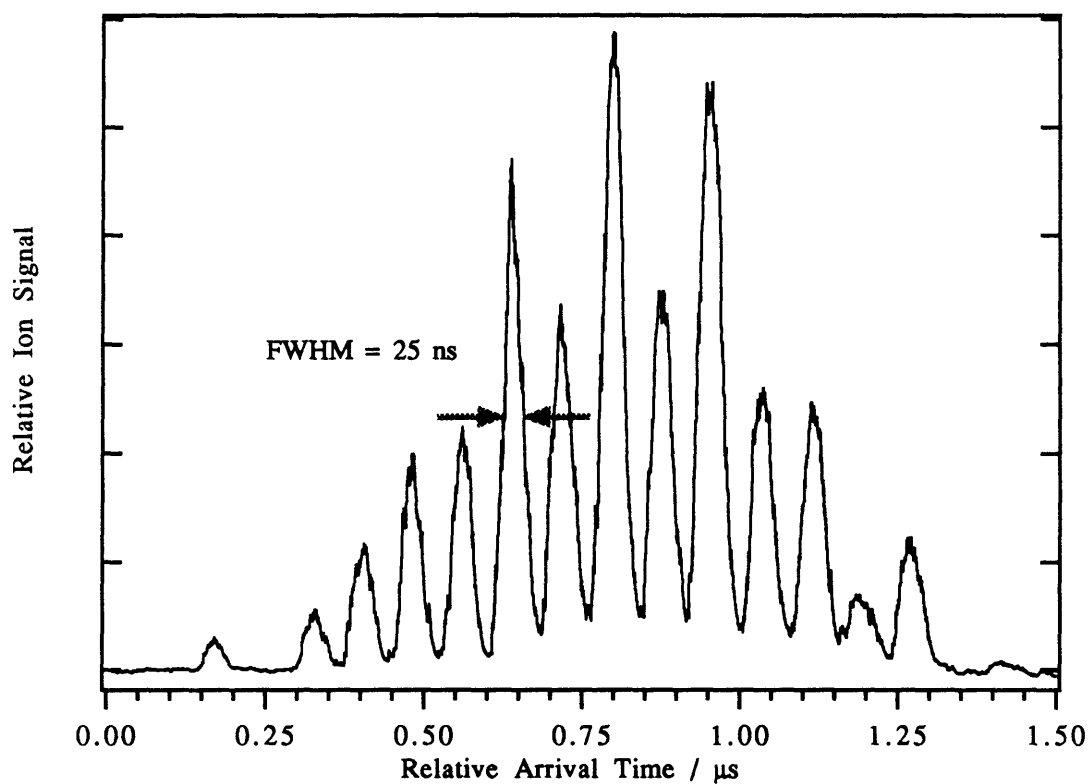


Figure 1.12a. Time-of-Flight mass spectrum of  $\text{Mo}_2^+$  generated by 1+1 REMPI at 314 nm. Spectrum plotted to demonstrate time resolution.

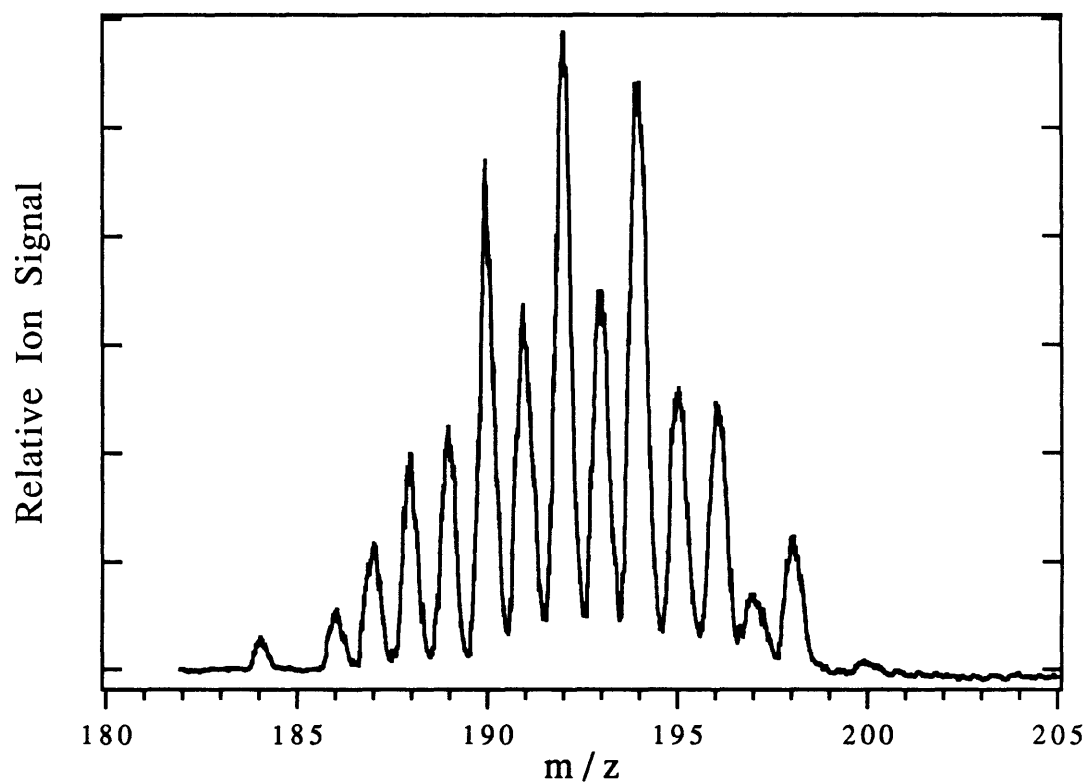


Figure 1.12b. Time-of-Flight mass spectrum of Mo<sub>2</sub><sup>+</sup> generated by 1+1 REMPI at 314 nm. Spectrum plotted to demonstrate mass resolution.

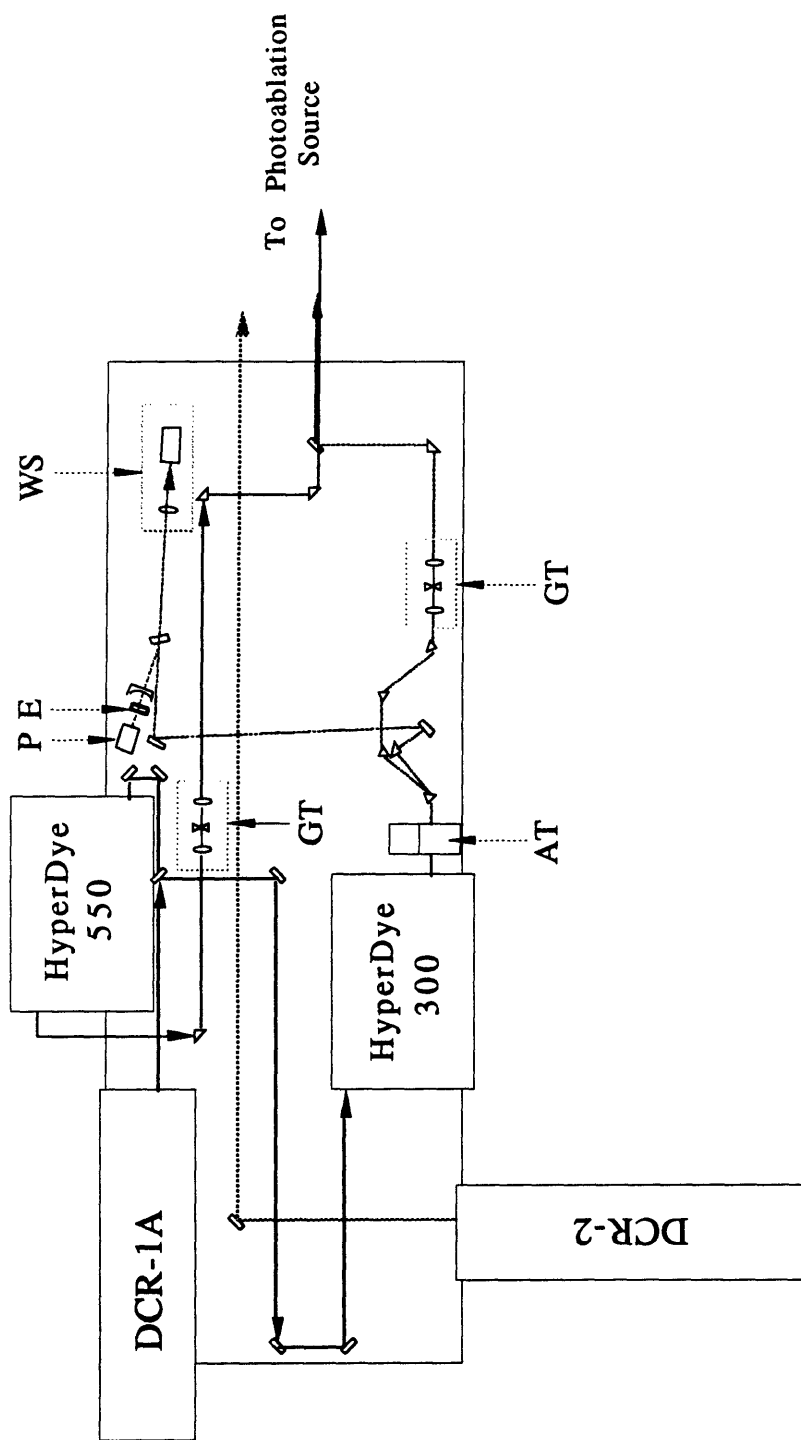


Figure 1.13. Laser Table Arrangement for Ionization Detected OODR experiments. The HyperDye 550 is the PUMP laser and the HyperDye 300 is the PROBE laser. Label codes: AT =  $\beta$ -BBO Crystal w/ Autotracker, E = Extracavity Etalon, GT = Galilean Telescope, P = Photodiode, WS = Wavelength Standard ( $I_2$  fluorescence cell or Ne optogalvanic lamp).

## CHAPTER 2

### Experimental Strategies

During the course of characterizing the laser ablation source and developing new strategies for probing CaF Rydberg states, four different laser spectroscopic techniques were considered:

- Fluorescence Excitation / Fluorescence Detected Optical-Optical Double Resonance (OODR),
- Fluorescence Dip,
- 1+1 (one color) Resonance Enhanced Multi-Photon Ionization (REMPI),
- Ionization Detected Optical-Optical Double Resonance (ID-OODR).

All of the data analyzed in Chapters 4 and 5 was recorded using ID-OODR. The experiments involved populating a single rotational, parity level in the  $A^2\Pi_{3/2}$ ,  $v=0$  or  $C^2\Pi_{3/2}$ ,  $v=0$  excited state with a narrow bandwidth ( $\Delta\nu = 0.10 \text{ cm}^{-1}$ ), wavelength tunable, pulsed dye laser and then exciting transitions to Rydberg levels from the intermediate level with a second dye laser possessing operating characteristics (bandwidth, pulse duration, pulse energy) similar to the first. The vibronic energy of the Rydberg levels prepared by the second laser pulse was in excess of the lowest ionization threshold of the neutral molecule. The Rydberg levels promptly ( $\sim 1 \text{ ns}$  or less) ionized by transferring one quantum of vibrational energy from the  $\text{CaF}^+$  ion-core to the Rydberg electron. The energy from one quantum of vibration was sufficient to excite the Rydberg electron into the electronic continuum and generate a  $\text{CaF}^+$  cation in its vibrational ground state. The  $\text{CaF}^+$  cations produced in this manner were promptly detected in the TOF-MS described in the previous section.

While ID-OODR proved to be the most efficient detection scheme for the Rydberg states discussed in this document, each of the other three techniques have their strong points. One should not be beholden to a particular scheme, but be open to switching strategies to suit the goals of the experiments. Fluorescence excitation and fluorescence detected OODR generated virtually all of the data on CaF electronic structure prior to this work. Fluorescence dip has proved useful in the analysis of CaCl electronic structure.

Each technique's advantages and disadvantages is discussed individually. Particular attention is paid to the advantages of ID-OODR over alternative schemes. A generalized experimental strategy for probing molecular Rydberg states is presented and discussed with respect to investigations of CaF electronic structure.

In double resonance experiments, the laser pulse which excites the molecule from its initial state to the intermediate state is called the "PUMP" pulse. The laser pulse which excites the intermediate level to the final resonant state is called the "PROBE" pulse.

## 2.1. Fluorescence Excitation

Fluorescence Excitation, commonly referred to as Laser Induced Fluorescence, is likely the most commonly used laser spectroscopic molecular probe. Fluorescence excitation experiments typically involve one or two narrow band tunable dye lasers and a photosensitive device (photomultiplier tube, CCD camera, intensified diode array) capable of detecting emission from the molecules of interest. A typical one laser experiment involves excitation of a molecule from its vibronic ground state to an electronic state with several eV of electronic energy ( $1 \text{ eV} = 8065 \text{ cm}^{-1}$ ). The wavelength of the laser is scanned to generate high resolution spectrum over a wide region,  $O(10^2 - 10^3 \text{ cm}^{-1})$ . If fluorescence from the excited state is detected at a wavelength longer than that used to excite the transition, the scattered light from the excitation laser can then be suppressed with a dichroic mirror or colored glass filter and the emission from the excited state may be detected against near zero background.

The fluorescence excitation experiment may be modeled mathematically as a two-level system having relaxation channels. [See Fig.2.1] The time-dependent populations of states  $|0\rangle$  and  $|1\rangle$  are functions the rates of induced absorption, stimulated emission, spontaneous emission, and non-radiative relaxation rates. The relevant rate equations are [e.g. 1]:

$$\dot{N}_0(t) = -B_{10}\rho(\omega, t)N_0(t) + [B_{01}\rho(\omega, t) + A_{01}]N_1(t), \quad (2.1a)$$

$$\dot{N}_1(t) = B_{10}\rho(\omega, t)N_0(t) + [B_{01}\rho(\omega, t) + A_{01} + A_{1, \text{bath}} + \beta_1]N_1(t). \quad (2.1b)$$

The quantities  $B_{10}$  and  $B_{01}$  are the Einstein coefficients of induced absorption and stimulated emission;  $A_{01}$  is the coefficient of spontaneous emission from  $|1\rangle$  to  $|0\rangle$ ;  $A_{\text{bath}}$  is the coefficient of spontaneous emission of  $|1\rangle$  to states other than  $|0\rangle$ ;  $\beta$  is the rate of

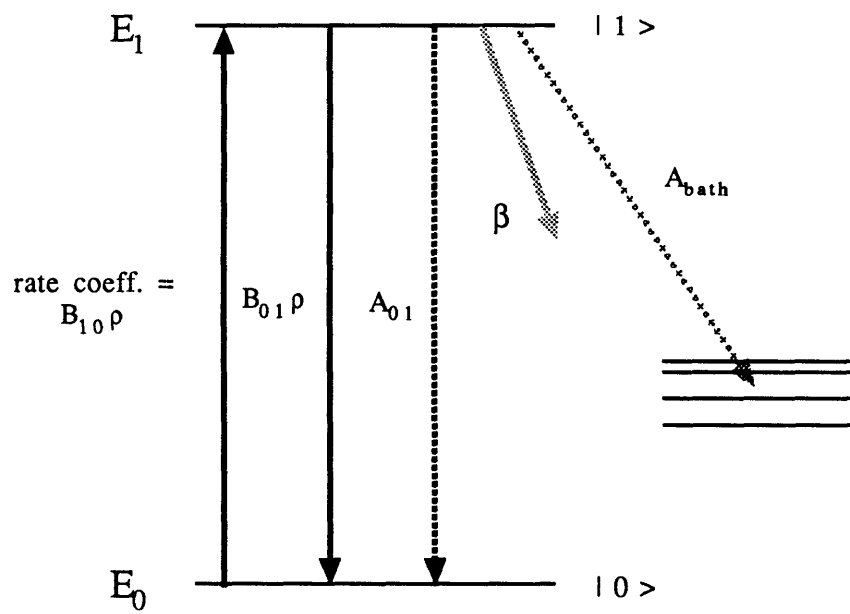


Figure 2.1. Kinetic Rate Model of Fluorescence Excitation.

non-radiative relaxation of  $|1\rangle$ , and  $\rho(\omega)$  is the spectral energy density [ $\text{J m}^{-3}$ ] of the radiation field at excitation frequency  $\omega$ . For the purpose of evaluating these expressions in terms physically intuitive, experimentally measurable parameters is useful to rewrite Eqs.(2.1a-b) in terms of the absorption cross-section [ $\text{cm}^2 \text{ photon}^{-1}$ ] of the  $|1\rangle\text{-}|0\rangle$  transition and the excitation laser flux [ $\text{photons cm}^{-2} \text{ s}^{-1}$ ]. The system responds to the square of the electric field amplitude. Assuming the square of the field amplitude is constant over the duration of the excitation pulse, the energy density may be approximated as,  $\rho(\omega,t) = \rho(\omega)$ . The laser flux is related to the spectral energy density by,

$$F(\omega, t) \equiv \frac{c}{\hbar\omega} \rho(\omega, t), \quad (2.2)$$

where  $\omega$  is the angular frequency of the excitation field. The induced absorption and stimulated emission rates may be expressed as the product of the laser flux and a frequency integrated absorption cross-section. The frequency dependent cross-section reflects the lineshape of the absorption feature.

$$\sigma_{10}(\omega_{\text{PUMP}})F(\omega_{\text{PUMP}}) \approx \bar{F} \int_{\omega_{\text{PUMP}} - \delta\omega}^{\omega_{\text{PUMP}} + \delta\omega} \sigma_{10}(\omega) d\omega \equiv \int_{\omega_{\text{PUMP}} - \delta\omega}^{\omega_{\text{PUMP}} + \delta\omega} B_{10}(\omega) \rho(\omega) d\omega. \quad (2.3)$$

Dropping the  $\omega_{\text{PUMP}}$  notation, the population rate equations in the new notation are:

$$\dot{N}_0(t) = -\sigma_{10}FN_0(t) + (\sigma_{10}F + k_{1,\text{rad}})N_1(t), \quad (2.4a)$$

$$\dot{N}_1(t) = \sigma_{10}FN_0(t) + (\sigma_{10}F + k_{1,\text{rad}} + k_{1,\text{bath}} + \beta_1)N_1(t), \quad (2.4b)$$

where,

$$\sigma_{10} \equiv \frac{\hbar\omega}{c} B_{10}, \quad (2.5)$$

$k_{1,\text{rad}} = A_{01}$ , and  $k_{1,\text{bath}} = A_{1,\text{bath}}$ . A more sophisticated derivation of Eq.(2.5) has been demonstrated elsewhere [2]. The integrated absorption cross-section can also be expressed in terms of the transition dipole moment by substituting the expression for the coefficient of induced absorption [2] into Eq.(2.5):



$$\sigma_{10} = \frac{\pi}{3\hbar\epsilon_0} \tilde{\nu}_{10} |\mu_{10}|^2 = 2.69 \cdot 10^{-16} \tilde{\nu}_{10} |\mu_{10}|^2 \text{ cm}^2, \quad (2.6)$$

where  $\tilde{\nu}_{10}$  is the transition energy in  $\text{cm}^{-1}$  and  $\mu_{10}$  is the transition dipole moment in Debye.

Eqs.(2.4a-b) form a system of two linear, first-order differential equations and may be solved as an eigenvalue problem:

$$\det \begin{bmatrix} -\sigma_{10}F - \lambda & \sigma_{10}F + k_{1,\text{rad}} \\ \sigma_{10}F & -(\sigma_{10}F + k_{1,\text{rad}} + k_{1,\text{bath}} + \beta_1) - \lambda \end{bmatrix} = 0. \quad (2.7)$$

The solution to Eqs.(2.4a-b) is:

$$\begin{bmatrix} N_0(t) \\ N_1(t) \end{bmatrix} = c_1 \begin{bmatrix} \sigma_{10}F + k_{\text{rad}} \\ \sigma_{10}F + \lambda_+ \end{bmatrix} e^{\lambda_+ t} + c_2 \begin{bmatrix} \sigma_{10}F + k_{\text{rad}} \\ \sigma_{10}F + \lambda_- \end{bmatrix} e^{\lambda_- t} \quad (2.8)$$

where  $\lambda_+$  and  $\lambda_-$  are the two roots of Eq.(2.7), and  $c_1$  and  $c_2$  are determined by the boundary conditions,

$$\begin{bmatrix} N_0(t=0) \\ N_1(t=0) \end{bmatrix} \equiv \begin{bmatrix} N_0(0) \\ 0 \end{bmatrix} \quad (2.9)$$

Our interest is in the relative populations of  $N_0$  and  $N_1$  at time  $\tau$ , when the excitation laser pulse terminates. The solution of Eq.(2.7) evaluated at time  $\tau$  is:

$$N_0(\tau) = N_0(0) \left[ \frac{1}{B} \right] \left[ \left( \sigma_{10}F - \frac{1}{2}(A-B) \right) e^{-\frac{1}{2}(A+B)\tau} - \left( \sigma_{10}F - \frac{1}{2}(A+B) \right) e^{-\frac{1}{2}(A-B)\tau} \right], \quad (2.10a)$$

$$N_1(\tau) = N_0(0) \frac{\left( \sigma_{10}F - \frac{1}{2}(A-B) \right) \left( \sigma_{10}F - \frac{1}{2}(A+B) \right)}{(\sigma_{10}F + k_{\text{rad}})B} \left[ e^{-\frac{1}{2}(A+B)\tau} - e^{-\frac{1}{2}(A-B)\tau} \right], \quad (2.10b)$$

$$A \equiv 2\sigma_{10}F + (k_{1,\text{rad}} + k_{1,\text{bath}} + \beta_1),$$

$$B \equiv \left[ (2\sigma_{10}F)^2 + (k_{1,\text{rad}} + k_{1,\text{bath}} + \beta_1)^2 + 4\sigma_{10}Fk_{1,\text{rad}} \right]^{1/2},$$

$$B \geq A.$$

At higher laser powers, the dominant rates in Eq.(2.10) are those arising from induced absorption and stimulated emission. Each rate is the product of the absorption cross-section and the excitation laser field. When the absorption and stimulated emission rates greatly exceed the radiative and non-radiative decay rates,

$$N_1(\tau) \cong \frac{1}{2} N_0(0) [1 - e^{-2\sigma_{10}F\tau}]. \quad (2.11)$$

At low PUMP energies ( $2\sigma_{10}F\tau \ll 1$ ), the number of molecules excited to  $|1\rangle$  is linearly proportional to the excitation pulse energy,  $N_1(\tau) \cong \sigma_{10}F\tau \cdot N_0(0)$ . At higher PUMP energies ( $\sigma_{10}F\tau > 1$ ), the exponential term in Eq.(2.11) approaches zero and  $N_1(\tau) \cong 0.5 \cdot N_0(0)$ . This condition is referred to as saturation of the PUMP transition.

After termination of the PUMP pulse, the population in  $|1\rangle$  decays exponentially:

$$\dot{N}_1(t + \tau) = -(k_{1,\text{rad}} + k_{1,\text{bath}} + \beta_1) \cdot N_1(t + \tau) \quad (2.12a)$$

$$N_1(t + \tau) = N_1(\tau) \exp[-(k_{1,\text{rad}} + k_{1,\text{bath}} + \beta_1)t] \quad (2.12b)$$

One-laser fluorescence excitation spectra are recorded by collecting emission from  $|1\rangle$ . The number of photons collected is equal to the product of the photon detection efficiency,  $\epsilon$ , the rate of photon emission,  $k_{1,\text{rad}} + k_{1,\text{bath}}$ , and the population of  $|1\rangle$  at time  $t + \tau$ , all integrated over the collection time,  $t'$ :

$$N_{\text{collect}} = \epsilon \int_0^{t'} (k_{1,\text{rad}} + k_{1,\text{bath}}) N_1(t + \tau) dt. \quad (2.13)$$

In the limit of  $t' \gg (k_{1,\text{rad}} + k_{1,\text{bath}} + \beta_1)^{-1}$ ,

$$N_{\text{collect}} = \epsilon N_1(\tau) \Phi_f \quad (2.14)$$

where,

$$\Phi_f \equiv \frac{k_{1,\text{rad}} + k_{1,\text{bath}}}{k_{1,\text{rad}} + k_{1,\text{bath}} + \beta_1}. \quad (2.15)$$

The quantity  $\Phi_f$  is the fluorescence quantum yield of  $|1\rangle$ . If the primary mechanism of relaxation from  $|1\rangle$  is emission of a photon, i.e.  $\beta \ll k_{\text{rad}} + k_{\text{bath}}$  or  $\Phi_f \cong 1$ , then the

observation of PUMP resonances is limited only by the efficiency of photon collection and the ability of the PUMP laser to populate  $|1\rangle$ . Fluorescence excitation is an extremely efficient technique for recording high resolution (laser linewidth limited) spectra of transitions with large absorption cross-sections and near unity values of  $\Phi_f$ . If non-radiative relaxation depopulates  $|1\rangle$  at a rate greater than radiative processes, i.e.  $\beta > k_{\text{rad}} + k_{\text{bath}}$  or  $\Phi_f \ll 1$ , the technique can prove problematic.

One-laser fluorescence excitation spectra are often recorded for the purpose of thoroughly characterizing an excited state which will be used as an intermediate in a two-laser experiment. Optical-Optical Double Resonance (OODR) spectroscopy is the two laser analogue of fluorescence excitation. An OODR experiment (ideally) involves populating a single rovibronic level with the PUMP laser, and then scanning a second (PROBE) laser. The PROBE laser populates higher excited levels. [See Fig.2.2] If all final states have equal (and non-zero) detection efficiency, an OODR spectrum has information content equivalent to an excited state absorption spectrum.

The principal advantages of two-color fluorescence excitation spectra over one-color fluorescence excitation are the detection of resonances from a single level and access to new states unobservable from  $|0\rangle$  (but observable from  $|1\rangle$ ) due to quantum mechanical selection rules. PROBEing from a single excited level greatly reduces the density of spectral features, thereby facilitating the assignment of individual transitions. The efficacy of two-color fluorescence excitation may be hampered by the lack of a long lived (i.e. lifetime longer than the PUMP pulse duration) intermediate state or by fluorescence quantum yield,  $\Phi_f$ , of the final state. Fluorescence detected OODR was not successful for CaF Rydberg states with  $n^* > 10$  because those states had poor fluorescence quantum yield.

## 2.2. Fluorescence Dip

The Fluorescence Dip technique is a variation on OODR. Instead of detecting the PROBE resonance as a positive signal on a near zero background, PROBE resonances are observed as a decrease in a steady state signal. One chooses fluorescence dip over fluorescence excitation when the fluorescence quantum yield of the target state is low, but the intermediate state is an efficient emitter. Two classes of electronic states which are well suited to fluorescence dip detection are: 1) predissociated states ( $\Phi_f \approx 0$ ), and 2) highly excited electronic (Rydberg) states, where the fluorescence lifetime greatly exceeds the mean time between deactivating collisions or other non-radiative processes, again  $\Phi_f \approx 0$ .

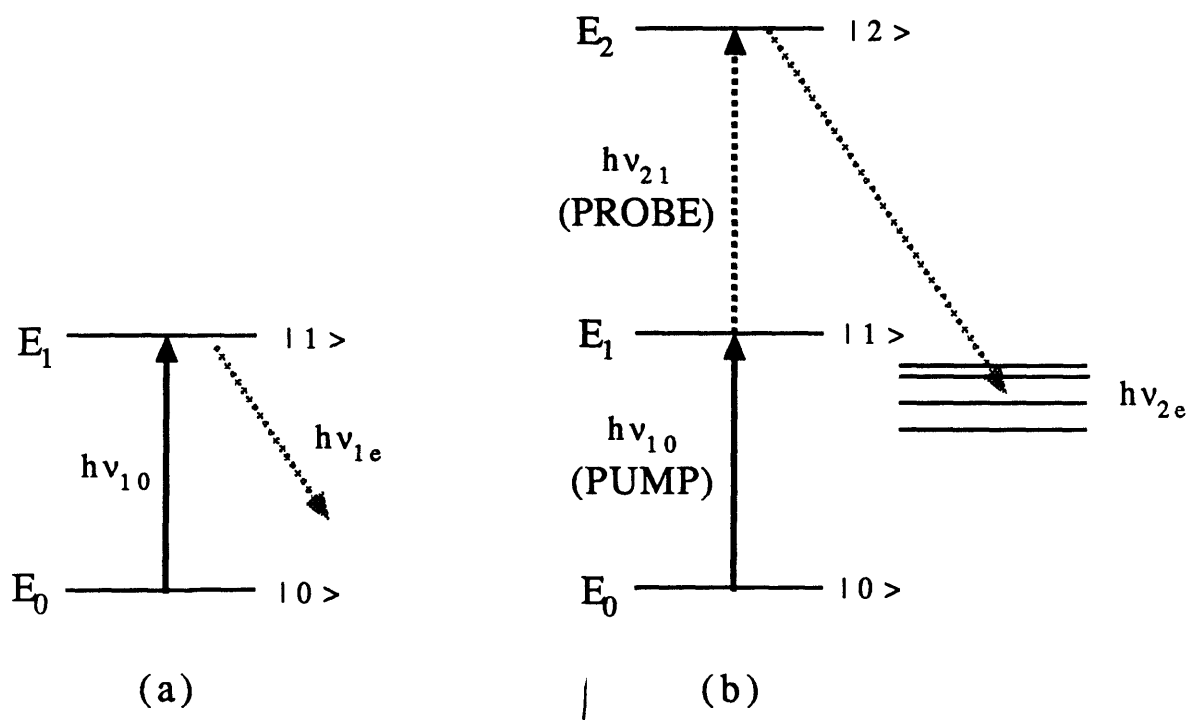


Figure 2.2. States involved in fluorescence excitation and OODR experiments. (a) One-color excitation. The PUMP frequency,  $\nu_{10}$ , is scanned. Emission at  $\nu_{1e}$  is detected. (b) Optical-Optical Double Resonance. The PUMP frequency,  $\nu_{10}$ , is fixed and the PROBE frequency,  $\nu_{21}$ , is scanned. Emission at  $\nu_{2e}$  is detected.

The disadvantage of fluorescence dip is that it is not a zero-background technique. The principal difficulty with the technique is that it requires an extremely stable molecule source and PROBE laser.

One typically analyzes absorption and emission spectra to obtain the transition frequency, intensity, and sometimes lineshape of spectral features. It will be shown here that while fluorescence dip spectroscopy is a reasonably efficient means of determining line positions, it is a much less efficient means of establishing the relative strength of transitions. The dynamic range of the method is significantly less than that for fluorescence detected OODR. In order to bring weak transitions above the detection threshold, it is necessary to use PROBE pulse energies which will saturate the stronger lines. In order to obtain intensity information equivalent to that in a fluorescence excitation spectra, it would be necessary to record fluorescence dip spectra at multiple laser powers. The relative intensities of transitions would be recorded for each spectra and the correct relative intensity would be determined by extrapolating back to zero PROBE laser intensity.

The fluorescence dip,  $D$ , is defined as the ratio of the difference in fluorescence signal from  $|1\rangle$  when  $\lambda_2$  is off- and on-resonance to the off-resonance fluorescence signal:

$$D \equiv \frac{N_1(\lambda_2^{\text{off}}) - N_1(\lambda_2^{\text{on}})}{N_1(\lambda_2^{\text{off}})}, \quad (2.16)$$

where  $\lambda_2$  is the PROBE laser wavelength. The signal on which the dip is detected is proportional to the number of molecules in  $|1\rangle$ ,

$$S(\lambda_1) = k(\lambda_1)N_1(\lambda_1) \equiv k^0 N_1(\lambda_1), \quad (2.17)$$

where  $\lambda_1$  is the PUMP laser wavelength. The fluctuations in the fluorescence signal limit the sensitivity of the experiment. When  $\lambda_2$  is off-resonance,

$$\frac{\delta S(\lambda_2^{\text{off}})}{S(\lambda_2^{\text{off}})} = \frac{\delta N_1(\lambda_2^{\text{off}})}{N_1(\lambda_2^{\text{off}})}. \quad (2.18)$$

If the PUMP and the PROBE pulses do not temporally overlap, then the  $|2\rangle$ - $|1\rangle$  transition is a two-level problem like that discussed for fluorescence excitation. Evaluation of Eq.(2.11) shows that fluctuations in  $N_1$  are minimized when the PUMP transition is saturated and,

$$\frac{\delta S(\lambda_2^{\text{off}})}{S(\lambda_2^{\text{off}})} = \frac{\delta N_0(\lambda_2^{\text{off}})}{N_0(\lambda_2^{\text{off}})}. \quad (2.19)$$

For an oven source operating in conjunction with a 10 Hz pulsed laser system,  $(\delta N_0/N_0) \sim O(0.01)$ . Fluctuations in number density in a high-temperature oven typically occur on a time scale much greater than 100 ms. If the sample is a permanent gas  $(\delta N_0/N_0) \approx 0$ . For a laser ablation source, 30% shot-to-shot fluctuations in number density are not uncommon due to inhomogeneities in the target surface.

As there is no coherence between the PUMP and PROBE transitions, the PROBE depletes the population in  $|1\rangle$  in the same manner that the PUMP transition depleted population in  $|0\rangle$ . Eqs.(2.4-2.7) may be used to describe the PROBE transition simply by changing the "1" and "0" subscripts to "2" and "1" and treating the problem in the same way as the fluorescence excitation problem. It is then straightforward to determine the population in  $|1\rangle$  at the termination of the PROBE pulse,  $t=\tau_2$ .

$$N_1(\tau_2) \approx N_1(\tau_1) \left[ \frac{1}{B} \right] \left[ \left( \sigma_{21}F - \frac{1}{2}(A-B) \right) e^{-\frac{1}{2}(A+B)\tau_2} - \left( \sigma_{21}F - \frac{1}{2}(A+B) \right) e^{-\frac{1}{2}(A-B)\tau_2} \right], \quad (2.20)$$

$$A \equiv 2\sigma_{21}F + (k_{2,\text{rad}} + k_{2,\text{bath}} + \beta_2),$$

$$B \equiv \left[ (2\sigma_{21}F)^2 + (k_{2,\text{rad}} + k_{2,\text{bath}} + \beta_2)^2 + 4\sigma_{21}Fk_{2,\text{rad}} \right]^{1/2}.$$

There are four limiting cases of Eq.(2.20) which need to be considered:

1. Weak PROBE ( $2\sigma_{21}F\tau \ll 1$ ), slow non-radiative relaxation of  $|2\rangle$  ( $\beta_2 \ll k_{2,\text{rad}} + k_{2,\text{bath}}$ ); ( $\sigma_{21}F\tau \gg \beta_2$ ),
2. Weak PROBE ( $2\sigma_{21}F\tau \ll 1$ ), fast relaxation ( $\beta_2 \ll k_{2,\text{rad}} + k_{2,\text{bath}}$ ); ( $\sigma_{21}F\tau \ll \beta_2$ ),
3. Strong PROBE ( $2\sigma_{21}F\tau \gg 1$ ), slow relaxation ( $\beta_2 \ll k_{2,\text{rad}} + k_{2,\text{bath}}$ ); ( $\sigma_{21}F\tau \gg \beta_2$ ),
4. Strong PROBE ( $2\sigma_{21}F\tau \gg 1$ ), fast relaxation ( $\beta_2 \ll k_{2,\text{rad}} + k_{2,\text{bath}}$ ); ( $\sigma_{21}F\tau \ll \beta_2$ ).

The fluorescence dips in each of the four limiting cases are given in Table 2.1.

Table 2.1 Fluorescence Dip Signal from Eq.(2.16) in the Four PROBE/Relaxation Limiting Cases

	Slow losses	Rapid losses
Weak PROBE	$\sigma_{21}F\tau \ll 1$	$\sigma_{21}F\tau \ll 1$
Strong PROBE	0.5	1

In the weak PROBE cases, the rate limiting step in the depletion of  $|1\rangle$  is the induced absorption rate. The dip signal depends linearly on the PROBE pulse energy,  $F\tau$ . When the PROBE is strong, but the losses are weak, the transition saturates and the maximum dip reaches 50% of the off-resonance fluorescence signal. This is the result expected from Eq.(2.11). When the loss rate is large, population in  $|2\rangle$  is immediately lost forever upon excitation from  $|1\rangle$ ; the ratio  $N_2/N_1$  remains  $\approx 0$ , the induced absorption rate remains high, and the transition never saturates; increasing PROBE energy bleaches  $N_1$  entirely. These results are valid for incoherent PUMP and PROBE excitation. Coherent excitation can generate dips  $> 50\%$  for a system having  $\beta_2 \approx 0$ . Coherent excitation does not occur in the experiments discussed in this document. Both the PUMP and PROBE lasers operate on multiple cavity modes. Neither the PUMP and PROBE pulses, nor the oscillations on the cavity modes within each pulse have an analytic phase relationship.

In order to unambiguously identify PROBE resonances, the dip signal must be greater than or equal to the fluctuations in the signal level. Equation (2.16) may be analyzed to find the critical value of the dip for which its signal-to-noise ratio is greater than the fluctuation level of  $N_0$ , the number of molecules produced by the source. Equation (2.16) may be rewritten as:

$$D = 1 - \frac{x}{y}, \quad (2.21)$$

where,

$$x \equiv N_1(\lambda_2^{\text{on}}) = \frac{1}{2}(1-k)N_0, \quad (2.22)$$

where  $k$  is defined as the fraction of population removed from  $|1\rangle$  by the PROBE pulse, and,

$$y \equiv N_1(\lambda_2^{\text{off}}) = \frac{1}{2}N_0, \quad (2.23)$$

when the PUMP transition is saturated. The fluctuations in the dip may be expressed in terms of the on- and off- resonance populations of  $|1\rangle$  by differentiating Eq.(2.21) and utilizing the relations in Eqs.(2.22) and (2.23):

$$\delta D = \sqrt{(\delta x)^2 + \left(\frac{x}{y}\right)^2 (\delta y)^2}, \quad (2.24)$$

$$\frac{\partial D}{\partial x} = -\frac{1}{y}, \quad (2.25)$$

$$\frac{\partial D}{\partial y} = \frac{x}{y^2}. \quad (2.26)$$

The mathematical treatment is simplified by making the assumption that the parameter  $k$  does not fluctuate from shot to shot. This is certainly not literally true, as  $k$  is dependent upon PROBE laser intensity, however it is physically reasonable for the fluctuations in  $k$  to be small relative to the fluctuations in number of molecules produced from shot to shot. The remainder of this derivation proceeds with  $\delta k = 0$ :

$$\delta x = (1 - k)\frac{1}{2}\delta N_0, \quad (2.27)$$

$$\delta y = \frac{1}{2}\delta N_0. \quad (2.28)$$

The source-related noise on the fluorescence dip is:

$$\delta D = \left(\frac{1}{N_1^{\text{off}}}\right) \sqrt{(\delta N_1^{\text{on}})^2 + \left(\frac{N_1^{\text{on}}}{N_1^{\text{off}}}\right)^2 (\delta N_1^{\text{off}})^2}. \quad (2.29)$$

Substituting into Eq.(2.24),

$$\delta D = \left(\frac{1}{\frac{1}{2}N_0}\right) \sqrt{\frac{1}{4}(1-k)^2(\delta N_0)^2 + (1-k)^2\frac{1}{4}(\delta N_0)^2} = \sqrt{2}(1-k)\frac{\delta N_0}{N_0}. \quad (2.30)$$



The fluorescence dip may be expressed in terms of initial state population, fluorescence collection efficiency,  $\epsilon$ , and the depletion of the intermediate state,

$$D = \frac{\frac{1}{2}N_0\epsilon - \frac{1}{2}(1-k)N_0\epsilon}{\frac{1}{2}N_0\epsilon} = k. \quad (2.31)$$

The S/N ratio on the fluorescence dip may be determined by combining Eqs.(2.19), (2.30), and (2.31),

$$\frac{\delta D}{D} = \sqrt{2} \frac{(1-k)}{k} \frac{\delta N_0}{N_0} \quad (2.32)$$

While simply identifying the presence of a dip is sufficient to identify a line position, a  $S/N \gg 1$  is necessary to accurately determine the relative intensity of spectral features. For a given level of fluctuations in the molecule number density, one needs to know whether the fluctuations in the dip signal will be greater than or less than the fluctuations in number density. The dip signal will converge to its average value faster than the off-resonance fluorescence signal when,

$$\sqrt{2} \frac{(1-k)}{k} < 1, \quad (2.33)$$

$$k > \frac{\sqrt{2}}{1+\sqrt{2}} \cong 0.586. \quad (2.34)$$

The critical value of the dip,  $D_{crit}$ , above which the S/N on the calculated dip is less than the S/N on the fluorescence signal is  $\sim 0.6$ . For dips in excess of  $D_{crit}$ , the shot-to-shot fluctuations in  $N_0$  are damped by the fact that the PROBE transition is saturated. Unfortunately, PROBE transitions which generate only weak dips require very stable off-resonance fluorescence signals in order to be detected. Evaluation of Eq.(2.32) indicates that for a 10% dip induced by the PROBE laser the S/N on the off-resonance fluorescence signal must be at least 13:1 to have dip S/N greater than unity. If the PROBE transition is saturated,  $k = \frac{1}{2}$ , the S/N on the dip is  $\sim 1.4$  times the fluctuations in the population of the initial state. The dip will always be detectable if the intermediate state can be entirely bleached. This makes intuitive sense if one considers the case of a 100% dip. If there is zero signal when the PROBE is on resonance, the ratio of the off-resonance to on-resonance signal is infinite.

If the signal-to-noise ratio on the dip exceeds that of the fluorescence signal, then the dip itself must be larger than the background fluctuations in order to be observed:

$$N_1(\lambda_2^{\text{off}}) - N_1(\lambda_2^{\text{on}}) > \delta S = \frac{1}{2} \delta N_0. \quad (2.35)$$

When the PUMP transition is saturated, the LHS of Eq.(2.35) is the numerator of Eq.(2.31), and Eq.(2.35) becomes:

$$\frac{1}{2} k N_0 > \frac{1}{2} \delta N_0, \quad (2.36)$$

$$D = k > \frac{\delta N_0}{N_0}. \quad (2.37)$$

This criterion clearly places practical limits on fluorescence dip experiments. If the molecule source is noisy then the PROBE resonance must strongly deplete population in  $|1\rangle$  in order to be observed. Because the laser ablation source is prone to large shot-to-shot fluctuations in CaF production, the technique was not used to detect CaF Rydberg states. It should be noted however that the technique was quite successful for probing low-Rydberg states of CaCl[4]. These states are strongly predissociated and did not have an appreciable fluorescence quantum yield.

### 2.3. 1+1 REMPI

One color REMPI has become an increasingly popular technique over the past decade. It retains much of the simplicity of fluorescence excitation (one laser, low tech. detector and detection electronics, e.g. biased wire plus pre-amplifier plus boxcar signal averager), but does not rely on the resonant intermediate state having an appreciable fluorescence quantum yield. Because both photons are absorbed within the pulse duration of the exciting laser ( $\tau \sim 10$  ns), only very rapid relaxation processes ( $k > 10^8 \text{ s}^{-1}$ ) significantly reduce signal levels.

While fluorescence excitation relies on the detection of emission from the excited state or states populated by fast relaxation of the excited state, REMPI relies on the excited state absorbing a second photon at the excitation wavelength to generate an electron-ion pair. The resonances are not detected by observing emitted photons, but by collecting

photoelectrons or ions. In practice, there are three factors to weigh when considering a 1+1 REMPI experiment:

1. Energy of intermediate state with respect to the ionization threshold.
2. Difference in initial state, intermediate state, and ion geometries.
3. Electronic transition strengths of resonant and ionization steps.

The energy criterion can be understood from Fig. 2.3. The resonant level,  $|1\rangle$ , will be ionized by the absorption of a second photon of energy  $h\nu_1$  only if  $(E_1 - E_0) \geq (IP - E_1)$ . The ionization potential of a neutral molecule is seldom less than 6 eV and more typically closer to 10 eV. This fact precludes the use of 1+1 REMPI as a probe of low-lying,  $< 3$  eV, valence states of many free radicals. The geometry of the intermediate state,  $|1\rangle$ , must be similar to that of the ion in order for the ionization cross-section to be appreciable. This is because the transition moment from the intermediate state to the ionization continuum is proportional to the Franck-Condon factor of the intermediate-continuum transition.

The REMPI process may be treated as a kinetic rate problem as was fluorescence excitation. The two processes may then be compared in terms of sensitivity to the resonant state,  $|1\rangle$ . While the efficacy of fluorescence excitation relies on the intermediate state having an appreciable fluorescence quantum yield, REMPI detection relies on the intermediate state having an appreciable photoionization cross-section. After deriving an expression for the ionization yield in terms of absorption and photoionization cross-sections and radiative and non-radiative relaxation rates, that expression will be evaluated under typically encountered experimental conditions.

The kinetic rate model is not new [5-7], but it is instructive to review and incorporate realistic values of laser flux and absorption cross-sections for the purpose of comparison to fluorescence excitation and other ion detection-based techniques. One can formulate the rate equations from Figure 2.3. The result is simplified if the excited state,  $|1\rangle$ , can only relax to the initial state,  $|0\rangle$ . The relevant equations are as follows:

$$\dot{N}_0(t) = -\sigma_{10}FN_0(t) + [\sigma_{10}F + k_{\text{rad}}]N_1(t), \quad (2.38a)$$

$$\dot{N}_1(t) = \sigma_{10}FN_0(t) + [(\sigma_{10} + \sigma_i)F + k_{\text{rad}} + k_{\text{bath}} + \beta]N_1(t), \quad (2.38b)$$

$$\dot{N}_i(t) = \sigma_iFN_1(t), \quad (2.38c)$$

where  $N_q(t)$  = Population in state  $|q\rangle$  at time,  $t$ .

Implicit in the preceding equations is the assumption that the system is responding to an incoherent excitation/ionization laser field of constant intensity over the pulse duration.

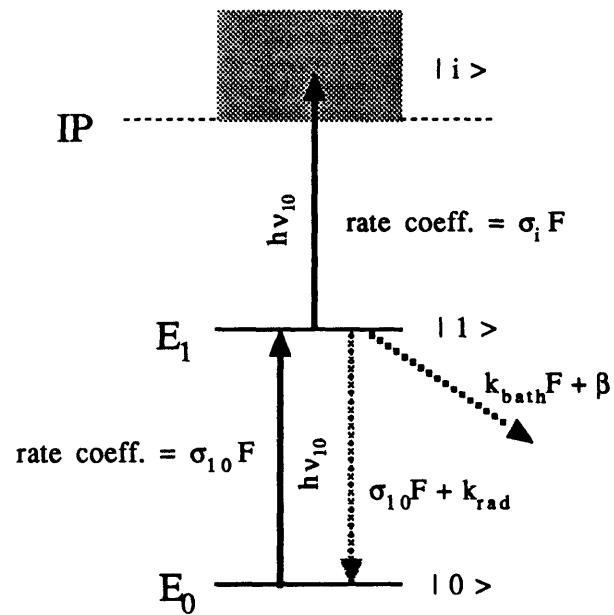


Figure 2.3. Kinetic rate model for 1+1 REMPI.  
 $E_1 - E_0 = h\nu_{10} > IP - E_1$ .

This approximation has been shown to be valid [7] when the duration of the laser pulse is short relative to the lifetime of excited state,  $|1\rangle$ . The system of linear, first-order differential equations in Eq.(2.38a-c) is solved as an eigenvalue problem nearly identical to Eq.(2.7):

$$\det \begin{bmatrix} -\sigma_{10}F - \lambda & \sigma_{10}F + k_{\text{rad}} & 0 \\ \sigma_{10}F & -((\sigma_{10} + \sigma_i)F + k_{\text{rad}} + k_{\text{bath}} + \beta) - \lambda & 0 \\ 0 & \sigma_i F & -\lambda \end{bmatrix} = 0. \quad (2.39)$$

After considerable algebraic manipulation, the time-dependent populations may be expressed analytically in terms of cross-sections, laser flux, and initial population of the ground state.

$$N_0(\tau) = N_0(0) \left[ \frac{1}{k_2} \left[ \left( \sigma_{10}F - \frac{1}{2}(k_1 - k_2) \right) e^{-\frac{1}{2}(k_1 + k_2)\tau} - \left( \sigma_{10}F - \frac{1}{2}(k_1 + k_2) \right) e^{-\frac{1}{2}(k_1 - k_2)\tau} \right] \right], \quad (2.40a)$$

$$N_1(t) = N_0(0) \left[ \frac{k_{10}}{A} \right] \left[ e^{-\frac{1}{2}(A-B)t} - e^{-\frac{1}{2}(A+B)t} \right], \quad (2.40b)$$

$$N_i(t) = N_i(0) \left[ 1 - \frac{1}{2B} \left[ (A+B)e^{-\frac{1}{2}(A-B)t} - (A-B)e^{-\frac{1}{2}(A+B)t} \right] \right], \quad (2.40c)$$

where,

$$A \equiv 2\sigma_{21}F + (k_{2,\text{rad}} + k_{2,\text{bath}} + \beta_2),$$

$$B \equiv \left[ (2\sigma_{21}F)^2 + (k_{2,\text{rad}} + k_{2,\text{bath}} + \beta_2)^2 + 4\sigma_{21}Fk_{2,\text{rad}} \right]^{1/2}.$$

Our interest is in the relative populations of  $N_0$ ,  $N_1$ , and  $N_i$  at time  $\tau$ , after the laser pulse has terminated. One can evaluate these expressions in the low power,  $F\tau \rightarrow 0$ , and high power,  $F\tau \rightarrow \infty$ , regimes. At low laser powers, the number of ions created goes as the square of the laser pulse energy. At high power, both the resonant and non-resonant transitions saturate and ions are generated with near 100% efficiency.

At what pulse energies does one begin to see saturation of the resonant and ionization transitions? If the resonant transition is allowed, its cross-section will greatly exceed that of the excited state-ionization continuum transition. Equation (2.6) suggests that the integrated absorption cross-section of an allowed transitions is,

$$10^{-13} \text{ cm}^2 < \sigma_{10}(\text{typical}) < 10^{-11} \text{ cm}^2 \quad (2.41)$$

A transition at 300 nm having a transition dipole of 1 Debye has an absorption cross-section of  $10^{-11} \text{ cm}^2$ .

Typical photoionization cross-sections are several orders of magnitude smaller than typical absorption cross [6,8]:

$$10^{-18} \text{ cm}^2 < \sigma_{\text{photoionization}} < 10^{-17} \text{ cm}^2 \quad (2.42)$$

The photoionization cross-section depends on the transition dipole moment of the bound-continuum transition in the same way the absorption cross-section depends on the transition dipole moment between the two bound states. Fano and Cooper [9] derive a general expression for the frequency dependent cross-section of a discrete transition in terms of the oscillator strength of the transition (Berkowitz [8] examined their expression qualitatively to get order of magnitude estimates of photoionization cross-sections.):

$$\sigma_i = \frac{2\pi^2 e^2}{mc} f(\omega), \quad (2.43)$$

where  $f(\omega)$  is defined as the oscillator strength of the transition.

$$f(\omega) \equiv \frac{2m}{3\hbar} \omega \left| \langle \Psi_{\text{final}} | \hat{r} | \Psi_{\text{initial}} \rangle \right|^2. \quad (2.44)$$

Equation (2.44) must be integrated over the bandwidth of the exciting radiation to obtain the result of Eq.(2.6). Fano and Cooper show that for a continuous absorption, Eq.(2.43) has a slightly different form:

$$\sigma_{i0} = \frac{2\pi^2 e^2}{mc} \frac{df(\omega)}{d\omega}. \quad (2.45)$$

Substituting in the derivative of Eq.(3.30):

$$\sigma_{i0} = \frac{2\pi^2 e^2}{mc} \cdot \frac{2m}{3\hbar} \left| \langle \Psi_\varepsilon | \hat{r} | \Psi_0 \rangle \right|^2 = \frac{4\pi^2}{3} \alpha \left| \langle \Psi_\varepsilon | \hat{r} | \Psi_0 \rangle \right|^2, \quad (2.46)$$

where  $\alpha$  is the fine structure constant. If the state being ionized is a valence state, the transition moment integral accumulates at small  $r$ . (Valence state electronic wavefunctions do not significant probability density at large  $r$ , but continuum wavefunctions do have amplitude at small  $r$ .) A crude estimate of  $\sigma_{i0}$  may be made using the knowledge that the radial integral,  $\langle R_{n\ell} | r | R_{\ell\ell} \rangle$ , is  $O(1 \text{ \AA}) = 1 \cdot 10^{-8} \text{ cm}$ . The fine structure constant is  $O(10^{-2})$ ,  $\alpha = 1/137.037$ , and  $4\pi^2/3 \approx 10$ . The product of those three quantities suggests that valence state photoionization cross-sections  $O(10^{17} - 10^{18} \text{ cm}^2)$  may reasonably be expected.

The assumption that  $\langle \Psi_{\text{initial}} | r | \Psi_{\text{final}} \rangle = \langle R_{n\ell} | r | R_{\ell\ell} \rangle \approx 1 \cdot 10^{-8} \text{ cm}$  neglects the contribution of the vibrational wavefunctions to the transition moment integral. Under the constraint of the Born-Oppenheimer approximation, the bound and continuum wavefunctions may be expressed as the product of electronic and rovibrational wavefunctions. When vibration occurs on a timescale much faster than rotational motion, the wavefunction may be further separated:

$$\Psi_q = \Psi_q^{\text{el}} \Psi_q^{\text{rot}} \Psi_q^{\text{vib}}. \quad (2.47)$$

The dipole moment operator operates only on the electronic and rotation coordinates of the wavefunctions, so the Eq.(2.14) may be expressed as the product of an electronic-rotational factor and a vibrational, Franck-Condon, factor:

$$\sigma_{i0} = \frac{4\pi^2\omega}{3c} \left| \langle \Psi_e^{\text{el}} \Psi_e^{\text{rot}} | e\hat{r} | \Psi_0^{\text{el}} \Psi_0^{\text{rot}} \rangle \right|^2 \left| \langle \Psi_e^{\text{vib}} | \Psi_0^{\text{vib}} \rangle \right|^2 \quad (2.48)$$

The rotational linestrengths of photoionization transitions have been previously investigated [10], however as the detection process usually does not discriminate different rotational levels of the ion, the term on the LHS of Eq.(2.45) involving rotational and electronic wavefunctions is treated simply as an electronic factor. The Franck-Condon factor will be unity if the bound and continuum states have identical geometries. The Franck-Condon factor may be calculated assuming the bound state and ion move on displaced harmonic oscillator potential energy curves or, more accurately, by calculating vibrational overlap integrals using RKR potential energy curves.

A more rigorously derived 'canonical' value of  $\sigma_i$  may be determined by calculating the cross-section for the hydrogen atom. The transition dipole moment of the H 1s- $\epsilon_p$  absorption has been calculated exactly (assuming no relativistic effects) by Bethe and Salpeter [11]. Because the radial wavefunction of the H 1s orbital has a simple analytic form,

$$R_{10}(r) = e^{-r}, \quad (2.49)$$

the transition dipole moment was found to have a relatively simple analytic form,

$$\langle R_{\varepsilon 0} | r | R_{10} \rangle^2 = \frac{2^8 a_0^3}{e^2} \left[ \frac{\kappa^2}{1 + \kappa^2} \right] \left[ \frac{e^{-4\kappa \arccos \cot \kappa}}{1 - e^{-2\pi\kappa}} \right] \quad (2.50)$$

where  $\kappa \equiv 1/\sqrt{2\varepsilon}$ , and  $\varepsilon$  is the energy of photoelectron (in atomic units). The cross-section depends on the wavelength of the ionizing photon. The particular dependence of  $\sigma_{\text{exp}-1s}$  on the energy,  $E$ , of the ionizing photon is determined by substituting for  $\kappa$ :

$$E = \frac{1}{2} + \varepsilon = \frac{1}{2} \left( 1 + \frac{1}{\kappa^2} \right). \quad (2.51)$$

The photon energy may be expressed in terms of the frequency of the ionizing photon,  $\omega$ , and the electron binding energy,  $E_b$ :

$$E = \hbar\omega = E_b \left[ 1 + \frac{\hbar\omega - E_b}{E_b} \right]. \quad (2.52)$$

The binding energy of the H electron in atomic units is  $(2n^2)^{-1}$ , where  $n$  is the electron's principal quantum number. Eqs.(2.51) and (2.52) are equated to determine the relation between  $\kappa$  and photon frequency,

$$\kappa^2 = \frac{E_b}{\hbar\omega - E_b}. \quad (2.53)$$

The expression for the  $\sigma_i$  then becomes,

$$\sigma_i = \frac{2^9 \pi^2 \alpha}{3} \left( \frac{IP}{\hbar\omega} \right)^4 \left( \frac{e^{-4\kappa \arccos \cot \kappa}}{1 - e^{-2\pi\kappa}} \right) a_0^2, \quad (2.54)$$

where  $\alpha = 1/137.037$ . Near the ionization threshold,  $\frac{E_b}{\hbar\omega} \approx 1$ ,  $\kappa \gg 1$ , and



$$\frac{e^{-4\pi\alpha\cot\kappa}}{1 - e^{-2\pi\kappa}} \approx e^{-4\left(\frac{E_b}{\hbar\omega}\right)^{4/3}}. \quad (2.55)$$

Near threshold, Eq.(2.54) is well approximated as

$$\sigma_{\epsilon p \leftarrow 1s} = 6.4 \cdot 10^{-18} \left(\frac{E_b}{\hbar\omega}\right)^{8/3} \text{ cm}^2 \quad (2.56)$$

The energy dependent photoionization cross-sections of other ns levels of H may also be expressed analytically, however the fact that the radial wavefunctions of the ns orbitals do not have as simple a form as that of the 1s, Eq.(2.49), leads to complex expressions. The energy dependent H ns photoionization cross-sections are well approximated by [12],

$$\sigma_{\epsilon p \leftarrow ns} \cong \frac{64\pi\alpha}{3\sqrt{3}} \left(\frac{(2n^{-2})}{\hbar\omega}\right)^3 \frac{a_0^2}{n^5} = 7.9 \cdot 10^{-18} \left(\frac{1}{1 + 0.0735n^2\epsilon}\right)^3 \frac{1}{n^5} \text{ cm}^2, \quad (2.57)$$

where the excess energy of the photon,  $\epsilon$ , is expressed in eV.

Cooper [13] has shown that for systems more complex than H  $\epsilon p \leftarrow 1s$ , i.e. systems where the radial wavefunction of the bound state has at least one node, the photoionization cross-section may be zero at certain energies above the ionization threshold. The regions in which the photoionization cross-section is (indistinguishably different from) zero are referred to as "Cooper Minima". Cooper Minima are understood in terms of the variation of the bound-continuum transition dipole moment with photoelectron energy.

The spatial frequency of the continuum radial wavefunction oscillations increases with photoelectron energy. At threshold,  $\epsilon=0$ , the free electron has infinite deBroglie wavelength. As  $\epsilon$  increases, the electron's deBroglie wavelength becomes finite and its radial wavefunction oscillates more rapidly. As discussed previously, the transition dipole moment integral accumulates primarily at small  $r$ . When one considers the integral qualitatively, one can see that the integral approaches zero as  $\epsilon$  increases. Figure 2.4 illustrates the continuum wavefunction behavior which gives rise to a Cooper minimum. The integrand oscillates both positive and negative as pictured, however by adjusting  $\epsilon$ , the integrand can be made primarily positive or more equally positive and negative. Near threshold (top graph), the integrand accumulates in the region of  $r \sim 10$  a.u. The negative lobe near  $r \sim 4$  a.u. does little to cancel the positive lobe and the photoionization cross-section is (relatively) large. At higher photoelectron energies (middle graph), the contributions of the positive and negative lobes cancel nearly perfectly and the integral is

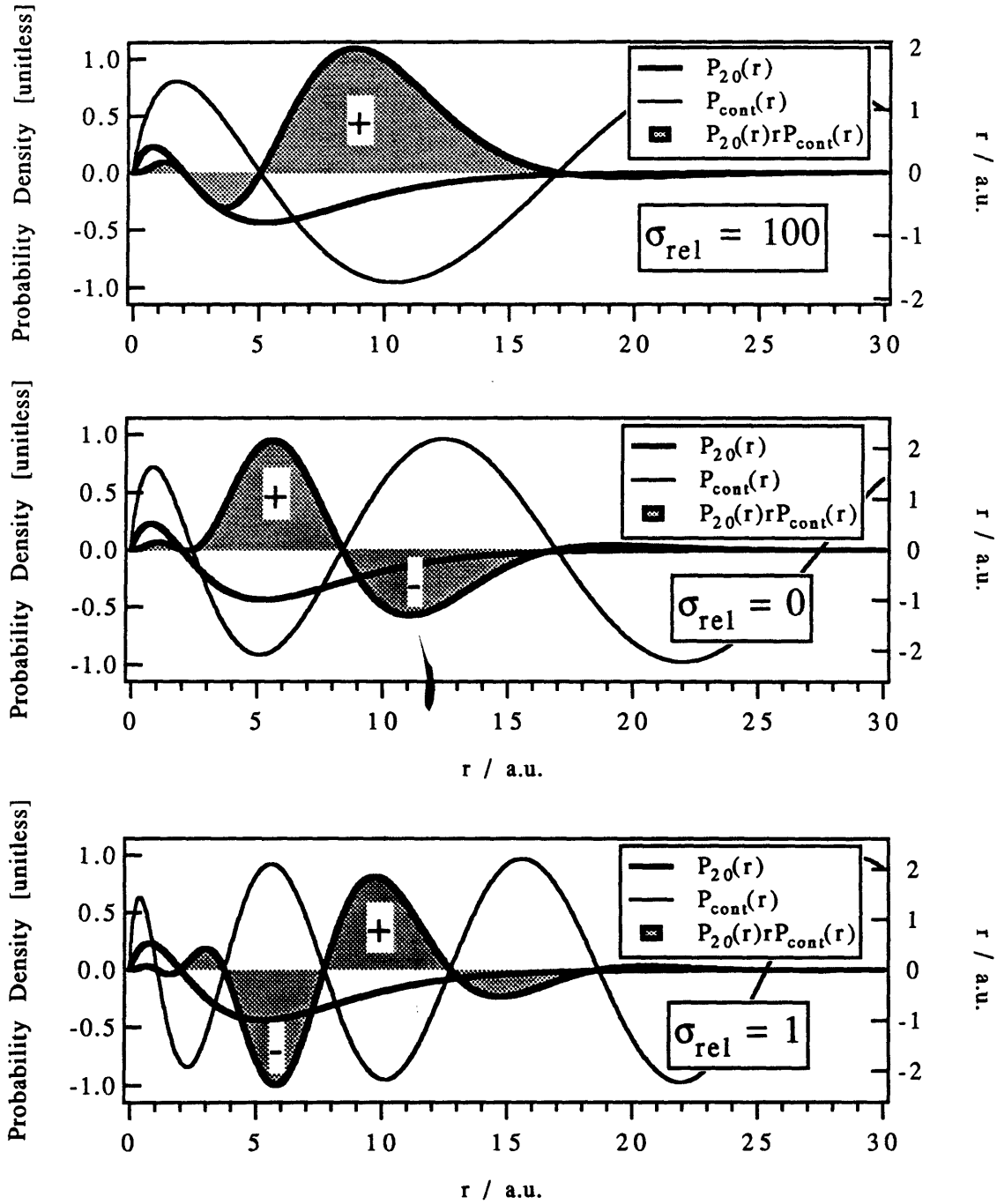


Figure 2.4. Qualitative behavior of the bound-continuum transition moment which gives rise to a Cooper Minimum. The integrand of the transition moment integral oscillates between positive and negative values. When the positive and negative contributions cancel, the transition moment integral is zero and the photoionization cross-section has a Cooper Minimum.

zero (actually 0.1% the value in the top graph). This is the situation which causes a Cooper Minimum in the photoionization cross-section. At still higher photoelectron energies (bottom graph), the positive and negative lobes no longer cancel perfectly and the transition moment is no longer zero. However the more rapid oscillations of the continuum wavefunction cause the value of the integrand to be much smaller than at threshold. (Note: Eq.(2.43) must be used with caution. It does not account for Cooper Minima and will give reasonable predictions of  $\sigma_i$  only within several eV of threshold, i.e. while the continuum wavefunction is still oscillating slowly.) The resonant step of the REMPI scheme is easily saturated with a typical pulse from a pulsed dye laser. A transition dipole moment of 1 Debye, typical for an allowed transition, would be easily saturated by a 10 ns laser pulse with a flux of  $1 \mu\text{J}/\text{cm}^2$ . The result of Eq.(2.40b) for a variety of transition dipole moments of the  $|1\rangle\text{-}|0\rangle$  transition is shown in Fig.2.5. Bound-continuum transitions require much higher fluences to saturate, however saturation is still well within the realm of typical dye laser pulses.

It is instructive to evaluate the predictions of Eq.(2.40a-c) under a variety of conditions: absorption cross-section  $\gg$  ionization cross-section, absorption cross-section  $\approx$  ionization cross-section, rapid losses from intermediate state, no losses from intermediate state, low and high laser powers. Of particular interest are the relative populations of  $|1\rangle$  and  $|i\rangle$  at the termination of the excitation laser pulse. Fluorescence detection depends upon the ability of the PUMP to populate  $|1\rangle$ . Ion detection requires population of  $|i\rangle$ . Crudely, a 1+1 REMPI experiment will be preferable to a fluorescence excitation experiment when  $N_i(\tau) > N_1(\tau)$ .

Figure (2.6) depicts  $N_1(\tau)$  over a wide range of laboratory accessible dye laser fluxes;  $1 \text{ mJ cm}^{-2}$  is roughly the maximum achievable flux with the unfocussed output of our laboratory's dye lasers. In Fig.(2.6)  $N_1(\tau)$  is calculated using Eq.(2.40b) and modest values for the absorption and ionization cross-section,  $\sigma_{10}/\sigma_i = 10^5$ . At low laser fluxes,  $N_1(\tau)$  increases linearly with PUMP energy. When the induced absorption and stimulated emission rates of the PUMP transition exceed the loss rate from  $|1\rangle$ ,  $N_1(\tau)$  remains constant at  $\sim 0.5 N_0(0)$ . When the natural loss rate from  $|1\rangle$  roughly equals the PUMP rate ( $\beta=10^8 \text{ s}^{-1}$ ), but the PUMP transition is saturated,  $N_1(\tau)$  remains constant, but well below  $0.5 N_0(0)$ . This is because the net population,  $N_0(t) + N_1(t) + N_i(t)$ , is decreasing on the time scale of the PUMP pulse. The curve for  $\beta=10^9 \text{ s}^{-1}$  has a maximum near PUMP flux of  $10^3 \text{ mJ/cm}^2$  because when  $|0\rangle$  is excited to  $|1\rangle$ ,  $|1\rangle$  has a higher probability of being destroyed than being returned to  $|0\rangle$ . Only when the stimulated emission rate exceeds the loss rate does the population reach a steady state value.  $N_1(\tau)$  decreases at higher fluxes because the ionization step in the REMPI experiment starts to become efficient.

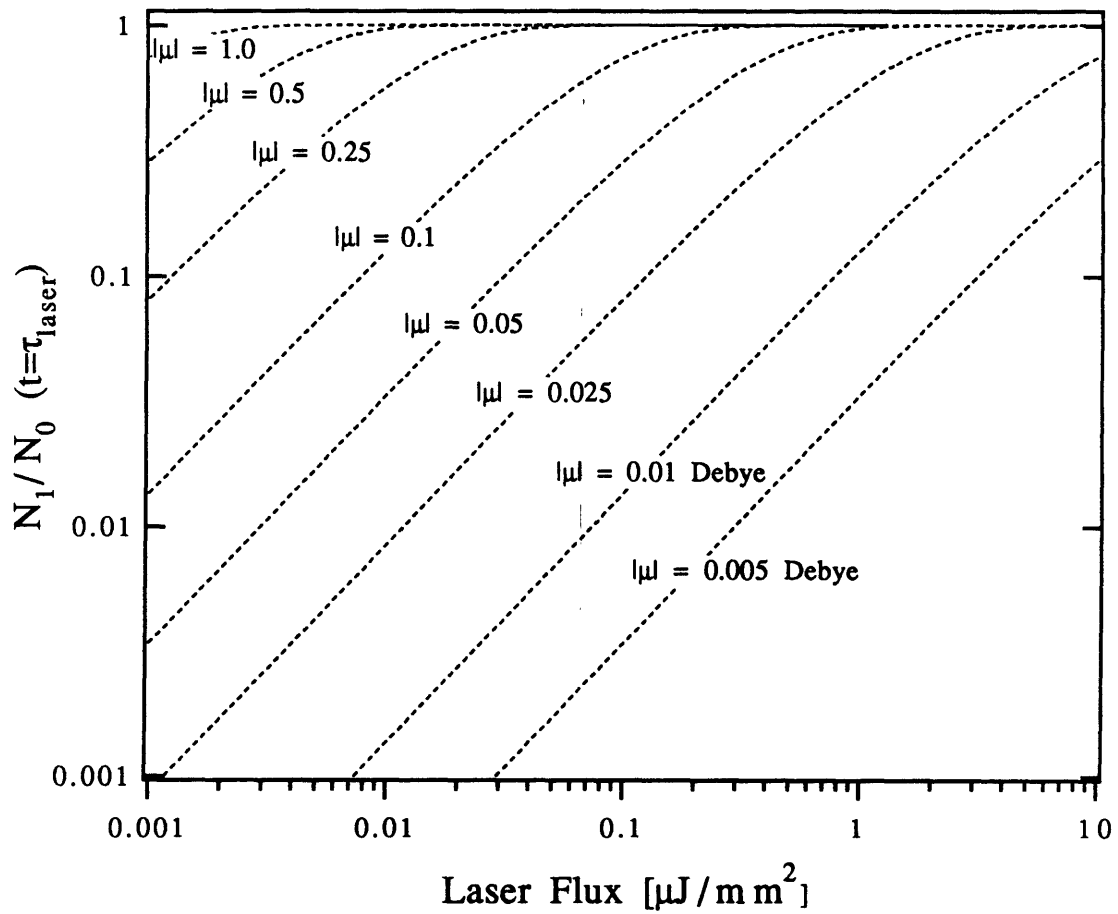


Figure 2.5. Ratio of intermediate to ground state population at the termination of the PUMP pulse as a function to transition dipole moment and PUMP laser flux. The PUMP wavelength is to be 300 nm and the pulse duration 10 ns.

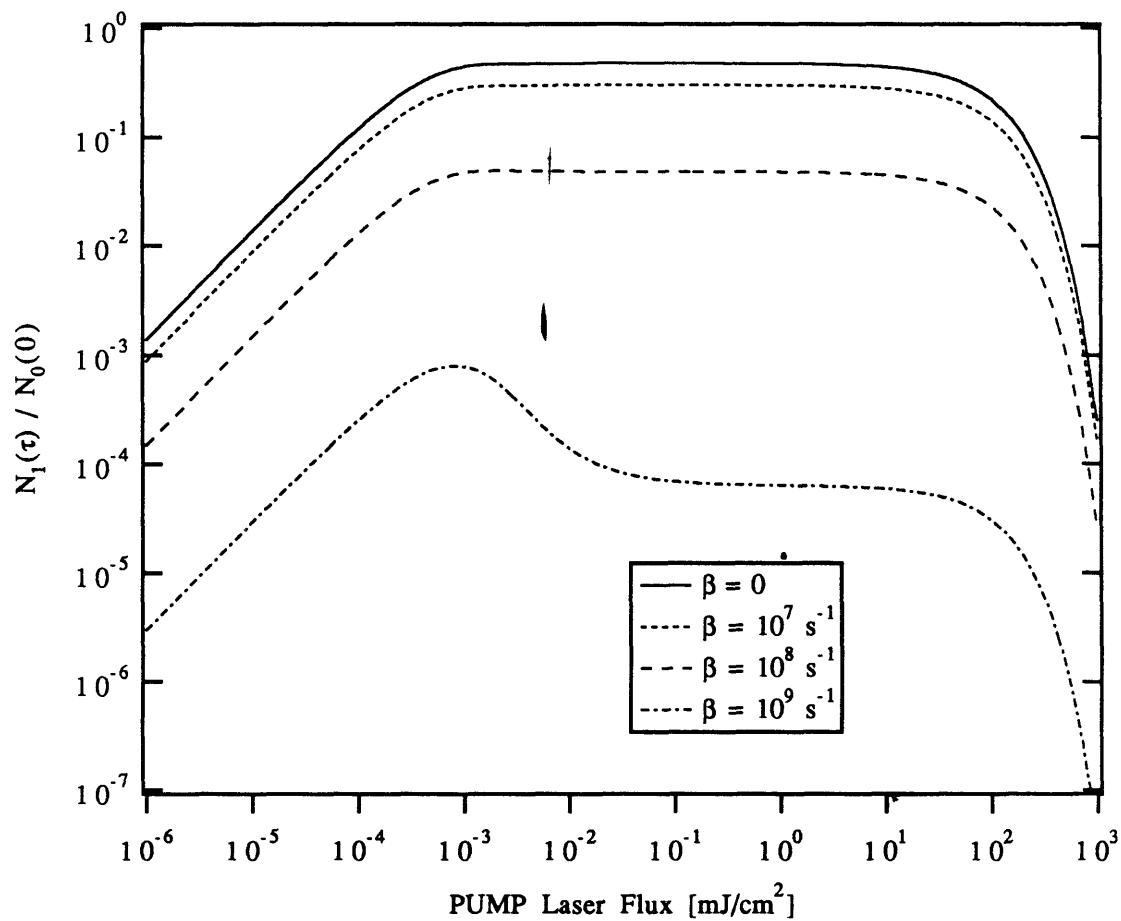


Figure 2.6. Relative population in the intermediate state at termination of the PUMP pulse as a function of PUMP laser flux for various non-radiative loss rates in the intermediate. The absorption cross-section for the PUMP transition is  $10^{-12} \text{ cm}^2$  and the ionization cross-section is  $10^{-17} \text{ cm}^2$ . The radiative relaxation of  $|1\rangle$  to the ground state and to the bath states is  $10^7 \text{ s}^{-1}$ .

Figure 2.7 depicts ionization efficiency as a function of laser flux. The ionization efficiency is calculated using Eq.(2.40c). At fluxes below saturation of the PUMP transition, 0.001 mJ/cm<sup>2</sup>, ionization efficiency increases quadratically with PUMP laser flux. After the PUMP transition saturates, ionization efficiency increases linearly with PUMP flux. At fluxes of ~100 mJ/cm<sup>2</sup>, the ionization transition begins to saturate. The ionization yield goes to unity when the PUMP and ionization rates exceed the sum of the non-radiative loss and stimulated emission rates. Figure 2.8 presents a direct comparison of the ionization efficiency and the fluorescence excitation efficiency. The fluorescence excitation efficiency is the product of  $N_1(\tau)$  and the fluorescence quantum yield of  $|1\rangle$ . The circled intersections on the figure are the points at which the fluorescence excitation efficiency and the ionization efficiency are equal for a given loss rate from the intermediate state,  $|1\rangle$ . When losses are slow relative to the PUMP rate, fluorescence excitation is more efficient than REMPI for all but the highest laser fluxes. As the loss rate is increased, the break-even point shifts to lower flux, but the overall efficiency of the process becomes low. The overall efficiency of the process can be increased markedly by increasing laser power, however the resonant transition will become power broadened.

At what point will power broadening begin to degrade the resolution of the REMPI spectra? Saturation broadening results in a Lorentzian line profile [14],

$$\Delta\nu_{pb} = [1 + I/I_{sat}]^{1/2} \Delta\nu_{hom} \quad (2.58)$$

The natural linewidth,  $\Delta\nu_{hom}$ , is due to the lifetime of the excited state:

$$\Delta\nu_{hom} = 5.3 \text{ ps cm}^{-1} / \tau_{rad} \quad (2.59)$$

$\Delta\nu_{hom} = 0.0001 \text{ cm}^{-1}$  for an excited state with a 50 ns lifetime.

If the absorption cross-section is six orders of magnitude larger than the photoionization cross-section, not an atypical situation, and the ionization step of the REMPI transition is sufficiently irradiated that it is near 100% efficient, then the power broadened linewidth will be  $O(10^3)$  times the natural linewidth. Substituting  $I / I_{sat} = \sigma_{i0} / \sigma_i = 10^6$  into Eq.(2.58),

$$\Delta\nu_{pb} = [1 + 10^6]^{1/2} (0.0001 \text{ cm}^{-1}) = 0.1 \text{ cm}^{-1} \quad (2.60)$$

The lasers used in the experiments described here have linewidths ranging from  $0.08 \text{ cm}^{-1} \leq \Delta\nu_L \leq 0.20 \text{ cm}^{-1}$  (for the Lumonics HyperDye 300 the linewidth is typically  $0.15 \text{ cm}^{-1}$  and

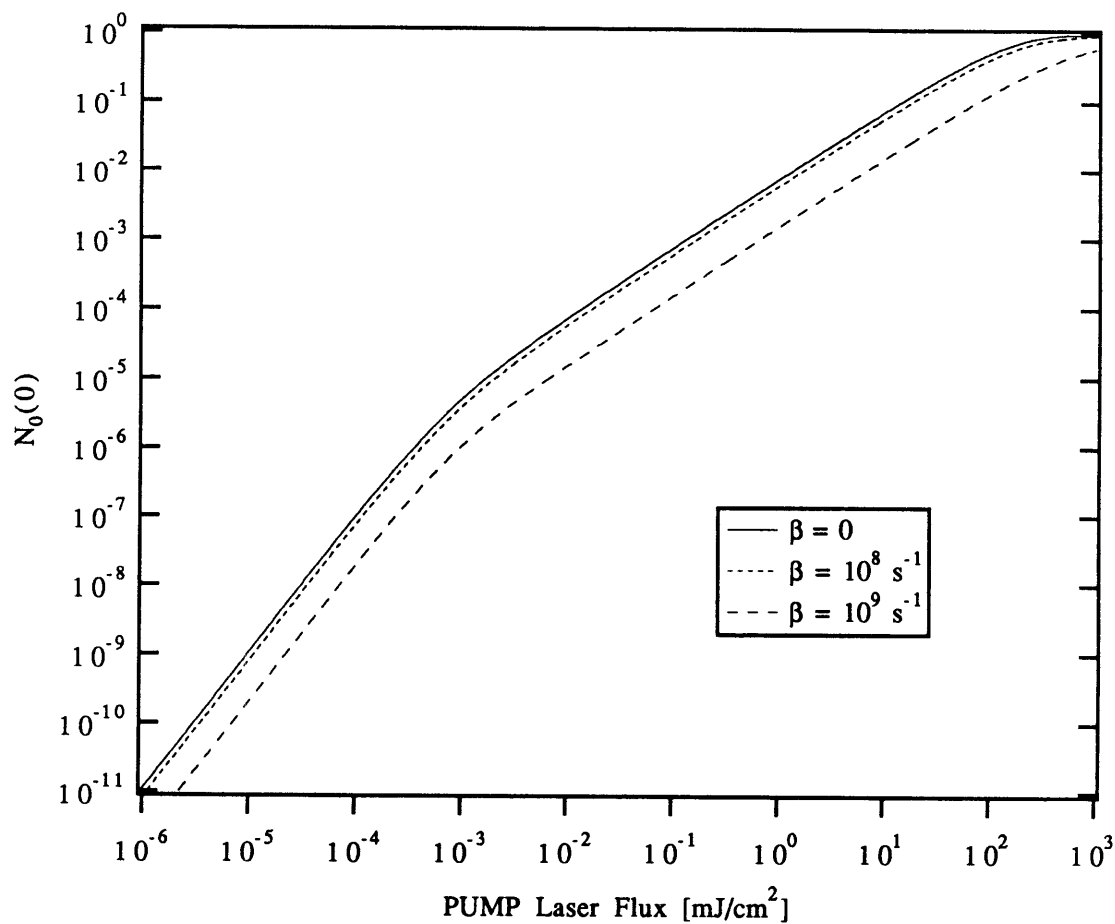


Figure 2.7. 1+1 REMPI efficiency as a function of PUMP laser flux for a range of non-radiative loss rates in the resonant state. The absorption cross-section for the PUMP transition is  $10^{-12} \text{ cm}^2$  and the ionization cross-section is  $10^{-17} \text{ cm}^2$ . The radiative relaxation rate of the intermediate to the ground state and to the bath states is  $10^7 \text{ s}^{-1}$ .

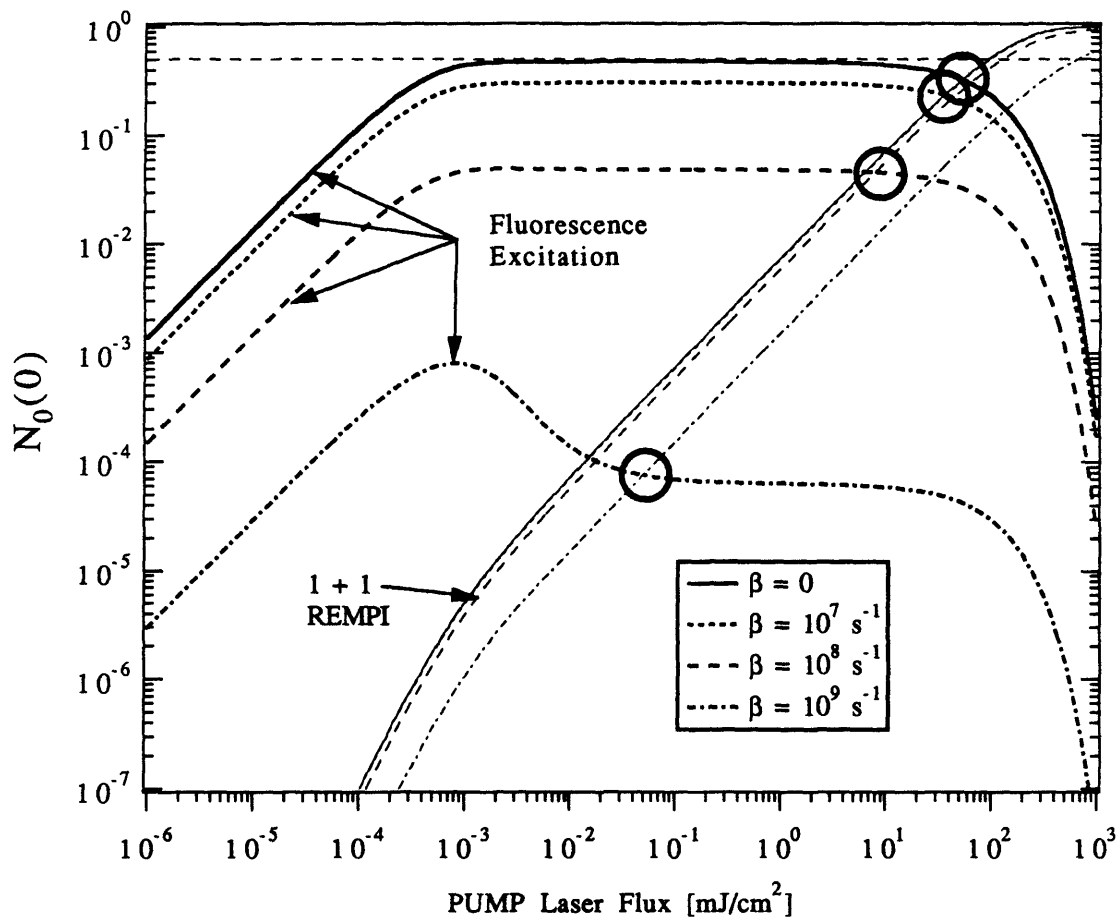


Figure 2.8. Relative Efficiency of Fluorescence Excitation and 1+1 REMPI for a range of loss rates,  $\beta$ . The circled intersections represent the break even points for fluorescence excitation and REMPI detection. Detection of ions and photons are both assumed to be 100% efficient. The absorption cross-section for the PUMP transition is  $10^{-12} \text{ cm}^2$  and the ionization cross-section is  $10^{-17} \text{ cm}^2$ .



or the HyperDye 550 it is closer to  $0.10 \text{ cm}^{-1}$ ). Power broadening was observed when using the HyperDye 300 to perform 1+1 REMPI of  $\text{Al}_2$  through the  $E^3\Sigma_g^- - X^3\Pi_u$  transition with  $O(10 \text{ mJ/mm}^2)$  of UV. Power broadening of the CaF  $A^2\Pi_{3/2} - X^2\Sigma^+(0,0)$  and  $C^2\Pi_{3/2} - X^2\Sigma^+(0,0)$  transitions occurs with  $\ll 1 \text{ }\mu\text{J/mm}^2$ .

#### 2.4. Ionization Detected Optical-Optical Double Resonance (ID-OODR)

UV fluorescence detected OODR was not a successful investigatory technique for CaF Rydberg states with  $n^* > 10$ . In general, UV fluorescence detection is not an efficient means of detecting high Rydberg states because high Rydberg states typically have poor a fluorescence quantum yield and prefer to emit in the infrared and far infrared, often out of the range commonly/inexpensively available detectors. While the strength of Rydberg-valence transitions decreases as  $(n^*)^{-3}$  [15], the pulse energy of a typical laboratory dye laser,  $O(10^2 \text{ }\mu\text{J})$  in a 10 ns pulse, is usually sufficient to populate Rydberg states with  $n^* \gg 10$ . The problem with detecting Rydberg states with  $n^* \geq 10$  is that their fluorescence lifetime increases as  $(n^*)^3$  and they radiate most efficiently in the infrared to other Rydberg states with just slightly lower  $n^*$ . Rydberg states with  $n^* \approx 10$  have radiate lifetimes  $O(10^1 \text{ }\mu\text{s})$ , thereby making them prone to non-radiative relaxation (e.g. collisions, predissociation).

While fluorescence detection of high Rydberg states is not efficient, they may be field ionized and the ions efficiently collected. The application of an electric field lowers the ionization potential of the molecule by  $\sim 6F^{1/2} \text{ cm}^{-1}$  [5,17], where  $F$  is the applied field in V/cm. The binding energy of the Rydberg electron is  $\sim 10^5(n^*)^{-2} \text{ cm}^{-1}$ , so the field necessary to ionize an  $n^* = 15$  Rydberg state is  $\sim 6.6 \text{ kV/cm}$ ;  $\sim 28 \text{ kV/cm}$  is necessary to field ionize  $n^* = 10$ . While electric fields of this magnitude are not extraordinarily difficult to generate, they are not particularly convenient to work with.

Another possible double resonance based detection scheme would be to perform 1+1 REMPI out of an intermediate state. The PUMP step of the CaF OODR scheme, either the  $A^2\Pi_{3/2} - X^2\Sigma^+$  or  $C^2\Pi_{3/2} - X^2\Sigma^+$  transition, is saturated with just a few  $\mu\text{J}$  of PUMP energy. The limitation of 1+1+1' REMPI is the 1'+1' step. The drawback of 1+1 REMPI was outlined in the previous section. The resonant (PROBE) step of the REMPI process is typically far more efficient than the ionization step. While the technique is better than fluorescence excitation for detecting a state which undergoes rapid non-radiative relaxation, it is not a particularly efficient means of detecting that state except at very high PROBE

laser powers. The 1+1 REMPI technique turns out to decrease in efficiency as  $n^*$  of the state being probed increases. The relative efficiency of the resonant step goes as  $(n^*)^{-3}$ . Unfortunately, the efficiency of the ionization step falls off even faster. Equation (2.56) suggests that the efficiency of one-photon ionization decreases as the binding energy of the electron over the photon energy all to the 8/3 power. The energy of the ionizing photon in the REMPI transition is equal to the energy of the resonant photon,  $E_{\text{res}}$ :

$$E_{\text{res}} = \text{IP} - \mathfrak{R}(n^*)^{-2} - E_1, \quad (2.44)$$

where IP is the ionization potential and  $E_1$  is the energy of the intermediate state. When probing Rydberg states,  $\text{IP} - E_1 \gg \mathfrak{R}(n^*)^{-2}$ . The relative efficiency of photoionization is:

$$\epsilon_i = \left[ \frac{\mathfrak{R}(n^*)^{-2}}{(\text{IP} - E_1) - \mathfrak{R}(n^*)^{-2}} \right]^{8/3}, \quad (2.45)$$

but because  $\text{IP} - E_1 \gg \mathfrak{R}(n^*)^{-2}$ ,  $\epsilon_i$  falls off as  $\sim (n^*)^{-16/3}$ . The meaning of this result is that not only is it eight times more difficult to excite  $n^*=20$  than  $n^*=10$  (for members of the same Rydberg series), but it is also forty times more difficult to photoionize them. The 1+1'+1' REMPI scheme has been tested for low Rydberg states of CaCl [17] and the result of Eq.(2.45) has been qualitatively confirmed.

The most efficient means of detecting CaF Rydberg states with  $n^* > 12.5$  was to monitor the production of  $\text{CaF}^+$  produced by vibrational autoionization. While the electronic energy of these states was less than the molecular ionization potential, they were prepared with at least one quanta of vibration in the  $\text{CaF}^+$  ion-core and their total energy exceeded the lowest ionization threshold.

Molecular states whose total energy (electronic plus spin-orbit plus vibrational plus rotational) exceeds the molecular ionization potential, but whose electronic energy alone is less than the IP may give rise to anomalously large values of effective photoionization cross-section. Such states are called "superexcited" or "quasi-bound". Electronic, vibrational, and rotational motions are not completely decoupled in the molecule. Terms neglected in the Born-Oppenheimer potential, e.g. dependence of the electronic wavefunction on the vibrational coordinates, couple superexcited states to the electronic continuum (hence the term "quasi-bound"). Bound-superexcited transitions may have greater oscillator strength than bound-continuum transitions owing to better overlap of the the initial and final state electronic wavefunctions. Superexcited states ionize by

irreversibly transferring energy from their rotational, spin-orbit, or vibrational degrees of freedom to the electronic degree of freedom. This process is known as "autoionization". In contrast to ionization of the bound state by direct absorption to the continuum, rotational and vibrational autoionization involves at least two Born-Oppenheimer excited states.

Spin-orbit and electronic coupling may be stronger than vibrational coupling, however the ion must possess multiple low-lying spin-orbit and electronic states in order for these relaxation mechanisms to be open. (The  $\text{CaF}^+$  cation possesses  $^1\Sigma^+$  ground state; no spin or electronic orbital angular momentum. The first excited state of  $\text{CaF}^+$  lies 10's of eV above the ionization potential of the neutral molecule and therefore there is no electronic ionization channel open to the molecule.) In atoms, autoionization of quasi-bound spin-orbit and doubly excited electronic states gives rise to 'anomalous' increases in photoionization cross-section. Fano [18] has quantified the lineshapes of transitions to quasibound states. His derivation of lineshapes and photoionization cross-section enhancement in atoms serves as a paradigm for vibrational autoionization induced cross-section enhancements and lineshapes in molecules. It should be noted that while it was hoped that Fano lineshapes would be observed in the vibrational autoionization detected OODR spectra of  $\text{CaF}$ , no such profiles were identified.

Herzberg and Jungen [19] developed a phenomenological model for predicting the linewidth of bound-superexcited transitions broadened by rapid autoionization in the superexcited state. They developed a simple expression for calculating lifetime broadening by  $\Delta v = 1$  vibrational autoionization from the assumption that the ion and the superexcited state move on slightly different potential energy curves,  $U^+(\text{R})$  and  $U(\text{R})$ . The lifetime broadening due to vibrational autoionization may be predicted from  $n^*$ , the vibrational constant of the ion, and the derivative of the quantum defect with internuclear separation:

$$\Gamma_{v,v-1} = 2\pi \frac{2\mathfrak{R}}{(n^*)^3} \left[ \frac{d\delta_i}{dR} \right]_{R^*}^2 \frac{16.858}{\mu\omega} \text{ cm}^{-1}, \quad (2.46)$$

where  $d\delta/dR$  is the quantum defect derivative in  $\text{\AA}^{-1}$  (the quantum defect is defined as the hydrogenic principal quantum number,  $n$ , minus  $n^*$ ),  $\mu$  is the reduced mass of the cation in amu, and  $\omega$  is the vibrational constant of the cation. The quantum defect derivative may be thought of as arising from the modulation of the electric multipole moments of the cation due molecular vibration. The value of the quantum defect is typically 0.01-1.0  $\text{\AA}^{-1}$ . Rydberg states possessing one quanta of vibration in the ion core may undergo vibrational autoionization when their total energy exceeds the ionization threshold for  $v=0$ , or:

$$IP_{v=1} - \frac{\mathfrak{R}}{(n^*)^{-2}} = IP_{v=0} + \Delta G_{1/2} - \frac{\mathfrak{R}}{(n^*)^{-2}} \geq IP_{v=0}. \quad (2.47)$$

In  $\text{CaF}^+$ ,  $\Delta G_{3/2} = 685 \text{ cm}^{-1}$ , so the lowest value of  $n^*$  for which  $v = 1$  Rydberg states may autoionize is 12.66. The linebroadening due to autoionization is:

$$\Gamma_{v,v-1} = 1.30 \left[ \frac{12.66}{n^*} \right]^3 \left[ \frac{d\delta_i}{dR} \right]_{R^*}^2 \text{ cm}^{-1}. \quad (2.46)$$

The vibrational autoionization rate is  $\Gamma_{v,v-1} / 5.3 \cdot 10^{-12} \text{ s cm}^{-1}$ . An  $n^*=14$  CaF Rydberg state may be expected to have a vibrational autoionization rate  $O(10^9-10^{11} \text{ s}^{-1})$ . The radiative relaxation rate of an  $n^*=14$  Rydberg state is on the order of  $(10 \mu\text{s})^{-1}$ . Vibrational autoionization is believed to be the primary mechanism for relaxation of superexcited states of CaF lying just above its  $v=0$  ionization threshold. Vibrational autoionization rates of several CaF Rydberg states are measured in Chapter 5. In conclusion,  $\Delta v = 1$  vibrational autoionization in superexcited CaF is so rapid relative to other relaxation processes (even for the smallest expected values of the quantum defect derivative) that once Rydberg levels above the threshold are prepared by the PROBE laser, they autoionize and are subsequently detected with near unit efficiency. This made ionization detected double resonance preferable to fluorescence detected double resonance, fluorescence dip, and  $1+1'+1'$  REMPI for the Rydberg states under investigation.

## 2.5. References

1. W. Demtröder, "Laser Spectroscopy", 1st ed., Springer-Verlag, 1981.
2. R.C. Hilborn, *Am.J.Phys.*, v.50 (1982), p.982.
3. A. Yariv, "Quantum Electronics", 2nd ed., Wiley, 1975.
4. N.A. Harris, Ph.D. thesis, MIT, 1995.
5. D.S. Zakheim and P.M. Johnson, *Chem.Phys.*, v.65 (1980), p.263.
6. V.S. Letokhov, "Laser Photoionization Spectroscopy", Ch.3, Academic Press, 1987.
7. D.C. Jacobs, R.J. Madix, and R.N. Zare, *J.Chem.Phys.*, v.85 (1986), p.5469.
8. J. Berkowitz, "Photoabsorption, Photoionization, and Photoelectron Spectroscopy", 2nd ed., Academic Press, 1979.
9. U. Fano and J.W. Cooper, *Rev. Mod. Phys.*, v.40 (1968), p.441.
10. J. Xie and R.N. Zare, *J. Chem. Phys.*, v.97 (1992), p. 2891.
11. H.S. Bethe and E.E. Salpeter, "Quantum Mechanics of One- and Two-Electron Atoms", Section 71, Springer-Verlag, 1957.
12. I.I. Sobelman, "Atomic Spectra and Radiative Transitions, 2nd ed.", Ch.9., Springer-Verlag, 1992.
13. J.W. Cooper, *Phys. Rev.*, v.128 (1962), p.681.
14. A.E. Seigman, "Lasers", University Science, 1986, p.295.
15. C.Fabre and S.Haroche in "Rydberg States of Atoms and Molecules", Ch.3., R.F.Stebbins and F.B.Dunning, eds., Cambridge University Press, 1983.
16. J.L. Persson and R.L. Whetten, *Chem. Phys. Lett.*, v.147 (1988), p.168.
17. C.M. Gittins and N.A. Harris, unpublished results.
18. U. Fano, *Phys. Rev.*, v.124 (1961), p.1866.
19. G. Herzberg and Ch. Jungen, *J. Mol. Spectro.*, v.41 (1972), p.425.

## CHAPTER 3

### Background for Data Analysis: Effective Hamiltonian Matrix Models and Assigning ID-OODR Spectra

#### 3.1. Effective Hamiltonian for Rydberg States

The Hamiltonian for CaF is a sum of electronic, spin-orbit, vibrational and rotational Hamiltonians:

$$\mathbf{H} = \mathbf{H}^{\text{el}} + \mathbf{H}^{\text{so}} + \mathbf{H}^{\text{vib}} + \mathbf{H}^{\text{rot}}. \quad (3.1)$$

The full wavefunctions for CaF Rydberg states are constructed from Born-Oppenheimer basis states:

$$|\Psi_{\text{total}}\rangle = |\phi_{\text{el}}\rangle |\phi_{\text{rot,vib}}\rangle. \quad (3.2)$$

The factorization of  $|\phi_{\text{rot,vib}}\rangle$  into rotational and vibrational wavefunctions is an accurate approximation when vibrational and rotational motion occur on very different timescales:

$$|\phi_{\text{rot,vib}}\rangle = |\phi_{\text{rot}}\rangle |\phi_{\text{vib}}\rangle. \quad (3.3)$$

For vibrational states near the bottom of the CaF<sup>+</sup> potential well,  $v < 10$ , vibrational motion occurs on a much faster timescale than rotational motion. (The rotational period goes as the inverse of the rotational number,  $J$ .) For a given electronic state, Eq.(3.3) is a good approximation when the separation between adjacent vibrational energy levels is much greater than the separation between rotational energy levels:

$$\omega_{\text{vib}} \gg 2BJ, \quad (3.4)$$

where  $\omega_{\text{vib}}$  is the vibrational frequency of the cation in cm<sup>-1</sup>,  $B$  is its rotational constant in cm<sup>-1</sup>, and  $J$  is the cation rotational quantum number. Evaluation of Eq.(3.4) using

experimentally determined values of  $B$  and  $\omega_{\text{vib}}$  [1] suggests that separation of rotational and vibrational wavefunctions is legitimate when  $J \ll 900$ . In the experiments discussed here,  $J < 15$ .

### 3.1.1. The Vibrational Hamiltonian

The vibrational wavefunction of a CaF Rydberg state is characterized by the vibrational quantum number,  $v$ :

$$|\phi_{\text{vib}}\rangle = |v\rangle. \quad (3.5)$$

The vibrational energy levels are well-described as those of a Morse oscillator:

$$\mathbf{H}_{v,v}^{\text{vib}} = \hbar \left[ \omega_e \left( v + \frac{1}{2} \right) - \omega_e x_e \left( v + \frac{1}{2} \right)^2 \right] \delta_{v,v}, \quad (3.6)$$

where  $\delta$  is the Kronecker delta function. The vibrational constant and anharmonic terms in Eq.(3.6) for CaF Rydberg states are essentially those of the  $\text{CaF}^+$  cation. The Rydberg electron is non-bonding and only minimally shields the core electrons from the nuclei. (Shielding decreases as (effective principal quantum number)<sup>-3</sup> and will be discussed later.) Hamiltonian matrix elements involving vibrational wavefunctions, i.e.  $\langle v | (R - R_e^+)^n | v' \rangle$ , may be calculated most accurately by numerical integration of wavefunctions determined by RKR potential curve inversion. Near the bottom of its vibrational potential well,  $\text{CaF}^+$  may be approximated as a Morse or harmonic oscillator. The harmonic oscillator approximation not only results in simple analytic expressions for matrix elements, but more importantly results in accurate estimation of matrix elements when one has not observed a sufficient number of levels to construct an accurate RKR or Morse potential energy curve. Morse matrix element expressions are also analytic, but not as simple [2].

### 3.1.2. The Electronic Hamiltonian

The fact that the electronic structure of CaF may be described in terms of a single, unpaired electron makes the electronic and spin-orbit matrix elements relatively simple to evaluate. CaF electronic wavefunctions are characterized by a minimum of four quantum numbers: the effective principal quantum number,  $n^*$ ; the projection of the electron orbital angular momentum on the molecular axis,  $\lambda$ ; electron spin angular momentum,  $s \equiv \frac{1}{2}$ ; and the projection of  $s$  on the molecular axis,  $\sigma$ . Core non-penetrating electronic states,  $\ell \geq 3$ , are characterized by a fifth quantum number,  $\ell$ , the orbital angular momentum quantum number of the Rydberg electron:

$$|\phi_a\rangle = |n^*, (\ell), \lambda, s, \sigma\rangle. \quad (3.7)$$

The electronic term value of a Rydberg state is calculated using the Rydberg formula:

$$E_{n_i^*} = IP - \frac{\mathfrak{R}}{(n_i^*)^2} \quad (3.8)$$

The quantity  $\mathfrak{R}(n_i^*)^{-2}$  is the binding energy of the Rydberg electron;  $\mathfrak{R}$  is the Rydberg constant for CaF,  $109736.30 \text{ cm}^{-1}$ , IP is the ionization potential of Rydberg series, and  $n_i^*$  is the effective principal quantum number of the Rydberg state. Equation (3.8) may also be inverted to determine the effective principal quantum number for a Rydberg state if both the ionization potential and electronic term value of the state are well-known. Equation (3.8) is typically used to calculate a rotationless term value for a Rydberg state, in which case the quantity IP refers the rotationless term value of vibrational state of the cation to which the series converges. Equation (3.8) may also be used to calculate the term value of rotational levels or spin-orbit states, in which case IP would be the term value of an excited rovibrational or spin-orbit level of the ion core. In this document, IP is always the rotationless term value of the cation having the same vibrational quantum number as the Rydberg state.

The effective principal quantum number is defined as equal to an integer value hydrogenic principal quantum number minus the quantum defect,  $\delta$ , for the Rydberg series. The most general notation for effective principal quantum number is,



$$n^* = n - \delta. \quad (3.9)$$

The quantum defect is approximately constant for a Rydberg series [3]. Physically, the quantum defect is the  $(\pi)^{-1}$  times the phase shift of the Rydberg orbital relative to a 'parent' hydrogenic atomic orbital with integer value  $\ell$ . Rydberg states which sample the non-point charge nature of the ion core at short range will, as a general rule, have larger quantum defects than states which sample the ion core only weakly. When the Rydberg formula is inverted to determine  $n^*$ , the absolute magnitude of  $\delta$  is ambiguous. Determination of  $n^*$  using the Rydberg formula yields  $\text{mod}(\delta, 1)$ . The absolute magnitude of  $\delta$  must be determined by experimental observation of the first member of the Rydberg series or by a quantum chemical or Quantum Defect Theory [4] calculation.

Additional notation may be added to Eq.(3.9) to better specify the Rydberg state, as the effective principal quantum number itself may not distinguish one state from all others. The expression,

$$n_{i,\Lambda}^* = n_i - \delta_{i,\Lambda}, \quad (3.10)$$

denotes the effective principal quantum number of a state in the  $i^{\text{th}}$  Rydberg series of a particular value of  $\Lambda$ . Many physical properties of Rydberg states obey  $n^*$  scaling relationships. In addition to determining the electronic energy of the Rydberg state, the effective principal quantum number is also useful in extrapolating molecular constants (e.g. spin-orbit splittings, spin-rotation constants, transition strengths) from lower energy Rydberg states [5].

Herzberg and Jungen [6] have shown that Eq.(3.8) implies an effective Hamiltonian of the form:

$$H^{\text{el}}(\mathbf{R}) = \text{IP} - \mathfrak{R} \left[ \frac{1}{n_i^2} + \frac{2\delta(\mathbf{R})}{(n_i n_j)^{3/2}} \right]. \quad (3.11)$$

This Hamiltonian consists of a zero-order, hydrogenic term:

$$H^{0,\text{el}} \equiv \left[ \text{IP} - \frac{\mathfrak{R}}{n_i^2} \right] |n_i\rangle \langle n_i|, \quad (3.12)$$

and a first-order, internuclear separation dependent, non-hydrogenic correction with diagonal terms:

$$\mathbf{H}^{1,el}(\mathbf{R}) = -\frac{2\mathfrak{R}}{n_i^3} \delta(\mathbf{R}) |n_i\rangle \langle n_i|, \quad (3.13)$$

and off-diagonal terms,

$$\mathbf{H}^{1,el}(\mathbf{R}) = -\frac{2\mathfrak{R}}{(n_i n_j)^{3/2}} \delta(\mathbf{R}) |n_i\rangle \langle n_j|. \quad (3.14)$$

The phenomenological Hamiltonian in Eq.(3.14) is most accurate when  $n_i$  and  $n_j$  are members of the same Rydberg series, i.e., referring to Eq.(3.10):

$$n_{j,\Lambda}^* = n_{i,\Lambda}^* \pm m, \quad (3.15)$$

where  $m$  is an integer. The electronic term value of a Rydberg state with principal quantum number  $n_i$ , quantum defect  $\delta_i$ , and vibrational quantum  $v$  is:

$$\langle n_i^*, v | \mathbf{H}^{el} | n_i^*, v \rangle = \text{IP} - \frac{\mathfrak{R}}{(n_i)^2} - \frac{2\mathfrak{R}}{(n_i)^3} \delta_i = \text{IP} - \frac{\mathfrak{R}}{(n_i^*)^2}. \quad (3.16)$$

The quantum defect function,  $\delta(\mathbf{R})$  in Eqs.(3.11) and (3.13), may be analyzed to extract information about the multipole moments of the cation core and the exchange of electronic and vibrational or rotational energy between the Rydberg electron and the cation. All information concerning deviation from hydrogenic behavior is contained in the quantum defect function.

The quantum defect function may be expanded as a Taylor series. One typically expands about the equilibrium internuclear separation of the  $\text{CaF}^+$  cation,  $R_e^+$ , because  $R_e$  for high Rydberg states,  $n^* > 10$ , rapidly approaches  $R_e^+$ :

$$\delta(\mathbf{R}) \cong \delta(R_e^+) + \left( \frac{d\delta}{dR} \right)_{R_e^+} (R - R_e^+) + \frac{1}{2} \left( \frac{d^2\delta}{dR^2} \right)_{R_e^+} (R - R_e^+)^2. \quad (3.17)$$

For small variations about  $R_e^+$ , only the first two terms on the RHS of Eq.(3.17) contribute significantly to  $\delta(\mathbf{R})$ . The  $R$ -dependent Hamiltonian in Eq.(3.13) may give rise to

"intrachannel" perturbations between Rydberg states in the same series, i.e.  $n_j = n_i - m$ , where  $m$  is an integer, but differing in degree of electronic and vibrational excitation. The effect of the Hamiltonian in Eq.(3.13) on two basis states  $|n_i, v\rangle$  and  $|n_i - m, v + 1\rangle$  is:

$$\langle n_i, v | \mathbf{H}^{1,el}(\mathbf{R}) | n_i - m, v + 1 \rangle = -\frac{2\mathfrak{R}}{[n_i(n_i - m)]^{3/2}} \langle n_i, v | \delta(\mathbf{R}) | n_i - m, v + 1 \rangle, \quad (3.18)$$

substituting Eq.(3.15) into Eq.(3.16) yields,

$$\langle n_i, v | \mathbf{H}^{1,el}(\mathbf{R}) | n_i - m, v + 1 \rangle \approx -\frac{2\mathfrak{R}}{[n_i(n_i - m)]^{3/2}} \left[ \delta(\mathbf{R}_e^+) \langle v | v + 1 \rangle + \left( \frac{d\delta}{d\mathbf{R}} \right)_{\mathbf{R}_e^+} \langle v | (\mathbf{R} - \mathbf{R}_e^+) | v + 1 \rangle \right]. \quad (3.19)$$

Because the  $v$  and  $v+1$  vibrational wavefunction do not overlap, the matrix element between  $|n_i, v\rangle$  and  $|n_i - m, v + 1\rangle$  is determined by the second term in brackets in Eq.(3.19). An expression for "interchannel" matrix elements,  $n_i^*$  and  $n_j^*$  not members of the same Rydberg series, could be formulated in the same manner as that for "intrachannel" matrix elements. The  $(n_i n_j)^{-3/2}$  scaling relation in Eq.(3.14) is not as accurate however between members of two different Rydberg series as it is for members of the same Rydberg series. The reason for this will be discussed later in this section.

The strongest intrachannel interactions are for  $\Delta v = \pm 1$ . Referring to Eq.(3.18), this is because near the equilibrium internuclear separation, the magnitude of the first derivative of the quantum defect at  $\mathbf{R}_e^+$  is much larger than the magnitude of the second derivative. The matrix element of the first-order,  $\mathbf{R} - \mathbf{R}_e^+$ , term in Eq.(3.17) between states in the same series is:

$$\langle n_i^* + m, v | \mathbf{H}^{el} | n_i^*, v' \rangle = -\frac{2\mathfrak{R}}{[n_i(n_i + m)]^{3/2}} \left[ \left( \frac{d\delta_i}{d\mathbf{R}} \right)_{\mathbf{R}_e^+} \langle v | \mathbf{R} - \mathbf{R}_e^+ | v' \rangle \right], \quad (3.20)$$

where  $m$  is an integer. The quantity  $\langle v | \mathbf{R} - \mathbf{R}_e^+ | v' \rangle$  may be evaluated analytically using harmonic oscillator wavefunctions, in which case it has the selection rules  $v' = v \pm 1$ :

$$\langle v|R - R_e^+|v' \rangle = \sqrt{\frac{\hbar}{2c\mu\omega_e^+}} \sqrt{v+1} = \frac{4.106}{\sqrt{\mu\omega_e^+}} \sqrt{v+1} \text{ \AA}. \quad (3.21)$$

$\mu$  = cation reduced mass [amu],  $\omega_e^+$  = cation vibrational frequency [ $\text{cm}^{-1}$ ]

For  $\text{CaF}^+$ :  $\langle v=1|R - R_e^+|v=0 \rangle = 0.0437 \text{ \AA}$ ;  $R_e^+ = 1.874 \text{ \AA}$ .

The quantum defect derivative is typically determined by observing an intrachannel perturbation and setting the expression in Eq.(3.20) equal to an experimentally determined matrix element. The matrix element between two states in the same Rydberg series,  $n_i^*$  and  $n_i'^* = n_i^* + m$ , is:

$$V_{n_i^*, v - n_i'^*, v'} \equiv \langle n_i^*, v | H^{\text{el}} | n_i'^*, v' \rangle = -\frac{2\mathfrak{R}}{[n_i n_i']^{3/2}} \left[ \left( \frac{d\delta_i}{dR} \right)_{R_e^+} \langle v | R - R_e^+ | v' \rangle \right], \quad (3.22)$$

where the matrix element is in units of  $\text{cm}^{-1}$  and the quantum defect derivative is in units of  $\text{\AA}^{-1}$ . Setting  $v' = v + 1$ ,

$$\left( \frac{d\delta_i}{dR} \right)_{R_e^+} \equiv -\frac{[n_i n_i']^{3/2}}{2\mathfrak{R}} \frac{\sqrt{\mu\omega_e^+}}{4.106\sqrt{v+1}} V_{n_i^*, v - n_i'^*, v+1}. \quad (3.23)$$

Quantum defect derivatives of the 0.36  $\Pi$  and 0.14  $\Delta$  series have been previously calculated [1] using the observation of a single interchannel perturbation. The quantum defect derivative for the 0.36  $\Pi$  series is  $0.73_2 \text{ \AA}^{-1}$  and is  $0.3_6 \text{ \AA}^{-1}$  for the 0.14  $\Delta$  series. Ideally, the quantity would be determined by the observation of multiple perturbations, i.e. multiple values of  $n_i$ ,  $n_i'$ , and  $v$ . The relationship through the quantum defect derivative between bound-bound and bound-continuum interactions will be discussed later. An accurate determination of the derivative by observation of a single two-state interaction is entirely dependent upon the validity of the  $(n_i n_i')^{-3/2}$  scaling relation. This is an excellent approximation. The quantitative accuracy of this relationship demonstrate will be demonstrated shortly.

The quantum defects of  $\text{CaF}$  Rydberg states are not zero because the  $\text{CaF}^+$  cation is not a point charge. For core-penetrating states, the quantum defect accumulates primarily at short-range due to an increase in effective charge of the core as the electron penetrates inside the core. When the Rydberg electron is close to the ion core, the Ca and F nuclei are

no longer screened completely by their core electrons and the Rydberg electron experiences a higher  $Z_{\text{eff}}$ ,  $Z_{\text{eff}} > 1$ , than when it is far from the cation. In contrast, core non-penetrating states experience the  $\text{CaF}^+$  cation primarily at long range, and their quantum defects arise not so much from the  $r$ -dependence of  $Z_{\text{eff}}$ , but from the difference in the long-range effective potentials of  $\text{CaF}^+$  and  $\text{H}^+$ :

$$\lim_{r \rightarrow \infty} [V_{\text{CaF}^+}(r, \theta) - V_{\text{H}^+}(r, \theta)] = \frac{\mu}{r^2} P_{10}(\cos \theta) + \frac{Q}{r^3} P_{20}(\cos \theta) + \dots \quad (3.24)$$

The quantities  $\mu$  and  $Q$  being the electric dipole and quadrupole moments of the  $\text{CaF}^+$  cation and the  $P_{n0}(\cos \theta)$  terms are Legendre polynomials. The electrostatic matrix elements between Rydberg states will involve integrating the product of radial wavefunctions and an  $r^{-k}$  factor.

The  $n^*$ -scaling properties of these integrals may be understood in terms of the overlap of the innermost lobes of Rydberg orbitals. Analysis of hydrogenic radial wavefunctions shows that the shape of the inner part, i.e. the portion up to the second node, of an  $n\ell$  wavefunction is nearly identical to that of the  $(n-1)\ell$  state if the  $n\ell$  wavefunction is multiplied by  $[n/(n-1)]^{-3/2}$ . This scaling relationship would not be valid if the locations of the inner nodes were  $n$ -dependent. Fortunately, the location of the inner nodes rapidly approaches a fixed value as  $n$  increases. This may be understood by examining the  $r$ -dependence of the electron kinetic energy as a function of principal quantum number. The total energy of an electron in a hydrogenic orbital is easily separated into kinetic energy and potential energy contributions:

$$E = T - V, \quad (3.25)$$

which in atomic units is:

$$-\frac{1}{2n^2} = T(n, r) - \frac{1}{r}. \quad (3.26)$$

The kinetic energy is:

$$T(n, r) = \frac{1}{r} - \frac{1}{2n^2}. \quad (3.27)$$

The nodal structure of the radial wavefunction depends on  $T(n,r)$ . The radial wavefunction undergoes rapid oscillations when  $T$  is large, and oscillates slowly when  $T$  is small. At short range, the  $r^{-1}$  term will dominate the  $(2n^2)^{-1}$  contribution to  $T(n,r)$ . This effect increases with  $n$ . The kinetic energy of the Rydberg electron at small  $r$  is essentially independent of the total energy of the electron and the nodal structure of successive members of the Rydberg series is therefore nearly identical. The difference in kinetic energy between  $n=10$  and  $n=11$  at  $r = 2$  a.u. is  $< 0.2\%$  of the total kinetic energy. The innermost node of the H  $ns$  radial wavefunctions is located at  $\sim 1.8$  a.u. Figure 3.1 depicts the position of the first and second nodes of the H atom radial wavefunction as a function of principal quantum number,  $n$ . The node locations as  $n$  tends towards infinity are indicated by dashed lines.

The inner portions of H  $ns$  radial wavefunctions may be fit to  $(n' \neq n)s$  orbitals assuming  $R_{n_s}(r) = k_{nn'} R_{n'_s}(r)$ . In order to demonstrate the quantitative accuracy of the  $[n/n']^{-3/2}$  scaling relation, the H 5s and 6s orbitals were fit to H 3s, 4s, and 5s orbitals from  $r = 0$  up to the  $r = 6.5$  a.u., roughly the location of the second node. The results are listed in Table 3.1. The quantity  $k_{nn'}$ , as was determined by best fit, is compared to the predicted scale factor,  $(n/n')^{3/2}$ . The percentage difference between the two scale factors is the difference between the calculated and fit scale factors divided by the fit value, all multiplied by 100%. The percentage difference increases with increasing  $\Delta n$ , but decreases with increasing  $n$ .

Table 3.1 Principal Quantum Number Scaling in H  $ns$  Radial Wavefunctions

$R_{n_s}(r) \sim R_{n'_s}(r)$	$\Delta n$	$k_{nn'}$	$(n/n')^{3/2}$	% Difference
$R_{5_s}(r) \sim R_{3_s}(r)$	2	0.459(2)	0.465	1.3
$R_{5_s}(r) \sim R_{4_s}(r)$	1	0.713(1)	0.716	0.4
$R_{6_s}(r) \sim R_{3_s}(r)$	3	0.348(2)	0.354	1.7
$R_{6_s}(r) \sim R_{4_s}(r)$	2	0.541(1)	0.544	0.6
$R_{6_s}(r) \sim R_{5_s}(r)$	1	0.759(1)	0.760	0.1

This scaling relation has been tested for systems other than hydrogen using effective, rather than hydrogenic, principal quantum numbers. For example, using the results of Hartree-Fock calculations, Slater [7] demonstrated that the inner two lobes of the Na 4s orbital may be scaled directly onto those of the 3s simply by multiplying the 4s by 2.095 (see Fig.7.6, Ref.[7]). The effective principal quantum number of the 3s state of Na, as

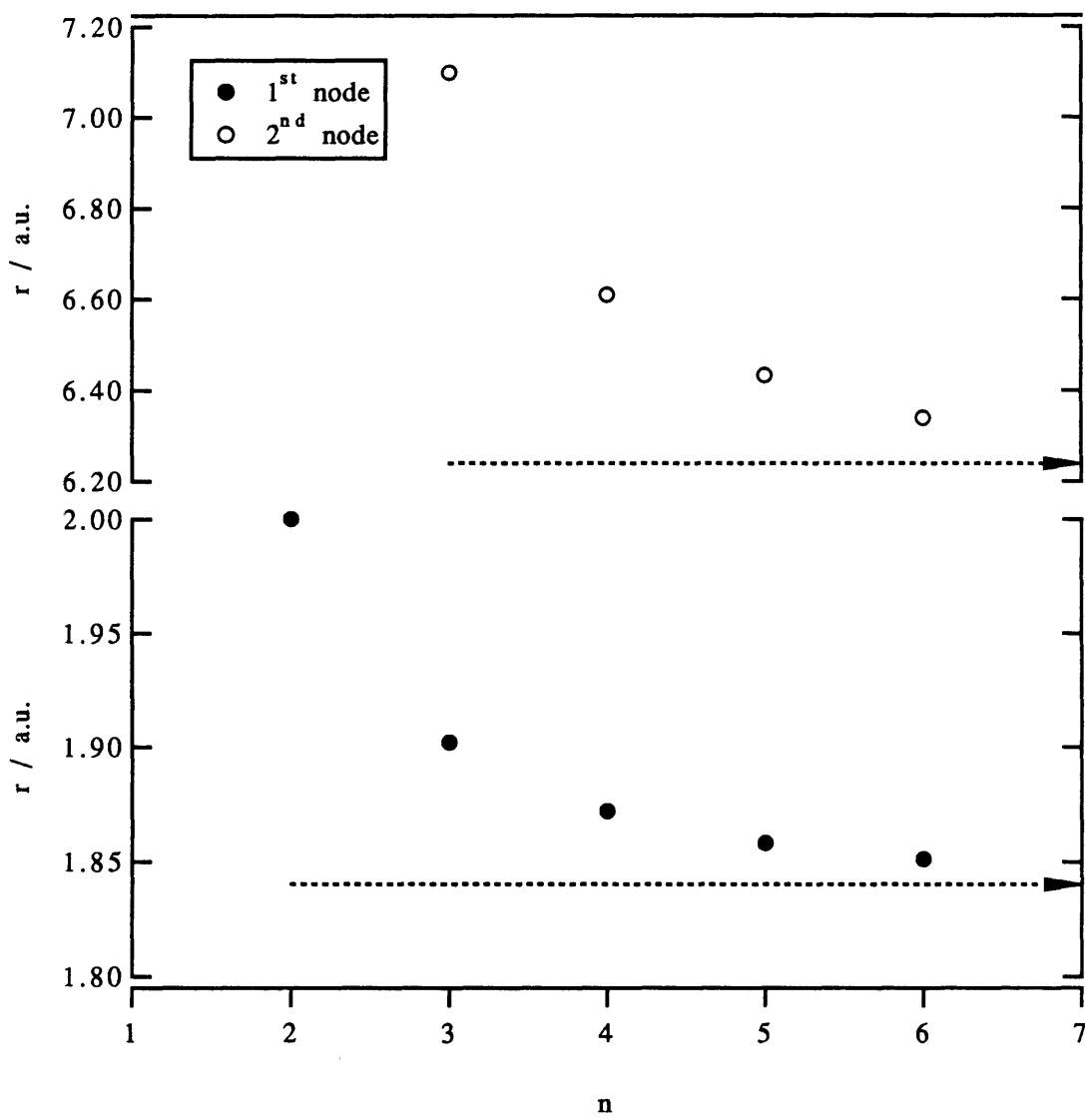


Fig. 3.1. Location of two innermost nodes of H ns radial wavefunctions.

determined by inversion of the Rydberg formula, is 1.627. The effective principal quantum number of the Na 4s state is 2.643. The calculated  $n^*$  scale factor,  $[2.643/1.627]^{3/2} = 2.070$ , is within 1.2% of Slater's empirical 'best fit' multiplicative factor. As  $\langle n_i^* | r^{-k} | n_j^* \rangle$  matrix elements depend on the product of the amplitudes of the wavefunctions, their scaling behavior goes as  $(n_i^* n_j^*)^{-3/2}$ . This scaling relation would not hold if the integral accumulated at values of  $r$  where the radial portions of  $ln_i^*$  and  $ln_j^*$  are no longer in phase. When  $R_{n_i}(r)$  and  $R_{n_j}(r)$  are in phase, which is true at short-range for members of the same Rydberg series, the sign of their product is  $r$ -independent. The  $\langle n_i^* | r^{-k} | n_j^* \rangle$  matrix elements accumulate monotonically with increasing  $r$ . If  $R_{n_i}(r)$  and  $R_{n_j}(r)$  are not in phase, the sign of their product will be  $r$ -dependent. The  $\langle n_i^* | r^{-k} | n_j^* \rangle$  matrix elements might accumulate at small  $r$ , where  $r^{-k}$  is largest, only to be reduced at large  $r$  where the overlap of the radial wavefunctions is greater. As this latter contribution is  $n^*$  dependent, integrals involving radial wavefunctions which are out of phase at short-range, i.e. integrals between members of different Rydberg series, will not adhere as well to the  $(n_i^* n_j^*)^{-3/2}$  scaling relation. The  $(n_i^* n_j^*)^{-3/2}$  scaling relation remains accurate so long as the phase difference between the two radial wavefunctions remains approximately constant over the range on which the integral accumulates.

The approximations invoked are more apparent when one examines radial integrals explicitly. It is assumed that the term in  $H^{\text{el}}$  which couples the two Rydberg states has the form  $r^{-k}$ :

$$I \equiv \langle n_i | r^{-k} | n_j \rangle = \int_0^{\infty} \frac{R_{n_i}^*(r) R_{n_j}(r)}{r^k} r^2 dr \equiv \int_0^{r_0} \frac{R_{n_i}^*(r) R_{n_j}(r)}{r^k} r^2 dr. \quad (3.28)$$

The integrals in Eq.(3.23) accumulate primarily at small  $r$  because the  $r^{-k}$  term rapidly approaches zero as  $r$  increases. This allows one to terminate the integration at a finite value of  $r$ ,  $r_0$ , without significantly affecting the result. In principle, one can then evaluate all radial matrix elements between  $n_i$  and other members of the same Rydberg series simply by employing the  $(n_i/n_j)^{-3/2}$  scaling relation. The crucial assumption is that

$$R_{n_i+m}(r) = \left( \frac{n_i}{n_i + m} \right)^{3/2} R_{n_i}(r) \quad (3.29)$$



over the range on which the integral accumulates. An integral involving the product of two radial wavefunctions,  $R_{n_j}(r)$  and  $R_{n_i+m}(r)$  may be approximated using Eqs.(3.28) and (3.29):

$$\int_0^{\infty} \frac{R_{n_i+m}(r)R_{n_j}(r)}{r^k} r^2 dr \cong \int_0^{r_0} \frac{R_{n_i+m}(r)R_{n_j}(r)}{r^k} r^2 dr \cong \left( \frac{n_i}{n_i+m} \right)^{3/2} \int_0^{r_0} \frac{R_{n_i}(r)R_{n_j}(r)}{r^k} r^2 dr;$$

$$= \left( \frac{n_i}{n_i+m} \right)^{3/2} I. \quad (3.30)$$

All of the details about the phase difference between the  $i$  and  $j$  Rydberg series are in  $I$ . All of the  $n^*$ -scaling behavior is in the  $n_i$  wavefunction. Electrostatic matrix elements of this form for the NO molecule are tabulated in Table 4.5 of ref.[8].

### 3.1.3. The Spin-Orbit Hamiltonian

Atomic and molecular spin-orbit constants decrease as  $(n^*)^{-3}$ . This dependence is exact for the hydrogen atom, and is empirically confirmed by the measurement of spin-orbit constants in atoms and molecules having more than one electron. For species with more than one electron, the accuracy of the  $(n^*)^{-3}$  scaling behavior improves with increasing  $n^*$ . The one-electron molecular spin-orbit Hamiltonian is:

$$H^{so} = a(r)\boldsymbol{\ell} \cdot \mathbf{s} = a(r)[\ell_z s_z + \frac{1}{2}(\ell^+ s^- + \ell^- s^+)]. \quad (3.31)$$

The operator  $a(r)$  is defined in Ref.[8] and acts only on the radial coordinates of the electronic wavefunction. The operator  $a(r)$ , integrated over electronic coordinates is the one-electron molecular spin-orbit constant,  $a$ , and is proportional to  $\langle r^{-3} \rangle$ . It is the  $\langle r^{-3} \rangle$  dependence which gives rise to the  $(n_i^*)^{-3}$  scaling behavior. The diagonal matrix elements of  $a(r)$  are:

$$\langle n_i^*, \lambda | a(r) | n_i^*, \lambda \rangle = a_{n_i^*} \approx \frac{k_{i,\lambda}}{(n_i^*)^3}. \quad (3.32)$$

The off-diagonal matrix elements follow a similar scaling relationship:

$$\langle n_i^*, \lambda | a(r) | n_j^*, \lambda \rangle = a_{n_i^*, n_j^*} \approx \frac{k_{ij, \lambda}}{(n_i^* n_j^*)^{3/2}}. \quad (3.33)$$

The quantitative accuracy of Eq.(3.33) has been established from the results of quantum chemical calculations[9]. The expectation value of the spin-orbit Hamiltonian may be separated into a quantity involving only electron coordinates and a quantity involving only electron angular momenta:

$$\begin{aligned} \langle n_i^*, (\ell_i), \lambda_i, s_i, \sigma_i | \mathbf{H}^{so} | n_i^*, (\ell_i), \lambda_i, s_i, \sigma_i \rangle = \\ \langle n_i^*, (\ell_i) | a(r) | n_i^*, (\ell_i) \rangle \langle (\ell_i), \lambda_i, s_i, \sigma_i | \ell \cdot s | (\ell_i), \lambda_i, s_i, \sigma_i \rangle. \end{aligned} \quad (3.34)$$

The  $\ell \cdot s$  operator has selection rules  $\Delta \ell = \Delta s = 0$  and  $\Delta \lambda = -\Delta \sigma = 0, \pm 1$ . The spin-orbit operator has the following effect on atomic basis functions:

$$\ell_z s_z | \ell, \lambda, s, \sigma \rangle = \lambda \sigma | \ell, \lambda, s, \sigma \rangle \quad (3.35)$$

$$\ell^\pm s^\mp | \ell, \lambda, s, \sigma \rangle = \sqrt{\ell(\ell+1) - \lambda(\lambda \pm 1)} \sqrt{s(s+1) - \sigma(\sigma \mp 1)} | \ell, \lambda \pm 1, s, \sigma \mp 1 \rangle. \quad (3.36)$$

Although  $\mathbf{H}^{so}$  may mix states of different  $\lambda$ , it will be shown that its primary effect is to lift the degeneracy of states having  $\ell$  and  $s$  coupled parallel versus anti-parallel. Combining the results of Eqs.(3.34-36) to determine this splitting:

$$\left\langle n_i^*, \lambda, \frac{1}{2}, \frac{1}{2} \middle| a(r) \middle| n_i^*, \lambda, \frac{1}{2}, \frac{1}{2} \right\rangle = \frac{\lambda}{2} a \quad (3.37)$$

$$\left\langle n_i^*, \lambda, \frac{1}{2}, -\frac{1}{2} \middle| a(r) \middle| n_i^*, \lambda, \frac{1}{2}, -\frac{1}{2} \right\rangle = -\frac{\lambda}{2} a. \quad (3.38)$$

The energy difference between the two spin-orbit components is

$$\left\langle n_i^*, \lambda, \frac{1}{2}, \frac{1}{2} \middle| a(r) \middle| n_i^*, \lambda, \frac{1}{2}, \frac{1}{2} \right\rangle - \left\langle n_i^*, \lambda, \frac{1}{2}, -\frac{1}{2} \middle| a(r) \middle| n_i^*, \lambda, \frac{1}{2}, -\frac{1}{2} \right\rangle = \lambda a \quad (3.39)$$

Berg, et al. [10] determined  $k$  for the 0.36  $\Pi$  and 0.98  $\Pi$  series to be  $\sim 300 \text{ cm}^{-1}$  and  $\sim 450 \text{ cm}^{-1}$ , respectively, from measurements of the spin-orbit constants of Rydberg states with

$n^* < 7$  and  $v = 0$ . The spin-orbit constant should be only weakly dependent on  $v$ , so Eq.(3.32) implies a spin-orbit constant of  $\sim 0.13 \text{ cm}^{-1}$  for  $13.36 \Pi$ ,  $v=1$ ;  $\sim 0.21 \text{ cm}^{-1}$  for  $12.98 \Pi$ ,  $v=1$ ;  $\sim 0.62 \text{ cm}^{-1}$  for  $8.98 \Pi$ ,  $v=2$ ; and  $\sim 0.36 \text{ cm}^{-1}$  for  $9.36 \Pi$ ,  $v=2$ . The observability of splittings of this magnitude will be discussed after the analysis of rotational energy level patterns of the CaF Rydberg states under investigation. For all CaF Rydberg states with  $n^* > 10$ , the spin-orbit constant,  $a$ , is too small to give rise to an observable splitting in the experiments performed for this work.

In addition to giving rise to a first-order spin-orbit splitting,  $H^{so}$  can couple electronic states within an  $n^*$  complex. The intra-complex  $\ell\lambda$ -mixing due to the off-diagonal spin-orbit coupling (mixing angle) remains constant with increasing  $n^*$ . This is clear from examination of the first-order spin-orbit correction to the wavefunction of a Rydberg state  $|n_i^*\rangle$ . The first-order corrected wavefunction is:

$$|n_i^{*'}\rangle = |n_i^*\rangle + \frac{\langle H^{so} \rangle}{\Delta E} |n_j^*\rangle, \quad (3.40)$$

where  $\langle H^{so} \rangle$  is the matrix element in Eq.(3.34). All reference to electronic and spin angular momentum quantum numbers has been dropped from the previous expression. The integral  $\langle n_i^*, (\ell_i), \lambda_i, s_i, \sigma_i | H^{so} | n_j^*, (\ell_j), \lambda_j, s_j, \sigma_j \rangle$  may be factored into a term involving angular momentum quantum numbers and a term involving only the radial portion of the electronic wavefunctions. The former term will be a constant of  $O(10^0)$ . As mentioned previously, the latter term is well approximated as:

$$\langle n_i^* | a(r) | n_j^* \rangle = k_{ij} (n_i^* n_j^*)^{-3/2}. \quad (3.41)$$

For two states within an  $n^*$  block, we may make the substitutions  $\bar{n} = \frac{1}{2}(n_i^* + n_j^*)$  and  $\Delta = n_+^* - n_-^*$ , where  $n_{\pm}^*$  refers to the greater and lesser of  $n_i^*$  and  $n_j^*$ ;  $n_{\pm}^* = \bar{n} \pm \frac{\Delta}{2}$ . In the limit of large  $n_i^*$ ,

$$\langle n_i^* | a(r) | n_j^* \rangle = k_{ij} (\bar{n})^{-3} \left[ 1 + \left( \frac{\Delta}{2\bar{n}} \right)^2 \right]^{-3/2} \cong k_{ij} (\bar{n})^{-3}. \quad (3.42)$$

The energy difference between  $n_j^*$  and  $n_i^*$  also scales as  $(\bar{n})^{-3}$ :

$$\Delta E = \mathfrak{R} \left[ \frac{1}{(\bar{n} - \frac{\Delta}{2})^2} - \frac{1}{(\bar{n} + \frac{\Delta}{2})^2} \right] \cong \frac{2\mathfrak{R}}{(\bar{n})^3} \Delta. \quad (3.43)$$

For the purpose of establishing the magnitude of the intra- $n^*$  complex spin-orbit mixing,  $\langle H^{so} \rangle$  is taken to be equal to  $\langle a(r) \rangle$  as determined using Eq.(3.42). The fractional  $|n_i^* \rangle$  character in  $|n_j^* \rangle$  is

$$\frac{\langle H^{so} \rangle}{\Delta E} \equiv \frac{k_{ij}(\bar{n})^{-3}}{2\mathcal{R}\Delta(\bar{n})^{-3}} \approx 0.02, \quad (3.44)$$

which is  $n^*$  independent. The value 0.02 was determined by using the maximum value of  $k$  determined in Ref.[10],  $450 \text{ cm}^{-1}$  for the 0.98II series, and the minimum value of  $\Delta$  observed between states which could be spin-orbit coupled (for states with  $\Delta\Lambda = \pm 1$ ,  $\Delta = 0.10$ ). This value calculated in Eq.(3.44) should be an overestimate. Because molecular states have mixed  $\ell$  character, the spin-orbit interaction between two states of a given  $n^*$  complex is typically much smaller than that within each state. The crucial result of Eq.(3.44) is that the spin-orbit operator produces no  $n^*$ -dependent mixings. The electronic states coupled in by  $H^{so}$  contaminate the zero-order basis states at much less than the 0.1% level;  $(0.02)^2 \cdot 100\% = 0.04\% < 0.1\%$ .

### 3.1.4. The Rotational Hamiltonian

The rotational Hamiltonian has been given by Hougen [10],

$$H^{rot} = \frac{\hbar^2}{2\mu R^2} \mathbf{R}^2, \quad (3.45)$$

where  $\mathbf{R}$  is the pure rotational angular momentum which, by definition, is perpendicular to the axis of a diatomic molecule. The total angular momentum,  $\mathbf{J}$ , of the molecule may be expressed as the vector sum of the rotational, electron-orbital, and electron-spin angular momenta in the molecule,

$$\mathbf{J} = \mathbf{R} + \mathbf{L} + \mathbf{S}. \quad (3.46)$$

Equation (3.46) may be rearranged to obtain an expression for  $\mathbf{R}$ ,

$$\mathbf{R} = \mathbf{J} - \mathbf{S} - \mathbf{L} \quad (3.47)$$

A completely rigorous treatment of the problem would require inclusion of the nuclear spin angular momentum,  $\mathbf{I}$ , of the  $^{19}\text{F}$  nucleus. The vector  $\mathbf{I}$  couples to  $\mathbf{J}$  to form  $\mathbf{F}$ . In these experiments,  $\mathbf{I}$  introduces no observable splittings of rotational levels, does not introduce any anomalous selection rules for dipole allowed transitions, and does not introduce any nuclear spin statistical weighting of rotational levels. As the effects of  $\mathbf{I}$  are not and cannot be detected here, they are ignored for the rest of this document. The hyperfine splitting in the  $X^2\Sigma^+$  state is  $O(50 \text{ MHz} = 0.0017 \text{ cm}^{-1})$  [12] and should decrease with electronic excitation as the probability amplitude of the electronic wavefunction at the  $^{19}\text{F}$  nuclei decreases.

The most convenient basis set to use in constructing the rotational Hamiltonian is suggested by determining the Hund's case (as per Table 2.3 of Ref.[8]) of the Rydberg states under consideration. Hund's case (b) is a good choice when  $A\Lambda \ll BJ$ . The rotational constant of the  $\text{CaF}^+$  cation is  $0.37 \text{ cm}^{-1}$ . The maximum predicted value for the spin-orbit constant among states observed here is  $0.62 \text{ cm}^{-1}$  for  $8.98 \text{ } \Pi, v=2$ , calculated using Eq.(3.32). For this state, Hund's case (b) is appropriate when  $J \gg 0.62/0.37 \approx 1.5$ . The maximum predicted spin-orbit constant amongst the observed  $n^*=13-14, v=1$  levels is  $0.21 \text{ cm}^{-1}$  in the  $12.98 \text{ } \Pi$  state. For this state, Hund's case (b) is valid when  $J \gg 0.21/0.37 \approx 0.5$ .

The transition from Hund's case (b) to Hund's case (d) occurs when the separation between rotational energy levels becomes large relative to the separation between electronic states having the same  $\ell$  parentage and  $\Delta\lambda = \pm 1$  (see Table 2.3 of Ref.[7]). For the core-penetrating series of  $\text{CaF}$ , where  $\ell = 0, 1, \text{ and } 2$  are strongly mixed, Hund's case (d) will be descriptive when the rotational interaction,  $\sim BJ$ , is large relative to the energy difference of states having  $\Delta\lambda = \pm 1$ . The nearest neighbor of the  $12.98 \text{ } \Pi, v=1$  state cited in the previous paragraph, is the  $12.88 \text{ } \Sigma^+, v=1$  state. A good estimate of the point of transition from Hund's case (b) to case (d) behavior is the  $J$  at which  $BJ \geq E(12.98 \text{ } \Pi) - E(12.88 \text{ } \Sigma^+)$ . The energy difference between the two states may be calculated using the Rydberg formula:

$$\Delta E = \mathfrak{R} \left[ \frac{1}{(12.88)^2} - \frac{1}{(12.98)^2} \right] = 10.2 \text{ cm}^{-1}. \quad (3.48)$$

The criterion for case (d) behavior is that  $A\Lambda$  and  $\Delta E \ll BJ$ . The Hund's case (b) basis will be best for representing the  $12.98 \text{ } \Pi, v=1$  state when  $0.5 \ll J \ll 27.5$ . A similar range of  $J$  over which case (b) is a good description applies for *all* of the other  $n^*=13$  and

14 states observed. The range over which case(b) is a good basis extends to even higher J for the n\*=9, v=2 states observed. Therefore a Hund's case (b) basis is used throughout.

In all of the Rydberg states which will be discussed here, the electron-spin is decoupled from the electron orbital angular momentum. Spin is only weakly coupled to the total rotational angular momentum, J. Equation (3.47) may be simplified by defining the vector N where,

$$\mathbf{N} = \mathbf{J} - \mathbf{S}. \quad (3.49)$$

The splitting of the  $J = N \pm S$  components of each N value by  $\mathbf{H}^{\text{ro}}$  will be addressed shortly. The effective rotational Hamiltonian depends on  $\mathbf{R}^2$ :

$$\mathbf{R}^2 = (\mathbf{N} - \mathbf{L})^2 = \mathbf{N}^2 + \mathbf{L}^2 - 2\mathbf{N} \cdot \mathbf{L}. \quad (3.50)$$

The  $\mathbf{N} \cdot \mathbf{L}$  term may be expressed in terms of raising and lowering operators

$$\mathbf{N} \cdot \mathbf{L} = N_z L_z + \frac{1}{2}(\mathbf{N}^+ \mathbf{L}^- + \mathbf{N} \mathbf{L}^+). \quad (3.51)$$

Substituting Eqs.(3.50) and (3.51) into Eq.(3.45), one obtains:

$$\mathbf{H}^{\text{ro}} = B(\mathbf{R}) [ \mathbf{N}^2 + \mathbf{L}^2 - 2N_z L_z - \mathbf{N}^+ \mathbf{L}^- - \mathbf{N} \mathbf{L}^+ ]. \quad (3.52)$$

The quantity  $B(\mathbf{R})$ , integrated over the vibrational coordinate, is the rotational constant of the molecule.

The alkaline earth monohalides are effectively one-electron systems. This means that the electronic orbital angular momentum in the molecule is that of the single unpaired electron, i.e.  $\mathbf{L} = \boldsymbol{\ell}$ . Equation (3.52) may be rewritten as:

$$\mathbf{H}^{\text{ro}} = B(\mathbf{R}) [ \mathbf{N}^2 + \boldsymbol{\ell}^2 - 2N_z \ell_z - \mathbf{N}^+ \boldsymbol{\ell}^- - \mathbf{N} \boldsymbol{\ell}^+ ]. \quad (3.53)$$

The Hamiltonian in Eq.(3.53) is a Hund's Case (b) Rotational Hamiltonian and has been widely discussed in the literature of diatomic molecule spectroscopy [8, 11 (and refs. therein)]. The unsymmetrized Hund's case (b) basis functions are of the form

$$|\phi_{\text{rot}}\rangle = |N, \lambda; \ell, \lambda\rangle = |N, N_z; \ell, \ell_z\rangle. \quad (3.54)$$

The quantum number  $\lambda$  is the projection of  $N$  (and  $\ell$ ) on the molecular axis. The first three terms in square brackets on the RHS of Eq.(3.53) leave the case (b) basis functions unchanged:

$$[N^2 + \ell^2 - 2N_z \ell_z] |N, \lambda; \ell, \lambda\rangle = [N(N+1) + \ell(\ell+1) - 2\lambda^2] |N, \lambda; \ell, \lambda\rangle. \quad (3.55)$$

However, the raising and lowering operators in Eq.(3.53) lead to matrix elements between Eq.(3.54) basis functions by acting on the projection quantum number  $\lambda$ :

$$N^\pm \ell^\mp |N, \lambda; \ell, \lambda\rangle = \sqrt{N(N+1) - \lambda(\lambda \mp 1)} \sqrt{\ell(\ell+1) - \lambda(\lambda \mp 1)} |N, \lambda \mp 1; \ell, \lambda \mp 1\rangle. \quad (3.56)$$

The basis functions in Eq.(3.54) are eigenfunctions of the case (b) Hamiltonian only for the non-rotating molecule. The  $N^\pm \ell^\mp$  operator mixes basis states with  $\Delta\lambda = \pm 1$ . For low  $N$  values however, these matrix elements are small relative to the zero-order difference in term values between case (b) basis states.

The basis functions in Eqs.(3.54)-(3.56) are expressed in terms of signed values of  $\lambda$  and are therefore not symmetrized with respect to reflection in the plane of the molecular axis. It is more convenient to work in terms of basis functions labeled by  $\Lambda$ ,  $\Lambda = |\lambda|$ , and the reflection symmetry of the wavefunction in the plane of the molecule than it is to work in terms of the signed quantum number basis functions. Basis functions which are properly symmetrized with respect to reflection in the molecular plane are linear combinations of the functions in Eq.(3.54). The properly symmetrized case (b) basis functions for  $\lambda \neq 0$  are:

$$|N, \ell, \Lambda^+\rangle = \frac{1}{\sqrt{2}} [|N, \lambda; \ell, \lambda\rangle + |N, -\lambda; \ell, -\lambda\rangle] \quad (3.57)$$

$$|N, \ell, \Lambda^-\rangle = \frac{1}{\sqrt{2}} [|N, \lambda; \ell, \lambda\rangle - |N, -\lambda; \ell, -\lambda\rangle]. \quad (3.58)$$

The symmetrized basis states are distinguished by their transformation properties upon reflection of the electronic portion of the wavefunction through the molecular plane (Kronig symmetry [13]). For  $\Lambda \neq 0$ ,

$$\sigma_v^{\text{el}} |N, \ell, \Lambda^+\rangle = + |N, \ell, \Lambda^+\rangle \quad (3.59)$$

$$\sigma_v^{el} |N, \ell, \Lambda^+ \rangle = -|N, \ell, \Lambda^- \rangle. \quad (3.60)$$

For  $\Lambda = 0$ ,

$$|N, \ell, \Sigma^+ \rangle = |N, \ell, 0 \rangle = |N, 0; \ell, 0 \rangle \quad (3.61)$$

$$\sigma_v^{el} |N, \ell, \Sigma^+ \rangle = +|N, \ell, \Sigma^+ \rangle. \quad (3.62)$$

The  $|N, \ell, \Lambda^+ \rangle$  and  $|N, \ell, 0 \rangle$  basis states have positive Kronig symmetry. The  $|N, \ell, \Lambda^- \rangle$  basis states have negative Kronig symmetry. The utility of Kronig symmetry is that the case (b) rotational Hamiltonian, Eq.(3.53), does not couple basis states which belong to opposite Kronig symmetries. The spin-orbit Hamiltonian mixes case (b) states of opposite Kronig symmetry, giving rise to Hund's case (a) or Hund's case (c) behavior in the limit or large spin-orbit splitting. As mentioned previously, the spin-orbit splitting in all CaF electronic states with  $n^* > 10$  is too small to be observable at the resolution of our experiment,  $\sim 0.1 \text{ cm}^{-1}$ . It is therefore reasonable to construct separate Hamiltonians for the opposite Kronig symmetries.

The non-zero matrix elements between properly symmetrized Hund's case (b) basis functions are, for  $\Delta\Lambda = 0$ :

$$\langle N, \ell, \Lambda | H^{so} | N, \ell, \Lambda' \rangle = B(R) [N(N+1) + \ell(\ell+1) - 2\Lambda^2] \cdot \delta_{\Lambda', \Lambda}; \quad (3.63)$$

and, for  $\Delta\Lambda = \pm 1$ :

$$\langle N, \ell, \Lambda | H^{so} | N, \ell, \Lambda' \rangle = -B(R) \sqrt{N(N+1) - \Lambda(\Lambda \pm 1)} \sqrt{\ell(\ell+1) - \Lambda(\Lambda \pm 1)} \cdot \delta_{\Lambda', \Lambda \pm 1} \cdot F \quad (3.64)$$

where  $F = \sqrt{2}$  when either  $\Lambda$  or  $\Lambda' = 0$  and  $F = 1$  when neither  $\Lambda$  nor  $\Lambda' = 0$ .

Before moving on to explicitly construct the Hund's case (b) Hamiltonian, the effect of  $H^{so}$  on the case (b) basis states will be evaluated. The diagonal and off-diagonal matrix elements of  $H^{so}$  in the case (b) basis are given by Kovacs [14]. For the  $\Delta N = 0$  matrix elements,

$$\langle n^* JSN\Lambda | H^{so} | n^* JSN\Lambda \rangle = A\Lambda^2 \left[ \frac{J(J+1) - N(N+1) + S(S+1)}{2N(N+1)} \right]. \quad (3.65)$$



CaF is a one-electron molecule with  $S = 1/2$ , therefore  $J$  must be equal to  $N \pm 1/2$ . The spin-orbit matrix element in Eq.(3.65) is the first order correction to the term value:

$$\langle n^*, N \pm \frac{1}{2}, \frac{1}{2}, N, \Lambda | \mathbf{H}^{so} | n^*, N \pm \frac{1}{2}, \frac{1}{2}, N, \Lambda \rangle \approx \pm \frac{A\Lambda^2}{2N}. \quad (3.66)$$

The off-diagonal matrix elements,  $\Delta N = \pm 1$ , of  $\mathbf{H}^{so}$  in case (b) are:

$$\begin{aligned} \langle n^* J, S, N+1, \Lambda | \mathbf{H}^{so} | n^* J, S, N, \Lambda \rangle = \\ A\Lambda \sqrt{[(N+1)^2 - \Lambda^2][(J+N+2)(J+N+1) - S(S+1)]} \frac{\sqrt{S(S+1) - (J-N)(J-N-1)}}{2(N+1)\sqrt{(2N+1)(2N+3)}}. \end{aligned} \quad (3.67)$$

These matrix elements are diagonal in  $J$  and give rise to the Hund's case (a) level pattern in the limit of  $A\Lambda \gg BN$ . For  $J = N + S$  and  $S = 1/2$ :

$$\langle n^* J, S, N+1, \Lambda | \mathbf{H}^{so} | n^* J, S, N, \Lambda \rangle = A\Lambda \frac{\sqrt{(N+1)^2 - \Lambda^2}}{2(N+1)} \approx \frac{A\Lambda}{2}. \quad (3.68)$$

Because  $S = 1/2$ , the only levels,  $N'$ , which may interact with  $N$  are  $N' = N \pm 1$ . There is no  $J = N + 1/2$  component of the  $N - 1$  rotational level, only  $J = N - 1/2$  and  $J = N - 3/2$ . Likewise, there is no  $J = N - 1/2$  component of the  $N + 1$  level, only  $J = N + 1/2$  and  $J = N + 3/2$ . The second-order correction to the energy,

$$E^{(2)}(J, N) = \sum_{N' \neq N} \frac{|\langle J, N, \Lambda | \mathbf{H}^{so} | J, N', \Lambda \rangle|^2}{E^0(N) - E^0(N')}, \quad (3.69)$$

therefore reduces to a single term:  $N' = N + 1$  for  $J = N + 1/2$  and  $N' = N - 1$  for  $J = N - 1/2$ . Equations (3.65) and (3.68) may be used to determine the splitting between the  $J = N + 1/2$  and  $J = N - 1/2$  levels of a given  $N$ . Equation (3.65) gives the first-order correction to the rotational term value and Eq.(3.68) gives the second-order correction:

$$E(J = N \pm \frac{1}{2}) = E^0(N) + \langle J, N, \Lambda | \mathbf{H}^{so} | J, N, \Lambda \rangle + \frac{|\langle J, N, \Lambda | \mathbf{H}^{so} | J, N \pm 1, \Lambda \rangle|^2}{E^0(N) - E^0(N \pm 1)}. \quad (3.70)$$

Under the constraint  $A\Lambda \ll BN$ , the corrected term values are:

$$E(N + \frac{1}{2}) \approx BN(N+1) + \frac{1}{2} \frac{A\Lambda^2}{N} - \frac{1}{4} \frac{A^2\Lambda^2}{BN} \quad (3.71)$$

and,

$$E(N - \frac{1}{2}) \approx BN(N+1) - \frac{1}{2} \frac{A\Lambda^2}{N} + \frac{1}{4} \frac{A^2\Lambda^2}{BN}. \quad (3.72)$$

The splitting between the  $J = N \pm 1/2$  components of  $N$  rapidly approaches zero:

$$\Delta E \equiv E(N + \frac{1}{2}) - E(N - \frac{1}{2}) \approx \frac{A\Lambda^2}{N} \left[ 1 - \frac{A\Lambda}{2B} \right]. \quad (3.73)$$

The splitting coefficient may be calculated using Eq.(3.32) and the observed value of  $\text{CaF}^+$  rotational constant,  $0.37 \text{ cm}^{-1}$ .

Table 3.2

Vibronic State	$A(\text{calc}) / \text{cm}^{-1}$	$A\Lambda^2 [1 - A\Lambda(2B)^{-1}] / \text{cm}^{-1}$
8.98 $\Pi$ , $v=2$	0.62	0.10
9.36 $\Pi$ , $v=2$	0.36	0.18
12.98 $\Pi$ , $v=1$	0.21	0.15
13.36 $\Pi$ , $v=1$	0.13	0.11

The coefficients tabulated in Table 3.2 predict that the spin-orbit splittings would be difficult to resolve in the  $N$  levels probed in the experiments discussed here. This is consistent with the lack of observed spin-orbit splittings in the  $n^*=9$ ,  $v=2$  and  $n^*=13$  and  $14$ ,  $v=1$   $\Pi$  states.

### 3.2. Interpretation of CaF ID-OODR Spectra

The CaF Rydberg states discussed in this chapter were probed by vibrational autoionization detected optical-optical double resonance. The experimental apparatus was discussed in Chapter 1 and the specifics of the technique were discussed in Chapter 2. ID-OODR spectra were recorded using both the  $A^2\Pi_{3/2}$ ,  $v=0$  and  $C^2\Pi_{3/2}$ ,  $v=0$  states as intermediates. The intermediate state is hereafter referred to as the " $^2\Pi_{3/2}$ ". The  $^2\Pi_{3/2}$ - $X^2\Sigma^+(0,0)$  transition is referred to as the PUMP transition. The Rydberg- $^2\Pi_{3/2}(v_{\text{Rydberg}},0)$  transition is referred to as the PROBE transition. The choice of a  $^2\Pi$  state as the intermediate allows access to  $^2\Sigma^+$ ,  $^2\Pi$ , and  $^2\Delta$  Rydberg states. The  $A^2\Pi_{3/2}$ ,  $v=0$  state has been the state of choice for previously published work on CaF Rydberg states [10,15,16].

A single rovibronic, parity level in the  $A^2\Pi_{3/2}$ ,  $v=0$  or  $C^2\Pi_{3/2}$ ,  $v=0$  state is excited by a tunable wavelength Nd:YAG pumped dye laser (Lumonics HD-550 or Lumonics HD-300, laser specifications are discussed in Chapter 1). Levels of e-parity in  $A^2\Pi_{3/2}$ ,  $v=0$  were excited by PUMPing blended  $Q_2(J) + P_{21}(J+1)$  lines in the  $A^2\Pi_{3/2}$ - $X^2\Sigma^+(0,0)$  band; f-parity levels were populated by PUMPing transitions in the  $P_2$  branch. Levels of e-parity in  $C^2\Pi_{3/2}$ ,  $v=0$  were excited by PUMPing  $R_{21}(J)$  lines in the  $C^2\Pi_{3/2}$ - $X^2\Sigma^+(0,0)$  band. It was difficult to populate single f-parity levels in  $C^2\Pi_{3/2}$ ,  $v=0$  because most low-J transitions in the  $P_2$  and  $R_2$  branches are not well resolved. The  $P_2(6.5)$ ,  $P_2(8.5)$ ,  $P_2(10.5)$  lines in  $C^2\Pi_{3/2}$ - $X^2\Sigma^+(0,0)$  were the 'least-blended' transitions to f-parity levels, but still resulted in some population of undesired J's in the intermediate. The PUMP transitions used are summarized in Table 3.3. Figures 3.2 and 3.3 show typical PUMP spectra recorded by non-resonant ionization of the  $^2\Pi_{3/2}$  intermediate. (The ionizing photon was energetic enough to create a  $\text{CaF}^+$  cation in its vibrational ground state and a photoelectron with  $\sim 0.01$  eV of kinetic energy.)

Table 3.3 ID-OODR PUMP transitions

Band	PUMP lines	$X^2\Sigma^+$ parity (e/f)	$^2\Pi_{3/2}$ parity (e/f)	J's
$A^2\Pi_{3/2}$ - $X^2\Sigma^+(0,0)$	$\left\{ \begin{array}{l} Q_2(J) \\ P_{21}(J+1) \end{array} \right\}$	f e	e e	1.5 - 6.5
$A^2\Pi_{3/2}$ - $X^2\Sigma^+(0,0)$	$P_2(J)$	f	f	5.5 - 11.5
$C^2\Pi_{3/2}$ - $X^2\Sigma^+(0,0)$	$R_{21}(J)$	e	e	3.5 - 10.5
$C^2\Pi_{3/2}$ - $X^2\Sigma^+(0,0)$	$P_2(J)$	f	f	6.5, 8.5, 10.5

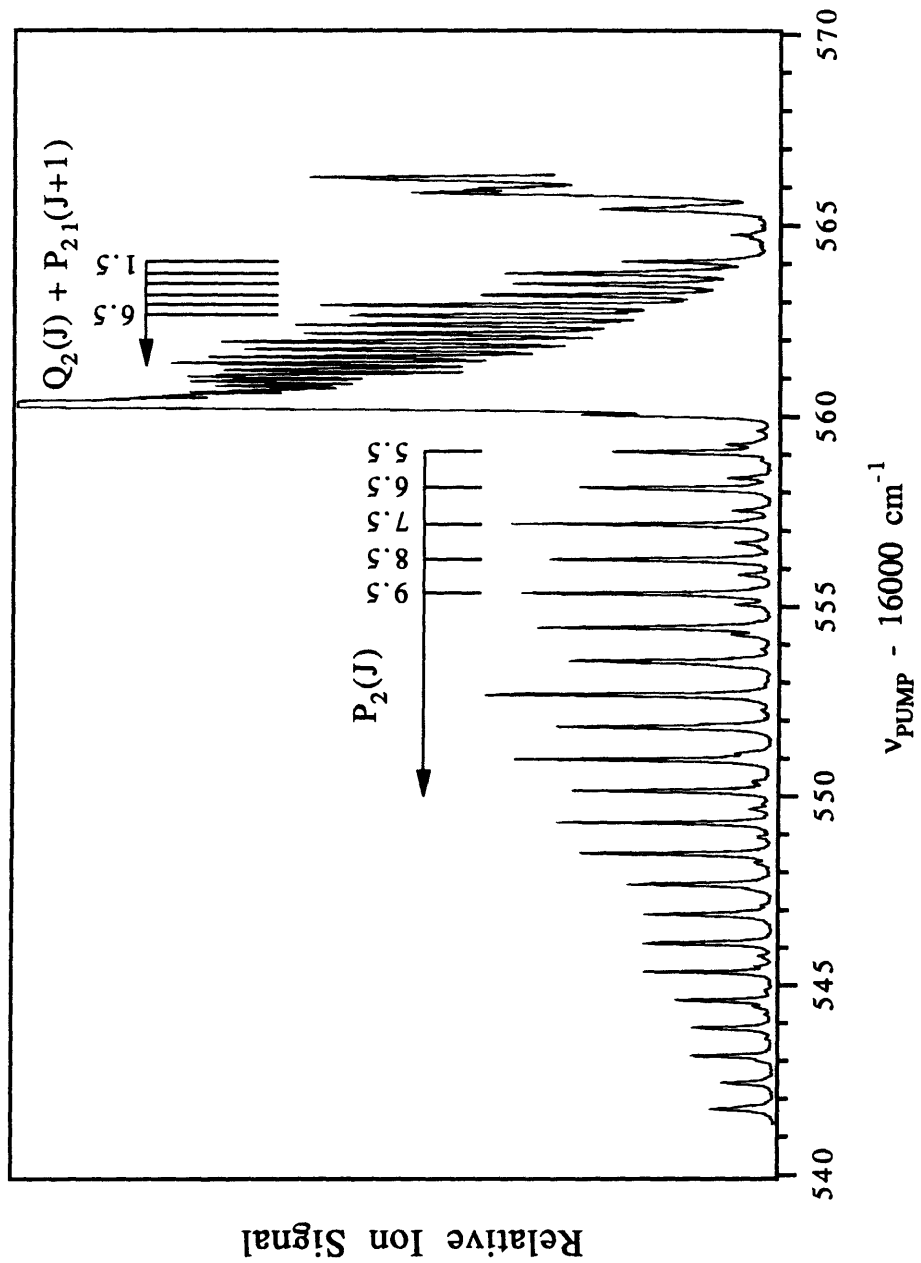


Figure 3.2. Ionization detected  $A^2\Pi_{3/2} - X^2\Sigma^+(0,0)$  absorption spectrum.  $A^2\Pi_{3/2}$  levels are non-resonantly ionized by 328 nm light.

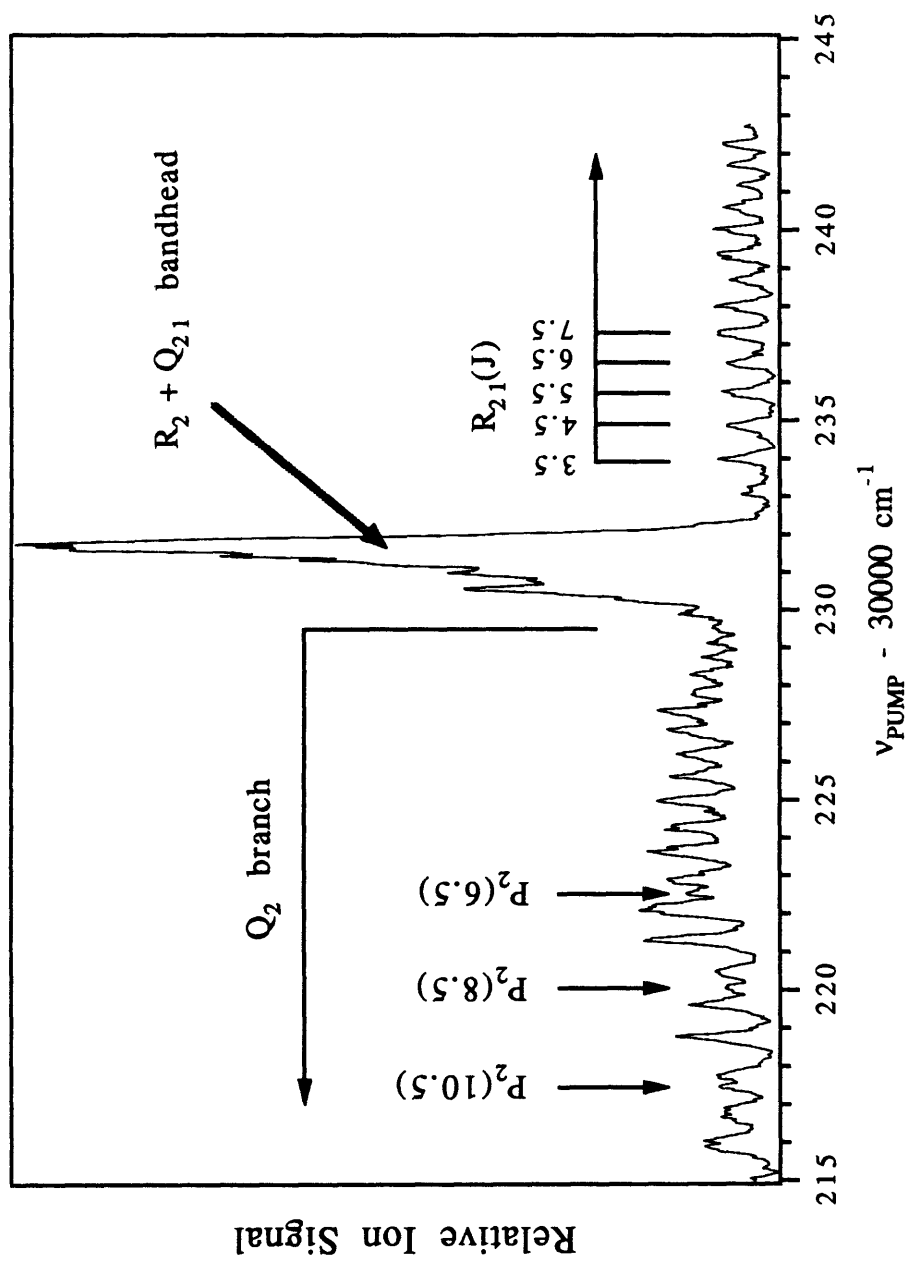


Figure 3.3. Ionization detected  $C^2\Pi_{3/2} - X^2\Pi^+(0,0)$  absorption spectrum.  $C^2\Pi_{3/2}$  levels are non-resonantly ionized by 595 nm laser light.

The term values of levels in the  $A^2\Pi_{3/2}$ ,  $v = 0$  state were determined by adding the  $A^2\Pi_{3/2}-X^2\Sigma^+(0,0)$  transition energies measured by Nakagawa, et al. [17] to the rotational term values of the  $X^2\Sigma^+$ ,  $v=0$  state[12]. The  $C^2\Pi_{3/2}$ ,  $v=0$  term values were calculated using the constants and Hamiltonian of Gittins *et al*[18] and the ground state data from Ref.[12]. The term values of Rydberg levels are determined by adding the Rydberg- $^2\Pi_{3/2}$  transition energy to the  $^2\Pi_{3/2}$  level term value. All term values are referenced to  $v=0$ ,  $N=0$  of  $X^2\Sigma^+$ . The uncertainty in  $^2\Pi_{3/2}-X^2\Sigma^+$  line positions is  $\pm 0.01 \text{ cm}^{-1}$ . Rydberg- $^2\Pi_{3/2}$  transition energies were calibrated by monitoring laser excited fluorescence of  $I_2$  as described in Chapter 1. The spacing between levels is accurate to  $\pm 0.01 \text{ cm}^{-1}$ . Term values are accurate to  $\pm 0.03 \text{ cm}^{-1}$ .

A thorough understanding of the  $A^2\Pi_{3/2}-X^2\Sigma^+$  and  $C^2\Pi_{3/2}-X^2\Sigma^+$  rotational branch structure facilitates straightforward assignment of Rydberg states belonging to core-penetrating series. The two, three, and four line patterns characteristic of Hund's case (b) Rydberg - case(a) valence transitions have been discussed previously [10]. The assignment of Kronig symmetry in Rydberg states follows simply from those observations. The selection rules of  $^2\Pi_{3/2}-X^2\Sigma^+$  transitions are completely understood. The total parity of the intermediate level is known because it is excited by PUMPing an assigned PUMP transition. The levels involved in PUMPing lines from various branches are depicted in Fig.3.4. Electric dipole selection rules require that the total parity of the final level is opposite that of the initial level. The total parity of states with positive Kronig symmetry transform identically as those of a  $\Sigma^+$  state, i.e.  $(-1)^N$ . Rotational level parity in states with negative Kronig symmetry goes as  $-(-1)^N$ . The selection rules for  $J$  are  $\Delta J = 0, \pm 1$ . Each rotational level,  $N'$ , in a case(b)  $^2\Lambda$  Rydberg state is doubly degenerate, having  $J' = N' \pm 1/2$ .

The  $\Omega = 3/2$  component of the  $A^2\Pi$  and  $C^2\Pi$  states is the  $F_2$  component of the doublet. A rotational level in  $^2\Pi_{3/2}$  with quantum number  $J$  has  $N = J + 1/2$ . The  $N'$  levels it is possible to observe from level  $J$  in  $^2\Pi_{3/2}$  are listed in Table 3.4. (Rotational levels in the intermediate state are labeled by  $J$  and  $N$ ; rotational levels in the Rydberg state are labeled  $J'$  and  $N'$ .) Branches are labeled as  $^{\Delta N}\Delta J(J)$ . The six branches one may observe from a  $^2\Pi_{3/2}$  intermediate level are  $^{\text{R}}\text{R}$ ,  $^{\text{Q}}\text{R}$ ,  $^{\text{Q}}\text{Q}$ ,  $^{\text{P}}\text{Q}$ ,  $^{\text{P}}\text{P}$ , and  $^{\text{O}}\text{P}$ .

Table 3.4 Observed Branches for case(b)  ${}^2\Lambda$  - case(a)  ${}^2\Pi_{3/2}$  Transitions

	$\Delta J$	N	J'	N'	$\Delta N$	$\Delta^N \Delta J$
R branch	+1	$J + \frac{1}{2}$	$J + 1$	$J + 1 \mp \frac{1}{2}$	+1, 0	${}^R R, {}^Q R$
Q branch	0	$J + \frac{1}{2}$	J	$J \mp \frac{1}{2}$	0, -1	${}^Q Q, {}^P Q$
P branch	-1	$J + \frac{1}{2}$	$J - 1$	$J - 1 \mp \frac{1}{2}$	-1, -2	${}^P P, {}^O P$

The total parity selection rule dictates that only odd total parity levels in the Rydberg state may be accessed from even total parity levels in  ${}^2\Pi_{3/2}$ . The consequence is that odd N levels of  $\Sigma^+$  and positive Kronig symmetry,  $\Lambda \neq 0$  states may be excited from even parity levels in  ${}^2\Pi_{3/2}$ . Only even N levels of negative Kronig symmetry states may be excited from even parity levels of  ${}^2\Pi_{3/2}$ . The parity of the level in  ${}^2\Pi_{3/2}$  is determined by the experimenter's choice of PUMP transition. The allowed transitions from  $J = 8.5$  of  ${}^2\Pi_{3/2}$ , excited by PUMPing the  $P_2(9.5)$  line, are depicted in Fig.3.5. The assignment of N in the Rydberg state is made by observing the lowest N's in the state. The core-penetrating Rydberg states discussed in this document adhere to Hund's case (b) rotational energy level patterns. The f-states discussed here start out in intermediate case (b) - case (d) pattern but quickly evolve (by  $N \sim 5$ ) to a case (d) pattern. The information on g-states is fragmentary, but it appears that they follow a Hund's case (d) level pattern. Assignments based on parity selection rules are universal, but assignments based on the spacing of lines in the ID-OODR spectrum are *strongly* dependent upon the Hund's case of the Rydberg state. The line patterns of case (b) Rydberg - case (a)  ${}^2\Pi_{3/2}$  are the simplest to interpret and are characteristic of transitions to core-penetrating Rydberg series.

By PUMPing the  $Q_2(1.5)+P_{21}(2.5)$  line in the  $\Pi_{3/2} - X^2\Sigma^+(0,0)$  band one populates  $J = 1.5$ ,  $N = 2$  (odd total parity) in the  $\Pi_{3/2}$  intermediate. The allowed transitions out of this level are to  $N' = 0$  and  $N' = 2$  (even total parity) of positive Kronig symmetry states ( ${}^O P$  and  $Q+{}^Q R$  lines, respectively) and to  $N' = 1$  and  $N' = 3$  (also even total parity) of negative Kronig symmetry states ( $P+{}^P Q$  and  $R$  lines, respectively). This is depicted in Fig.3.6. No  $N = 0$  level exists for  $\Pi$  or  $\Delta$  states and no  $N = 1$  level exists for  $\Delta$  states. In Hund's case (b), the spacing between the N and  $N+1$  levels of a Rydberg state is  $\sim 2B(N+1)$ , where B is the rotational constant of the cation. From the  $J = 1.5$ ,  $N = 2$  level in  ${}^2\Pi_{3/2}$ ,  $\Sigma^+$  states will appear in the spectrum as two lines separated by  $6B$ ,  $\Pi$  states will appear as three line patterns (spacing =  $4B, 6B$ ), and  $\Delta$  states will appear as two lines separated by  $6B$ . This allows for a preliminary sorting of states. One then PUMPs the  $Q_2(2.5)+P_{21}(3.5)$   ${}^2\Pi_{3/2} - X^2\Sigma^+(0,0)$  to populate  $J = 2.5$ ,  $N = 3$  (even total parity). The PROBE transition may then excite  $N' = 1$  and  $3$  of positive Kronig symmetry states and  $N' = 2$  and  $4$  of negative

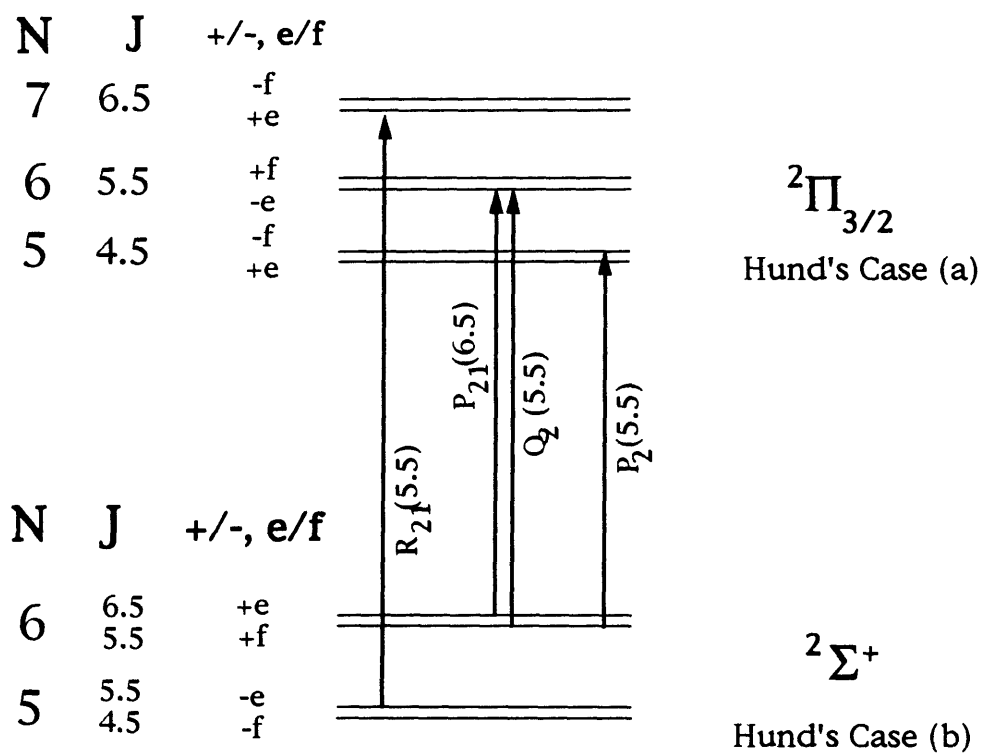


Figure 3.4 ID-OODR PUMP transitions



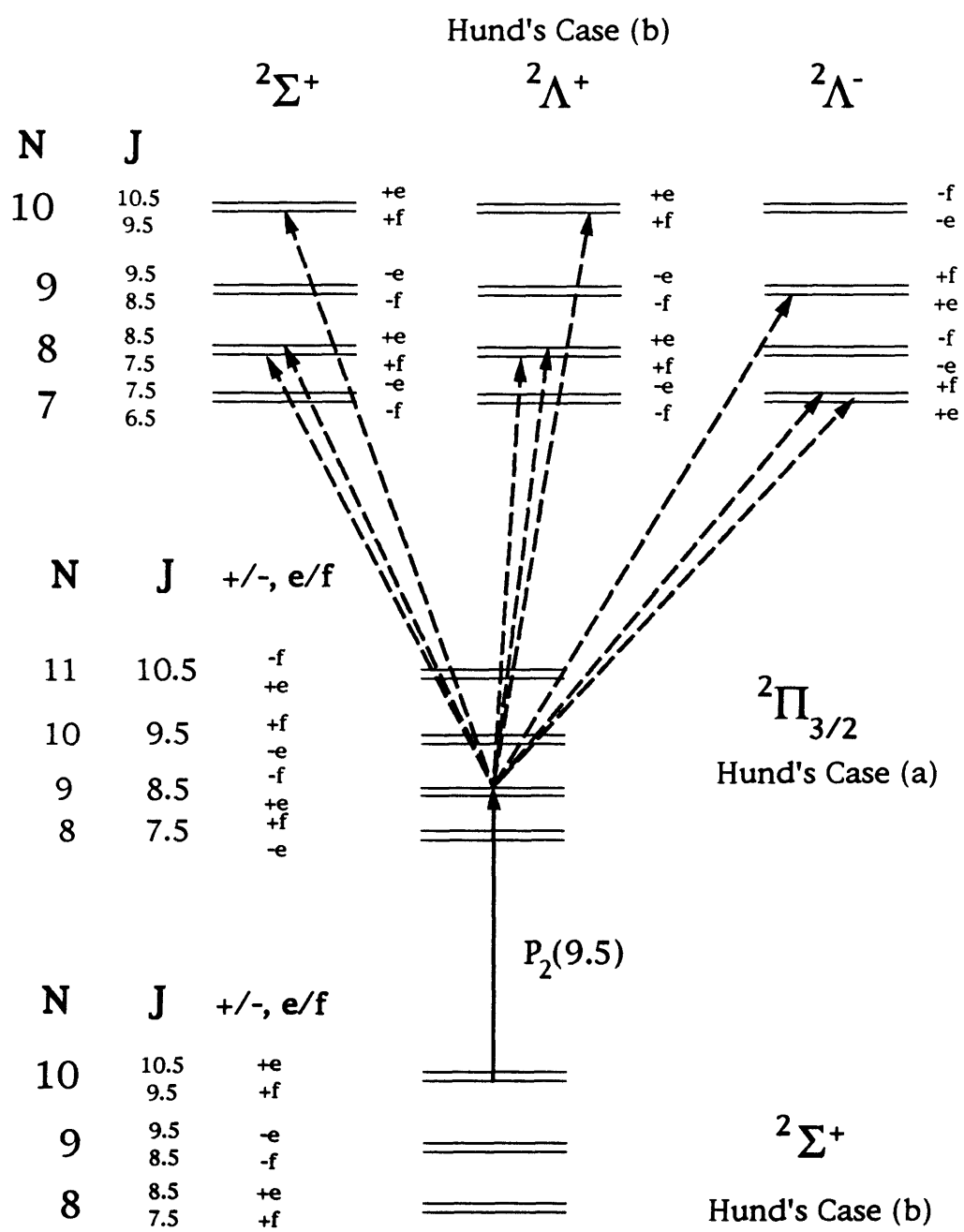


Figure 3.5. ID-OODR PUMP-PROBE scheme

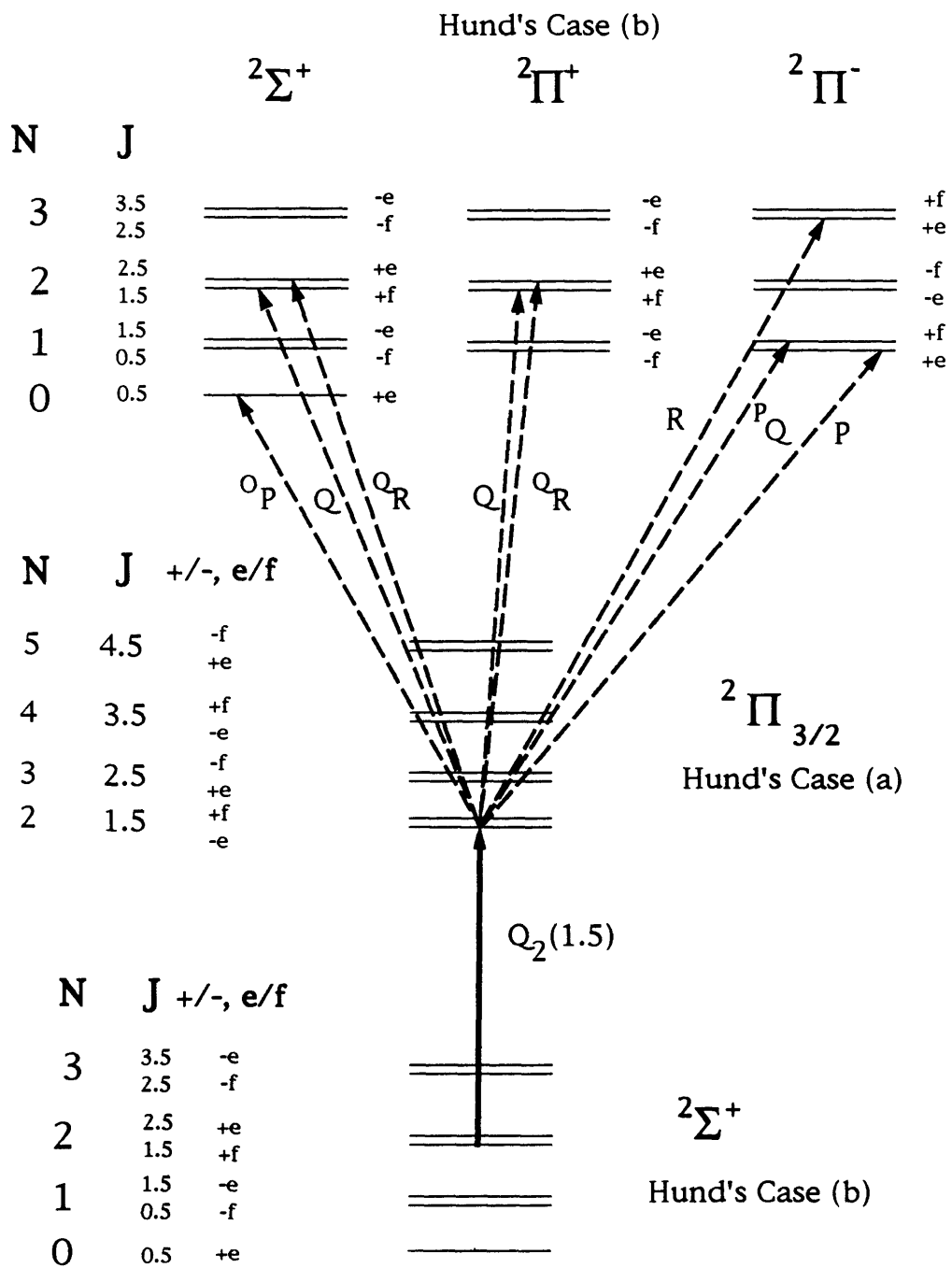


Figure 3.6 ID-ODR PUMP-PROBE scheme

symmetry states. The  $\Sigma^+$  states again appear as two lines, but this time separated by 10B,  $\Pi$  states as four line patterns (spacing = 4B, 6B, 10B), and  $\Delta$  states as three lines (spacing = 6B and 10B). The observation of this change in number of lines in a pattern provides an unambiguous assignment of core-penetrating Rydberg states. Figs.3.7 and 3.8 show ID-OODR spectra recorded in the region  $n^*=13$  and the assignment of states observed. The dashed arrows in Fig.3.7 indicate the general line-of-sight one should follow to observe the evolution of branch structure.

If low-N/J lines can not be excited in the PUMP step, then the assignments may be significantly more difficult. Core-penetrating  $\Sigma^+$  states always appear as two lines, but as N increases,  $\Pi$  states go from appearing as four line patterns to also appearing as two line patterns. In 0.36  $\Pi$  states, the two strongest transitions are  $\Delta N = -1$  and  $-2$ , the  $^pP + ^pQ$  and  $^oP$  lines. In 0.98  $\Pi$  states, the two strongest transitions are  $\Delta N = +1$  and  $0$ ,  $^R R$  and  $^oR + ^oQ$  lines. The two strongest transitions to 0.14 $\Delta$  states are the  $^oQ + ^oR$  and  $^pP + ^pQ$  lines, however the  $^oP$  and  $^R R$  lines are still observable up through  $N=11$ .

Assignment of  $\ell \geq 3$ , f, and other core-non-penetrating states is more complicated than the assignment of core-penetrating states. Only one member,  $\ell = -3$ , of the seven members of the f-complex was observed to have significant transition intensity from the  $A^2\Pi_{3/2}$  state. Several other states showed up weakly,  $\ell = -1$  and  $\ell = 0$ , or through perturbations with core-penetrating states,  $\ell = -2$  and  $\ell = +1$ . In addition, several levels belonging to members of the g-complex,  $\ell = -4$  and  $\ell = +1$ , were observed through perturbations with core-penetrating states. In contrast, members of the f-complex were easily excited from the  $C^2\Pi_{3/2}$  state. Curiously, the ID-OODR spectra recorded from the C state intermediate contained virtually none of the information obtained from the A state intermediate. Transitions which were strongest from the  $A^2\Pi_{3/2}$  were weak or unobserved from the  $C^2\Pi_{3/2}$ , e.g. the 13.14 and 14.14  $\Delta$  states. Virtually the only lines common to both spectra were to levels which had mixed core-penetrating/non-penetrating character. Mixed character levels were more abundant at low N. Figure 3.9 depicts spectra recorded from the  $J = 5.5e$  level of both the  $A^2\Pi_{3/2}$  and  $C^2\Pi_{3/2}$ . The spectra recorded from  $J = 4.5e$  and  $5.5e$  are far more similar in appearance than for higher J's.

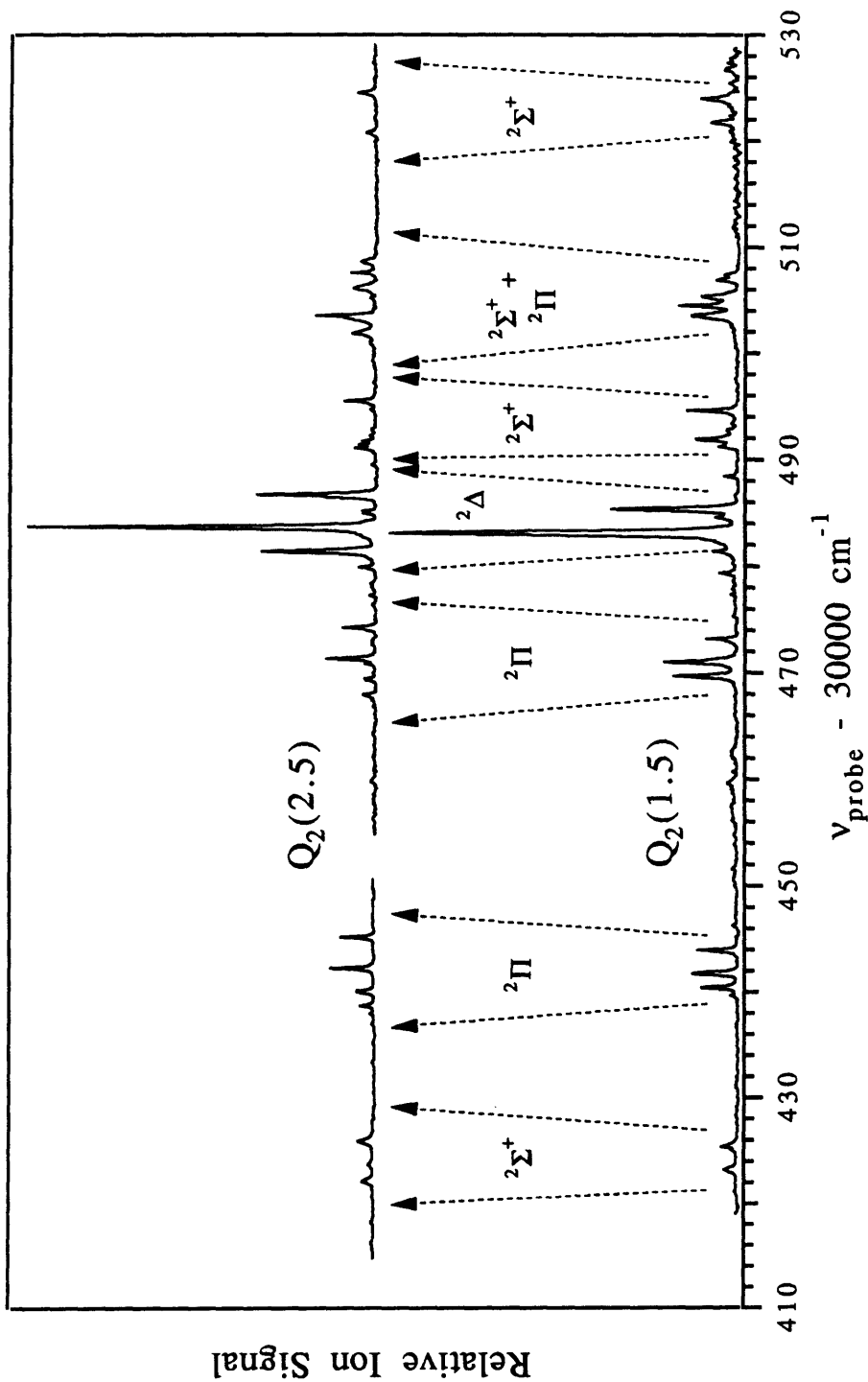


Figure 3.7. Assignment of Rydberg States near  $47050 \text{ cm}^{-1}$ . Lower Trace:  $A^2\Pi_{3/2} - X^2\Pi^+(0,0)$   
 $Q_2(1.5) + P_{21}(2.5)$  PUMP. Upper trace:  $Q_2(2.5) + P_{21}(3.5)$  PUMP.

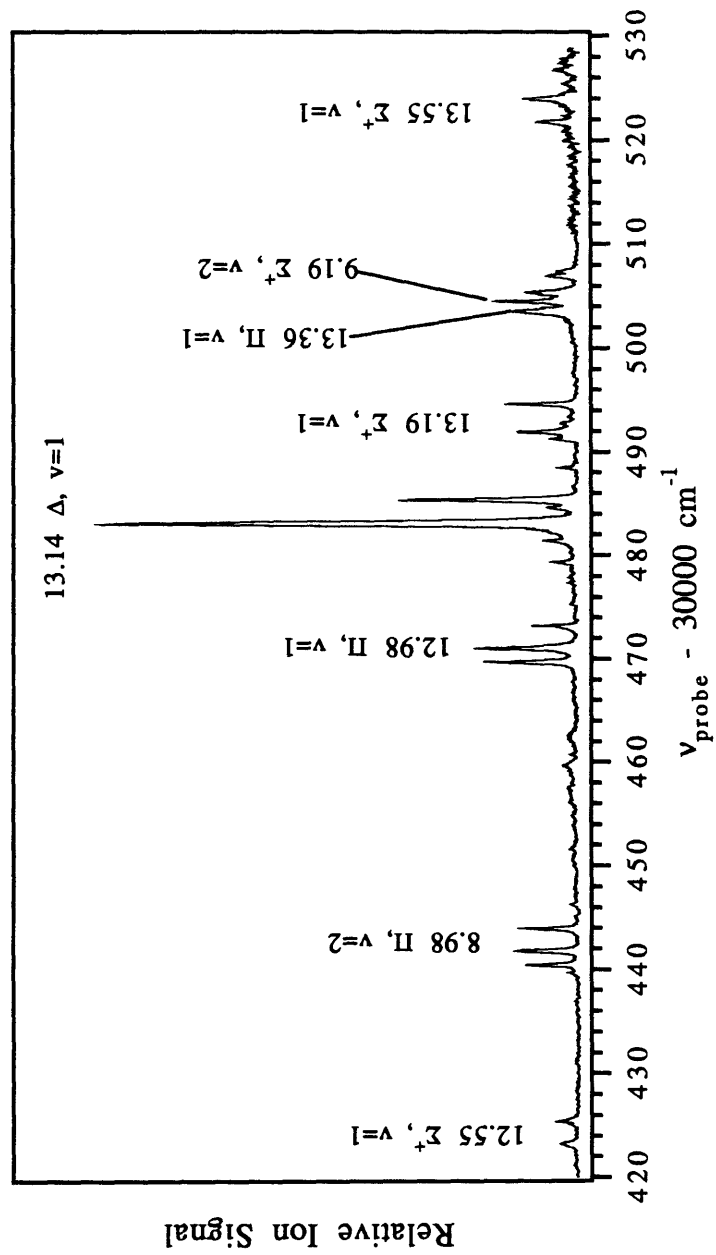


Figure 3.8. Assignment of CaF  $n^*=13, v=1$  and  $n^*=9, v=2$  core-penetrating states. Excitation from  $A^2\Pi_{3/2}, v=0, J=1.5e$ .

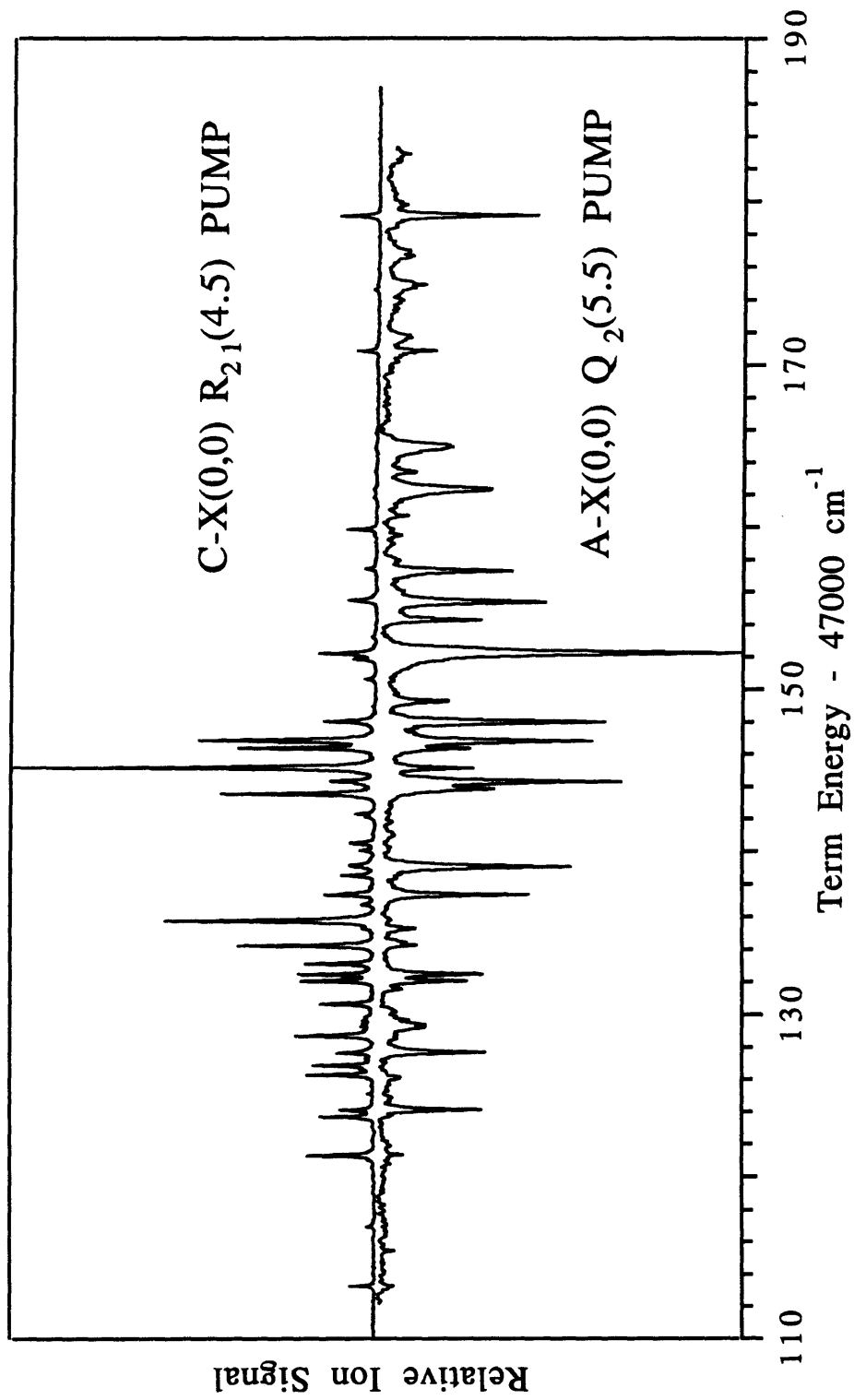


Figure 3.9. Comparison of ID - OODR Spectra recorded through  $C^2\Pi_{3/2}$  and  $A^2\Pi_{3/2}$  States. Spectra are plotted back-to-back.

Table 3.5 n\* = 13 and 14 Core Penetrating States Observed

	n = 13, v=1	n = 14, v = 1	n = 9, v = 2
n.55 $\Sigma^+$	x (also n*=12)	x	x
n.18 $\Sigma^+$		x	x
(n-1).88 $\Sigma^+$	x	x	
n.36 $\Pi$	x	x	x
(n-1).98 $\Pi$	x	x	x
n.14 $\Delta$	x	x	

### 3.3. Identification of Core Non-Penetrating States

The f and g-states of CaF exhibit fundamentally different ID-OODR line patterns and possess different pattern forming quantum numbers than the core-penetrating states. Core-non-penetrating states are characterized by near-zero quantum defects and anomalously large or small rotational constants. The effective rotational constants of core-non-penetrating Rydberg states differ significantly from that of the ion because of the  $\ell$ -uncoupling term,  $-2BN \cdot \ell$ , in  $H^{\text{rot}}$ . In the case of n\*=13 and 14 core-penetrating states, the differences in rotationless term values exceed the  $\ell$ -uncoupling matrix elements through  $N \gg 10$ . For f and g states, the difference in term energies of the  $\ell\Lambda$  states is  $O(10^0 \text{ cm}^{-1})$ . The matrix element between the  $f\Sigma^+$  and  $f\Pi$  states,  $\sim 5BN$ , exceeds the difference in their vibronic term values by  $N = 5$ . Core-non-penetrating states behave according to Hund's case (d) and core-penetrating states according to Hund's case(b).

There are four positive Kronig symmetry and three negative symmetry states of an f-complex. (The total number of states for a given  $\ell$  is always equal to the degeneracy of the electron orbital angular momentum,  $2\ell + 1$ .) The three-by-three Hamiltonian for negative symmetry states is:

$$\mathbf{H} = \mathbf{H}^{\text{el,vib}} + \mathbf{H}^{\text{rot}} = \begin{bmatrix} T_{\Pi} + B_v x & -\sqrt{10}B_v \sqrt{x-2} & 0 \\ -\sqrt{10}B_v \sqrt{x-2} & T_{\Delta} + B_v x & -\sqrt{6}B_v \sqrt{x-6} \\ 0 & -\sqrt{6}B_v \sqrt{x-6} & T_{\Phi} + B_v x \end{bmatrix}, \quad (3.74)$$

where  $x \equiv N(N+1)$ . In the limit of high N,  $N \sim 10$  for n\*=13 and 14, the difference in vibronic term energies is quite small relative to the diagonal and off-diagonal elements of

$H^{\text{rot}}$ . For this case, the approximate eigenvalues and eigenvectors of  $H$  may be determined by treating the diagonal terms as a constant offset, approximating  $\sqrt{x-m}$  as  $N$  and diagonalizing the matrix,

$$H^{\text{approx}} = \begin{bmatrix} 0 & -\sqrt{10}B_v N & 0 \\ -\sqrt{10}B_v N & 0 & -\sqrt{6}B_v N \\ 0 & -\sqrt{6}B_v N & 0 \end{bmatrix}, \quad (3.75)$$

where  $H = [\bar{T} + B_v N(N+1)]I + H^{\text{approx}}$ . The eigenvalues and eigenvectors of  $H^{\text{approx}}$  are:

$$E_1 = +4BN, |1\rangle = \sqrt{\frac{5}{16}}|f\Pi\rangle + \sqrt{\frac{1}{2}}|f\Delta\rangle + \sqrt{\frac{3}{16}}|f\Phi\rangle, \quad (3.76)$$

$$E_2 = 0, |2\rangle = \sqrt{\frac{3}{8}}|f\Pi\rangle - \sqrt{\frac{5}{8}}|f\Phi\rangle, \quad (3.77)$$

$$E_3 = -4BN, |3\rangle = -\sqrt{\frac{5}{16}}|f\Pi\rangle + \sqrt{\frac{1}{2}}|f\Delta\rangle - \sqrt{\frac{3}{16}}|f\Phi\rangle. \quad (3.78)$$

The analogous procedure may be performed on the positive Kronig symmetry effective Hamiltonian with the following results:

$$E_1 = +6BN, |1\rangle = -\sqrt{\frac{5}{16}}|f\Sigma^+\rangle + \sqrt{\frac{15}{32}}|f\Pi\rangle - \sqrt{\frac{3}{16}}|f\Delta\rangle + \sqrt{\frac{1}{32}}|f\Phi\rangle, \quad (3.79)$$

$$E_2 = +2BN, |2\rangle = +\sqrt{\frac{3}{16}}|f\Sigma^+\rangle - \sqrt{\frac{1}{32}}|f\Pi\rangle - \sqrt{\frac{5}{16}}|f\Delta\rangle + \sqrt{\frac{15}{32}}|f\Phi\rangle, \quad (3.80)$$

$$E_3 = -2BN, |3\rangle = -\sqrt{\frac{3}{16}}|f\Sigma^+\rangle - \sqrt{\frac{1}{32}}|f\Pi\rangle + \sqrt{\frac{5}{16}}|f\Delta\rangle + \sqrt{\frac{15}{32}}|f\Phi\rangle, \quad (3.81)$$

$$E_4 = -6BN, |4\rangle = +\sqrt{\frac{5}{16}}|f\Sigma^+\rangle + \sqrt{\frac{15}{32}}|f\Pi\rangle + \sqrt{\frac{3}{16}}|f\Delta\rangle + \sqrt{\frac{1}{32}}|f\Phi\rangle. \quad (3.82)$$

Adding the eigenvalues to the average energy of the complex,  $\bar{T} + B_v N(N+1)$ , one finds that the term values of f-levels go approximately as:

$$E = \bar{T} + B_v N(N+1) + 2B_v \ell^* N, \quad (3.83)$$

where  $-\ell \leq \ell^* \leq \ell$ , where  $\ell^*$  is an integer. If one examines a reduced term value plot which includes core-non-penetrating states, one will be able to identify those states as the ones



radiating out from near integer  $n^*$ <sup>1</sup>. This is Hund's case (d) behavior. It is interesting to note that the transition to Hund's case(d) removes most traces of the original  $f\Lambda$  character. The  $f(-3)$  state, which started out as  $f\Sigma^+$ , has only 31%  $f\Sigma^+$  character in the limit of high N. Its leading character is  $f\Pi$ . The  $f(+3)$  state, which started out as  $f\Phi$ , has only 3%  $\Phi$  character in the case(d) limit! Its leading character is also  $f\Pi$ .

Hund's case (d) is more rigorously derived by allowing the electron orbital angular momentum,  $\ell$ , to couple to the rotational angular momentum of the ion core,  $N^+$ , to form the vector N. The term values of Hund's case (d) levels go as:

$$E = T_{n^*\ell} + B_v N^+(N^+ + 1), \quad (3.84)$$

where  $N^+ \equiv N - \ell$ . Equation (3.84) expanded to obtain the expression in terms of N and  $\ell$ :

$$E = T_{n^*\ell} + B_v [ N(N+1) - 2N\ell + \ell(\ell-1) ], \quad (3.85)$$

which is essentially the same result as Eq.(3.83) in the limit of high N. Hund's case (d) states are labeled  $|n\ell\ell\rangle$ , but are often in text as  $n\ell(\ell)^\pm$ , where  $\pm$  denotes the Kronig symmetry of the state. The  $\pm$  label is redundant. Kronig symmetry alternates with  $\ell$  for a given  $\ell$ , and with  $\ell$  for a given  $\ell$ . For odd values of  $\ell$ , odd  $\ell$ 's have positive Kronig symmetry. Plotting the quantity  $E - B_v N(N+1)$ , equal to  $[T_{n^*\ell} + B_v \ell(\ell-1)] - 2B_v N\ell$ , versus N should reveal the  $\ell$  of value of core-non-penetrating states.

Jungen and Miescher [19] did a qualitative analysis of case (d)  $nf^2(\ell)$  - case (a)  $^2\Pi_{3/2}$  branch intensities and predicted the following branches to be the strongest:  $^{+3/2}P_{-3}$ ,  $^{+3/2}P_{-2}$  +  $^{+3/2}Q_{-2}$ ,  $^{+3/2}Q_{-1}$ ,  $^{-1/2}R_{+2}$ ,  $^{-1/2}Q_{+1}$ ,  $^{-1/2}P_0$ , and  $^{-5/2}R_{+3}$ . The  $^{+3/2}R_{+2}$ ,  $^{-1/2}P_0$ , and  $^{-5/2}Q_{+2}$  branches are also expected to be visible. The branch notation corresponds to  $N^+ - J \Delta J_\ell$ . Jungen and Miescher's predictions were quite accurate for their NO absorption spectra and they agree well here for the  $^{+3/2}P_{-3}$ ,  $^{+3/2}P_{-2}$  +  $^{+3/2}Q_{-2}$ , and  $^{+3/2}Q_{-1}$  branches observed in the 14f -  $C^2\Pi_{3/2}$  spectrum (transitions to f states from the  $A^2\Pi_{3/2}$  state were relatively weak and the data set fragmentary), but the  $^{-1/2}R_{+2}$  does not appear to be present. The  $^{-5/2}R_{+3}$  branch is strong, but the  $^{-5/2}Q_{+2}$ , which is predicted to be weak, does not appear to be present. Also, the  $^{-5/2}P_{+1}$  is not expected to have any intensity, but is present and quite strong at high N.

---

<sup>1</sup> A reduced term value plot is generated by subtracting the quantity  $B_v N(N+1)$  from observed rotational term values and plotting the result versus  $N(N+1)$ . Levels of unperturbed Hund's case (b) states will fall on a line with near zero slope. The reduced term value extrapolated to  $N = 0$  is the vibronic term energy of the state.

Figure 3.10 depicts the evolution of the  $n^*=14 - C^2\Pi_{3/2}$  ID-OODR spectrum with increasing rotational quantum number in the  $C^2\Pi_{3/2}$  intermediate state. The  $C^2\Pi_{3/2} - X^2\Sigma^+$  PUMP transition is indicated on the left side of the figure. The strongest transitions terminate on  $14f(\mathcal{L})$  levels. Figure 3.11 is an expanded view of Fig.3.10. Transitions terminating on  $14f(+3)$  and  $14f(+1)$  levels are indicated with gray arrows. Extra lines in the spectrum due to perturbations between core-penetrating and core-non-penetrating states are found within the black rectangles. Figure 3.12 is another expanded view of Fig.3.10, only this time with transitions terminating on  $14f(-3)$ ,  $14f(-2)$ ,  $14f(-1)$ , and  $14f(0)$  levels indicated by gray arrows. Perturbations with core-penetrating states are found within the gray rectangles. The perturbation highlighted on the  $R_{21}(5.5)$  PUMP spectrum is  $14f(-2)$ ,  $v=1 \sim 14.14\Delta$ ,  $v=1$ . The perturbation highlighted on the  $R_{21}(6.5)$  PUMP spectrum is  $14f(0)$ ,  $v=1 \sim 13.98\Pi$ ,  $v=1$ . The perturbation highlighted on the  $R_{21}(8.5)$  PUMP spectrum is  $14g(-1)$ ,  $v=1 \sim 9.36\Pi$ ,  $v=2$ .

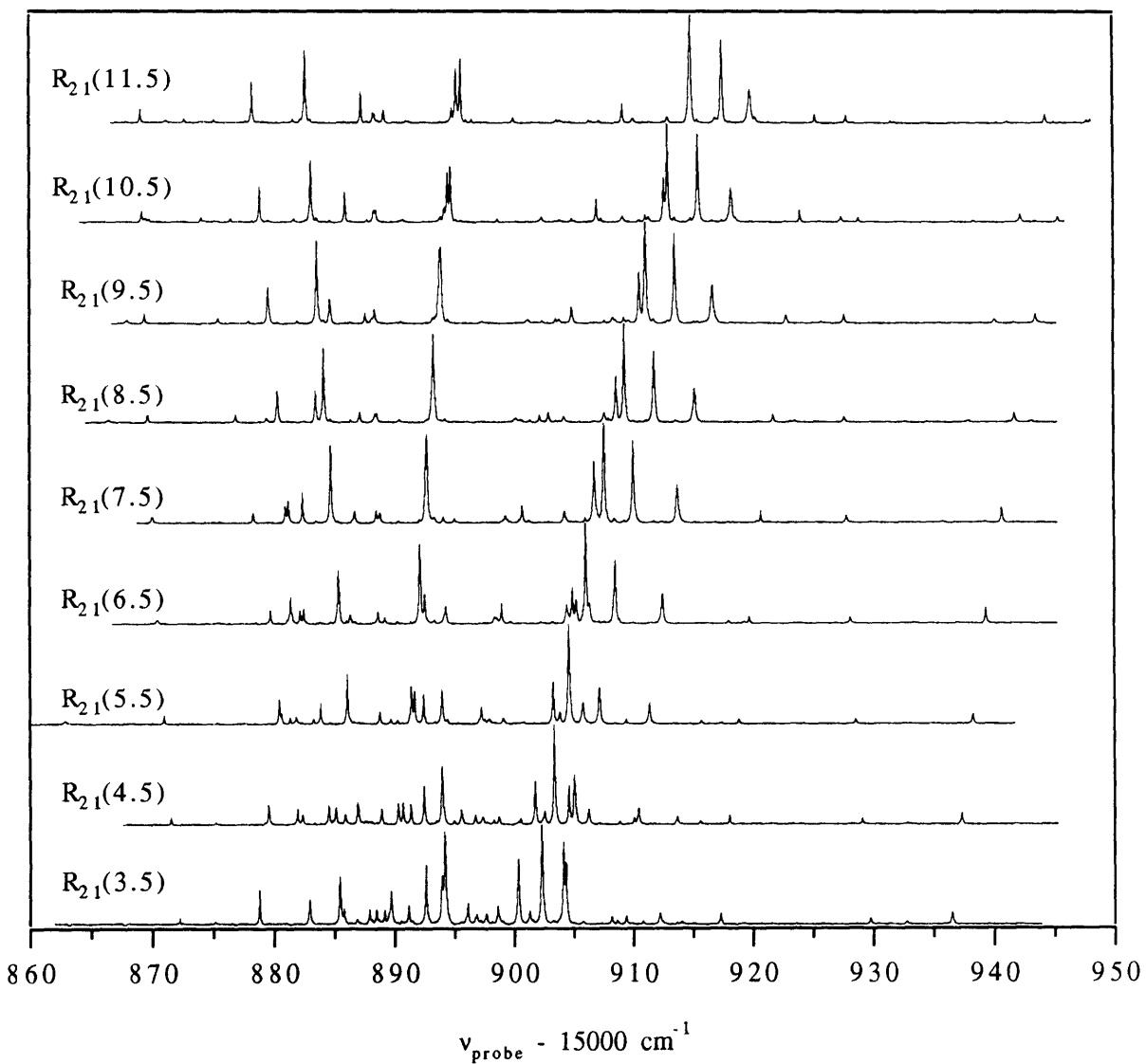


Figure 3.10. ID-OODR spectra of the  $n^*=14$ ,  $v=1$  region. Spectra recorded from levels in the  $C^2\Pi_{3/2}$ ,  $v=0$  intermediate state excited by PUMPing transitions in the  $R_{21}$  branch of  $C^2\Pi_{3/2}-X^2\Sigma^+(0,0)$  band.

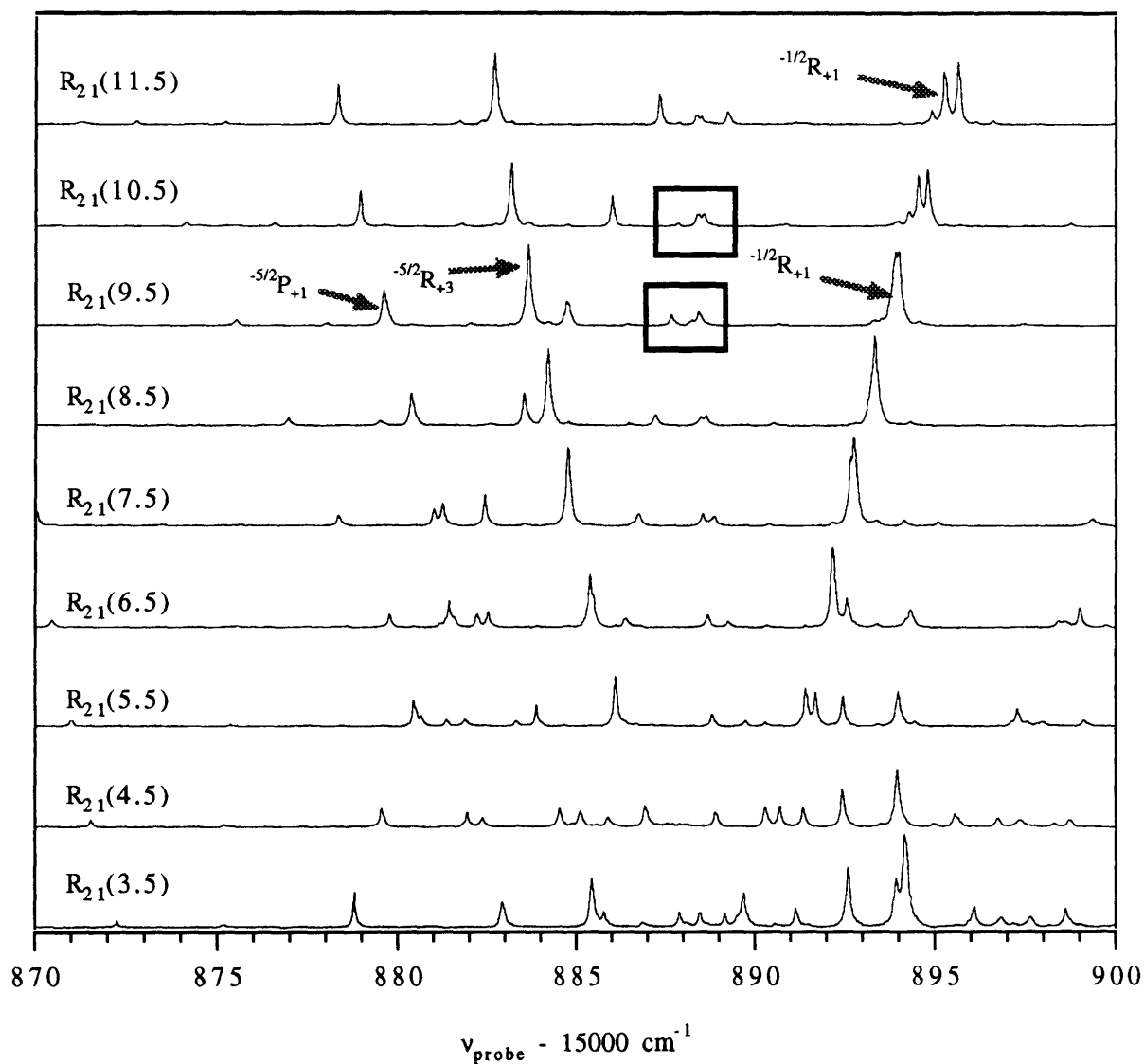


Figure 3.11. Expanded scale of ID-OODR spectra of  $n^*=14, v=1$ . The  $R_{21}(J)$  is the  $C^2\Pi_{3/2}-X^2\Sigma^+(0,0)$  PUMP transition. ID-OODR transitions terminating on  $14f(+3)$  and  $14f(+1)$  are indicated by gray arrows. Perturbation between core-penetrating and core-non-penetrating states are highlighted by black boxes.

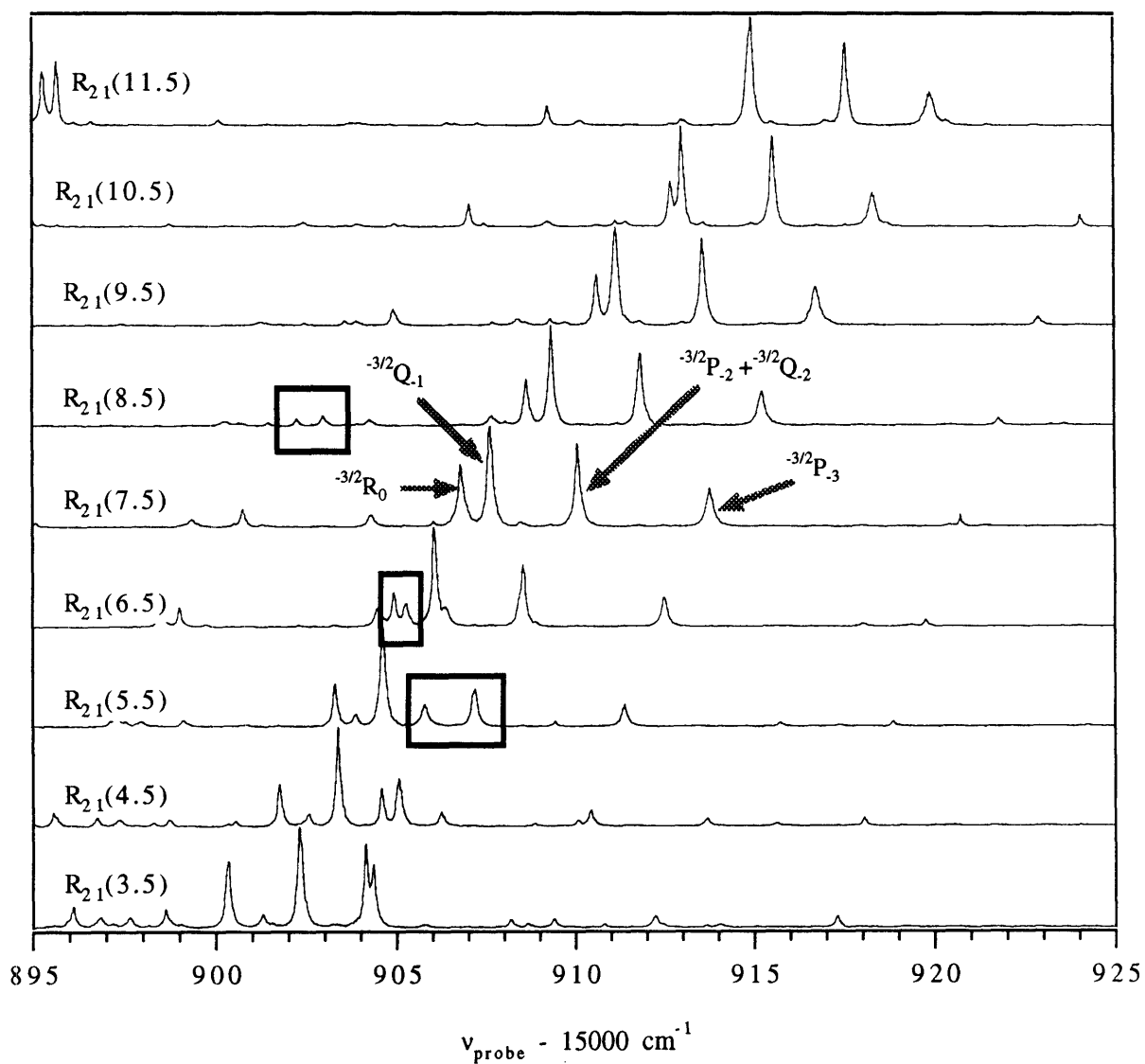


Figure 3.12. Expanded scale of ID-OODR spectra of  $n^*=14$ ,  $v=1$ . The  $R_{21}(J)$  is the  $C^2\Pi_{3/2}-X^2\Sigma^+(0,0)$  PUMP transition. ID-OODR transitions terminating on  $14f(-3)$ ,  $14f(-2)$ ,  $14f(-1)$ , and  $14f(0)$  are indicated by gray arrows. Perturbation between core-penetrating and core-non-penetrating states are highlighted by black boxes.

## References

1. J. E. Murphy, Ph.D. Thesis, MIT, 1992.
2. P. Felenbok, *Ann. Astrophys.*, v.26 (1963), p.393.
3. D.R. Hartree, *Proc. Camb. Phil. Soc.*, v.24 (1928), p. 426
4. (a) M. J. Seaton, *Mon. Not. R. Astr. Soc.*, v.118 (1958), p. 501. (b) M. J. Seaton, *Proc. Phys. Soc.*, v.88(1966), p. 801.
5. R.F. Stebbings, *Science*, v.193 (1976), p.537.
6. G. Herzberg and Ch. Jungen, *J. Mol. Spec.*, v.41 (1972), p.425-486.
7. J. C. Slater, "Quantum Theory of Atomic Structure", McGraw-Hill, 1960.
8. H. Lefebvre-Brion and R. W. Field, "Perturbations in the Spectra of Diatomic Molecules", Academic Press, 1986.
9. R. Pitzer, private communication.
10. J.M. Berg, J.E. Murphy, N.A. Harris, and R.W. Field, *Phys. Rev. A*, v.48 (1993), p.3012.
11. J. T. Hougen, *Monograph 115*, Nat. Bur. Stand. (US), 1970.
12. W.J. Childs, G.L. Goodman, and L.S. Goodman, *J.Mol.Spec.*, v.86 (1981), p.365.
13. R. de L. Kronig, Ch.2., "Band Spectra and Molecular Structure", Cambridge University Press, 1930.
14. I. Kovacs, "Rotational Structure in the Spectra of Diatomic Molecules", Am. Elsevier, 1969.
15. J.E.Murphy, J.M.Berg, A.J.Merer, N.A.Harris, and R.W.Field, *Phys. Rev. Lett.*, v.65 (1990), p.1861.
16. N. A. Harris and R. W. Field, *J. Chem. Phys.*, v.98 (1993), p.2642.
17. J. Nakagawa, P. J. Domaille, T. C. Steimle, and D. O. Harris, *J. Mol. Spec.*, v. 70 (1978), p.374.
18. C.M. Gittins, N.A. Harris, R.W. Field, J. Vergès, C. Effantin, A. Bernard, J. d'Incan, W.E. Ernst, P. Bündgen, and B. Engels, *J. Mol. Spec.*, v.161 (1993), p.303.
19. Ch. Jungen and E. Miescher, *Can. J. Phys.*, v.47 (1969), p. 1769.

## CHAPTER 4

### Analysis of $n^*=13$ and $n^*=14$ Data

#### 4.1. Construction of $s\sim p\sim d$ "Supercomplex" Hamiltonians

Although  $\ell$  is not a rigorously good quantum number in a system lacking spherical symmetry, considerable insight into the electronic structure of CaF may be gained by building molecular (non-spherically symmetric) electronic states from pure- $\ell$  atomic states. Rice, Martin, and Field [1] used Crystal Field Theory to demonstrate that the lowest energy electronic states of CaF could be well described in terms of strongly mixed  $\text{Ca}^+$   $s$ ,  $p$ , and  $d$  orbitals. The highly polar nature of the  $\text{CaF}^+$  core lifts the  $2\ell+1$  degeneracy of the  $\text{Ca}^+$   $n\ell$  orbitals and mixes states of identical- $\Lambda$ . Murphy, et al. [2] have observed all six Rydberg series arising from mixed  $\text{Ca}^+$   $s$ ,  $p$ , and  $d$  orbitals. Although  $s\sim d$  mixing has been observed in NO [3] and  $\text{H}_2$  [4], and  $p\sim d$  mixing has been observed in  $\text{H}_2\text{O}$  [5], strong  $s\sim p\sim d$  mixing had not previously been identified.

The purpose of this section is to construct the  $s\sim p\sim d$  Hamiltonian matrix and to demonstrate both the strengths and shortcomings of the Hamiltonian fit model in accounting for the behavior of the  $n^*=13$  and  $n^*=14$ ,  $v=1$  supercomplexes. The quantitative accuracy of the Hamiltonian fit to the negative Kronig symmetry states allows for precise determination of an  $nd\sim nf$  electrostatic (electric dipole) matrix element. This core penetrating-core non-penetrating perturbation may be used in conjunction with a quantum mechanically calculated  $nd\sim nf$  radial matrix element to estimate the dipole moment of the  $\text{CaF}^+$  cation.

The six core-penetrating Rydberg series are distinguished by  $\Lambda$  and their quantum defects,  $\delta_{i,\Lambda}$ , where the quantum defect is used to calculate the electronic term value of the state:

$$E_{n,i,\Lambda} = \text{IP} - \frac{\mathfrak{R}}{(n - \delta_{i,\Lambda})^2}. \quad (4.1)$$

In practice, electronic term values are usually calculated using  $\text{mod}(\delta_{i,\Lambda}, 1)$ , not  $\delta_{i,\Lambda}$ :

$$E_{n_i, \Lambda} = IP - \frac{\mathfrak{R}}{[n' - \text{mod}(\delta_{i, \Lambda}, 1)]^2}, \quad (4.2)$$

where  $n'$  is also an integer, but not necessarily equal to  $n$ .

It is tempting to group the members of each Rydberg series nearest a given  $n'$ . One can then model the group of core-penetrating states nearest  $n'$  as deriving from single  $s$ ,  $p$ , and  $d$  orbitals. This model is appealing not only for its conceptual simplicity, but that the Rydberg states of CaF seem to be clustered about  $\text{mod}(\delta_{i, \Lambda}, 1) = 0.8$ . The separation between the two uppermost members of an  $n'$  cluster is about half that between the uppermost member of the  $n'$  cluster and lowermost member of the  $n'+1$  cluster. The distribution of states and the thereby implied  $n'$ -grouping is depicted in Figure 4.1. The physical significance of using  $n'$  rather than  $n$  in a quantum chemical calculation is that the  $n'$  radial wavefunction has  $\delta_{i, \Lambda} - \text{mod}(\delta_{i, \Lambda}, 1)$  fewer radial nodes than  $n$ . Core-penetrating states are named according to  $\text{mod}(\delta_{i, \Lambda}, 0)$  and their electronic symmetry. The  ${}^2\Pi$  state at  $44743 \text{ cm}^{-1}$  ( $n^*=6.98$ ) is referred to as the "six point nine-eight pi" state, and is a member of the "point nine-eight pi" Rydberg series.

CaF "supercomplexes" consist of all electronic states for a given value of  $n'$  which are admixtures of atomic basis states with  $\ell$  less than or equal to  $\ell_{\text{crit}}$ . It has been empirically determined that all CaF electronic states arising from  $\ell \leq 2$  parent states must be modeled as a group, i.e.,  $\ell_{\text{crit}} = 2$ . The  $\mathbf{H}^{\text{el}}$  portion of the full Hamiltonian strongly couples pure- $\ell$  basis states. The off-diagonal matrix elements of  $\mathbf{H}^{\text{el}}$  arise as a result of the charge distribution (electric multipole moments) of the  $\text{CaF}^+$  cation to which the Rydberg electron is bound. All electrostatic perturbations have selection rules  $\Delta S = \Delta \Sigma = \Delta \Lambda = \Delta \Omega = 0$ . The core dipole induced mixing has a  $\Delta \ell = \pm 1$  selection rule; the quadrupole mixing selection rule is  $\Delta \ell = 0, \pm 2$ ; the octopole selection rule is  $\Delta \ell = \pm 1, \pm 3$ ; etc. The Hamiltonian matrix necessary to describe the CaF electronic states derived from  $\ell \leq 2$  parent states is nine by nine. Fortunately, the matrix is block diagonal in positive and negative Kronig symmetries. The positive symmetry block is six by six and the negative symmetry block is three by three. As mentioned in the previous section, spin doubling is not observed at the resolution of these experiments, so the dimensions of each block are 2/3 are 1/3 that naively expected. The positive symmetry basis states are:  $s\Sigma^+$ ,  $p\Sigma^+$ ,  $p\Pi^+$ ,  $d\Sigma^+$ ,  $d\Pi^+$ , and  $d\Delta^+$ . The negative symmetry basis states are:  $p\Pi^-$ ,  $d\Pi^-$ , and  $d\Delta^-$ . The intra- $\ell$ -block elements of  $\mathbf{H}^{\text{el}}$  are:





$$\mathbf{H}^{\text{el}(+)} = \begin{bmatrix} T_{s\Sigma} + H_{s\Sigma} & V_{s-p\Sigma} & 0 & V_{s-d\Sigma} & 0 & 0 \\ V_{s-p\Sigma} & T_{p\Sigma} + H_{p\Sigma} & H_{p\Sigma-\Pi} & V_{p-d\Sigma} & 0 & 0 \\ 0 & H_{p\Sigma-\Pi} & T_{p\Pi} + H_{p\Pi} & 0 & V_{p-d\Pi} & 0 \\ V_{s-d\Sigma} & V_{p-d\Sigma} & 0 & T_{d\Sigma} + H_{d\Sigma} & H_{d\Sigma-\Pi} & 0 \\ 0 & 0 & V_{p-d\Pi} & H_{d\Sigma-\Pi} & T_{d\Pi} + H_{d\Pi} & H_{d\Pi-\Delta} \\ 0 & 0 & 0 & 0 & H_{d\Pi-\Delta} & T_{d\Delta} + H_{d\Delta} \end{bmatrix}. \quad (4.6)$$

The full Hamiltonian for the negative symmetry states is:

$$\mathbf{H}^{\text{el}(-)} = \begin{bmatrix} T_{p\Pi} + H_{p\Pi} & V_{p-d\Pi} & 0 \\ V_{p-d\Pi} & T_{d\Pi} + H_{d\Pi} & H_{d\Pi-\Delta} \\ 0 & H_{d\Pi-\Delta} & T_{d\Pi} + H_{d\Pi} \end{bmatrix}. \quad (4.7)$$

The diagonal matrix elements, evaluated using  $n^*\ell$  basis functions are:

$$\begin{aligned} \langle n^*, \ell, \Lambda, v, N | \mathbf{H} | n^*, \ell, \Lambda, v, N \rangle &= \langle n^* \ell \Lambda | \mathbf{H}^{\text{el}} | n^* \ell \Lambda \rangle + \langle v | \mathbf{H}^{\text{vib}} | v \rangle + \langle N, \ell \Lambda | \mathbf{H}^{\text{rot}} | N, \ell \Lambda \rangle \\ &= \left[ \text{IP} - \frac{\mathfrak{R}}{(n_{\ell\Lambda}^*)^2} \right] + \left[ h\omega_e(v + \frac{1}{2}) - h\omega_e x_e(v + \frac{1}{2})^2 \right] + \\ &\quad B_v [N(N+1) + \ell(\ell+1) - 2\Lambda^2] - D_v N^2(N+1)^2. \end{aligned} \quad (4.8)$$

All terms independent of  $N$  are typically collected into a rotationless term value,  $T$ , and Eq.(4.8) becomes:

$$\langle n^*, \ell, \Lambda, v, N | \mathbf{H} | n^*, \ell, \Lambda, v, N \rangle = T_{n^*, \ell, \Lambda, v} + B_v N(N+1) - D_v N^2(N+1)^2. \quad (4.9)$$

The Hamiltonian acting on an  $n^*s$  basis function gives rise to only a single electronic state:

$$\langle n^* s \Sigma^+, v, N | \mathbf{H} | n^* s \Sigma^+, v, N \rangle = T_{n^* s \Sigma^+, v} + B_v N(N+1) - D_v N^2(N+1)^2. \quad (4.10)$$

A p-electron in turn gives rise to three electronic states, two states of positive Kronig symmetry,  $p\Sigma^+$  and  $p\Pi^+$ , and one of negative symmetry,  $p\Pi^-$ . The eigenstates are determined by diagonalizing the matrix composed of elements calculated using Eqs.(3.63) and (3.64).

$$\langle n^* p\Pi^+, N | \mathbf{H} | n^* p\Pi^+, N \rangle = T_{n^*p\Pi^+,v} + B_v N(N+1) - D_v N^2(N+1)^2 \quad (4.11)$$

$$\langle n^* p\Sigma^+, N | \mathbf{H} | n^* p\Sigma^+, N \rangle = T_{n^*p\Sigma^+,v} + B_v N(N+1) - D_v N^2(N+1)^2 \quad (4.12)$$

$$\langle n^* p\Pi^+, N | \mathbf{H} | n^* p\Sigma^+, N \rangle = -2B_v \sqrt{N(N+1)} \quad (4.13)$$

$$\langle n^* p\Pi^-, N | \mathbf{H} | n^* p\Pi^-, N \rangle = T_{n^*p\Pi^-,v} + B_v N(N+1) - D_v N^2(N+1)^2. \quad (4.14)$$

The Hamiltonian block for the  $n^*p$  basis states consists of a two by two subblock for the positive Kronig symmetry states, and a one by one subblock for the negative Kronig symmetry state:

	$ p\Sigma^+, N\rangle$	$ p\Pi^+, N\rangle$	$ p\Pi^-, N\rangle$
$ p\Sigma^+, N\rangle$	$T_{n^*p\Sigma^+,v} + B_v x$	$-2B_v \sqrt{x}$	0
$ p\Pi^+, N\rangle$	$-2B_v \sqrt{x}$	$T_{n^*p\Pi^+,v} + B_v x$	0
$ p\Pi^-, N\rangle$	0	0	$T_{n^*p\Pi^-,v} + B_v x$

where  $x \equiv N(N+1)$  and the case (b)  $n^*p$  basis states are listed along the top and side of the matrix. The same procedure may be followed to set up the effective Hamiltonian for an  $n^*d$ -electron. The positive and negative Kronig symmetry subblocks are now written separately. Following the previous example, the positive Kronig-symmetry subblock is:

	$ d\Sigma^+, N\rangle$	$ d\Pi^+, N\rangle$	$ d\Delta^+, N\rangle$
$ d\Sigma^+, N\rangle$	$T_{n^*d\Sigma^+,v} + B_v x$	$-\sqrt{12}B_v \sqrt{x}$	0
$ d\Pi^+, N\rangle$	$-\sqrt{12}B_v \sqrt{x}$	$T_{n^*d\Pi^+,v} + B_v x$	$-2B_v \sqrt{x-2}$
$ d\Delta^+, N\rangle$	0	$-2B_v \sqrt{x-2}$	$T_{n^*d\Delta^+,v} + B_v x$

where  $x \equiv N(N+1)$ , and the negative Kronig symmetry subblock is:

	$ d\Pi^-, N\rangle$	$ d\Delta^-, N\rangle$
$ d\Pi^-, N\rangle$	$T_{n^*d\Pi^-,v} + B_v x$	$-2B_v \sqrt{x-2}$
$ d\Delta^-, N\rangle$	$-2B_v \sqrt{x-2}$	$T_{n^*d\Delta^-,v} + B_v x$

where  $x \equiv N(N+1)$ .

In principle, if one observes all core penetrating states in a CaF supercomplex, the observed term values may be fit to the matrices in Eqs.(4.6) and (4.7) using electronic term values, rotational constants, and electrostatic  $\ell$ -mixing elements as independent fit parameters.

In practice, there are several difficulties in fitting the observed levels to the effective Hamiltonian matrices. The primary problem with the fit of the positive symmetry levels to the six by six matrix is that the assignment of the proper six positive parity states to a particular  $n^*$  is more ambiguous than it first appears in Fig.4.1. The six positive symmetry states span  $\sim 2/3$  of an  $n^*$  unit, with each of the  $\Sigma^+$  states separated by  $\sim 1/3$  of an  $n^*$  unit. The obvious choice based on a visual analysis of Fig.4.1, implies a grouping  $n.55 \Sigma^+$ ,  $n.36 \Pi$ ,  $n.18 \Sigma^+$ ,  $n.14 \Delta$ ,  $(n-1).98 \Pi$ , and  $(n-1).88 \Sigma^+$ . This ordering is also appealing because the outlying  $(n-1).88 \Sigma^+$  states (lowest energy) clearly experience an N-dependent ( $\ell$ -uncoupling) interaction with higher energy states and  $n.55 \Sigma^+$  states (highest energy) clearly experience an  $\ell$ -uncoupling interaction with lower energy states. However, one drawback of this grouping is apparent when one looks at the  $\Sigma^+$  states alone (see Fig.4.2).

Unlike the  $\Pi$  and  $\Delta$  states, the intra-supercomplex separation between  $\Sigma^+$  states is of the same size as the inter-supercomplex separation. This suggests that inter-supercomplex  $\ell$ -mixing matrix elements could be of the same order of magnitude as the intra-supercomplex elements. Unfortunately, neither the grouping placing the  $n.55 \Sigma^+$  state at the top of the supercomplex, nor the grouping placing it at the bottom, may be fit to within the accuracy of the experimental data using the Hamiltonian matrix in Eq.(4.6). (The logic of placing  $n.55 \Sigma^+$  states at the bottom of a  $n'$ -grouping is that the ground state of CaF is nominally the  $1.55 \Sigma^+$  state.) Finite basis set Hamiltonians prove of limited utility in this situation. It has been suggested that in order to obtain an accurate fit to an  $n^*$ -supercomplex with positive symmetry, it will be necessary to include the  $n^*+1$  and  $n^*-1$  supercomplexes in the Hamiltonian matrix. The full effective Hamiltonian would be three times the dimension of the  $n^*$ -supercomplex effective Hamiltonian, but only the data from the  $n^*$ -supercomplex would be included in the fit. Inter-supercomplex electrostatic matrix elements, which obey  $n^*$ -scaling relations, would be introduced and allowed to vary to optimize the fit of the data to the effective Hamiltonian. The effective Hamiltonian necessary to accomplish this task rapidly becomes large (an 18 by 18 Hamiltonian matrix with at least 11 fit parameters for the positive Kronig symmetry states), and the problem is more aptly treated using Multichannel Quantum Defect Theory. MQDT has recently been used to model the negative Kronig symmetry data. Agreement between MQDT and the effective Hamiltonian fit is quite good up to  $N=8$ , where the MQDT fits stop. MQDT modelling of the positive Kronig symmetry data is presently underway [6].

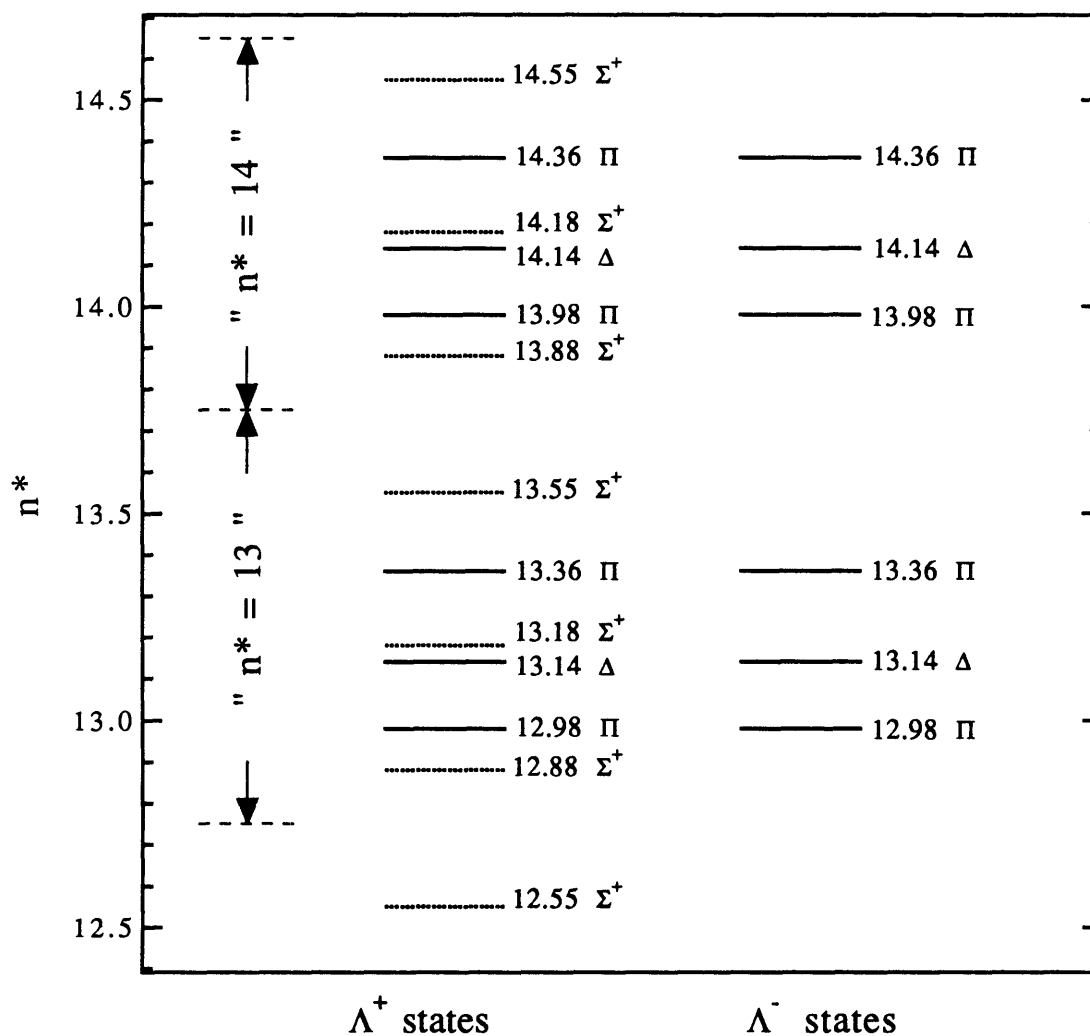


Figure 4.1. Core-penetrating Rydberg series,  $v=1$ . The positive Kronig-symmetry states are displayed on the left and the negative Kronig-symmetry states are displayed on the right. The electronic states between  $n - 0.4$  and  $n + 0.6$  constitute an  $n^*$ -supercomplex.

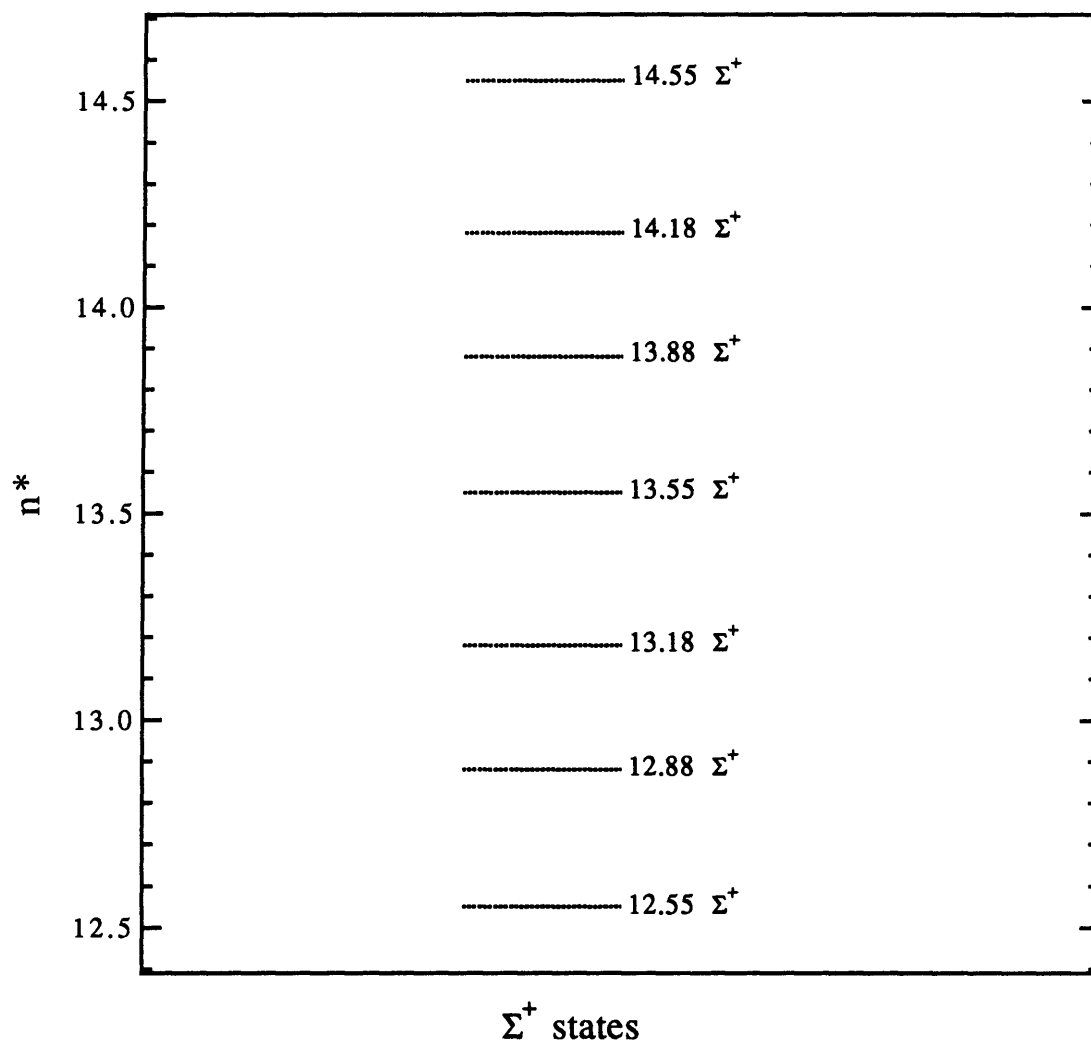


Figure 4.2. Core-penetrating  $^2\Sigma^+$  states,  $v=1$ . The inter- $n^*$  separation between states is comparable to the intra- $n^*$  separation.

#### 4.2. Fit of Experimental Data to the 3x3 p~d (-) symmetry Hamiltonian

The negative symmetry core penetrating states may be accurately modeled using the three by three Hamiltonian matrix of Eq.(4.7). The three negative symmetry states span only ~2/5 of an n\*-unit and are well isolated from neighboring complexes. The n\*=13 and n\*=14 negative symmetry supercomplexes have been separately fit using just five parameters: term values for the pΠ<sup>-</sup>, dΠ<sup>-</sup>, and dΔ<sup>-</sup> basis states, a p~d mixing angle, and an effective rotational constant for the complex. The advantage of fitting a p~d mixing angle instead of a p~d electrostatic matrix element is that the mixing angle is expected to be n\*-independent, but the matrix element should decrease as (n\*)<sup>-3</sup>. The disadvantage is that this model neglects inter-n\* interactions. As the data may be fit to the model Hamiltonian to within the accuracy of the measurements without incorporating inter-n\* interactions, this disadvantage appears to be minimal. The effective Hamiltonian fits were performed using p~d mixed Π basis states. The two negative symmetry Π basis states, expressed in terms of p~d mixing angle, θ, are:

$$|\Pi^-(1), N\rangle \equiv \sin \theta |d\Pi^-, N\rangle - \cos \theta |p\Pi^-, N\rangle, \quad (4.15)$$

$$|\Pi^-(2), N\rangle \equiv \cos \theta |d\Pi^-, N\rangle + \sin \theta |p\Pi^-, N\rangle. \quad (4.16)$$

The mixing angle θ is related to matrix elements in Eqs.(4.5) and (4.7):

$$\theta = \frac{1}{2} \tan^{-1} \left[ \frac{V_{p-d\Pi}}{T_{p\Pi} - T_{d\Pi}} \right]. \quad (4.17)$$

The argument that θ should be n\*-independent is based upon scaling relationships discussed in Chapter 3. The p~d electrostatic matrix element should scale as (n\*)<sup>-3</sup>, V<sub>p~dΠ</sub> = V<sub>0</sub>(n\*)<sup>-3</sup>, but difference in term values of the pΠ and dΠ states is proportional to the product of the difference in the quantum defects of the pΠ and dΠ series and (n\*)<sup>-3</sup> (see Eqs.(3.42) and (3.43)). The (n\*)<sup>-3</sup> factors in the numerator and denominator of Eq.(4.17) cancel and therefore θ will be n\*-independent.

The only negative symmetry core-penetrating Δ state is the dΔ, |dΔ<sup>-</sup>, N⟩. H<sup>rot</sup> couples zero-order dΠ and dΔ states and therefore the ℓ-mixed Π(1) and Π(2) basis states with dΔ:

$$\langle d\Pi, N | H^{\text{rot}} | d\Delta, N \rangle = -B_v \sqrt{N(N+1) - 2} \sqrt{2(3) - 1(2)} = -2B_v \sqrt{N(N+1) - 2}.$$

(4.18)

Diagonal terms of  $H(-)$  without any  $N$  dependence are folded into the vibronic term value. The Hamiltonian matrix is written here with the zero-order p~d mixed basis states listed across the top and to the left of the matrix:

	$ \Pi^-(1), N\rangle$	$ \Pi^-(2), N\rangle$	$ d\Delta^-, N\rangle$
$ \Pi^-(1), N\rangle$	$T_{p\Pi^-,v} + B_v x$	0	$-2 \sin \theta \cdot B_v \sqrt{x-2}$
$ \Pi^-(2), N\rangle$	0	$T_{d\Pi^-,v} + B_v x$	$-2 \cos \theta \cdot B_v \sqrt{x-2}$
$ d\Delta^-, N\rangle$	$-2 \sin \theta \cdot B_v \sqrt{x-2}$	$-2 \cos \theta \cdot B_v \sqrt{x-2}$	$T_{d\Delta^-,v} + B_v x$

where  $x \equiv N(N+1)$ .

Unlike the matrix in Eq.(4.7), where the off-diagonal electrostatic terms are large relative to the differences in diagonal terms for  $n^*=13, 14$  and  $N < 15$ , the matrix above is nearly diagonal at low  $N$ . The p~d mixing angle, rotational constant, and term values are varied in a non-linear least squares fit.<sup>1</sup> The arbitrary phase choice for in Eqs.(4.15) and (4.16) results in .98  $\Pi$  states being predominantly  $\Pi(1)$  and the .36  $\Pi$  states being predominantly  $\Pi(2)$ . The results of the fit to the  $n^*=13$  and 14 data are listed in Table 4.1.

The figure of merit for an effective Hamiltonian fit is the variance. The variance is defined as:

$$\sigma^2 = \frac{1}{n-p} \sum_{i=1}^N \frac{(E_{\text{obs}} - E_{\text{calc}})^2}{\delta E_{\text{obs}}^2},$$

where  $n$  is the number of data points fit,  $p$  is the number of variables in the fit, and  $\delta E_{\text{obs}}$  is the uncertainty in the experimentally determined quantity. If the Hamiltonian fit model accounts for the data to within the accuracy of the measurements, then the variance will be near unity. A variance of less than unity indicates inappropriately large uncertainties on the data points. The smaller the variance, the better the quality of the fit model. A detailed discussion of least-squares fitting may be found in Lefebvre-Brion and Field [7]. Readers interested in the specifics of the non-linear least squares fitting program used in this analysis should consult Appendix IV of Friedman-Hill's Ph.D. thesis [8] and references cited therein.

<sup>1</sup> The quantity varied in the fit is actually  $\tan(\theta/2)$ , not  $\theta$ . This is because  $\tan(\theta/2)$  may be continuously varied between  $-\infty$  and  $\infty$ . The value of  $\theta$  is calculated from inversion of the fit parameter and varies from  $-\pi$  to  $\pi$ .



Throughout this document, comparison of Hamiltonian fit results to the input data is displayed on reduced term value plots. The rotational term values of all core-penetrating states in an  $n^*$ -supercomplex are described fairly accurately by the expression:

$$E_{n^*\Lambda}(N) = T_{n^*\Lambda} + B_{n^*\Lambda}N(N+1).$$

A reduced term value plot is constructed by subtracting an average rotational energy,  $\bar{B}N(N+1)$ , from each observed  $N$  level and plotting this "reduced term value" versus  $N(N+1)$ . In all reduced term value plots in this document,  $\bar{B}$  is taken to be equal to the rotational constant of the cation,  $0.3704 \text{ cm}^{-1}$ . Readers interested in the construction of reduced term value plots should consult Herzberg's text [9].

Table 4.1 Molecular Constants of  $n^*=13$  and  $14$  Negative Kronig Symmetry States

Fit Parameter	Value: $n^*=13, v=1$	Value: $n^*=14, v=1$
$T_{.36\Pi} / \text{cm}^{-1}$	47068.90(1)	47153.42(3)
$T_{.14\Delta} / \text{cm}^{-1}$	47046.96(3)	47136.10(6)
$T_{.98\Pi} / \text{cm}^{-1}$	47035.07(1)	47124.88(2)
$B_v^+ / \text{cm}^{-1}$	0.3696(2)	0.3704(3)
$10^7 D_v^+ / \text{cm}^{-1}$	[4.4]	[4.4]
$\tan(\theta/2)$	2.64(2)	2.22(2)
$\theta / \text{radians}$	2.42	2.30
$100 \cdot \cos^2\theta$	56.1(3)	44.1(6)

Parameters in brackets were held fixed. Quantity in parentheses is  $2\sigma$ .

Reduced term value plots and the best fit term values for  $n^*=13$  and  $n^*=14$  negative symmetry states are shown in Figs. 4.3 and 4.4.<sup>2</sup> The observed and calculated term values may be found in Appendix II. There are two shortcomings of the three-by-three effective Hamiltonian fit: both of the  $0.14 \Delta$  states are perturbed by an electronic state with a lower electronic energy and anomalously large rotational constant which is not included in the fit, and the calculated fractional  $p$ -character in the  $12.98 \Pi$  state, 56%, is anomalously large relative to that for the  $13.98 \Pi$  state fit here as well as the  $5.98$ ,  $6.98$ , and  $7.98 \Pi$ ,

<sup>2</sup> Energy levels are calculated for discrete values of  $N$ . However, for the sake of reducing clutter on the reduced term value plot, best fit quantities are indicated by a dashed line.

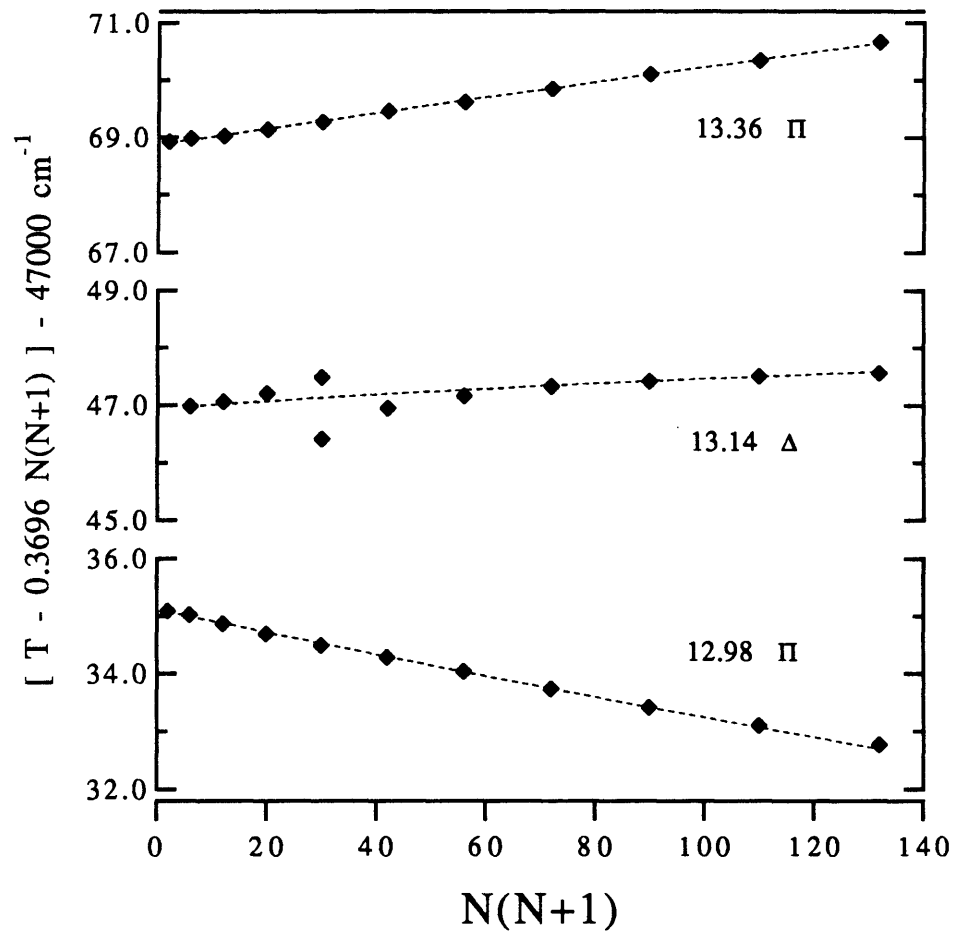


Figure 4.3. Reduced term value plot for  $n^*=13$  negative Kronig symmetry states. The dotted line represents the  $3 \times 3$ ,  $p \sim d$  effective Hamiltonian fit.

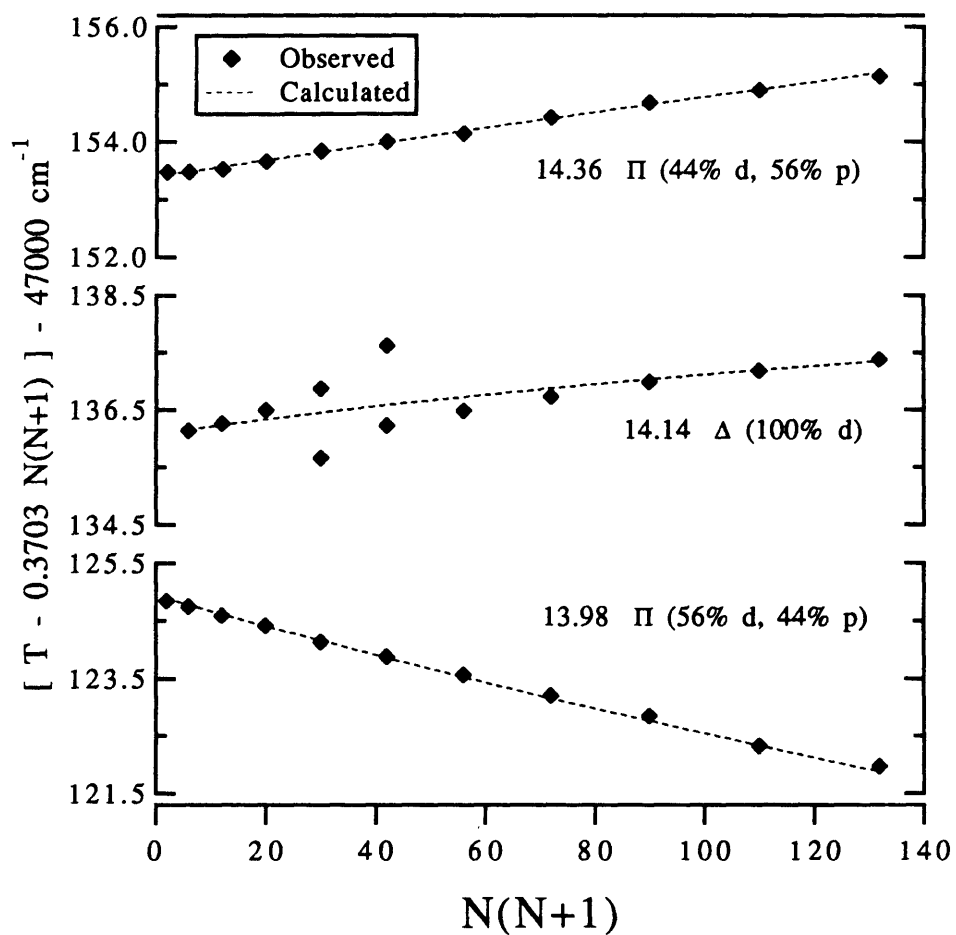


Figure 4.4. Reduced term value plot for  $n^*=14$  negative Kronig symmetry states. The dotted line represents the  $3 \times 3$ ,  $p \sim d$  effective Hamiltonian fit.

$v=0$  states fit by Murphy [10]. The avoided crossing may be treated as a two-state interaction using only the data collected via the  $A^2\Pi_{3/2}$ ,  $v=0$  intermediate, but may be more satisfactorily described using a six-by-six  $p\sim d\sim f$  Hamiltonian and 14f( $\mathcal{L}$ ) levels observed via the  $C^2\Pi_{3/2}$  intermediate. Both approaches have merit and will be discussed in later sections. The calculated anomalous fractional  $p$ -character in the 12.98  $\Pi$  state is a localized 'second-order' effect due to an accidental intrachannel perturbation between the 13.14  $\Delta$ ,  $v=1$  and 9.14  $\Delta$ ,  $v=2$  states, discussed below.

#### 4.3. 13.14 $\Delta$ , $v=1$ ~ 9.14 $\Delta$ , $v=2$ Intrachannel Perturbation

The Hamiltonian fit results listed in Table 4.1 may be substituted into Eqs.(4.15) and (4.16) to determine the  $p\Pi$  and  $d\Pi$  character in the 12.98 and 13.36  $\Pi$  states. One finds that the 12.98  $\Pi$  state has 56.1(3)%  $p$ -character and the 13.98  $\Pi$  state has 44.1(6)%  $p$ -character. The latter fraction is consistent with Murphy's MQDT and effective Hamiltonian fits to  $n^*=6, 7$ , and  $8$ ,  $v=0$  supercomplexes [10]. The calculated fractional  $p$ -character for the 12.98  $\Pi$  state is anomalous. Rydberg orbital hybridization should not change so dramatically between consecutive members of a Rydberg series. Fortunately, the anomalous increase in apparent  $p$ -character of the 12.98  $\Pi$  state may be accounted for by an intrachannel ( $\Delta v=1$ ) perturbation. The fractional  $p$ -character of the 12.98  $\Pi$  state returns to the expected, series invariant 44% when the intrachannel perturbation is included.

Figure 4.5 depicts the rotationless vibronic term values of the negative symmetry  $n^*=13$  and  $14$ ,  $v=1$  and  $n^*=9$ ,  $v=2$  states. The intrachannel matrix element was given by Eq.(3.22) and is listed again here:

$$V_{n_i^*, v \sim n_i^*, v'} = -\frac{2\Re}{[n_i^* n_i^*]^{3/2}} \left[ \left( \frac{d\delta_i}{dR} \right)_{R^*} \langle v | R - R_e^+ | v' \rangle \right]. \quad (4.19)$$

Murphy [6] calculated a quantum defect derivative of  $0.73_2 \text{ \AA}^{-1}$  for the 0.36  $\Pi$  series and estimated the quantity to be  $0.3_6 \text{ \AA}^{-1}$  for the 0.14  $\Delta$  series. Equation (4.19) predicts that the matrix element between the 13.14  $\Delta$ ,  $v=1$  and states 9.14  $\Delta$ ,  $v=2$  will be  $\sim -3.7 \text{ cm}^{-1}$ ,  $\sim -6.42 \text{ cm}^{-1}$  between the 14.36  $\Pi$ ,  $v=1$  and 9.36  $\Pi$ ,  $v=2$  states, and  $\sim -7.15 \text{ cm}^{-1}$  between the 13.36  $\Pi$ ,  $v=1$  and 9.36  $\Pi$ ,  $v=2$  states.

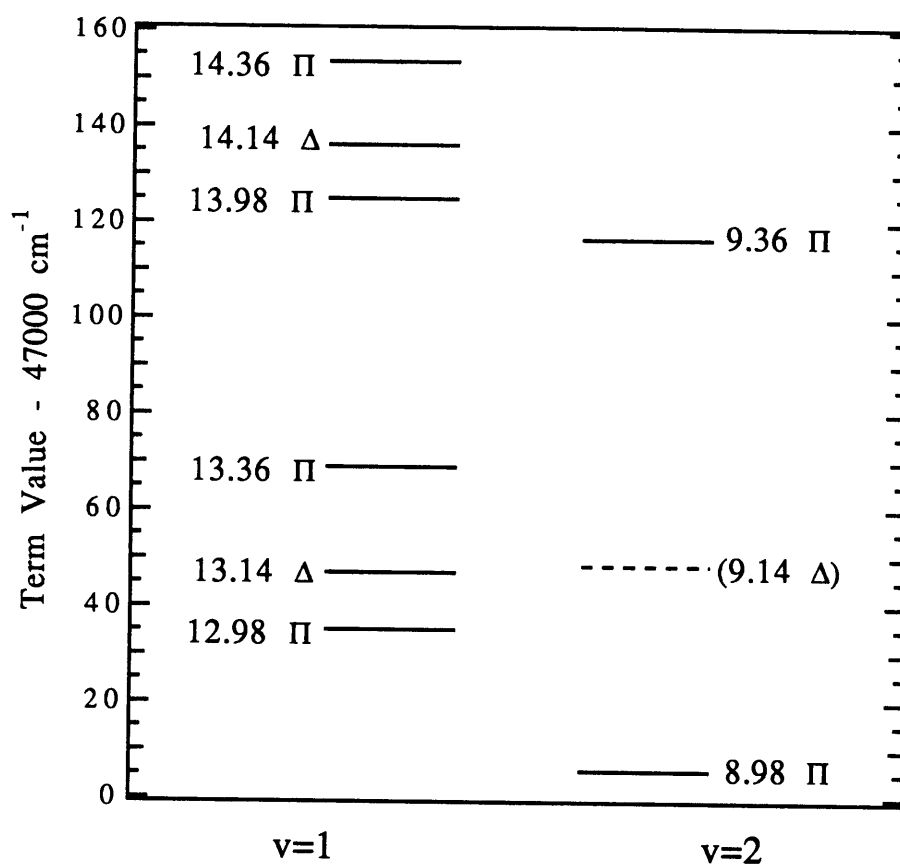


Fig.4.5. Term values of  $n^*=13$  and  $14$ ,  $v=1$  and  $n^*=9$ ,  $v=2$  negative Kronig symmetry states. (All relative to  $X^2\Sigma^+$ ,  $v=0$ ,  $N=0$ .)

The molecular constants of the 9.36  $\Pi$  and 8.98  $\Pi$ ,  $v=2$  states were determined by fitting the observed levels to the expression:

$$E = T_{n^*,v} + B_{n^*,v}N(N+1) - D_{n^*,v}N^2(N+1)^2. \quad (4.20)$$

The results of these fits are listed in Table 4.2.

Table 4.2 Molecular Constants of  $n^*=9$ ,  $v=2$  Negative Kronig Symmetry States

Parameter	Fit Value
$T_{9.36\Pi,v=2} / \text{cm}^{-1}$	47116.49(4)
$B_{9.36\Pi,v=2} / \text{cm}^{-1}$	0.3715(4)
$T_{8.98\Pi,v=2} / \text{cm}^{-1}$	47005.79(5)
$B_{8.98\Pi,v=2} / \text{cm}^{-1}$	0.3656(6)
$10^7 D_v / \text{cm}^{-1}$	[4.4]

Parameters in brackets were held fixed.

Quantity in parentheses is  $2\sigma$ .

The 9.14  $\Delta$ ,  $v=2$  state could not be unambiguously identified in the ID-OODR spectra. There were several weak but unassignable lines in the region where it was expected to be observed. One initially appealing assignment, based on the strongest of the weak features, yielded a term value of 47048.4(2)  $\text{cm}^{-1}$  and a rotational constant of 0.369(5)  $\text{cm}^{-1}$ , however this placed an upper limit on the intrachannel matrix element of 0.7  $\text{cm}^{-1}$ , roughly 1/5 of that predicted by Eq.(4.19), so that assignment was rejected.

The 'zero-order' term values of the 0.36  $\Pi$  states may be determined by diagonalizing a three by three matrix with the calculated intrachannel matrix elements in the off-diagonal positions and the zero-order term values (the unknowns) on the diagonal. The E-values which are solutions to the determinantal equation are the observed term values:

$$\det \begin{vmatrix} T_{14.36\Pi,v=1}^0 - E & -6.42 & 0 \\ -6.42 & T_{9.36\Pi,v=2}^0 - E & -7.15 \\ 0 & -7.15 & T_{13.36\Pi,v=1}^0 - E \end{vmatrix} = 0. \quad (4.21)$$

The zero-order term values could also be calculated using second-order perturbation theory. The values obtained by solution of Eq.(4.21) are listed in Table 4.3.

Table 4.3 0.36  $\Pi$  State Vibronic Term Values

State	Observed / $\text{cm}^{-1}$	Deperturbed / $\text{cm}^{-1}$	Level Shift / $\text{cm}^{-1}$
14.36 $\Pi$ , $v=1$	47153.42	47152.29	+1.13
9.36 $\Pi$ , $v=2$	47116.49	47116.54	-0.05
13.36 $\Pi$ , $v=1$	47068.90	47069.97	-1.07

The 14.36  $\Pi$  and 13.36  $\Pi$ ,  $v=1$  states have respectively 3% and 2% 9.36  $\Pi$ ,  $v=2$  character. Accordingly, the 9.36  $\Pi$ ,  $v=2$  state has ~5% .36  $\Pi$ ,  $v=1$  character. This has significant implications for the vibrational autoionization rate of the 9.36  $\Pi$  state, but changes the calculated  $n^*=13$  and 14  $p$ - $d$  mixing fraction by only ~2%.<sup>3</sup> The perturbation of the 13.36  $\Pi$ ,  $v=1$  state by the 9.36  $\Pi$ ,  $v=2$  does not account for the anomalous  $p$ - $d$  mixing angle in  $n^*=13$ . The 8.98  $\Pi$ ,  $v=2$  state lies about 30  $\text{cm}^{-1}$  below the 12.98  $\Pi$ ,  $v=1$  state. A 12.98  $\Pi$ ,  $v=1$  ~ 8.98  $\Pi$ ,  $v=2$  intrachannel matrix element as large as the 13.36  $\Pi$ ,  $v=1$  ~ 9.36  $\Pi$ ,  $v=2$  would shift the term value of the 12.98  $\Pi$ ,  $v=1$  state up by ~1.7  $\text{cm}^{-1}$ . This could change the calculated fractional  $p$ -character in the 12.98  $\Pi$ ,  $v=1$  state by another several percent.<sup>4</sup> The anomalous  $p$ -character can be attributed primarily to an intrachannel perturbation between 13.14  $\Delta$ ,  $v=1$  ~ 9.14  $\Delta$ ,  $v=2$  states.

An effective 9.14  $\Delta$ ,  $v=2$  ~ 13.14  $\Delta$ ,  $v=1$  matrix element may be determined by expanding the three by three negative-Kronig symmetry effective Hamiltonian to a five by five. The two additional basis states are the 9.14  $\Delta$ ,  $v=2$  and 9.36  $\Pi$ ,  $v=2$ . The term values of the  $v=2$  states are calculated using Eq.(4.20). The 8.98  $\Pi$ ,  $v=2$  state is not included in the fit because no value of the quantum defect derivative has been determined for this series, but as mentioned in the preceding paragraph the effect of the 8.98  $\Pi$ ,  $v=2$  state on the  $n^*=13$  complex is minimal.

The 9.14  $\Delta$ ,  $v=2$  ~ 13.14  $\Delta$ ,  $v=1$  matrix element is calculated by first setting the  $p$ - $d$  mixing angle and rotational constant of the  $n^*=13$  basis states equal to the non-anomalous values determined by the fit to the  $n^*=14$  data. The 9.36  $\Pi$ ,  $v=2$  ~ 13.36  $\Pi$ ,  $v=1$  matrix element is set equal to the value determined using Eq.(4.19), -7.15  $\text{cm}^{-1}$ . The fit

<sup>3</sup> The 14.36  $\Pi$  and 13.36  $\Pi$ ,  $v=1$  mixing coefficients have opposite sign. The calculated autoionization rate therefore depends on the difference of the squares of the mixing coefficients, 0.01, rather than their sum, 0.05. Even though this is a factor of 5 difference, 1/100 of the  $\Delta v = 1$  autoionization rate of the 0.36 $\Pi$  states is still several orders of magnitude larger than the  $\Delta v = 2$  autoionization rate.

<sup>4</sup> It will be shown in later sections that the 0.36  $\Pi$  quantum defect derivative is at least a factor of two larger than for any other core-penetrating Rydberg series. The intrachannel matrix element between two states  $n^*$  and  $n^{*}$  will be correspondingly larger in the 0.36  $\Pi$  series.

parameters which were allowed to vary are the term values for the 9.14  $\Delta$ , 13.14  $\Delta$ , 13.36  $\Pi$ , and 12.98  $\Pi$  states, and the 9.14  $\Delta$ ,  $v=2 \sim 13.14 \Delta$ ,  $v=1$  matrix element. The value of the matrix element determined by the fit is  $-3.3(3) \text{ cm}^{-1}$ , in excellent agreement with the value predicted by Eq.(4.19). Molecular constants used in this fit are listed in Table 4.4 and a reduced term value plot of the 13.36  $\Pi$ , 12.98  $\Pi$ , 13.14  $\Delta$  states, and the predicted location of the 9.14  $\Delta$  levels is shown in Fig.4.6.

Table 4.4 Molecular Constants from 9.14  $\Delta$ ,  $v=2 \sim 13.14 \Delta$ ,  $v=1$  Deperturbation

Fit Parameter	Value
$T_{13.36\Pi, v=1} / \text{cm}^{-1}$	47035.07(2)
$T_{13.14\Delta, v=1} / \text{cm}^{-1}$	47050.0(3)
$T_{12.98\Pi, v=1} / \text{cm}^{-1}$	47069.97(2)
$T_{9.36\Pi, v=2} / \text{cm}^{-1}$	[47116.54]
$T_{9.14\Delta, v=2} / \text{cm}^{-1}$	47050.4(2)
$\tan(\theta/2)$	[2.225]
$\theta / \text{radians}$	[2.297]
$B_{v=1}^+ / \text{cm}^{-1}$	[0.3704]
$10^7 D_v^+ / \text{cm}^{-1}$	[4.4]
$V_{9.14 \Delta, v=2 \sim 13.14 \Delta, v=1}$	-3.3(3)
$V_{9.36 \Pi, v=2 \sim 13.36 \Pi, v=1}$	[-7.15]
$B_{v=2}^+ / \text{cm}^{-1}$	[0.368]

Parameters in brackets were held fixed.

Quantity in parentheses is  $2\sigma$ .

It is initially disturbing that no  $\Delta$  state was observed with term value  $\sim 47054 \text{ cm}^{-1}$ . Fortunately, it is possible to explain this by a destructive interference effect in the  $n^* \Delta - A^2\Pi_{3/2}$  transition moment. The relative intensities of the  $A^2\Pi_{3/2}$ ,  $v=0$  to .14  $\Delta$  transitions may be estimated using the well-known  $n^*$ -scaling behavior for valence-Rydberg transition moments [11] and calculated vibrational overlap factors. For transitions within a given Rydberg series, the purely electronic factor scales as:

$$\frac{\langle n_0 \ll n^* | \hat{\mu} | n^* + m \rangle}{\langle n_0 \ll n^* | \hat{\mu} | n^* \rangle} \approx \left( \frac{n^*}{n^* + m} \right)^{\frac{3}{2}}, \quad (4.22)$$



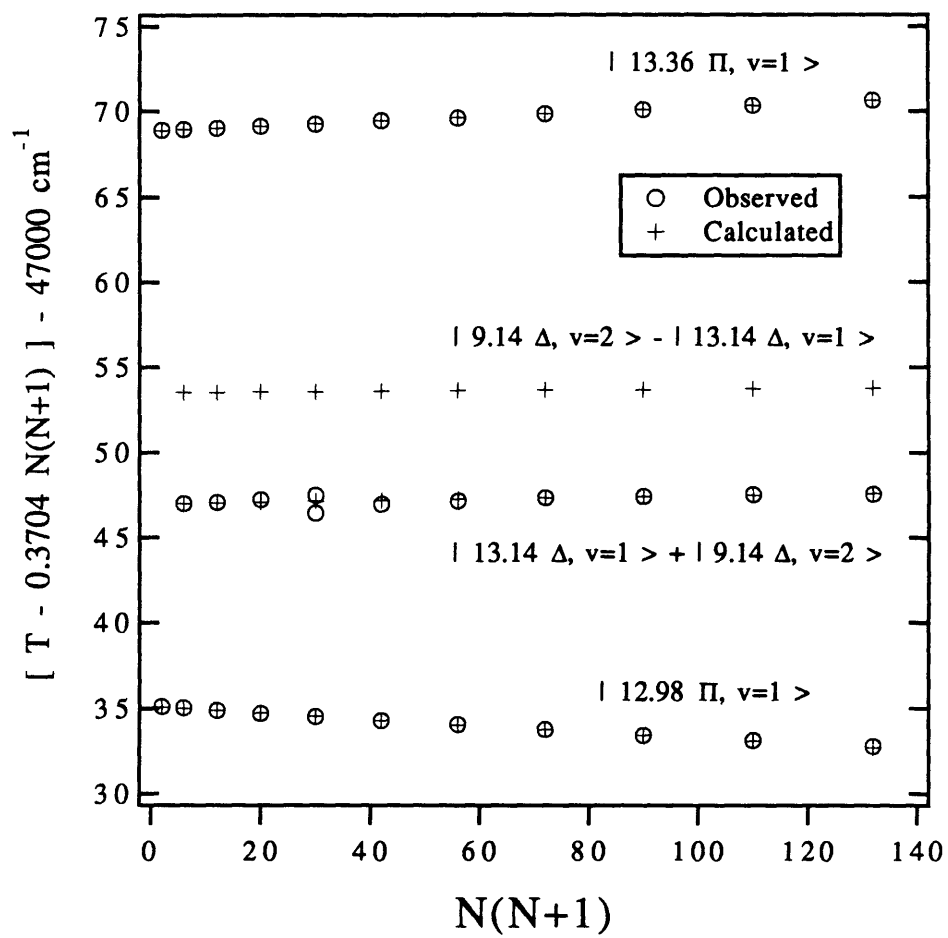


Figure 4.6. Reduced term value plot of deperturbed  $n^*=13$  negative Kronig symmetry states.

where  $m$  is an integer (the difference between the effective principal quantum number of the two Rydberg states). The expected ratio of transition intensities must also incorporate the Rydberg -  $A^2\Pi_{3/2}$  Franck-Condon Factor. The Rydberg -  $A^2\Pi_{3/2}$  Franck-Condon factors are calculated using an RKR-FCF program written by Zare and Cashion [12] and the molecular constants in Table 4.5. The calculated vibrational overlap integrals are listed in Table 4.6. The vibrational wavefunctions have positive phase at the inner turning point of vibrational potential.

Table 4.5 Molecular Constant for Calculation of RKR wavefunctions

Constant / $\text{cm}^{-1}$	CaF $A^2\Pi$	CaF <sup>+</sup> $X^1\Sigma^+$
$\omega_e$	594.86	685
$\omega_e x_e$	3.26	2.60
$B_e$	0.348744	0.3734
$\alpha_e$	0.002529	0.0020

Table 4.6 Rydberg~Cation Vibrational Overlap Factors

$v_{\text{Rydberg}}$	$\langle v_{\text{Rydberg}}   v_A = 0 \rangle$	$\langle v_{\text{Rydberg}}   v_A = 1 \rangle$
0	0.767	-0.549
1	0.564	0.350
2	0.282	0.595
3	0.112	0.416

If the Rydberg states were unmixed, the expected ratio of Rydberg -  $A^2\Pi_{3/2}$  transition strengths would be:

$$\frac{\left| \langle A, v_A = 0 | \hat{\mu} | 9.14\Delta, v^+ = 2 \rangle \right|^2}{\left| \langle A, v_A = 0 | \hat{\mu} | 13.14\Delta, v^+ = 1 \rangle \right|^2} \approx \left( \frac{13.14}{9.14} \right)^3 \left( \frac{0.282}{0.564} \right)^2 = 0.743. \quad (4.23)$$

While the electronic factor of the  $9.14 \Delta - A^2\Pi_{3/2}$  transition is three times greater than that for the  $13.14 \Delta - A^2\Pi_{3/2}$ , the Rydberg,  $v^* - A^2\Pi_{3/2}$ ,  $v=0$  Franck-Condon factor decreases by a factor of five in going from  $v^*=1$  to  $v^*=2$  in the excited state. However if the  $.14 \Delta$  states are mixed, the observed transition intensities may be considerably different than predicted by Eq.(4.23). The two  $\Delta$  eigenstates may be expressed as linear combinations of  $9.14 \Delta$ ,  $v=2$  and  $13.14 \Delta$ ,  $v=1$ :

$$|+\rangle \equiv \cos\theta|9.14\Delta, v=2\rangle + \sin\theta|13.14\Delta, v=1\rangle, \quad (4.24)$$

$$|-\rangle \equiv \cos\theta|13.14\Delta, v=2\rangle - \sin\theta|9.14\Delta, v=2\rangle, \quad (4.25)$$

where  $\theta$  is the 9.14  $\Delta \sim$  13.14  $\Delta$  mixing angle. (The "+" and "-" labels in the remainder of this section should not be confused with positive and negative Kronig symmetries. The intrachannel perturbation affects both symmetries.) The 'Mixed State' -  $A^2\Pi_{3/2}, v=0$  transition moments are:

$$\langle A|\hat{\mu}|-\rangle \equiv \cos\theta\langle A|\hat{\mu}|9.14\Delta, v=2\rangle - \sin\theta\langle A|\hat{\mu}|13.14\Delta, v=1\rangle, \quad (4.26)$$

$$\langle A|\hat{\mu}|+\rangle = \cos\theta\langle A|\hat{\mu}|13.14\Delta, v=1\rangle + \sin\theta\langle A|\hat{\mu}|9.14\Delta, v=2\rangle. \quad (4.27)$$

The  $|-\rangle$  state is the higher energy eigenstate. The transition intensity is proportional to the square of the transition moment. The scaling properties of valence-Rydberg transition dipole moments, Eq.(4.22), means that the substitution can be made:

$$\langle A|\hat{\mu}|9.14\Delta\rangle \approx \left(\frac{13.14}{9.14}\right)^2 \langle A|\hat{\mu}|13.14\Delta\rangle = 1.724 \mu_0, \quad (4.28)$$

where  $\mu_0 \equiv \langle A|\hat{\mu}|13.14\Delta\rangle$ , the electronic transition moment. Equation (4.26) then becomes,

$$\langle A|\hat{\mu}|-\rangle = [1.724 \cos\theta \langle v_A = 0|v=2\rangle - \sin\theta \langle v_A = 0|v=1\rangle] \mu_0. \quad (4.29)$$

The transition moment would be exactly zero if the term in brackets is zero:

$$0.282 \cdot 1.724 \cos\theta - 0.564 \cdot \sin\theta = 0. \quad (4.30)$$

The transition intensity to the '9.14  $\Delta, v=2$ ' state will be zero when the state acquires 43% 13.14  $\Delta, v=1$  character ( $\theta = 0.711$  rad). The matrix element determined using Eq.(4.19) and the effective Hamiltonian fit predicts that the 9.14  $\Delta, v=2$  and 13.14  $\Delta, v=1$  states will be nearly 50/50 mixed. For a 50/50 mixture, the ratio of the  $|+\rangle - A^2\Pi_{3/2}$  to  $|-\rangle - A^2\Pi_{3/2}$  transition intensities is  $\sim 180:1$ , as calculated using Eqs.(4.26) and (4.27):

$$\frac{|\langle A|\hat{\mu}|+\rangle|^2}{|\langle A|\hat{\mu}|-\rangle|^2} = \frac{|1.724 \cdot 0.282 \cdot 0.707 + 0.564 \cdot 0.707|^2}{|1.724 \cdot 0.282 \cdot 0.707 - 0.564 \cdot 0.707|^2} \approx 180. \quad (4.31)$$

This ratio is comparable to the signal-to-noise ratio of the experiment, so the absence of an observed '9.14  $\Delta$ ,  $v=2$ ' state has a quantitatively viable explanation. If the spectra were recorded from the  $v=1$ , rather than the  $v=0$ , level of the A state, one would expect an intensity ratio of 4:1 instead of 180:1. Inserting the appropriate vibrational overlap factors from Table 4.6, Eq.(4.31) yields:

$$\frac{|\langle A|\hat{\mu}|+\rangle|^2}{|\langle A|\hat{\mu}|-\rangle|^2} = \frac{|1.724 \cdot 0.595 \cdot 0.707 + 0.350 \cdot 0.707|^2}{|1.724 \cdot 0.595 \cdot 0.707 - 0.350 \cdot 0.707|^2} \approx 4. \quad (4.32)$$

If the '9.14  $\Delta$ ,  $v=2$ ' state is unobserved due to an interference effect, then the transition terminating on '13.14  $\Delta$ ,  $v=1$ ' should acquire additional intensity and be stronger relative to transitions to other members of the  $n^*=13$ ,  $v=1$  supercomplex than the 14.14  $\Delta$ ,  $v=1$  -  $A^2\Pi_{3/2}$  transition is to other members of the  $n^*=14$ ,  $v=1$  supercomplex. The relative intensities of these transitions may be established by examining ID-OODR spectra recorded from the  $J=1.5$ , e parity level of  $A^2\Pi_{3/2}$ ,  $v=0$ . The .98  $\Pi$  state is located  $\sim 10$   $\text{cm}^{-1}$  to the red of the .14  $\Delta$  state in both  $n^*=13$  and  $n^*=14$  and is not perturbed in either case. The ratio of intensities of the 12.98  $\Pi$  and 13.14  $\Delta$  -  $A^2\Pi_{3/2}$ ,  $v=0$  transitions is 3.8:1. The ratio of intensities of the 13.98  $\Pi$  and 14.14  $\Delta$  -  $A^2\Pi_{3/2}$ ,  $v=0$  transitions is 2.1:1.<sup>5</sup> If the 13.14  $\Delta$  state were unmixed, the ratio would be the same as for the 14.14  $\Delta$  state. The ratio of the intra- $n^*$  intensity ratios is equal to the 'Mixed State' -  $A^2\Pi_{3/2}$  to unmixed 13.14  $\Delta$  -  $A^2\Pi_{3/2}$  intensity ratio. The latter quantity is calculated using Eq.(4.26):

$$\frac{|\langle A|\hat{\mu}|+\rangle|^2}{|\langle A|\hat{\mu}|13.14\Delta, v=1\rangle|^2} = \frac{\left| \left( \frac{13.14}{9.14} \right)^{3/2} \frac{.282}{\sqrt{2}} + \frac{0.564}{\sqrt{2}} \right|^2 \mu_0^2}{|0.564|^2 \mu_0^2} = 1.73. \quad (4.33)$$

The numerator of Eq.(4.33) is calculated with  $\theta = \pi/2$  (50/50 mixing) and the denominator is calculated with  $\theta = 0$ . The calculated ratio compares favorably to the observed enhancement,  $3.8/2.1 = 1.8$ .

<sup>5</sup> Relative intensities were determined by integrating the area under lines belong to the Rydberg - A transition.

The signature of the 9.14  $\Delta$ ,  $v=2 \sim 13.14 \Delta$ ,  $v=1$  perturbation is in evidence from several phenomena. Murphy's estimate of the 0.14  $\Delta$  quantum defect derivative is therefore supported by this work. A more accurate determination of the quantum defect derivative should be made by observation of the  $l \rightarrow$  state by excitation from  $A^2\Pi_{3/2}$ ,  $v=1$ .

#### 4.4. Core-Penetrating $\sim$ Core-Non-Penetrating Perturbations: $n.14\Delta \sim nf$ , $\ell = -2$ Perturbations

The  $N=5$  level of the 13.14  $\Delta$  state and the  $N=5$  and 6 levels of the 14.14  $\Delta$  state are doubled in the ID-OODR spectra recorded from the  $A^2\Pi_{3/2}$  state (see Fig.4.7). These extra lines are due to an electrostatic perturbation between the  $\Delta$  state and the highest energy member of the negative Kronig-symmetry portion of the f-complex. The quality of the effective Hamiltonian fit in the previous section was sufficiently good that the observed deviations of levels from their calculated positions could be used to determine the matrix element between the .14  $\Delta$  state and the perturber, even without knowing the zero-order energies of the perturbing state.

The perturbation may be described using a two-by-two matrix:

$$\begin{vmatrix} E_1^0 - E & H_{12} \\ H_{12} & E_2^0 - E \end{vmatrix}, \quad (4.34)$$

where  $E_1^0$  and  $E_2^0$  are the unperturbed term values. The relation between the separation of observed levels, zero-order positions, and off-diagonal matrix element is:

$$\Delta E_{\text{obs}} = \sqrt{(\Delta E^0)^2 + 4H_{12}^2}. \quad (4.35)$$

Equation (4.35) may be inverted to determine  $|H_{12}|$ :

$$|H_{12}| = \frac{1}{2} \sqrt{(\Delta E_{\text{obs}})^2 - (\Delta E^0)^2}. \quad (4.36)$$

Because the zero-order positions of the perturber levels are not known to as high accuracy as the .14  $\Delta$  levels,  $|H_{12}|$  must be estimated from level shifts. The .14  $\Delta$  and perturber levels are shifted by equal amounts. The shift,  $\delta E$ , is defined by the relation:

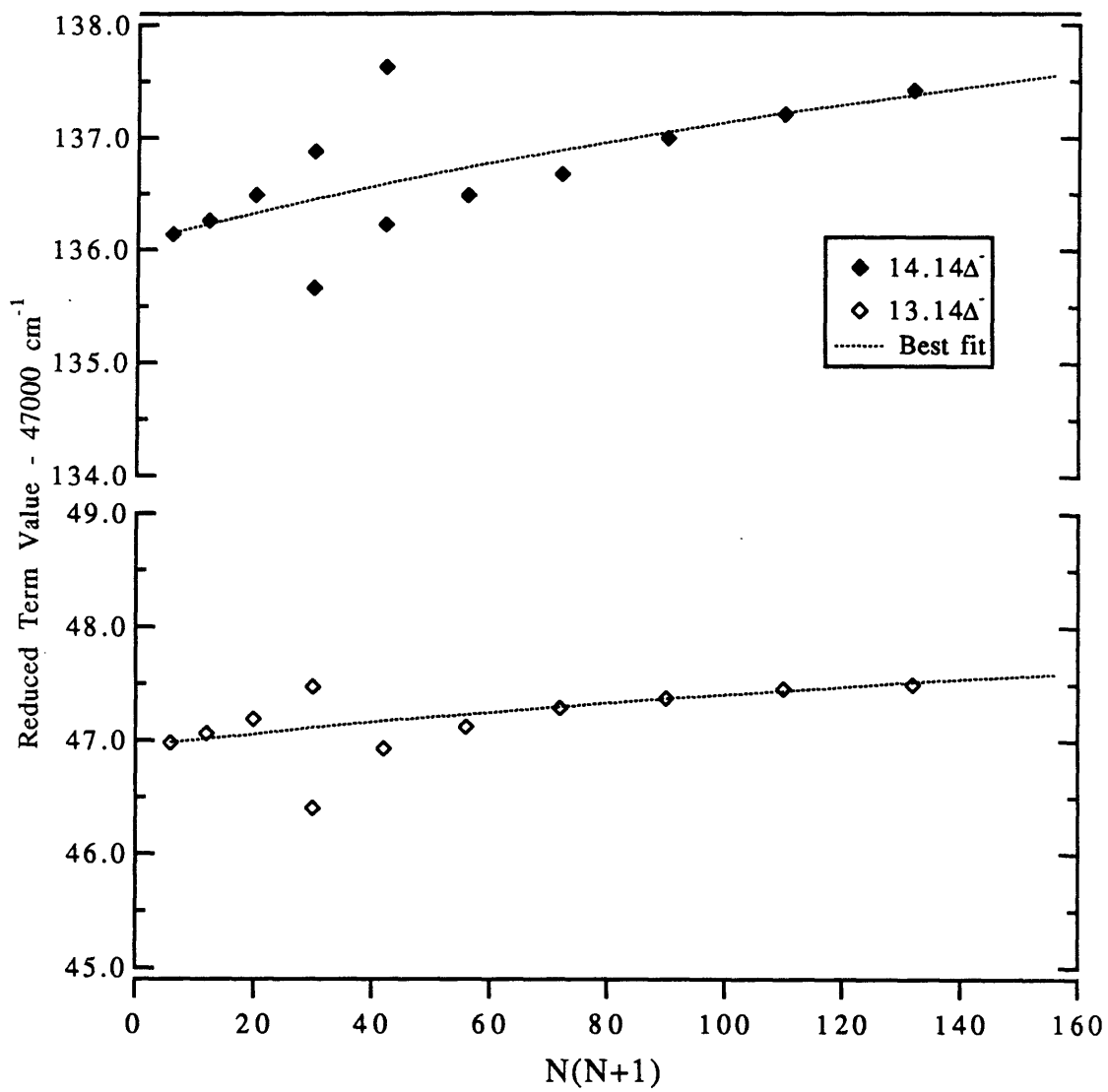


Figure 4.7. Reduced term value plots for 13.14 and 14.14 $\Delta$  states with best fit from 3x3 effective Hamiltonian.

$$\Delta E_{\text{obs}} - \Delta E^0 \equiv 2 \cdot \delta E. \quad (4.37)$$

Substitution of Eq.(4.37) into Eq.(4.36) yields,

$$|H_{12}| = \sqrt{\delta E(\Delta E_{\text{obs}} - \delta E)}. \quad (4.38)$$

The off-diagonal matrix element, calculated using Eq.(4.38), is listed in Table 4.7. Each shifted level yields a value of  $|H_{12}|$ . As the measurement uncertainty in term values is  $\pm 0.03 \text{ cm}^{-1}$ , the most accurate determinations of  $|H_{12}|$  are those which rely on the largest level shifts. The single point for the  $n^*=13$  perturbation yields a matrix element of  $\sim 0.5 \text{ cm}^{-1}$ . The perturbation matrix element in  $n^*=14$  is  $\sim 0.6 \text{ cm}^{-1}$ . As discussed in the first part of this chapter, perturbation matrix elements are expected to scale as  $(n_1 \cdot n_2)^{-3/2}$ . This  $n^*$ -scaling relation predicts that for  $n^*=13$  perturbation matrix element should be  $(14.1/13.1)^3 \approx 1.25$  times larger than the  $n^*=14$  matrix element. The value of  $|H_{12}|$  for the  $n^*=13$  perturbation determined using Eq.(4.38) is considerably smaller than the value predicted by scaling the  $n^*=14$  matrix element:

$$|H_{12}|_{n^*=13} = \left(\frac{14.1}{13.1}\right)^3 |H_{12}|_{n^*=14} = \left(\frac{14.1}{13.1}\right)^3 0.59 \text{ cm}^{-1} = 0.74 \text{ cm}^{-1}. \quad (4.39)$$

The observed perturbation matrix element is only  $\sim 70\%$  the value predicted by  $n^*$ -scaling. The ratio of the observed to calculated perturbation matrix elements is a fairly accurate measure of the coefficient of zero-order 13.14  $\Delta$  character in the mixed state. The square of the coefficient gives the fractional 13.14  $\Delta$  character in the bright state:

$$100\% \cdot \left(\frac{|H_{12}|_{\text{obs}}}{|H_{12}|_{\text{calc}}}\right)^2 = 100\% \cdot \left(\frac{0.51}{0.74}\right)^2 = 47\%. \quad (4.40)$$

Given the assumptions involved in the preceding calculations, it is fair to claim that the observed dilution of the perturbation matrix element is consistent with the expectation of nearly 50/50 mixing of the 13.14  $\Delta$ ,  $v=1$  and 9.14  $\Delta$ ,  $v=2$  states described in the previous section.

Table 4.7 Calculated Perturbation Matrix Elements

N	13.14 $\Delta$		14.14 $\Delta$	
	$\delta E / \text{cm}^{-1}$	$ H_{12}  / \text{cm}^{-1}$	$\delta E / \text{cm}^{-1}$	$ H_{12}  / \text{cm}^{-1}$
5	+0.36(1)	0.51(4)	+0.43(1)	0.58(4)
6	-	-	-0.36(1)	0.61(4)

Quantity in parentheses is  $1\sigma$ .

The perturbation may be treated more completely by including the negative symmetry f-states, observed in the ID-OODR spectra recorded from the  $C^2\Pi_{3/2}$ ,  $v=0$  intermediate, and expanding the effective Hamiltonian to include  $p\pi\sim f\pi$ ,  $d\pi\sim f\pi$ , and  $d\delta\sim f\delta$  electrostatic matrix elements. The f-subblock Hamiltonian is constructed in the same manner as were the p and d-subblocks. The  $\ell$ -mixing electrostatic matrix elements are  $V_{p\pi\sim f\pi}$ ,  $V_{d\pi\sim f\pi}$ , and  $V_{d\delta\sim f\delta}$ . The effective Hamiltonian for the p~d~f negative symmetry supercomplex is most more simply expressed with diagonal elements of  $H^{\text{rot}}$  subtracted:

$$\mathbf{H} - (B_v x - D_v x^2)\mathbf{I} = \begin{bmatrix} T_{\Pi(1)} & 0 & -2 \sin \theta B_v \sqrt{x-2} & V_{\Pi(1)-\Pi} & 0 & 0 \\ 0 & T_{\Pi(2)} & -2 \cos \theta B_v \sqrt{x-2} & V_{\Pi(2)-\Pi} & 0 & 0 \\ -2 \sin \theta B_v \sqrt{x-2} & -2 \cos \theta B_v \sqrt{x-2} & T_{\Delta} & 0 & V_{\Delta-\Lambda} & 0 \\ V_{\Pi(1)-\Pi} & V_{\Pi(2)-\Pi} & 0 & T_{\Pi} & -\sqrt{10} B_v \sqrt{x-2} & 0 \\ 0 & 0 & V_{\Delta-\Lambda} & -\sqrt{10} B_v \sqrt{x-2} & T_{\Lambda} & -\sqrt{6} B_v \sqrt{x-6} \\ 0 & 0 & 0 & 0 & -\sqrt{6} B_v \sqrt{x-6} & T_{\Phi} \end{bmatrix}, \quad (4.41)$$

where  $x = N(N+1)$ . Unfortunately, only five of the six negative symmetry states were observed. The lowest energy member of the f-complex,  $\mathcal{L} = +2$ , could not be identified. The fit of  $n^*=14$  data to the Hamiltonian in Eq. (4.41) was quite good. The parameter values determined by the non-linear least squares fit are listed in Table 4.8. Figure 4.8 is a reduced term value plot for  $n^*=14$  with calculated level positions as determined by Eq.(4.41) and the 'best fit' values of molecular constants.



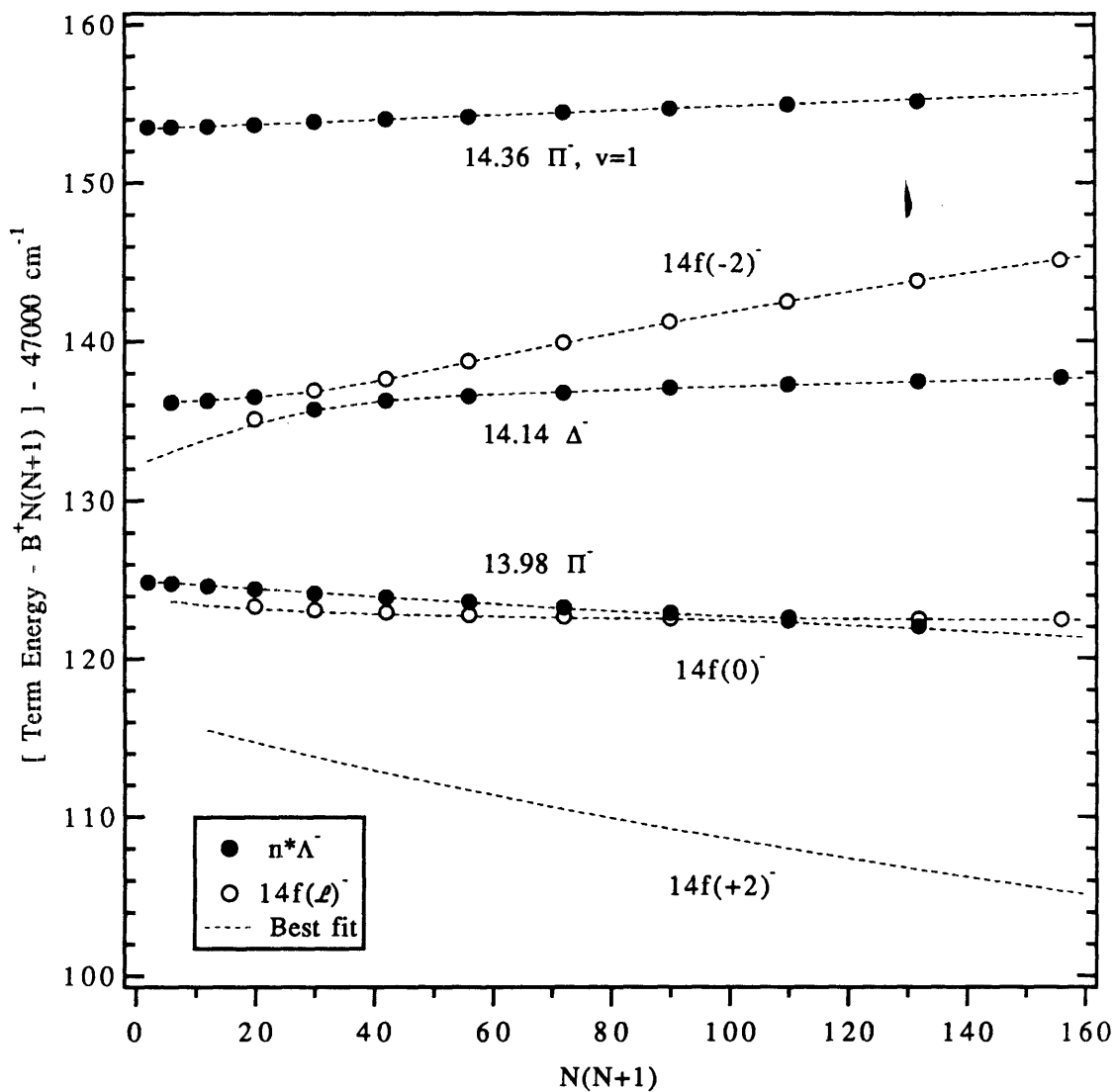


Figure 4.8. Reduced term value plot with best effective Hamiltonian fit for  $\text{CaF } n^*=14$  p~d~f Supercomplex, negative symmetry states.

Table 4.8 Molecular Constants from p-d-f Effective Hamiltonian Fit

Fit Parameter	Value
$T_{14.36\Pi} / \text{cm}^{-1}$	47153.0(3)
$T_{14.14\Delta} / \text{cm}^{-1}$	47136.08(5)
$T_{13.98\Pi} / \text{cm}^{-1}$	47124.92(4)
$T_{14f\Pi} / \text{cm}^{-1}$	47129.2(4)
$T_{14f\Delta f} / \text{cm}^{-1}$	47122.9(1)
$T_{14f\Phi f} / \text{cm}^{-1}$	47118.0(2)
$\tan(\theta/2)$	2.17(2)
$B_v / \text{cm}^{-1}$	0.3704(2)
$10^7 D_v / \text{cm}^{-1}$	[4.4]
$V_{13.98\Pi-14f\Pi} / \text{cm}^{-1}$	-0.2(2)
$V_{14.36\Pi-14f\Pi} / \text{cm}^{-1}$	3.1(8)
$V_{14.14\Delta-14f\Delta} / \text{cm}^{-1}$	0.45(3)
Variance	2.4

Parameters in brackets were held fixed.

Quantity in parentheses is  $2\sigma$ .

The matrix element between the 14.14  $\Delta$  and 14f(-2) states may be thought of as arising from  $\text{CaF}^+$  dipole-induced mixing. The dipole matrix element between two atomic orbitals  $|n\ell\lambda\rangle$  and  $|n'\ell'\lambda'\rangle$  is,

$$\langle n\ell\lambda | \frac{\mu \cos\theta}{r^2} | n'\ell'\lambda' \rangle, \quad (4.42)$$

where  $\mu$  is the electric dipole moment of the  $\text{CaF}^+$  cation and  $\theta$  is the angle between the dipole axis and the Rydberg electron. The matrix element may be separated into an angular portion and an integral over radial wavefunctions:

$$\langle n\ell\lambda | \frac{\mu \cos\theta}{r^2} | n'\ell'\lambda' \rangle = \mu \langle \ell\lambda | \cos\theta | \ell'\lambda' \rangle \langle n\ell | \frac{1}{r^2} | n'\ell' \rangle. \quad (4.43)$$

The  $\langle \ell\lambda | \cos\theta | \ell'\lambda' \rangle$  matrix element has selection rules  $\Delta\ell = \pm 1$ ,  $\Delta\lambda = 0$  and may be evaluated using Clebsch-Gordan coefficients by invoking the relations,

$$\cos \theta = \sqrt{\frac{4\pi}{3}} Y_{10}(\theta, \phi), \quad (4.44)$$

and,

$$\langle Y_{L_3 M_3} | Y_{L_2 M_2} | Y_{L_1 M_1} \rangle = \sqrt{\frac{(2L_1+1)(2L_2+1)}{4\pi(2L_3+1)}} \langle L_1 M_1, L_2 M_2 | L_3 M_3 \rangle \langle L_1 0, L_2 0 | L_3 0 \rangle, \quad (4.45)$$

where the  $Y_{LM}$  functions are spherical harmonics [13]. After some algebraic manipulation, the angular portion of Eq.(4.43) simplifies to,

$$\langle \ell+1, \lambda | \cos \theta | \ell \lambda \rangle = \sqrt{\frac{(\ell+1)^2 - \lambda^2}{(2\ell+3)(2\ell+1)}}. \quad (4.46)$$

The matrix element in Eq.(4.46), evaluated for  $\ell = \lambda = 2$ , is equal to  $1/\sqrt{7}$ .

The .14  $\Delta$  series terminates on the 2.14  $\Delta$  state. The 2.14  $\Delta$  state has primarily  $\text{Ca}^+$  3d $\delta$  character [14]. This may be generalized to mean that n.14  $\Delta$  states have primarily (n+1)d $\delta$   $\text{Ca}^+$  atomic parentage. The radial integral in Eq.(4.43) was calculated using a phase shifted hydrogenic d-orbital and a purely hydrogenic f-orbital [15]:

$$\langle 14.14d | \frac{1}{r^2} | 14f \rangle = 7.0 \cdot 10^{-6} \text{ a.u.} \quad (4.47)$$

The dipole moment of the cation may be calculated by inverting Eq.(4.43) and inserting the calculated value of  $\langle 14.14d | r^{-2} | 14f \rangle$  and the best fit value of  $\langle 14.14d\delta | \mu \cdot \cos \theta \cdot r^{-2} | 14f\delta \rangle$ :

$$\begin{aligned} \mu &= \frac{V_{14.14d\delta-14f(-2)}}{\langle 14.14d | r^{-2} | 14f \rangle \langle d\delta | \cos \theta | f\delta \rangle 2\mathfrak{R}} = \frac{0.45}{(7 \cdot 10^{-6}) (\frac{1}{\sqrt{7}}) (219474)} \text{ a.u.} \\ &= 1.9 \pm 1.0 \text{ Debye.} \end{aligned} \quad (4.48)$$

The dipole moment determined using Eq.(4.48) is about one fifth of that expected for  $\text{CaF}^+$ . There are several likely sources for this discrepancy. The first possible source of error is the value of the radial matrix element calculated in Eq.(4.47). Phase shifted hydrogenic orbitals are accurate representations of Rydberg orbitals only at long range. Unfortunately, the  $r^{-2}$  factor weights the integral at short-r. The second likely source of the

discrepancy is that the ion-core electric octopole moment also couples the d and f states. A much better estimate of the ion-core electric dipole moment may be made from the analysis CaF 14f and 14g state data.

#### 4.5. Fit of Experimental Data to 6x6 s~p~d and 10x10 s~p~d~f (+) symmetry Hamiltonian Models

Only five of the six positive Kronig symmetry, core-penetrating states were observed for  $n^*=13, v=1$ . The 13.18  $\Sigma^+$  state could not be unambiguously identified. In addition, the 13.14  $\Delta$  state is strongly perturbed by 9.14  $\Delta, v=2$ . At low  $N$ , the 12.88  $\Sigma^+$  state is dark from both the  $A^2\Pi_{3/2}, v=0$  and  $C^2\Pi_{3/2}, v=0$  intermediates, however rotational  $\ell$ -uncoupling does mix in some bright state character from the nearby 12.98  $\Pi$  state above  $N\sim 8$ . Vibronic states having  $n^*\approx 9.0$  and  $v=2$ , i.e.  $n^*=9$  core-non-penetrating states, lie right in the middle of the  $n^*=13$  supercomplex. These  $v=2$  core-non-penetrating states perturb both  $n^*=13$  core-penetrating and core-non-penetrating states, and make ID-OODR spectra recorded from the  $C^2\Pi_{3/2}$  state particularly difficult to analyze.

The  $n^*=14$  s~p~d supercomplex is relatively unperturbed in comparison to that for  $n^*=13$ . For the purpose of developing a model of s~p~d  $n^*$ -supercomplexes, it is the  $n^*=14, v=1$  supercomplex which receives attention here. Transitions terminating on 14.55  $\Sigma^+$  levels were anomalously weak in comparison to those to 13.55  $\Sigma^+$  levels and there is some doubt of the assignments of the weakest lines. Their lack of intensity may be due to an intrachannel perturbation between the 14.55  $\Sigma^+, v=1$  and 9.55  $\Sigma^+, v=2$  states analogous to the 13.14  $\Delta, v=1 \sim 9.14 \Delta, v=2$  interaction discussed previously. The Rydberg formula combined with the estimated value of  $\Delta G_{3/2}$ , predicts a difference in unperturbed term values of only several  $\text{cm}^{-1}$  between the 14.55  $\Sigma^+, v=1$  and 9.55  $\Sigma^+, v=2$  states, so an intrachannel,  $\Delta v = 1$  perturbation matrix element of only several  $\text{cm}^{-1}$  could result in significant mixing. The strongest transitions out of the  $A^2\Pi_{3/2}$  state terminated on core-penetrating states. While transitions to positive Kronig-symmetry  $14f(\mathcal{L})$  states, in particular  $14f(-3)^+$  and  $14f(+1)^+$ , were observable, they were comparatively weak. In contrast, transitions terminating on  $14f(\mathcal{L})$  states were by far the strongest observed out of the  $C^2\Pi_{3/2}$  intermediate.

Figure 4.9 is a reduced term value plot of all positive Kronig-symmetry states in the vicinity of  $n^*=14, v=1$ . Several  $n^* \approx 9, v=2$  states are also observed. Figure 4.10 is an expanded view of the reduced term value plot in Figure 4.9. The gray rectangle surrounds an avoided crossing between the 9.36  $\Pi, v=2$  and  $14f(+1), v=1$  states. The perturbation is not analyzed here, but the avoided crossing implies an  $N$ -independent matrix element of  $\sim 1.0 \text{ cm}^{-1}$ .

The remainder of this section is a comparison and contrast of the s~p~d and s~p~d~f effective Hamiltonian models of the  $n^*=14$  positive Kronig symmetry states. The goal is to

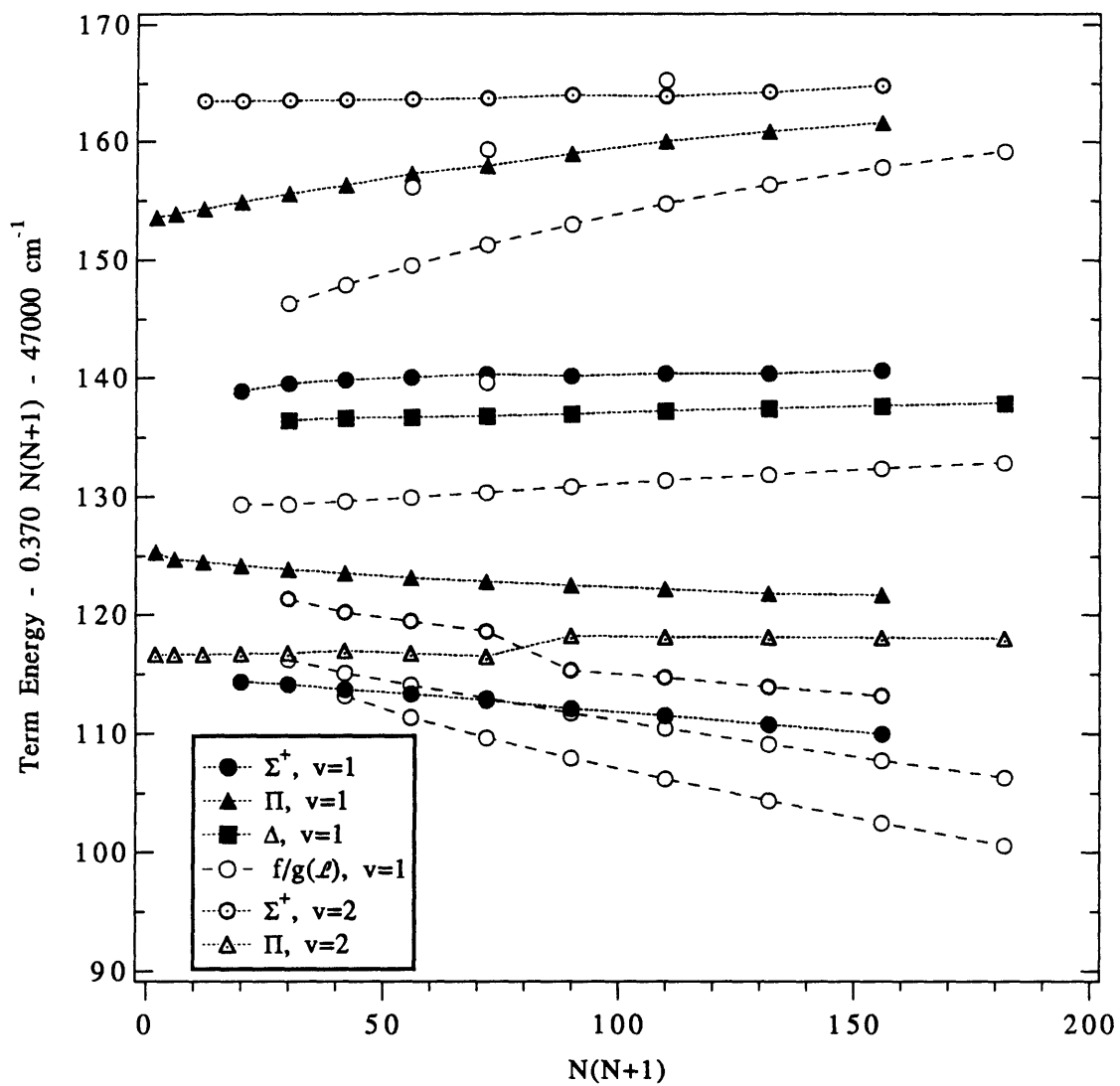


Figure 4.9. Reduced term value plot of positive Kronig symmetry states in the region of  $n^*=14, v=1$ .

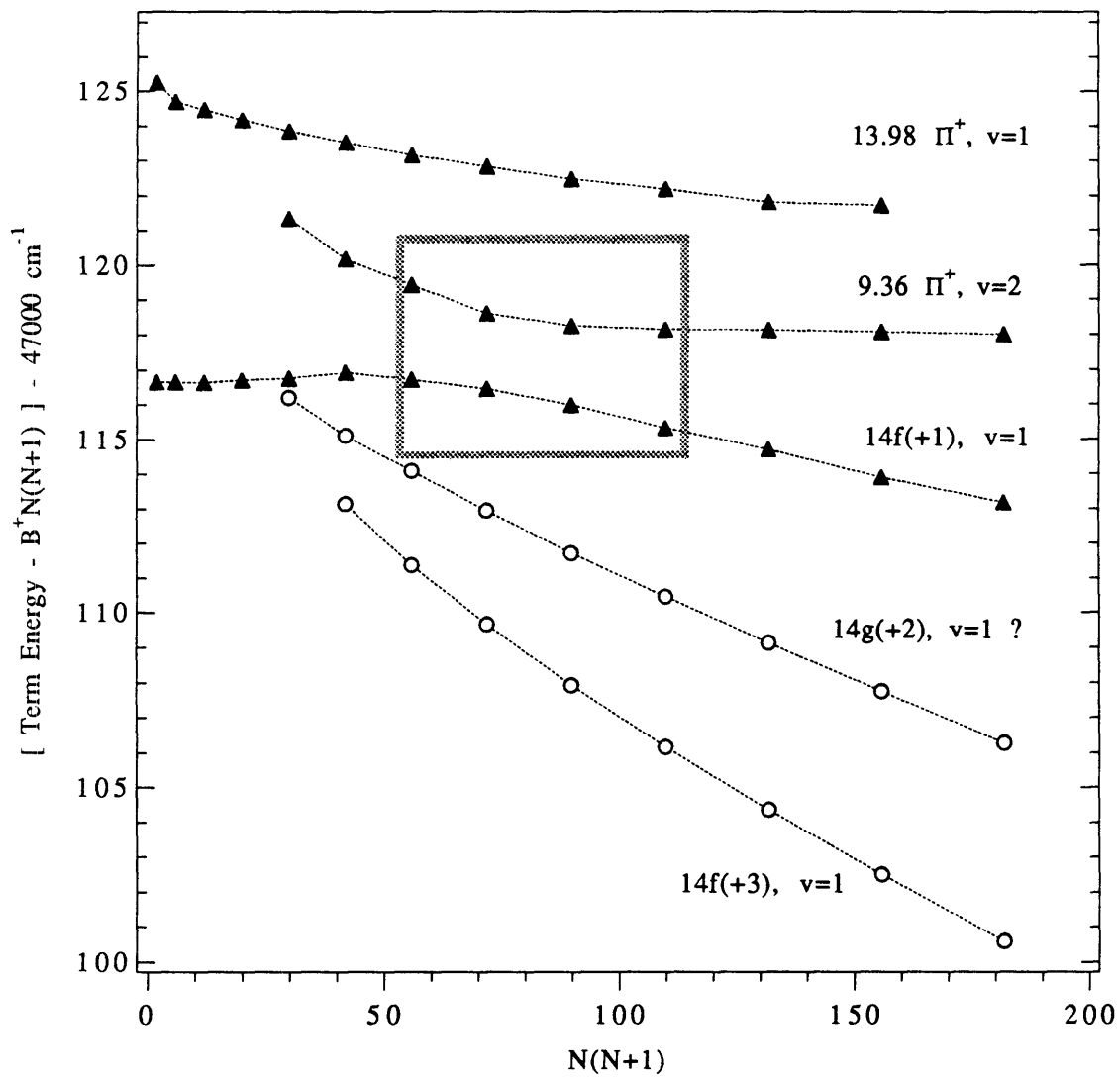


Figure 4.10. Reduced term value plots for states lying just below  $n^*=14.00$ ,  $v=1$ . An avoided crossing between  $9.36 \Pi$ ,  $v=2$  and  $14f(+2)$ ,  $v=1$  is highlighted by the rectangle.

understand the extent to which the f-states,  $\ell = 3$ , are mixed with the core-penetrating, derived from  $\ell \leq 2$ , states. With the exception of an avoided crossing between 14.14  $\Delta$  and 14f(-2) near  $N = 5$ , the negative Kronig-symmetry data was fit extremely well with the p~d effective Hamiltonian. Expanding the p~d effective Hamiltonian to include f states had little effect on the quality or the composition of the resultant eigenstates away from the very local avoided crossing. In going from negative to positive-Kronig symmetry, the effective Hamiltonian must be expanded to include an s,  $\ell = 0$ , basis state. The s~p~d effective Hamiltonian is given by Eq.(4.6). The ten-by-ten s~p~d~f effective Hamiltonian is given by Eq.(4.49). For the sake of clarity the six-by-six s~p~d subblock is not written explicitly and the diagonal contribution of the rotational energy is subtracted out:

$$\begin{aligned}
 & \mathbf{H}^{\text{eff}(+)} - (Bx - Dx^2)\mathbf{I} = \\
 & \left[ \begin{array}{cccccc}
 \bullet & \bullet & \bullet & \bullet & \bullet & \bullet & V_{s-\Sigma^+} & 0 & 0 & 0 \\
 \bullet & & & & & \bullet & V_{p-\Sigma^+} & 0 & 0 & 0 \\
 \bullet & & \text{Eq. (4.6)} & & & \bullet & 0 & V_{p-\Pi} & 0 & 0 \\
 \bullet & & -Bx & +Dx^2 & & \bullet & V_{d-\Sigma^+} & 0 & 0 & 0 \\
 \bullet & & & & & \bullet & 0 & 0 & V_{d-\Pi} & 0 \\
 \bullet & \bullet & \bullet & \bullet & \bullet & \bullet & 0 & 0 & 0 & V_{d-\Gamma_a} \\
 V_{s-\Sigma^+} & V_{p-\Sigma^+} & 0 & V_{d-\Sigma^+} & 0 & 0 & T_{\Sigma^+} + 12B & -\sqrt{24x}B & 0 & 0 \\
 0 & 0 & V_{p-\Pi} & 0 & V_{d-\Pi} & 0 & -\sqrt{24x}B & T_{\Pi} + 10B & -\sqrt{10(x-2)}B & 0 \\
 0 & 0 & 0 & 0 & 0 & V_{d-\Gamma_a} & 0 & -\sqrt{10(x-2)}B & T_{\Gamma_a} + 4B & -\sqrt{6(x-6)}B \\
 0 & 0 & 0 & 0 & 0 & 0 & 0 & 0 & -\sqrt{6(x-6)}B & T_{\Gamma_b} - 6B
 \end{array} \right]
 \end{aligned}
 \tag{4.49}$$

where  $x = N(N+1)$ .

As mentioned in Section 4.1, the intra- $n^*$ -supercomplex separation of states is comparable to the inter- $n^*$ -supercomplex separation (see Fig.4.2). Murphy [10] attempted both effective Hamiltonian and Multi-Channel Quantum Defect Theory modelling of the positive Kronig-symmetry states using s, p, and d basis states. Neither approach was able to model the data to within the accuracy of the measurements. It was hypothesized that f-states, in particular the  $f\Sigma^+$  states were interacting with core-penetrating states. Until this current set of experiments, there had not been a sufficient number of f-states identified so as to include them in the effective Hamiltonian fit.

The variance of the six-by-six, s~p~d effective Hamiltonian fit to core-penetrating positive Kronig-symmetry levels is about two orders of magnitude worse than that of the three-by-three, p~d fit to the negative symmetry data. While the average uncertainty in the



experimentally determined term values is  $0.03 \text{ cm}^{-1}$ , the root mean square of the difference between the observed and calculated values (for the positive symmetry levels) is  $\sim 0.3 \text{ cm}^{-1}$ . Figure 4.11 is a reduced term value plot for the six core penetrating states along with the effective Hamiltonian fit results using the six-by-six matrix of Eq.(4.6). One notices that the  $14.55 \Sigma^+$  levels are not well modelled by the fit. (The levels were deweighted considerably in the fit,  $\delta = 1.0 \text{ cm}^{-1}$ , due to the uncertainty in the measurements of the  $14.55 \Sigma^+$  level positions.) It was found that the variance could be lowered further by increasing the uncertainty in (or removing) the  $14.55 \Sigma^+$  term values and allowing the fitted term values for  $14.55 \Sigma^+$  to be much larger than is physically reasonable.

The variance of the fit using Eq.(4.49) is 4.5 times smaller than that using Eq.(4.6), i.e. the RMS difference in the fitted rotational term values is approximately half that using Eq.(4.6). The RMS difference in the calculated level positions is  $\sim 0.15 \text{ cm}^{-1}$ , while the uncertainty in experimentally determined term values is  $0.03 \text{ cm}^{-1}$ . There is clearly systematic error in the calculated level positions, so it is a bit misleading to state an RMS difference. Nonetheless, the RMS difference is a useful quantity in assessing the relative qualities of the calculations.

Figure 4.12 is a reduced term value plot of the positive Kronig-symmetry data and the s~p~d~f effective Hamiltonian fit results. With the exception of the fit of the  $14.55 \Sigma^+$  levels, the fit appear to be quite similar to that of the s~p~d Hamiltonian. However the fitted molecular constants reveal significant differences between the fits. The six-by-six effective Hamiltonian fit identifies the  $14.55 \Sigma^+$  state as having primarily s-character, the  $14.18 \Sigma^+$  state as having primarily d-character, and the  $13.88 \Sigma^+$  state as having primarily p-character. The calculated atomic  $\ell$ -parentages of the core-penetrating states using the s~p~d model are listed in Table 4.9.

Table 4.9 Calculated Atomic  $\ell$ -parentages Using s~p~d Effective Hamiltonian\*

	s	p	d
14.55 $\Sigma^+$	82	4	14
14.18 $\Sigma^+$	9	7	84
13.88 $\Sigma^+$	9	89	2
14.36 $\Pi$	-	57	43
13.98 $\Pi$	-	43	57
14.14 $\Delta$	-	-	100

\* Percentages are for non-rotating molecule.

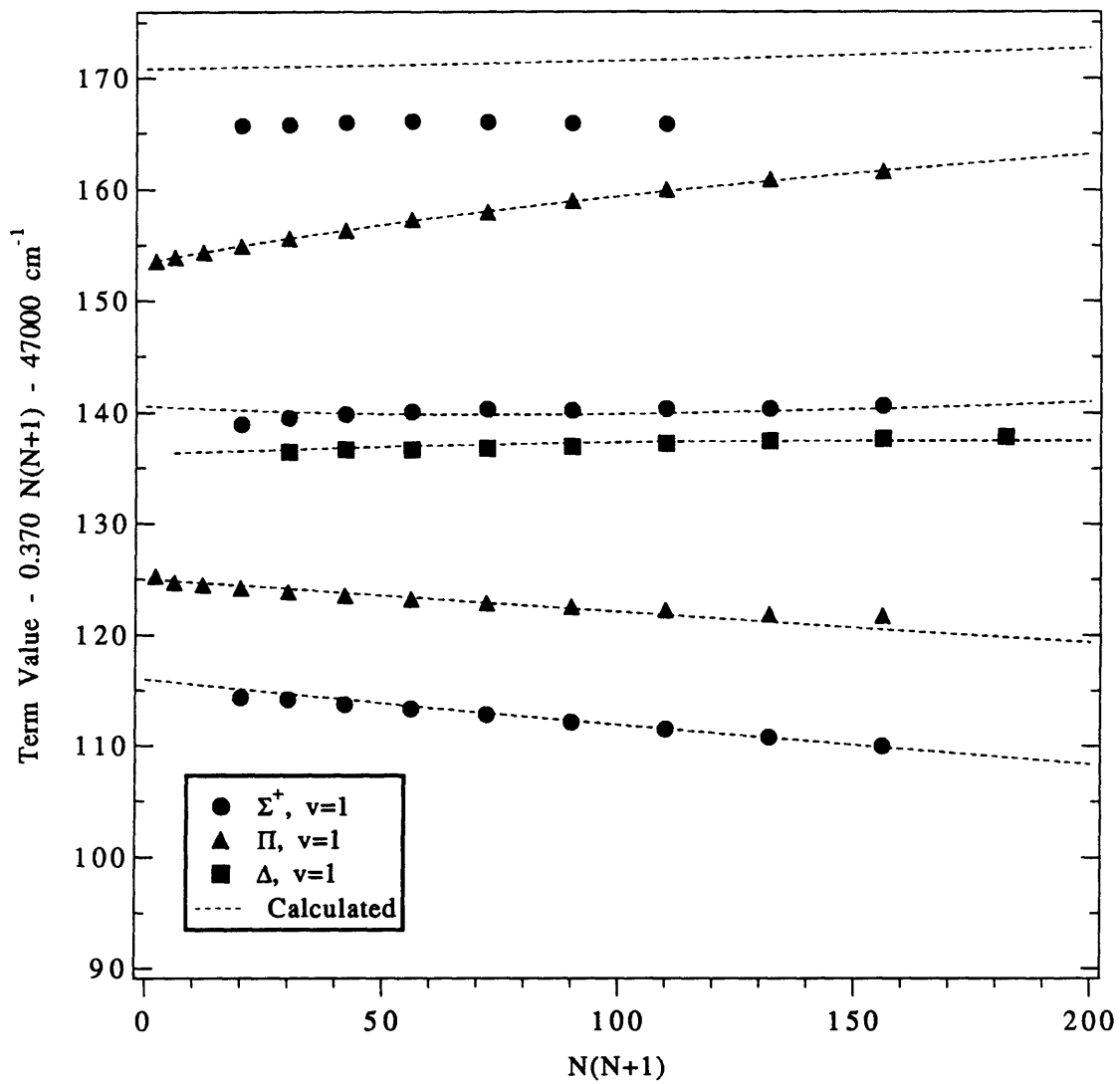


Figure 4.11 Reduced term value plot of positive Kronig-symmetry s~p-d mixed states in the region of n\*=14, v=1.

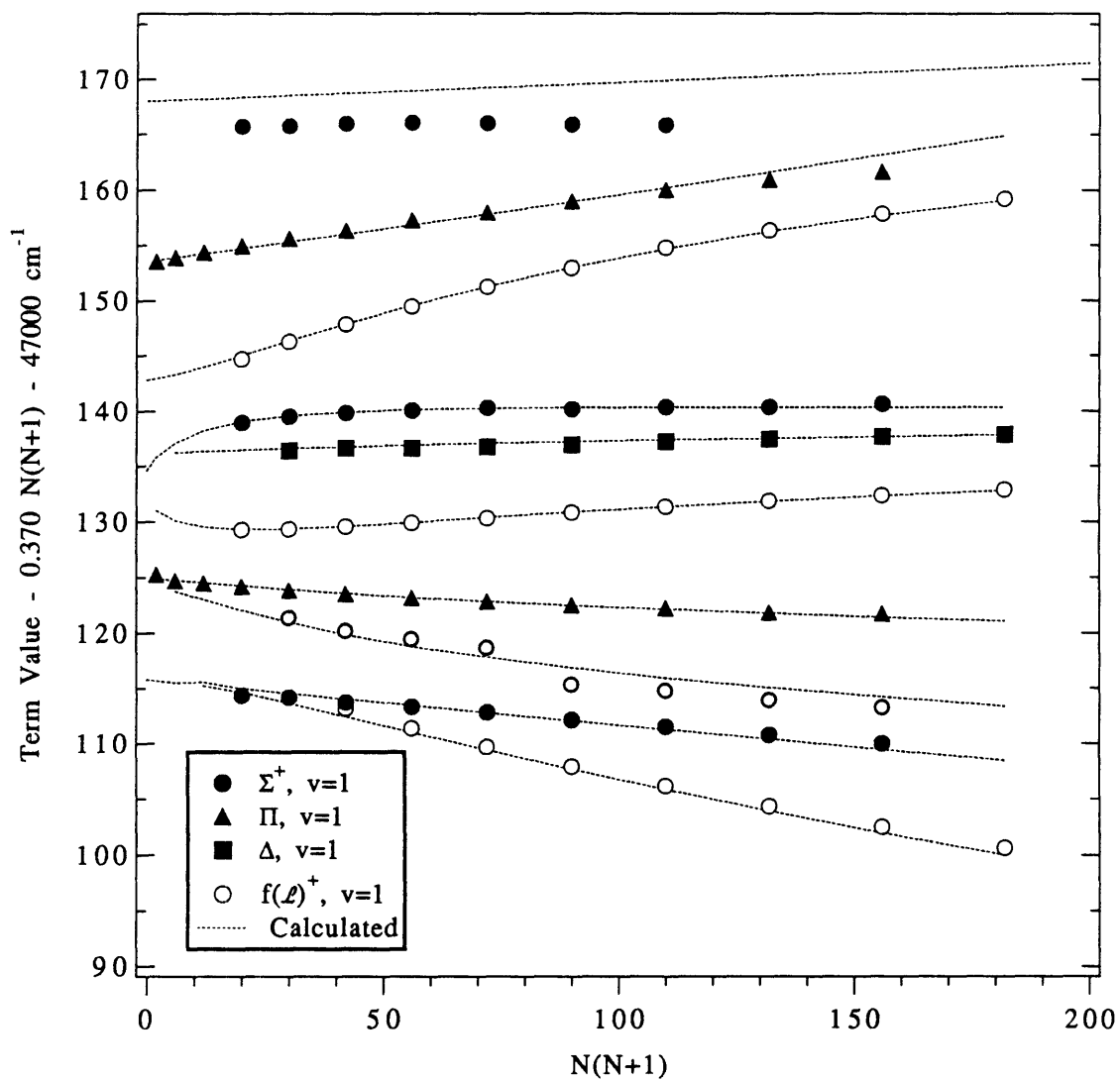


Figure 4.12 Reduced term value plot of positive Kronig-symmetry s-p-d-f mixed states in the region of  $n^*=14$ ,  $v=1$ .

The results of the  $s\sim p\sim d\sim f$  fit differ significantly. Table 4.10 lists the calculated  $l$ -parentages using the  $s\sim p\sim d\sim f$  model.

Table 4.10 Calculated Atomic  $l$ -parentages Using  $s\sim p\sim d\sim f$  Effective Hamiltonian\*

	s	p	d	f
14.55 $\Sigma^+$	8	71	20	<1
14.18 $\Sigma^+$	37	<1	24	37
13.88 $\Sigma^+$	22	27	47	<1
14f $\Sigma^+$	32	<1	8	60
14.36 $\Pi$	-	59	39	2
13.98 $\Pi$	-	40	54	5
14.14 $\Delta$	-	-	93	6

\* Percentages are for non-rotating molecule.

The  $\Pi$  and  $\Delta$  states remain largely unaffected by the inclusion of f-states (as was previously demonstrated by the fit of the negative Kronig-symmetry data to the six-by-six,  $p\sim d\sim f$  effective Hamiltonian), however the  $\Sigma^+$  states are affected dramatically. Figure 4.13 depicts the effect of the off-diagonal  $l$ -mixing matrix elements on the pure- $l$   $\Sigma^+$  basis states. The effective electronic term values of the pure- $l$  basis states are the leftmost horizontal bars in Fig.4.13. The  $s\sim p\sim d$  mixed  $\Sigma^+$  eigenstates are found at the end of the dashed arrows leading from the pure- $l$  basis state locations. For the six-by-six fit, the calculated  $l$ -mixing is weak. The zero-order basis states are only shifted several  $\text{cm}^{-1}$  by the off-diagonal matrix elements.

For the ten-by-ten  $s\sim p\sim d\sim f$  fit, the electrostatic  $l$ -mixing matrix elements are generally larger than the zero-order separations between pure- $l$  basis states, thus the resulting eigenstates are strongly  $l$ -mixed. In particular, the 14.18  $\Sigma^+$  state acquires a large amount of f-character. The effective electronic term values of the s, p, d, and f basis states are the rightmost horizontal bars in Fig.4.13. The  $s\sim p\sim d\sim f$  mixed  $\Sigma^+$  eigenstates are found at the end of the dashed arrows. One notices that while the electronic term values determined from the  $s\sim p\sim d$  and  $s\sim p\sim d\sim f$  fits do not differ greatly, the calculated atomic  $l$ -parentages for the non-rotating molecule (listed in Table 4.9 and 4.10) are drastically different.

As suspected by Murphy [10], the f-states have decidedly little impact on the composition of the  $\Pi$  and  $\Delta$  states. Figure 4.14 is the  $\Pi/\Delta$  analogue of Fig.4.13. In both the six-by-six and ten-by-ten fits the off-diagonal  $p\pi\sim d\pi$  matrix element is large relative to

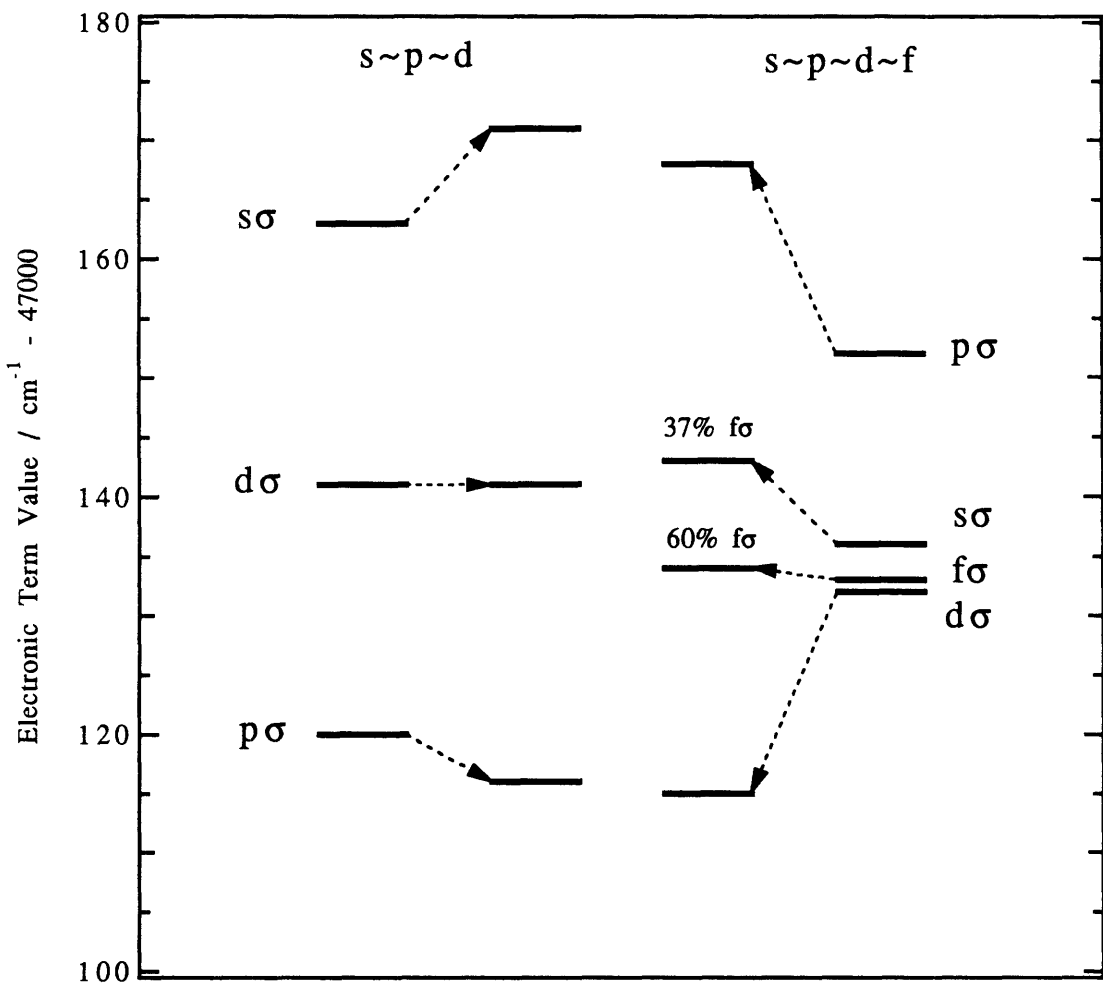


Figure 4.13 Calculated electronic term values of  $\Sigma^+$  states using s~p~d and s~p~d~f effective Hamiltonians.

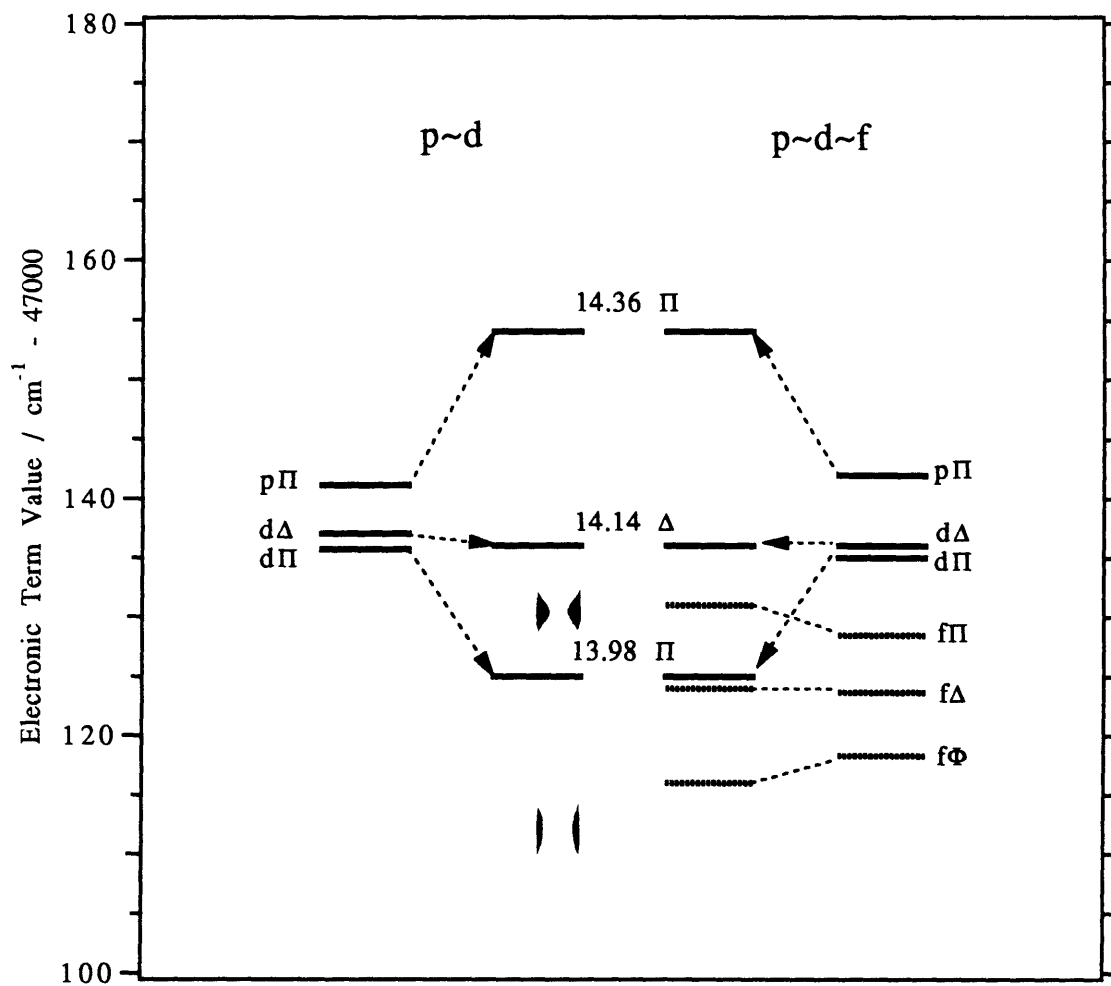


Figure 4.14. Calculated electronic term values of  $\Pi$  and  $\Delta$  states using  $s\sim p\sim d$  and  $s\sim p\sim d\sim f$  effective Hamiltonians.

the separation of the rotationless term values. In both cases it is calculated to be  $\sim 14 \text{ cm}^{-1}$ . The 14.36  $\Pi$  state has 55-60% p-character in both fits, and the 13.98  $\Pi$  state has 55-60% d-character. This is consistent with the fit of the negative Kronig-symmetry data alone (as discussed in Section 4.4).

It is worth noting that while the negative Kronig-symmetry levels could be fit in isolation, the positive Kronig-symmetry levels had to be fit simultaneously with the negative symmetry levels and negative Kronig-symmetry. If this was not done, the non-linear least squares fitting routine would artificially reduce the variance of the fit by converting the 14.36  $\Pi$  state to a  $\Sigma^+$  state. (As the number of states of a given  $\Lambda$  is conserved, the 14.18  $\Sigma^+$  state was consequently assigned as a  $\Pi$  state.) The variance of the fit to the positive Kronig-symmetry levels only drops from 18 to 12 with the 14.36  $\Pi$  state as (primarily)  $d\Sigma^+$  instead of  $d\Pi$ . If one then uses the constants determined with the 14.36  $\Pi$  state assigned incorrectly to simulate the negative symmetry levels, the variance of the fit soars to over 5000. The best fit constants for the  $s\sim p\sim d$  and  $s\sim p\sim d\sim f$  effective Hamiltonian fits are listed in Table 4.11.

The essential points of the fit results are that the core-penetrating  $\Pi$  and  $\Delta$  states are relatively unaffected by the presence of f-states (they have at most a few percent f-character), but  $\Sigma^+$  states seem to be strongly affected. The  $\ell\Sigma^+ \sim \ell'\Sigma^+$  electrostatic matrix elements are, in general, much larger than the corresponding  $\ell\Pi \sim \ell'\Pi$  and  $\ell\Delta \sim \ell'\Delta$  matrix elements. This makes qualitative sense, as the  $\sigma$  orbitals (which give rise to  $\Sigma^+$  states) are oriented along the axis of the  $\text{CaF}^+$  ion-core. Orbitals oriented along the molecular axis should experience the ion-core multipole moments most strongly and therefore be more prone to core-multipole induced mixing. Although the  $s\sim p\sim d\sim f$  positive Kronig symmetry effective Hamiltonian is not able to fit the data perfectly, it represents a significant improvement over the  $s\sim p\sim d$  effective Hamiltonian fit. The likely explanation for the observed discrepancies between the  $s\sim p\sim d\sim f$  fit and the data is the separation between intra- $n^*$  separation between  $\Sigma^+$  states is comparable to that the separation between the highest energy  $\Sigma^+$  state of that  $n^*$  complex,  $n.55 \Sigma^+$ , and the lowest energy  $\Sigma^+$  state of the  $(n^*+1)$  supercomplex,  $n.88 \Sigma^+$ .

Table 4.11 Best Fit Molecular Constants: Positive Kronig Symmetry Data

Parameter	s~p~d Value/cm <sup>-1</sup>	s~p~d~f Value/cm <sup>-1</sup>
T(sΣ <sup>+</sup> )	47164(6)	47136(2)
T(pΣ <sup>+</sup> )	47119(2)	47152(4)
T(pΠ)	47141(1)	47142.0(7)
T(dΣ <sup>+</sup> )	47141(2)	47132(3)
T(dΠ)	47136(1)	47135.0(6)
T(dΔ)	47137.0(2)	47136.2(2)
T(fΣ <sup>+</sup> )	-	47132.8(6)
T(fΠ)	-	47128.5(3)
T(fΔ)	-	47123.7(3)
T(fΦ)	-	47118.3(3)
B	[0.37042]*	[0.37042]
D	[4.4·10 <sup>-7</sup> ]	[4.4·10 <sup>-7</sup> ]
V(pΠ~dΠ)	14.1(2)	13.7(2)
V(sΣ <sup>+</sup> ~pΣ <sup>+</sup> )	-13(3)	13(2)
V(pΣ <sup>+</sup> ~dΣ <sup>+</sup> )	11(3)	4(2)
V(sΣ <sup>+</sup> ~dΣ <sup>+</sup> )	1.5(6)	-19(3)
V(sΣ <sup>+</sup> ~fΣ <sup>+</sup> )	-	-1.6(8)
V(pΣ <sup>+</sup> ~fΣ <sup>+</sup> )	-	-1(3)
V(dΣ <sup>+</sup> ~fΣ <sup>+</sup> )	-	-5(2)
V(pΠ~fΠ)	-	-2.8(5)
V(dΠ~fΠ)	-	-0.3(3)
V(dΔ~fΔ)	-	-2.7(3)

\* Parameters in brackets were held fixed during the fit.

#### 4.6. Analysis and Discussion of 14f and 14g (Core-non-penetrating) states

In 1969, Jungen and Miescher [16] used their observation of the splittings of the  $\Lambda$  components ( $\Sigma^+$ ,  $\Pi$ ,  $\Delta$ ,  $\Phi$ ) of the 4f and 5f Rydberg states of NO to infer the quadrupole



moment of  $\text{NO}^+$ . (The Rydberg states of  $\text{NO}$  are analogous to those of  $\text{CaF}$  in that the ground electronic states of the  $\text{NO}^+$  and  $\text{CaF}^+$  cations are  $^1\Sigma^+$ . Neither cation has a non-zero electron orbital or spin angular momenta to couple to the Rydberg electron.) Jungen and Miescher's determination of the electric quadrupole moment was based on the assumption that the energy of interaction between the core-non-penetrating Rydberg electron and the cation could be calculated as a first-order correction to hydrogenic energy levels:

$$E_{n\ell\Lambda} = E_{n\ell}^{(0)} + E_{n\ell\Lambda}^{(1)}, \quad (4.50)$$

where the zero-order energy of the  $n\ell$  state is determined by the Rydberg formula:

$$E_{n\ell}^{(0)} = \text{IP} - \frac{\mathfrak{R}}{n^2}. \quad (4.51)$$

Their perturbation Hamiltonian was simply the difference between the  $\text{H}^+$  and  $\text{NO}^+$  potentials, i.e. an electric quadrupole potential:

$$H^{(1)} = V_{\text{NO}^+}(r, \theta) - V_{\text{H}^+}(r, \theta) = Q_{zz}^+ \left[ \frac{3\cos^2\theta - 1}{2r^3} \right], \quad (4.52)$$

where  $Q_{zz}^+$  is the electric quadrupole moment of  $\text{NO}^+$  along the molecular axis, and  $\theta$  is the angle between the Rydberg electron and the molecular axis. The first-order energy correction to the hydrogenic energy is:

$$\langle n\ell\Lambda | H^{(1)} | n\ell\Lambda \rangle = - Q_{zz}^+ \left\langle \frac{1}{r^3} \right\rangle_{n\ell} \frac{\ell(\ell+1) - 3\Lambda^2}{(2\ell+1)(2\ell+3)}. \quad (4.53)$$

When the expectation value of  $r^{-3}$  may be expressed in terms of hydrogenic quantum numbers  $n$  and  $\ell$  [17], Eq.(4.53) becomes, in atomic units,

$$\langle n\ell\Lambda | H^{(1)} | n\ell\Lambda \rangle = - Q_{zz}^+ \frac{2[\ell(\ell+1) - 3\Lambda^2]}{n^3(2\ell+1)(2\ell+3)(2\ell-1)\ell(\ell+1)}, \quad (4.54)$$

where  $\ell \neq 0$ . This simple analytic expression turned out to describe the splitting pattern of the  $\Lambda$  components of the 4f and 5f states quite accurately. Jungen and Miescher obtained an  $\text{NO}^+$  quadrupole moment of  $+0.59 \pm 0.04$  a.u. using this method. Recent ab initio

calculations predict the quadrupole moment to be +0.4833 a.u. [18]. Eyler and Pipkin [19] used a similar, but more mathematically involved approach in their analysis of the triplet 4d states of H<sub>2</sub>. (Eyler and Pipkin determined the polarizability and electric quadrupole moments of the lowest vibrational and rotational levels of H<sub>2</sub><sup>+</sup>. A more fully developed version of that model was later published by Sturru *et al.* [20])

The generalized Rydberg formula is:

$$E_{n\ell\Lambda} = \text{IP} - \frac{1}{2(n - \delta_{\ell\Lambda})^2}, \quad (4.55)$$

where  $\delta_{\ell\Lambda}$  is the quantum defect of the  $\ell\Lambda$  Rydberg series and the energy is in atomic units. Equation (4.54) may be expanded as a Taylor series when  $\delta_{\ell\Lambda} \ll n$ ,

$$E_{n\ell\Lambda} = \text{IP} - \frac{1}{2n^2} \left[ 1 + \frac{2\delta_{\ell\Lambda}}{n} + \dots \right]. \quad (4.56)$$

Equations (4.50), (4.54), and (4.56) may be combined to relate the electric quadrupole moment to the quantum defects of the  $\ell\Lambda$  series:

$$E_{n\ell\Lambda} = \text{IP} - \frac{1}{2n^2} - \frac{1}{n^3} \frac{2Q_{zz}^+ [\ell(\ell+1) - 3\Lambda^2]}{(2\ell+1)(2\ell+3)(2\ell-1)\ell(\ell+1)}, \quad (4.57)$$

which, by analogy to Eq.(4.55), leads to:

$$\delta_{\ell\Lambda} = Q_{zz}^+ \frac{2[\ell(\ell+1) - 3\Lambda^2]}{(2\ell+1)(2\ell+3)(2\ell-1)\ell(\ell+1)}. \quad (4.58)$$

The quantum defects of the  $f\Lambda$  Rydberg series in NO are O(0.001). For comparison, the quantum defects of the core-penetrating series in CaF are O(0.1-1) and the quantum defect for the s series in Na is ~1.38.

The observation of the  $\ell\Lambda$ -components of core-non-penetrating states and the determination of quantum defects is an appealingly simple way to determine the quadrupole moment of a molecular cation. It would be desirable to extend this approach to determine the dipole moment of a molecular cation. Ideally, one would calculate a first-order perturbation Hamiltonian analogous to Eq.(4.52):

$$H^{(1)} = V_{MX^+}(r, \theta) - V_{H^+}(r, \theta) = \mu^+ \frac{\cos\theta}{r^2}, \quad (4.59)$$

where  $\mu^+$  is the dipole moment of the cation. (There would also be an electric quadrupole term as in Eq.(4.52), but for this example the quadrupole contribution will be assumed to be a much smaller term than the dipole correction.) Unfortunately, the angular portion of the dipole matrix element,  $\langle n\ell\Lambda | \mu^+ \cdot \cos\theta \cdot r^{-2} | n\ell'\Lambda \rangle$ , between hydrogenic wavefunctions is zero unless  $\ell = \ell' \pm 1$  and the radial portion is zero unless  $\ell = \ell'$  [21]. Until recently, this fact frustrated the derivation of a simple, analytic expression for the splitting of the  $\Lambda$  components of high- $\ell$ , core-non-penetrating states by the core dipole. Using Dalgarno-Lewis perturbation theory [22], Watson has derived the second-order correction to the energy levels of a hydrogen atom with a dipolar nucleus [23]. Watson's approach was to introduce a first-order correction to the hydrogenic wavefunction:

$$\Psi_{n\ell\Lambda} \equiv \Psi_{n\ell\Lambda}^{(0)} + \Psi_{n\ell\Lambda}^{(1)}, \quad (4.60)$$

where,

$$\Psi_{n\ell\Lambda}^{(1)} \equiv R_{n\ell'}(r) Y_{\ell'\Lambda}(\theta, \phi) + R_{n\ell}(r) \sum_{\ell'=\ell\pm 1} C_{\ell'\ell\Lambda} Y_{\ell'\Lambda}(\theta, \phi). \quad (4.61)$$

This first-order correction to the wavefunction leaves the hydrogenic radial wavefunctions unchanged, but mixes states with  $\ell' = \ell \pm 1$  into the angular wavefunction. The second-order energy correction due to the electric dipole moment has a form identical to the first-order quadrupole correction given by Eq.(4.54):

$$E_{n\ell\Lambda}^{(2)}(\text{dipole}) = (\mu^+)^2 \frac{2[\ell(\ell+1) - 3\Lambda^2]}{n^3(2\ell+1)(2\ell+3)(2\ell-1)\ell(\ell+1)} \text{ a.u.} \quad (4.62)$$

The electric dipole and quadrupole moments in the preceding equations are treated as point multipoles located at the center-of-symmetry for the spherically symmetric system. It is implicitly assumed that, when applying the Watson model to a real molecule, the multipole moments may be calculated relative to the center-of-mass and that the center-of-mass may in turn be treated as the center-of-symmetry in which to evaluate integrals. By transforming the coordinate system in which the multipole moments are calculated from the center-of-mass to the center-of-charge, the dipole moment vanishes. The energy levels of the molecule are invariant to the coordinate system in which they are calculated. In his

derivation, Watson demonstrated that the quantity  $\mu^2 - Q$  in the center-of-mass system is equal to the quantity  $Q$  in the center-of-charge system. It is appropriate that his calculated second-order dipole correction has the same form as the first-order quadrupole correction determined by Jungen and Miescher.

The dipole and quadrupole moments of  $\text{CaF}^+$  may be estimated by assuming that the molecular cation consists of two point charges separated by the equilibrium internuclear separation in the cation. These estimated values may in turn be used to predict the term values of  $n\ell\Lambda$  states. Conversely, the  $n\ell\Lambda$  term values determined from the analysis of ID-OODR spectra may be used calculate the dipole and quadrupole moments of  $\text{CaF}^+$ . According to Watson's perturbation theory treatment, the electronic term values of core-non-penetrating Rydberg states are determined by the following expression:

$$E_{n\ell\Lambda} = T_{n\ell}^0 + (\mu^2 - Q) \frac{2[\ell(\ell+1) - 3\Lambda^2]}{n^3(2\ell+1)(2\ell+3)(2\ell-1)\ell(\ell+1)}, \quad (4.63)$$

where all quantities are in atomic units.

The prediction of Eq.(4.63) will cease to be accurate for dipoles which induce too large a mixing between  $\ell$  and  $\ell \pm 1$  and the first order correction to the wavefunction becomes too large. Examining Watson's derivation, a reasonable criterion for the use of Eq.(4.63) is  $2\mu^2[(2\ell-1)(2\ell+3)]^{-1} \ll 1$ , where  $\ell \neq 0$ . The dipole perturbed Hamiltonian for hydrogen atom is separable in spherical polar coordinates. Watson's compared numerical eigenvalues of the Hamiltonian with his perturbation treatment result and showed that as the perturbation model breaks down, the  $\Lambda$  components of the  $n\ell$  complex become more equally spaced.

For the purpose of predicting the splittings of the  $\Lambda$  sub-levels of the  $n\ell$  core non-penetrating states, the multipole moments of the ion-core are calculated relative to the center-of-mass:

$$m^+x_{\text{cm}} = m^-(R - x_{\text{cm}}), \quad (4.63)$$

$$x_{\text{cm}} = \frac{m^-}{m^- + m^+} R, \quad (4.64)$$

where  $x_{\text{cm}}$  is the center-of-mass along the molecular axis,  $m^-$  is the atomic mass of fluorine,  $m^+$  is the atomic mass of calcium, and  $R$  is their separation. The dipole moment is,

$$\mu \equiv q^+[0 - x_{\text{cm}}] + q^-[R - x_{\text{cm}}], \quad (4.65)$$

$$= -q^+ \frac{m^-}{m^- + m^+} R + q^- \left[ 1 - \frac{m^-}{m^- + m^+} \right] R \quad (4.66)$$

$$\mu = [q^- m^+ - q^+ m^-] \left[ \frac{1}{M} \right] R, \quad (4.67)$$

where  $M$  is the mass of  $\text{CaF}^+$ ;  $q^-$  and  $q^+$  are the charges of the ions. The effective charge of the fluorine may be expressed as the difference between the net charge of the cation and the effective charge of the calcium ion,  $q^- = 1 - q^+$ . Equation (4.67) may be reduced to a function of  $q^+$  and the internuclear separation:

$$\mu = \left[ \frac{m^+}{M} - q^+ \right] R. \quad (4.68)$$

At the equilibrium internuclear separation of  $\text{CaF}^+$ , the calculated dipole moment of the +2 / -1 ion-pair is:

$$\mu = \left[ \frac{40}{59} - 2 \right] \cdot 3.54 = -4.68 \text{ a.u.} = -11.9 \text{ Debye}. \quad (4.69)$$

The sign of the dipole moment simply indicates that the dipole points towards  $\text{Ca}^{2+}$ . For the sake of comparison, the electric dipole moment of  $\text{NaCl}$  is -9.00 Debye,  $\mu(\text{HCl}) = -1.08$  Debye, and  $\mu(\text{CO}) = 0.112$  Debye [24].

The calculation of the quadrupole moment,  $Q$ , using the point charge model is straightforward,

$$Q = q^+ [0 - x_{\text{cm}}]^2 + q^- [R - x_{\text{cm}}]^2, \quad (4.70)$$

with the substitution  $q^- = 1 - q^+$ ,

$$Q = \left\{ \left[ \frac{m^+}{M} \right]^2 + \left[ \frac{(m^-)^2 - (m^+)^2}{M^2} \right]^2 q^+ \right\} R^2. \quad (4.71)$$

The quadrupole moment of a +2/-1 cation at the equilibrium internuclear separation of  $\text{CaF}^+$  is -3.16 a.u.

It is useful to express the quantity  $\mu^2 - Q$  in terms of the nominal net charge of the calcium ion,  $q^+$ , and the equilibrium internuclear separation of the cation,  $R_e^+$ . A little algebra reveals:

$$\mu^2 - Q = q^+(q^+ - 1)(R_e^+)^2 \text{ a.u.} \quad (4.72)$$

For a +2/-1 cation,  $\mu^2 - Q = 25.1$  a.u., but for a +1.5/-0.5 cation,  $\mu^2 - Q = 9.4$  a.u. Equation (4.63) predicts that the term values of the 14f complex will be:

$$T_{14f\Lambda} = T_{14f}^0 + 0.04232 \cdot (\mu^2 - Q) \cdot (12 - 3\Lambda^2), \quad (4.73)$$

where E is in  $\text{cm}^{-1}$  and  $\mu^2 - Q$  is in a.u. The splitting between the  $f\Sigma^+$  and  $f\Pi$  components of the complex would be  $2 \text{ cm}^{-1}$  for  $\mu^2 - Q = 15$  a.u. Splittings of this magnitude are easily observable in the ID-OODR spectra. The remainder of this section compares the experimental observations of 14f states with the predictions of Eq.(4.73).

The effective Hamiltonian for the positive Kronig symmetry f states is determined from Eq.(3.67), (3.68), and (4.69). For the sake of clarity,  $H_f^{\text{eff}}(+)$  - [  $BN(N+1) - DN^2(N+1)^2$  ] I, not the full the effective Hamiltonian matrix, is written here:

$$H_f^{\text{eff}}(+)$$
 - [  $BN(N+1) - DN^2(N+1)^2$  ] I =
$$\begin{bmatrix} T_{f\Sigma^+} + 12B & -\sqrt{24x}B & 0 & 0 \\ -\sqrt{24x}B & T_{f\Pi} + 10B & -\sqrt{10(x-2)}B & 0 \\ 0 & -\sqrt{10(x-2)}B & T_{f\Delta} + 4B & -\sqrt{6(x-6)}B \\ 0 & 0 & -\sqrt{6(x-6)}B & T_{f\Phi} - 6B \end{bmatrix}, \quad (4.74)$$

where  $x=N(N+1)$  and I is the identity matrix. The effective Hamiltonian for negative Kronig symmetry states is identical to the lower right three-by-three subblock of  $H_f^{\text{eff}}(+)$ :

$$H_f^{\text{eff}}(-)$$
 - [  $BN(N+1) - DN^2(N+1)^2$  ] I =
$$\begin{bmatrix} T_{f\Pi} + 10B & -\sqrt{10(x-2)}B & 0 \\ -\sqrt{10(x-2)}B & T_{f\Delta} + 4B & -\sqrt{6(x-6)}B \\ 0 & -\sqrt{6(x-6)}B & T_{f\Phi} - 6B \end{bmatrix}. \quad (4.75)$$

The negative symmetry effective Hamiltonian fit results from earlier in this chapter indicate that, with the exception of the levels nearest the 14.14  $\Delta \sim 14f(-2)$  avoided

crossing, 14f states possess, on average, only 3-5% core-penetrating character. This fraction is significantly smaller than that obtained using the direct perturbation model from Ref.[23]. According to Ref.[23], the first-order corrected wavefunction is:

$$|n, \ell, \lambda\rangle = |n, \ell, \lambda\rangle - \frac{\mu}{\ell} \sqrt{\frac{\ell^2 - \lambda^2}{(2\ell - 1)(2\ell + 1)}} |n, \ell - 1, \lambda\rangle + \frac{\mu}{\ell + 1} \sqrt{\frac{(\ell + 1)^2 - \lambda^2}{(2\ell + 1)(2\ell + 3)}} |n, \ell + 1, \lambda\rangle \quad (4.76)$$

The  $\text{CaF}^+$  core dipole calculated assuming the cation to consist of +2 and -1 point charges separated at  $R_e^+$  is -4.68 a.u. or -11.9 Debye. Equation (4.76) becomes,

$$|14' f \sigma\rangle \approx |14f\sigma\rangle - 0.79|14d\sigma\rangle + 0.59|14g\sigma\rangle, \quad (4.77)$$

$$|14' f \pi\rangle \approx |14f\pi\rangle - 0.75|14d\pi\rangle + 0.57|14g\pi\rangle, \quad (4.78)$$

$$|14' f \delta\rangle \approx |14f\delta\rangle - 0.59|14d\delta\rangle + 0.51|14g\delta\rangle, \quad (4.79)$$

$$|14' f \phi\rangle = |14f\phi\rangle + 0.39|14g\phi\rangle. \quad (4.80)$$

The first-order correction terms are quite large relative to the zero-order wavefunction. (In fact, for a dipole moment of -4.68 a.u., f states do not meet the criterion,  $2\mu^2[(2\ell - 1)(2\ell + 3)]^{-1} \ll 1$ .) The mixing coefficients in Eqs.(4.76-79) may be 'normalized' by dividing by the square root of the sum of the squares of the coefficients. Using this method, one finds that for a dipole moment of 11.9 Debye, the nominally 14f states have only 50% to 85% f-character. If the  $\text{CaF}^+$  dipole moment were half that predicted by the point charge model, the mixing coefficients would drop by a factor of two, and the fractional f-character, proportional to the mixing coefficients squared, would rise to 80% to 95%.

It is of interest to know applicable the ion-core dipole perturbation treatment is to the f states of  $\text{CaF}$ . The effective Hamiltonian fits to the positive Kronig-symmetry data in the previous section implied that 14f $\Sigma^+$  character was mixed into the 14.18  $\Sigma^+$  state. With the exception of this local perturbation, f $\Sigma^+$  character did not appear to be spread through the  $\Sigma^+$  states. Similarly, the effective Hamiltonian fits suggest that there is very little f-character in the  $\Pi$  and  $\Delta$  states. Because only a single member of the f-complex, f $\Sigma^+$ , interacts strongly with core-penetrating states, it is tempting to fit the f-state data in isolation using the effective Hamiltonian matrices in Eqs.(4.73) and (4.74). This approach is made even more appealing by the fact that with increasing rotational quantum number, the fractional f $\Sigma^+$  character in the 14.18  $\Sigma^+$  state decreases. This is principally due to rotational  $\ell$ -uncoupling, the  $-BN \cdot \ell$  term in  $H^{\text{rot}}$ , in the f-states. As N increases, the rotational levels

in the  $14f\Sigma^+$  state go from a Hund's case(b) to Hund's case(d) level pattern, where the  $14f\Lambda$  label is replaced by  $14f(\mathcal{L})$ . The  $14f\Sigma^+$  state becomes the  $14f(-3)$  state, whose leading  $\Lambda$  character is  $\Pi$ , not  $\Sigma^+$ . By  $N = 5$ , the off-diagonal  $f\Sigma^+ \sim f\Pi$  matrix element in Eq.(4.73) is considerably larger the electrostatic matrix elements which mixed the  $14f\Sigma^+$  state with core-penetrating  $\Sigma^+$  states.

Because the electrostatic matrix elements between the f and core-penetrating states are smaller than  $\ell$ -uncoupling matrix elements for all but the lowest values of N, it is reasonable to fit the f-state data alone to the effective Hamiltonians in Eqs.(4.63) and (4.64), but with the low N data deweighted in the fit. It is not expected that the fit to the data will be nearly as good as for the full positive and negative Kronig-symmetry Hamiltonians, but the fit will determine a  $\mu^2 - Q$  parameter which may be compared to the value calculated for a  $\text{CaF}^+$  cation. The value of the rotational constant, B, was held constant in the fits. The rotational constant was previously determined quite accurately in the six-by-six,  $p \sim d \sim f$  effective Hamiltonian fits and was found to be in excellent agreement with Murphy's prediction [10].

A reduced term value plot of the positive Kronig-symmetry f state data, along with best effective Hamiltonian fit to the data, is shown in Fig.4.14. Figure 4.15 is a reduced term value plot for the negative Kronig-symmetry data. The value of  $\mu^2 - Q$  which best fits the data is  $11.2 \pm 1.2$  a.u. (The uncertainty is  $2\sigma$ .) In addition to the 14f states, several isolated 14g levels were also observed. These 14g levels were not included in the effective Hamiltonian fit, but the molecular constants determined from the fit to the f state data were used to predict the location of the g states. The predicted positions of 14g levels are included in Figures 4.14 and 4.15. The 14g levels will be discussed shortly.

The effective Hamiltonian in Eq.(4.63) predicts more severe  $\ell$ -uncoupling in the  $14f(-3)$  state than is observed. The  $14f(-3)$  levels appear to be pushed down by a state at higher energy. The explanation is that the  $14f(-3)$  state interacts with  $14.36 \Pi$  state, whose vibronic term value is  $\sim 47156 \text{ cm}^{-1}$ . The six-by-six,  $p \sim d \sim f$  effective Hamiltonian fit to the negative Kronig-symmetry data, which accounted for that data very accurately, yielded a  $14.36 \Pi \sim 14f\Pi$  electrostatic matrix element of  $3 \text{ cm}^{-1}$ . The interaction appears strongest at high N because the anomalously large effective rotational constant of the  $14f(-3)$  state causes the zero-order energies of the  $14f(-3)$  and  $14.36 \Pi$  to be quite nearly equal near  $N \sim 10$ .

The second anomaly of note on Fig. 4.14 is the effect of the avoided crossing of the  $14f(+1)$ ,  $v=1$  state with  $9.36 \Pi$ ,  $v=2$  states. (This is avoided crossing highlighted in Fig.4.10.) The crossing occurs between  $N = 8$  and  $N = 9$ . The avoided crossing appears as a discontinuity in the  $14f(+1)$  reduced term values because Fig. 4.14 includes only the



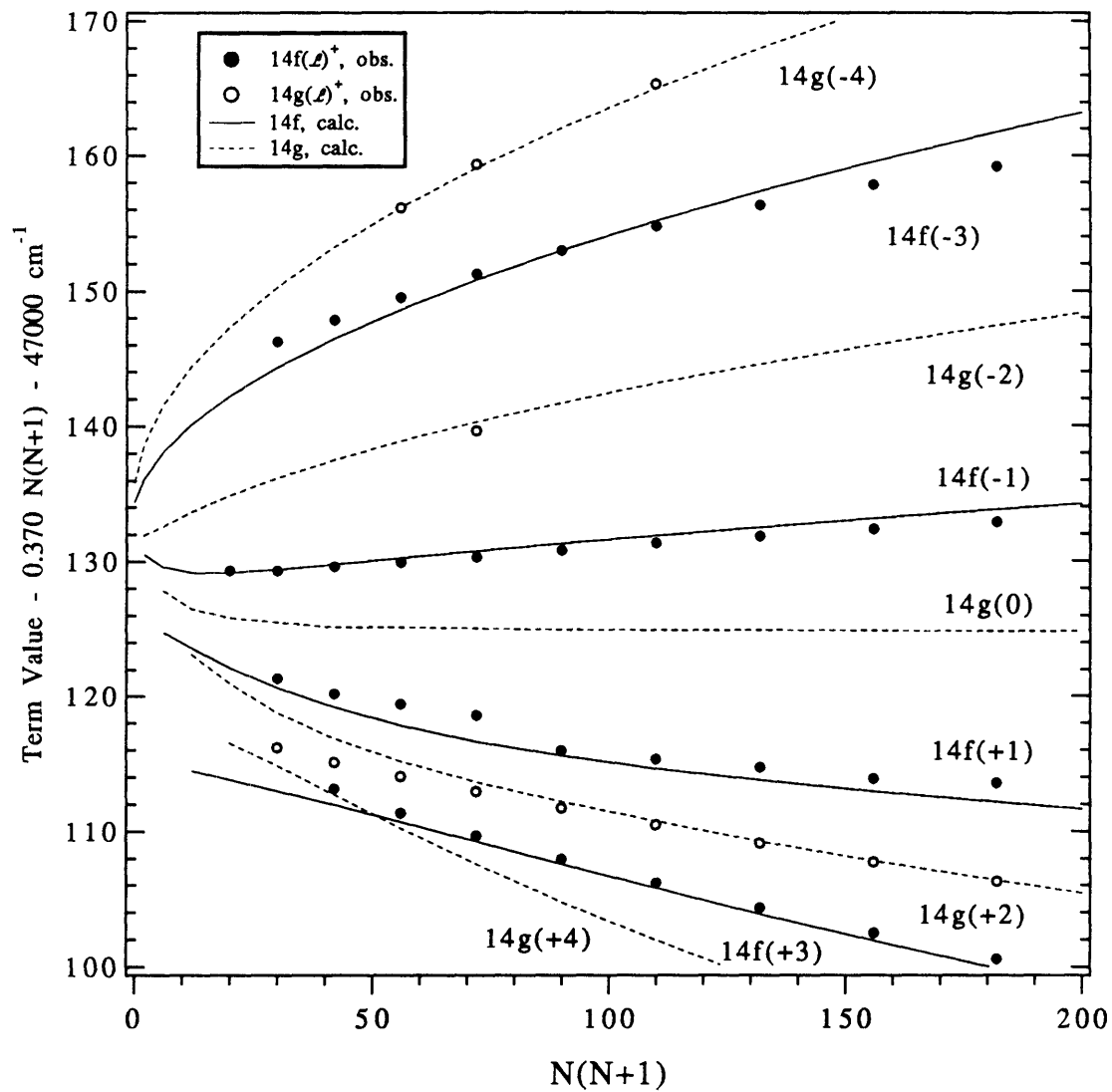


Figure 4.14. Positive symmetry 14f and 14g states. Calculated reduced term values for  $\mu^2 - Q = 11.2$  a.u.

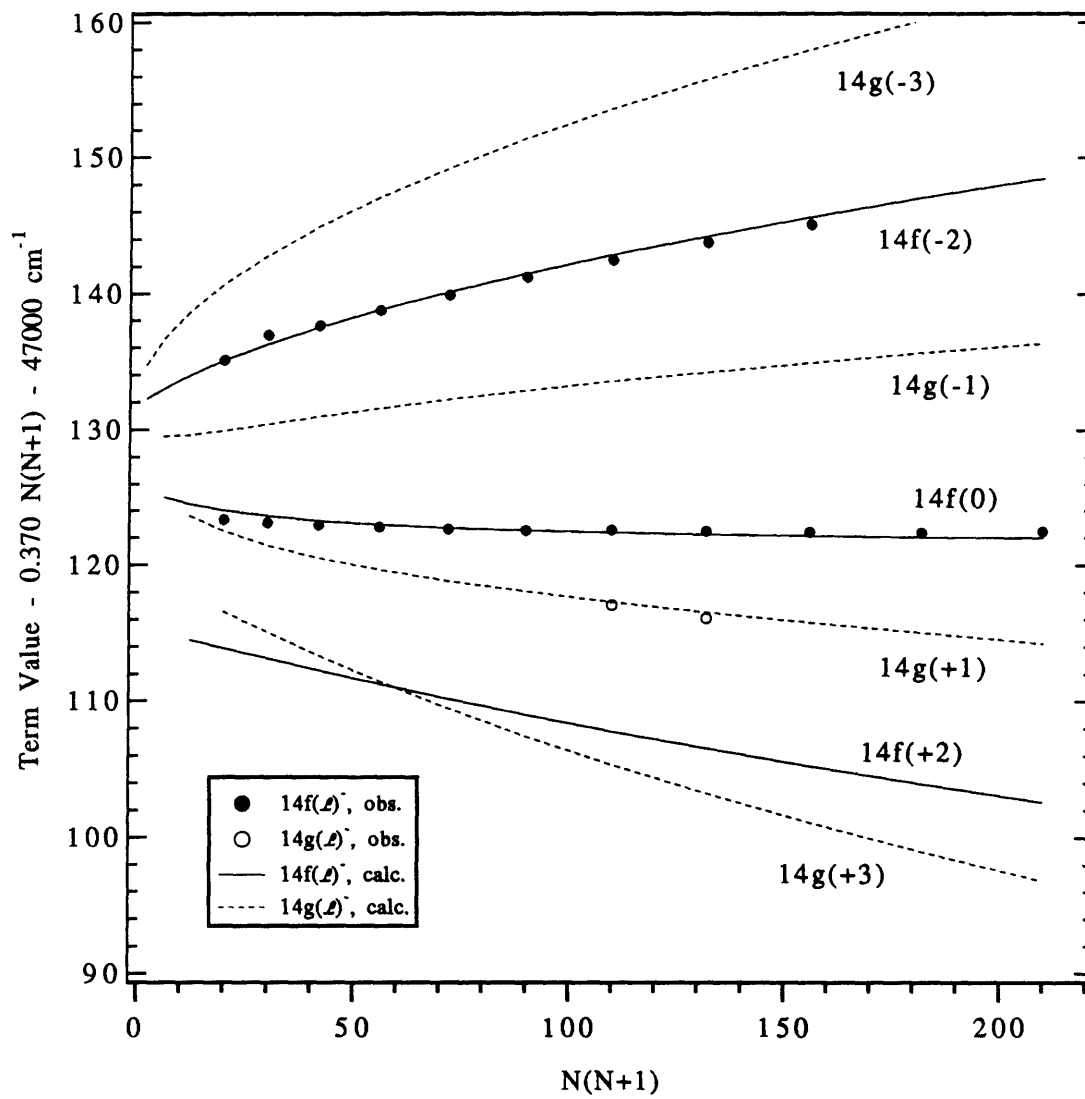


Figure 4.15. Negative symmetry 14f and 14g states. Calculated reduced term values for  $\mu^2 - Q = 11.2$  a.u.

levels with leading  $14f(+1)$  character (no extra lines due to the perturbation). The perturbation is not included explicitly in the effective Hamiltonian fit. Instead, the lines nearest the avoided crossing are strongly deweighted.

Even with these acknowledged shortcomings in treating the  $f$ -states as isolated from all other electronic states, the fit of the data to the  $f$ -state effective Hamiltonian is remarkably good. The value of  $\mu^2 - Q$  determined from the fit,  $11.2 \pm 1.2$  a.u., is equal to that for  $\text{Ca}^{+1.57}\text{F}^{-0.57}$  calculated using the point charge model, Eq.(4.72). The dipole moment of  $\text{Ca}^{+1.57}\text{F}^{-0.57}$  (again using the point charge model) is  $-3.2$  a.u. ( $-8.0$  Debye), which is slightly less than that of NaCl. For a dipole moment of this size, the nominal  $n\ell$  basis states in Eqs.(4.73) have between 70% and 93%  $f$ -character. (The low percentage is for  $f\Sigma^+$  and the high percentage is for  $f\Phi$ .) Core-non-penetrating states are characterized by near integer principal quantum number. The calculated effective principal quantum number for  $T_{14f}^0$  (as determined by inversion of the Rydberg formula and using  $47685 \pm 2$   $\text{cm}^{-1}$  as the ionization limit for  $v = 1$  Rydberg states) is  $13.99 \pm 0.02$ .

Figure 4.16 is a reduced term value plot depicting all observed  $14f$  and  $14g$  levels. The assignments of the  $14f(+3)^+$  and  $14g(+2)^+$  levels are less secure than the rest, as there were no observed avoided crossings with core-penetrating states which serve to unambiguously label  $N$ . All other assignments are very secure.

The goodness of the electron orbital angular momentum quantum number,  $\ell$ , improves as it increases. The observation of  $\ell = 4$ , "g", levels is important because they allow the Watson's model for the  $\text{CaF}^+$  ion-core induced splittings to be tested in a regime where they are likely to be more accurate. There were six individual levels belonging to  $14g$  states observed in the  $n^*=14$  supercomplex. (The several  $g(-4)$  levels were also observed in the  $n^*=13$  supercomplex.) These levels were identified through perturbations with core-penetrating states. Table 4.11 lists their rotational quantum numbers, the  $g$ -state to which they belong, their term value relative to  $X^2\Sigma^+$ ,  $v=0$ ,  $N=0$ , the core penetrating state which they perturb, and the intermediate state from which they were observed. It is plausible that an observed  $^{\circ}\text{P}$  branch from  $\text{C}^2\Pi_{3/2}$  terminates on  $14g(+2)^+$  levels, but the assignment is questionable and the levels are not included in the fit. (Inclusion of these levels in the fit significantly increased the variance of the fit, but the best fit molecular constants changed by less than  $2\sigma$ .) The  $14g(+2)^+$  assignment less certain than others because there are no observed avoided crossings with core-penetrating states to confirm the  $N$  labeling. In addition, the locations of the lower  $N$  levels,  $N < 10$ , are  $O(1 \text{ cm}^{-1})$  higher in energy than expected for the  $14g(+2)$  state.

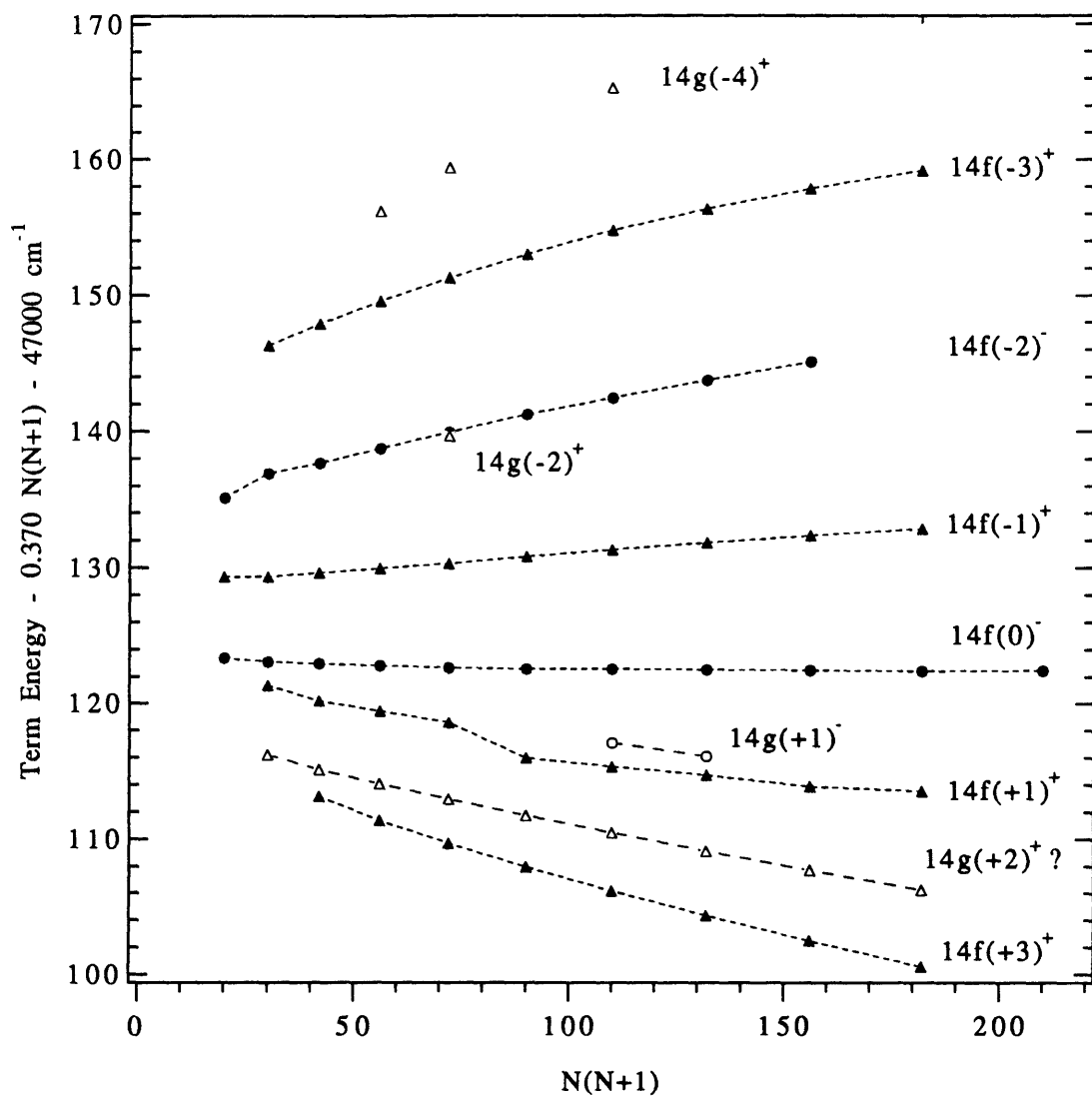


Figure 4.16. Reduced term value plot of observed n=14 core non-penetrating states.

Table 4.11 Observed 14g Levels

N	$\ell$	T/cm <sup>-1</sup>	Perturbed State	Intermediate
7	-4	47176.87(3)	14.36 $\Pi$ , v=1	A and C
8	-4	47185.98(3)	14.36 $\Pi$ , v=1	A and C
10	-4	47205.98(3)	9.55 $\Sigma^+$ , v=2	C
7	-2	47166.92(3)	14.18 $\Sigma^+$ , v=1	A
10	+1	47157.78(3)	9.36 $\Pi$ , v=2	A and C
11	+1	47164.95(3)	9.36 $\Pi$ , v=2	A and C

The effective Hamiltonian fit to the 14g levels proceeded in much the same way as did the fit to the 14f levels. The splitting of the  $g\Lambda$  components of 14g complex is determined by  $\mu^2 - Q$ . The effective Hamiltonian fit to the observed g levels involves just two parameters,  $\mu^2 - Q$  and  $T_{14g}^0$ . The rotational constant of the g-complex is set equal to the value determined by the effective Hamiltonian fit to the p-d-f mixed negative Kronig-symmetry states, 0.3704 cm<sup>-1</sup>. The diagonal matrix elements of the 14g effective Hamiltonian are determined by Eqs.(3.63) and (4.63):

$$E_{14g\Lambda}^0 = T_{14g\Lambda} + B[N(N+1) + 20 - 2\Lambda^2] - DN^2(N+1)^2. \quad (4.80)$$

The off-diagonal matrix elements are  $\ell$ -uncoupling terms in  $H^{\text{rot}}$ :

$$H_{14g\Lambda-\Lambda+1}^{\text{rot}} = -B\sqrt{20 - \Lambda(\Lambda+1)}\sqrt{N(N+1) - \Lambda(\Lambda+1)} \cdot F, \quad (4.81)$$

where  $F = \sqrt{2}$  when  $\Lambda = 0$ , and  $F = 1$  when  $\Lambda \neq 0$ .

The positive and negative Kronig-symmetry effective Hamiltonians have no matrix elements connecting them, but the 14g data is fit using the  $\mu^2 - Q$  and  $T_{14g}^0$  parameters equal for positive and negative Kronig-symmetry. (The positive Kronig symmetry effective Hamiltonian is five-by-five and the negative symmetry effective Hamiltonian is four-by-four.) The values of  $\mu^2 - Q$  and  $T_{14g}^0$  determined by the effective Hamiltonian fit are  $12.9 \pm 0.9$  a.u. and  $47125.8 \pm 0.1$  cm<sup>-1</sup> respectively. (Uncertainty is  $2\sigma$ .) Inversion of the Rydberg formula yield an effective principal quantum number of  $14.01 \pm 0.02$  for CaF 14g. This is consistent with the expectation that the quantum defect of g states should be extremely close to zero. The quantum defect of the atomic Ca<sup>+</sup> ng Rydberg series,  $\delta_g$ , is determined to be 0.004 by inversion of the Rydberg formula:

$$E_{ng}^0 = \text{IP}(\text{Ca}^+) - \frac{4\mathfrak{R}}{[n - \delta_g]}, \quad (4.82)$$

and data from Charlotte Moore's atomic energy level tables [25]. (Analysis of Moore's data for  $\text{Ca}^+$  nf states yields  $\delta_f = 0.025$ .)

The agreement of the best fit value of  $\mu^2 - Q$  for 14g and 14f effective Hamiltonian fits is very encouraging. It is unfortunate that transitions from the  $A^2\Pi_{3/2}$  and  $C^2\Pi_{3/2}$  intermediate states to 14g levels are not stronger (allowed), as it would be desirable to include more levels in the 14g-complex fit. The quality of the fit to those 14g levels observed is excellent however, especially considering the fit involved only two parameters. (The variance of the fit was  $\sim 2$ .) The goodness of  $\ell$ , and hence Watson's prediction for the splitting of  $\ell\Lambda$  components of core-non-penetrating states, is better for  $\ell = 4$  than for  $\ell = 3$ . The value of  $\mu^2 - Q$  determined from the g-state analysis should be a more accurate measure of the actual quantity than the value determined from the f-state analysis. On the basis of the 14f and 14g effective Hamiltonian fit results, the quantity  $\mu^2 - Q$  for  $\text{CaF}^+$  is established to be  $13 \pm 2$  a.u. Within the framework of the point charge model this corresponds to  $\text{Ca}^{+1.65}\text{F}^{-0.65}$ , and a  $\text{CaF}^+$  dipole moment of  $-8.6 \pm 1.6$  Debye.

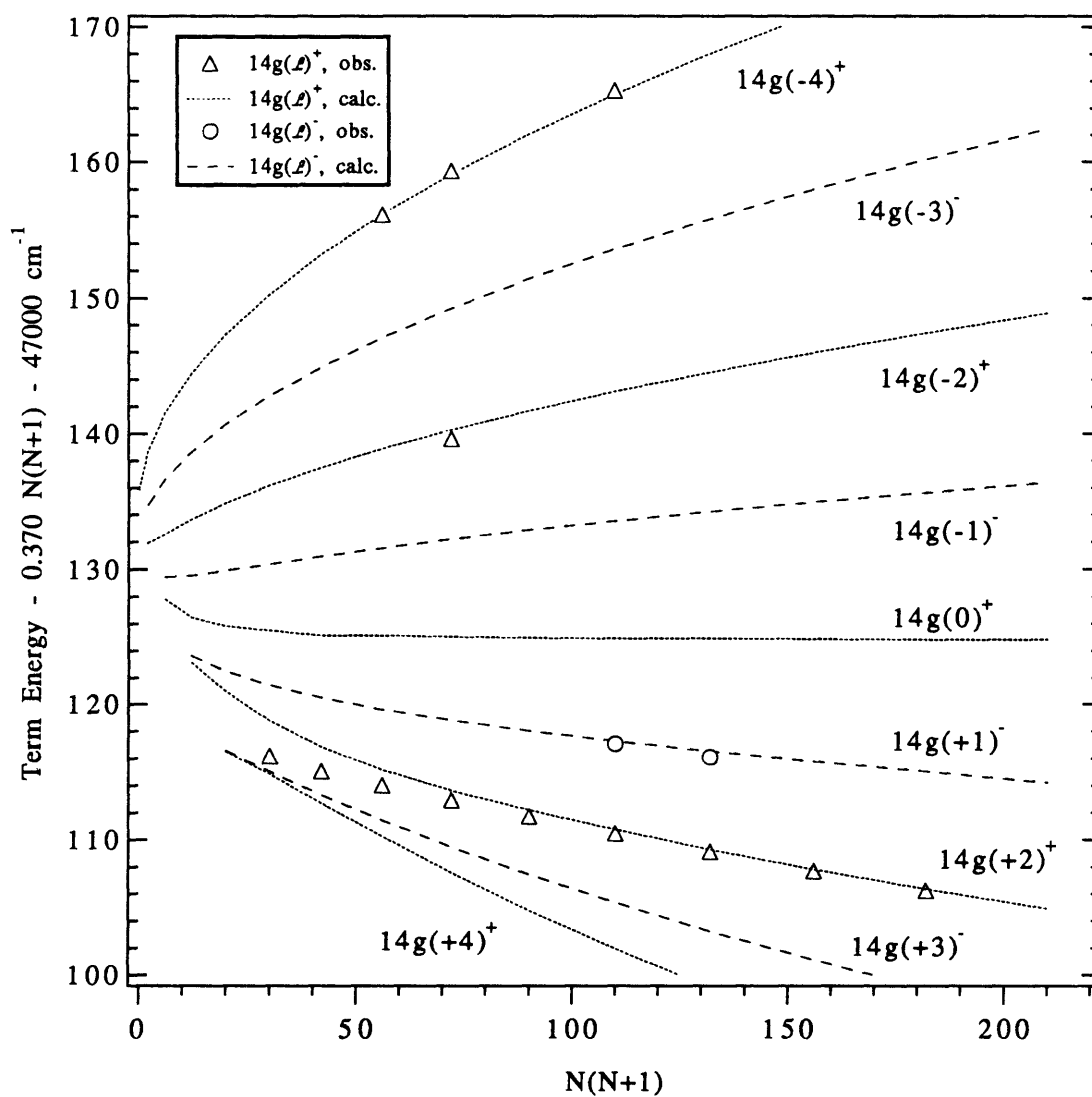


Figure 4.17. Observed  $14g$  levels and calculated locations from two parameter,  $T_{14g}$  and  $[\mu^2 - Q]$ , fit. The  $14\ell(+2)$  is assigned as a  $g$  state on the basis of its Kronig symmetry.

## References

1. S.F.Rice, H.Martin, and R.W.Field, *J. Chem. Phys.*, v. 82 (1985), p.5023.
2. J.E.Murphy, J.M.Berg, A.J.Merer, N.A.Harris, and R.W.Field, *Phys. Rev. Lett.*, v.65 (1990), p.1861.
3. Ch. Jungen, *J. Chem. Phys.*, v. 53 (1970), p.4168.
4. L.Józefowski, Ch. Ottinger, and T.Rox, *J. Mol. Spec.*, v.163 (1994), p.381.
5. R.D. Gilbert and M.S. Child, *Chem. Phys. Lett.*, v.287 (1991), p.153.
6. N.A. Harris and Ch. Jungen, private communication.
7. H. Lefebvre-Brion and R.W. Field, "Perturbations in the Spectra of Diatomic Molecules", Ch.3, Academic Press, 1986.
8. E.J. Friedman-Hill, Ph.D Thesis, MIT, 1992.
9. G. Herzberg, "Molecular Spectra and Molecular Structure. Vol. I. - Spectra of Diatomic Molecules", Krieger Publishing Co., Malabar FL, 1989.
10. J.E. Murphy, Ph.D. thesis, MIT, 1992.
11. C.Fabre and S.Haroche in "Rydberg States of Atoms and Molecules", Ch.3., R.F.Stebbins and F.B.Dunning, eds., Cambridge University Press, 1983.
12. R.N.Zare and J.Cashion, unpublished, 1963.
13. R. N. Zare, "Angular Momentum", Ch.3, Wiley-Interscience, 1988.
14. Z. Jakubek and R. W. Field, *J. Chem. Phys.*, v.98 (1993), p.6574.
15. Z. Jakubek, private communication.
16. Ch. Jungen and E. Meisher, *Can. J. Phys.*, v.47 (1969), p. 1769.
17. L. Pauling and E.B. Wilson, "Introduction to Quantum Mechanics", Dover, New York, 1985, p.145.
18. M. Feher and P.A.Martin, *Chem. Phys. Lett.*, v.213 (1993), p.565.
19. E. Eyler and F. Pipkin, *Phys. Rev. A*, v.27 (1983), p.2462.
20. W.G. Sturru, E.A. Hessels, P.W. Arcuni, and S.R. Lundeen, *Phys. Rev. A*, v.38 (1988), p.135.
21. S. Pasternack and R.N. Sternheimer, *J. Math. Phys.*, v.3 (1962), p.1280
22. A. Dalgarno and J.T. Lewis, *Proc. R. Soc. A.*, v.233 (1956) 70.
23. J.K.G. Watson, *Mol. Phys.*, v.81 (1994), p.277.
24. CRC Handbook of Chemistry and Physics, 60th ed., Section E-63, CRC Press, 1969.
25. C.E. Moore, "Atomic Energy Levels, Vol. I,  $^1\text{H} - ^{23}\text{V}$ ," NBS Publication 467, 1949.



## CHAPTER 5

### Vibrational Autoionization Rates of 13.36 $\Pi$ , $v=1$ and 14.36 $\Pi$ , $v=1$ states

Intrachannel perturbations occur not only between bound states, e.g. the 13.14  $\Delta$ ,  $v=1$  and 9.14  $\Delta$ ,  $v=2$  interaction discussed in Chapter 4, but also between bound states and the electronic continuum. This latter phenomenon is responsible for vibrational autoionization. Vibrational autoionization may occur when the vibronic energy of a Rydberg state exceeds the vibrationless ionization threshold of the molecule. Vibrational autoionization is most efficient for  $\Delta v = 1$  [1]. The criterion for the vibronic energy of the  $v=1$  Rydberg state exceeding the  $v=0$  ionization threshold is:

$$E(n^*, v=1) = IP_{v=0} + \Delta G_{1/2} - \frac{\mathfrak{R}}{(n^*)^2} \geq IP_{v=0}. \quad (5.1)$$

The minimum value of  $n^*$  for which  $v=1$  CaF Rydberg states may autoionize is determined by inverting Eq.(5.1) and substituting in  $\Delta G_{1/2}(\text{CaF}^+)$ ,  $685 \text{ cm}^{-1}$ :

$$n^* \geq \sqrt{\frac{\mathfrak{R}}{\Delta G_{1/2}}} = 12.66. \quad (5.2)$$

The minimum  $n^*$  for vibrational autoionization threshold is lower for lighter and more strongly bound molecules.

Both bound-bound and bound-continuum intrachannel couplings depend upon the variation of the quantum defect with internuclear separation. Intrachannel perturbations arise through  $H^{\text{el}}(\mathbf{R})$ . The internuclear distance dependence of  $H^{\text{el}}$  couples states belonging to the same Rydberg series, but converging on different vibrational levels of the ion core. If  $H^{\text{el}}$  is assumed to be defined by Eq.(3.11):

$$H_{ij}^{\text{el}}(\mathbf{R}) = -\frac{2\mathfrak{R}}{(n_i n_j)^{3/2}} \delta(\mathbf{R}), \quad (5.3)$$

and,

$$\delta(R) = \delta(R_c^+) + \left( \frac{d\delta}{dR} \right)_{R_c^+} (R - R_c^+), \quad (5.4)$$

then, within the harmonic approximation, the term linear in  $R - R_c^+$  couples states with  $\Delta v = \pm 1$ . Equation (3.20) may be used to calculate the strength of the coupling:

$$\langle n_i^* + m, v | \mathbf{H}^{el} | n_i^*, v + 1 \rangle = - \frac{2\mathfrak{R}}{[n_i(n_i + m)]^{3/2}} \frac{4.106}{\sqrt{\mu\omega_c^+}} \sqrt{v+1} \left( \frac{d\delta_i}{dR} \right)_{R_c^+},$$

where  $\mathfrak{R}$  is the Rydberg constant in  $\text{cm}^{-1}$ ,  $\mu$  is the reduced mass in amu, and  $\omega_c^+$  is the cation vibrational frequency in  $\text{cm}^{-1}$ . The quantum defect derivative may be determined by the analysis of intrachannel perturbations between bound states.

Coupling of the bound state to the continuum reduces the state's natural lifetime. The radiative lifetime of Rydberg states with  $n^* = O(10^1)$  is typically  $10^0$ - $10^2$   $\mu\text{s}$ . The natural linewidth would therefore be  $O(10^1$ - $10^2$  kHz). Autoionization may reduce the Rydberg state lifetime by many orders of magnitude. The linewidth of a vibrational autoionization broadened Rydberg level may be determined using Fermi's Golden Rule [2]:

$$\Gamma_i = 2\pi |H_{ij}|^2 \rho_j, \quad (5.5)$$

where  $H_{ij}$  is the bound-continuum coupling matrix element and  $\rho_j$  is the density of continuum states. The coupling matrix element is evaluated using Eq.(3.20), but instead of evaluating the matrix element where  $n_i^* + m$  is real, the calculation is performed for a continuum state,  $\epsilon_i$ , where the principal quantum number is complex. Fortunately, algebraic manipulation allows the bound-continuum interaction to be expressed in terms of the effective principal quantum number of the bound state and the quantum defect derivative of the Rydberg series.

The density of electronic states in the continuum is a continuous function of energy and is determined by extrapolating the density of states from below the ionization threshold. The density of states below the ionization threshold is calculated by inverting the derivative of the Rydberg formula:

$$\rho_j \equiv \left( \frac{dn_j}{dE_j} \right) = \left( \frac{dE_j}{dn_j} \right)^{-1}, \quad (5.6)$$

where,

$$\frac{dE_j}{dn_j} = \frac{d}{dn_j} \left[ IP - \frac{\mathfrak{R}}{n_j^2} \right]. \quad (5.7)$$

Substitution of Eq.(5.7) into Eq.(5.6) yields:

$$\rho_j = \frac{n_j^3}{2\mathfrak{R}}. \quad (5.8)$$

Combining the Eqs.(3.22), (5.5) and (5.8) yields the following expression for linewidth (in  $\text{cm}^{-1}$ ) as a function of effective principal quantum number and quantum defect derivative:

$$\Gamma_i = \frac{4\pi\mathfrak{R}}{n_i^3} \frac{16.858}{\mu\omega_e^+} v_{>} \left( \frac{d\delta}{dR} \right)_{R_0}^2 = 1.30 \left( \frac{12.66}{n_i} \right)^3 \left( \frac{d\delta}{dR} \right)_{R_0}^2 \text{ cm}^{-1}, \quad (5.9)$$

for  $n_i^*$ ,  $v = 1$  to  $\epsilon_i$ ,  $v^+ = 0$  autoionization in CaF. The autoionization linewidth of a typical state,  $n^* \approx 14$  with  $d\delta/dR \approx 0.4 \text{ \AA}^{-1}$ , is  $O(0.1 \text{ cm}^{-1})$ . While this is barely large enough to produce a reliably detectable broadening when using PROBE lasers with  $0.15\text{-}0.20 \text{ cm}^{-1}$  linewidths, the corresponding autoionization rate,  $(\Gamma/5.3 \cdot 10^{-12}) \text{ s}^{-1} = 7.5 \cdot 10^9 \text{ s}^{-1}$ , is orders of magnitude larger than the radiative relaxation rate. The vibrational autoionization rate will be largest near the ionization threshold, i.e. at the minimum possible value of  $n_i$ . Equation (5.9) has been derived phenomenologically by Herzberg and Jungen [3] and subsequently summarized by Lefebvre-Brion and Field [4].

Five of the six core-penetrating states in the  $n^*=13$ ,  $v=1$  supercomplex were observed. All six core-penetrating states were observed for  $n^*=14$ ,  $v=1$ . In addition, several f-states in  $n^*=13$  and six of the seven f-states in  $n^*=14$  have been observed. Of all the  $n^*=13$  and  $n^*=14$  states observed, the only ones which possessed a reliably detectable line broadening were the  $13.36 \Pi$  and  $14.36 \Pi$  states. This observation, combined with the prediction of Eq.(5.9), suggests that the  $0.36 \Pi$  series possesses the largest quantum defect derivative of all observed Rydberg series. The question arises, "Why should the  $0.36 \Pi$  series possess the largest quantum defect derivative?"

The  $0.36 \Pi$  series terminates on the  $C^2\Pi$  state. The  $C^2\Pi$  state is distinguished by the fact that it is the least ionic electronic state of CaF. The lowest energy  $^2\Pi$  state in CaF, the

$A^2\Pi$ , is well described as a linear combination of  $Ca^+$   $4p\pi$  and  $3d\pi$  atomic orbitals [5,6]. The  $A^2\Pi$  molecular orbital is polarized out the back side of CaF, away from the F<sup>-</sup> ligand. This polarization stabilizes the  $A^2\Pi$  state. One could initially consider the  $C^2\Pi$  state to be the reverse polarized, anti-bonding combination of the  $Ca^+$   $4p\pi$  and  $3d\pi$  atomic orbitals [1,7]. A quantum chemical treatment of the problem reveals that not only is the  $C^2\Pi$  state polarized towards the fluorine, but that it possesses a significant amount of F  $2p\pi$  character [6]. One consequence of this is that the Ca-F bond in the C state is the weakest of all CaF electronic states. The vibrational constant of the C state is only 80% that of the ground and A states, and only 70% that of  $CaF^+$ .

The anti-bonding character of the Rydberg electron causes the quantum defect derivative to be a positive quantity. If the Rydberg electron were bonding or non-shielding, the quantum defect would be negative. This may be understood by treating the electronic energy as a function of the internuclear distance dependent energy difference between the Rydberg state and the cation. The derivation is essentially the same as Mulliken's from 25 years ago [9]. The fundamental assumption is:

$$E^d(R) + U(R) = U^+(R), \quad (5.10)$$

where  $U(R)$  and  $U^+(R)$  are the potential energy functions of the Rydberg state and the cation. The function  $E^d(R)$  is defined by the Rydberg formula:

$$E^d(R) \equiv IP - \frac{\mathfrak{R}}{[n - \delta(R)]^2}. \quad (5.11)$$

An expression for the quantum defect derivative may be determined by substituting Eq(5.11) into Eq.(5.10) and taking the derivative:

$$\frac{2\mathfrak{R}}{[n - \delta(R)]^3} \left( \frac{d\delta}{dR} \right) = \frac{dU^+}{dR} - \frac{dU}{dR}. \quad (5.12)$$

The effective principal quantum number,  $n^*$ , is  $n - \delta(R_e)$ , but the quantum defect has a very weak R dependence, so  $n - \delta(R_e) \approx n - \delta(R_e^+)$ . Near the bottom of their vibrational potentials, both the Rydberg state and the cation may be approximated as harmonic oscillators:  $U(R) = \frac{1}{2}k(R - R_e)^2$  and  $U^+(R) = \frac{1}{2}k^+(R - R_e^+)^2$ , in which case the latter term on the RHS of Eq.(5.12) is:

$$\frac{dU}{dR} = k(R-R_e). \quad (5.13)$$

The first derivative of  $U^+(R)$  is zero at  $R_e^+$  by definition. The quantum defect derivative (in units of  $\text{\AA}^{-1}$ ) evaluated at  $R_e^+$  may be estimated as:

$$\left(\frac{d\delta}{dR}\right)_{R_e^+} = \frac{(n^*)^3 k}{2\mathfrak{R} hc} (R_e - R_e^+), \quad (5.14)$$

where  $k/hc = 2.966 \cdot 10^{-2} (\omega_e)^2 \mu$ ;  $\omega_e$  is the vibrational constant of the Rydberg state in  $\text{cm}^{-1}$ , and  $\mu$  is the reduced mass of the cation in amu;  $R_e$  and  $R_e^+$  are the equilibrium internuclear separations of the Rydberg state and the cation in  $\text{\AA}$ . At high  $n^*$ , the difference between  $R_e$  and  $R_e^+$  is extremely small and often difficult to determine accurately. Fortunately, the lowest energy core-penetrating electronic states adhere fairly closely to the Rydberg formula [10]. Quantum defect derivatives for each series may therefore be estimated using Eq.(5.14) and the values of  $n^*$ ,  $k$ , and  $R_e$  of the lowest member of each series. Estimated quantum defects are listed in Table 5.1. The Rydberg electron is always anti-bonding because the +2/-1 ionic bond in the cation is so strong. The Rydberg electron screens the +2 charge on the  $\text{Ca}^+$  and weakens the ionic bond. Inspection of Eq.(5.14) implies the quantum defect derivative for the 0.36  $\Pi$  series is largest because 0.36  $\Pi$  states have comparatively longer internuclear separations due to the anti-bonding character of the Rydberg electron.

Table 5.1 Predicted Quantum Defect Derivatives for Core-Penetrating Rydberg Series

Series	Terminus State	$\omega_e / \text{cm}^{-1}$	$R_e / \text{\AA}$	$\left(\frac{d\delta}{dR}\right)_{R_e^+} / \text{\AA}^{-1}$
0.88 $\Sigma^+$	B $^2\Sigma^+$	572	1.958	0.37
0.55 $\Sigma^+$	X $^2\Sigma^+$	589	1.955	0.18
0.18 $\Sigma^+$	F' $^2\Sigma^+$	693	1.873	0.03
0.98 $\Pi$	A $^2\Pi$	595	1.941	0.28
0.36 $\Pi$	C $^2\Pi$	482	2.012	0.93
0.14 $\Delta$	B' $^2\Delta$	523	1.997	0.57

Murphy [11] has analyzed an intrachannel perturbation between the 7.36  $\Pi, v=0$  and 6.36  $\Pi, v=1$  Rydberg states and obtained the value of quantum defect derivative,

$$\left(\frac{d\delta}{dR}\right)_{R^*} = +0.732 \text{ \AA}^{-1},$$

for the 0.36  $\Pi$  series. This is in good agreement with the value predicted using Eq.(5.14). At this time only the quantum defect derivative for the 0.36  $\Pi$  series has been determined from a  $\Delta v = +1 = -\Delta n^*$  perturbation analysis. The first member of the  $v=1$ , 0.36  $\Pi$  series capable of vibrational autoionization is the 13.36  $\Pi$  state. Eq.(5.9) predicts  $\Gamma(13.36 \Pi) = 0.59 \text{ cm}^{-1}$  and  $\Gamma(14.36 \Pi) = 0.45 \text{ cm}^{-1}$ . Line broadening of this magnitude is detectable in ID-OODR experiments. The minimum detectable broadening is limited by the linewidth of the PROBE laser, 0.15-0.20  $\text{cm}^{-1}$ . Tables 5.2 and 5.3 list the observed linewidths of the rotational levels of the 13.36  $\Pi$  and 14.36  $\Pi$  states.

The positive Kronig-symmetry components of the  $n.36 \Pi$ ,  $v=1$  states are subject to  $\ell$ -uncoupling by the nearby  $n.18 \Sigma^+$ ,  $v=1$  states. The  $n.36 \Pi$  states are also coupled to the  $n.55 \Sigma^+$  states, but as the  $n.36 \Pi$  levels are pushed up in energy, it is apparent that  $n.36 \Pi$  interacts more strongly with lower energy states. The negative Kronig symmetry component of the  $.36 \Pi$  states is only weakly perturbed through its interaction with the  $.14 \Delta$  and  $.98 \Pi$  states. The  $\Sigma^+$  states have no negative Kronig symmetry levels. As the zero-order  $.36 \Pi$  character in the positive Kronig-symmetry " $\Pi$ " levels is reduced by  $\ell$ -uncoupling with increasing  $N$ , one can observe a decrease in measured linewidths. The negative symmetry levels retain most of their zero-order  $.36 \Pi$  character and the measured linewidths appear to be independent of  $N$ .

Figure 5.1 depicts the ID-OODR spectrum of the 13.36  $\Pi$ ,  $v=1$  and 9.18  $\Sigma^+$ ,  $v=2$  states. The linewidths of the 13.36  $\Pi$  levels are quite broad,  $\sim 0.5 \text{ cm}^{-1}$ . The measured linewidth of the 9.18  $\Sigma^+$ ,  $v=2$  state is measurably larger than that of the PROBE laser for  $N > 4$ . While it is possible for the 9.18  $\Sigma^+$ ,  $v=2$  state to ionize via the loss of two quanta of vibration, this mechanism is not believed to be sufficiently rapid to generate an observable line broadening. It is most likely that the 9.18  $\Sigma^+$ ,  $v=2$  state experiences an intrachannel perturbation with the 13.18  $\Sigma^+$ ,  $v=1$  state lying at slightly lower energy. The 13.18  $\Sigma^+$ ,  $v=1$  character in the 9.18  $\Sigma^+$ ,  $v=2$  state results in strong  $\ell$ -uncoupling with the 13.36  $\Pi$  state, and it is likely the 13.36  $\Pi$  state character which gives the 9.18  $\Sigma^+$ ,  $v=2$  state its vibrational autoionization strength and observable line broadening. The 13.18  $\Sigma^+$ ,  $v=1$  state was not observed from in the ID-OODR experiments. Unfortunately, there was not enough information available from the spectrum to establish the extent of the mixing between 13.18  $\Sigma^+$ ,  $v=1$  and 9.18  $\Sigma^+$ ,  $v=2$  as was possible for 13.14  $\Delta$ ,  $v=1 \sim 9.14 \Delta$ ,  $v=2$  interaction analyzed in Chapter 4. The origin of the 9.18  $\Sigma^+$ ,  $v=2$  line broadening is of interest, but it

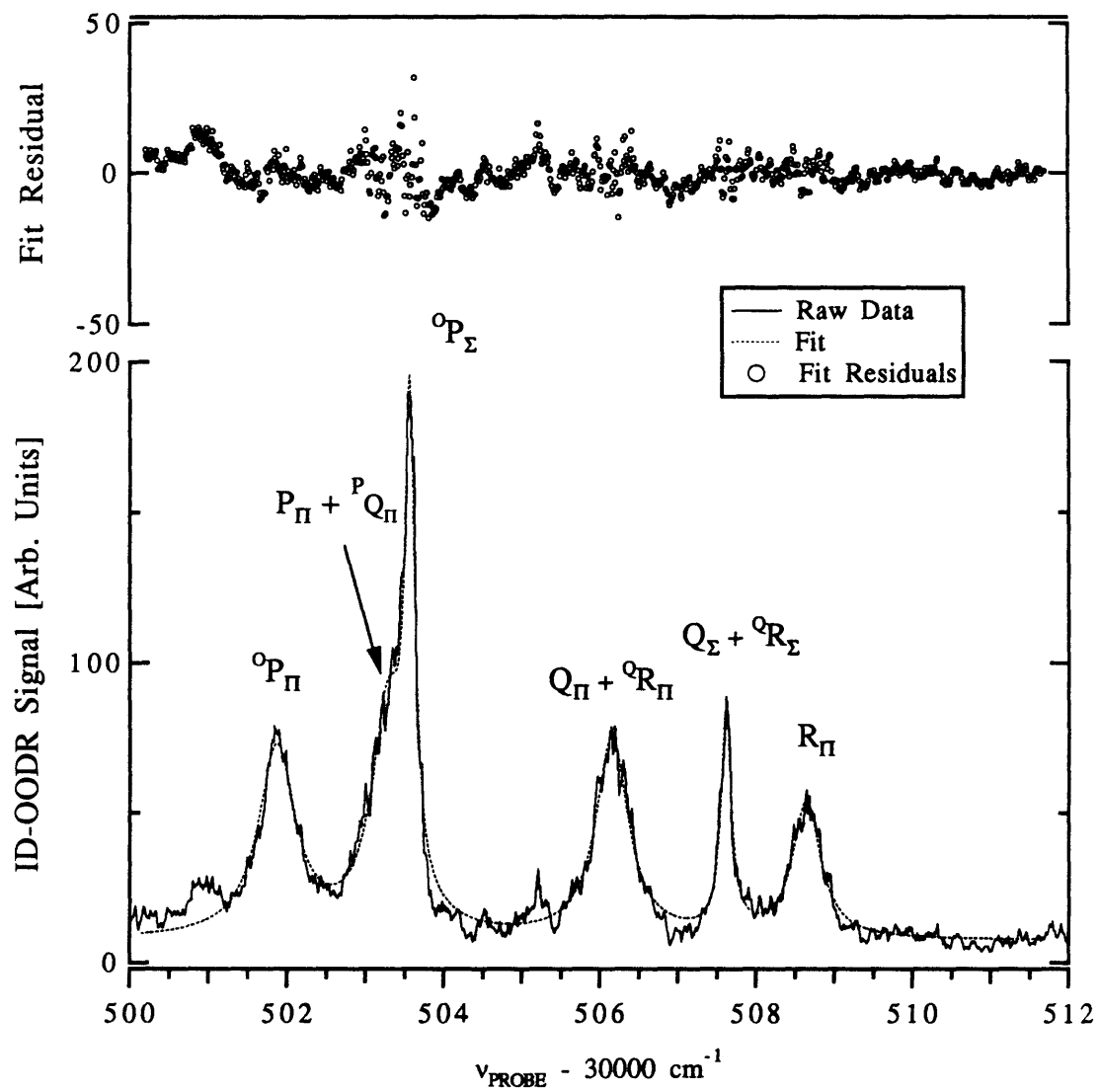


Figure 5.1 Autoionization Detected Optical-UV Double Resonance  
 CaF 13.36  $\Pi$ ,  $v=1$  and 9.18  $\Sigma^+v=2$  States.  $A^2\Pi_{3/2}-X^2\Sigma^+(0,0)$   $Q_2(2.5)$  PUMP.

is not essential to the analysis of 13.36  $\Pi$  linewidths. Any mixing between the 9.18  $\Sigma^+$ ,  $v=2$  and 13.36  $\Pi$ ,  $v=1$  states is  $N$ -dependent and equal to zero at  $N = 0$ . The linewidth of the 13.36  $\Pi$  levels extrapolated to  $N = 0$  is the value which is compared to the value calculated using Murphy's value for 0.36  $\Pi$  series quantum defect derivative.

The Figure 5.2 depicts a reduced term value plot of the 13.36  $\Pi$  levels and the corresponding measured linewidths. The extra points on the reduced term value plot arise from a perturbation of the positive Kronig-symmetry levels by the 13g(-4) state. Figure 5.3 provides a comparison of the  $N$  dependence of the measured linewidths of the 13.36 and 14.36  $\Pi$  states. Tables 5.2 and 5.3 list the average measured linewidth for ID-OODR transitions terminating on 13.36  $\Pi$ ,  $v=1$ ,  $1 \leq N \leq 12$  and 14.36  $\Pi$ ,  $v=1$ ,  $1 \leq N \leq 10$ . The linewidths listed in these tables were determined by fitting the observed ID-OODR line to a Lorentzian lineshape:

$$g(\tilde{\nu}) = \frac{A}{\pi} \frac{\Delta\tilde{\nu}}{(\tilde{\nu} - \tilde{\nu}_0)^2 + (\Delta\tilde{\nu})^2}, \quad (5.15)$$

where  $\tilde{\nu}_0$  is the line center of the transition and  $\Delta\tilde{\nu}$  is the full width at half-maximum. Equation (5.15) integrated over all frequencies gives the intensity of the line,  $A$ .

The measured linewidths of the 13.36  $\Pi$ ,  $v=1$  levels extrapolated to  $N=0$  is  $0.51 \pm 0.08 \text{ cm}^{-1}$ . The measured linewidths of the 14.36  $\Pi$ ,  $v=1$  levels extrapolated to  $N=0$  is  $0.53 \pm 0.05 \text{ cm}^{-1}$ . The measured, predicted, and deconvoluted (for laser linewidth) autoionization induced line broadenings are listed in Table 5.4.

Table 5.4 Measured, Predicted\*, and Deconvoluted Linewidths for 0.36  $\Pi$ ,  $v=1$  States in the Absence of Rotation

	$\Gamma(\text{meas.}) / \text{cm}^{-1}$	$\Gamma(\text{pred.}) / \text{cm}^{-1}$	$\Gamma(\text{decon.}) / \text{cm}^{-1}$
13.36 $\Pi$ , $v=1$	0.51(8)	0.59	0.49(8)
14.36 $\Pi$ , $v=1$	0.53(5)	0.45	0.51(5)

\*  $\Gamma(\text{pred.})$  is calculated using Murphy's value for the quantum defect derivative.

The observed decrease in the linewidth of the positive Kronig-symmetry levels with increasing rotational quantum number is attributable to the loss of .36  $\Pi$ ,  $v=1$  character by rotational  $\ell$ -uncoupling. The  $-BN \cdot \ell$  term in the effective Hamiltonian for the positive Kronig-symmetry states couples in electronic states which have a much lower autoionization rate. The decrease in autoionization rate due to  $\ell$ -uncoupling may be



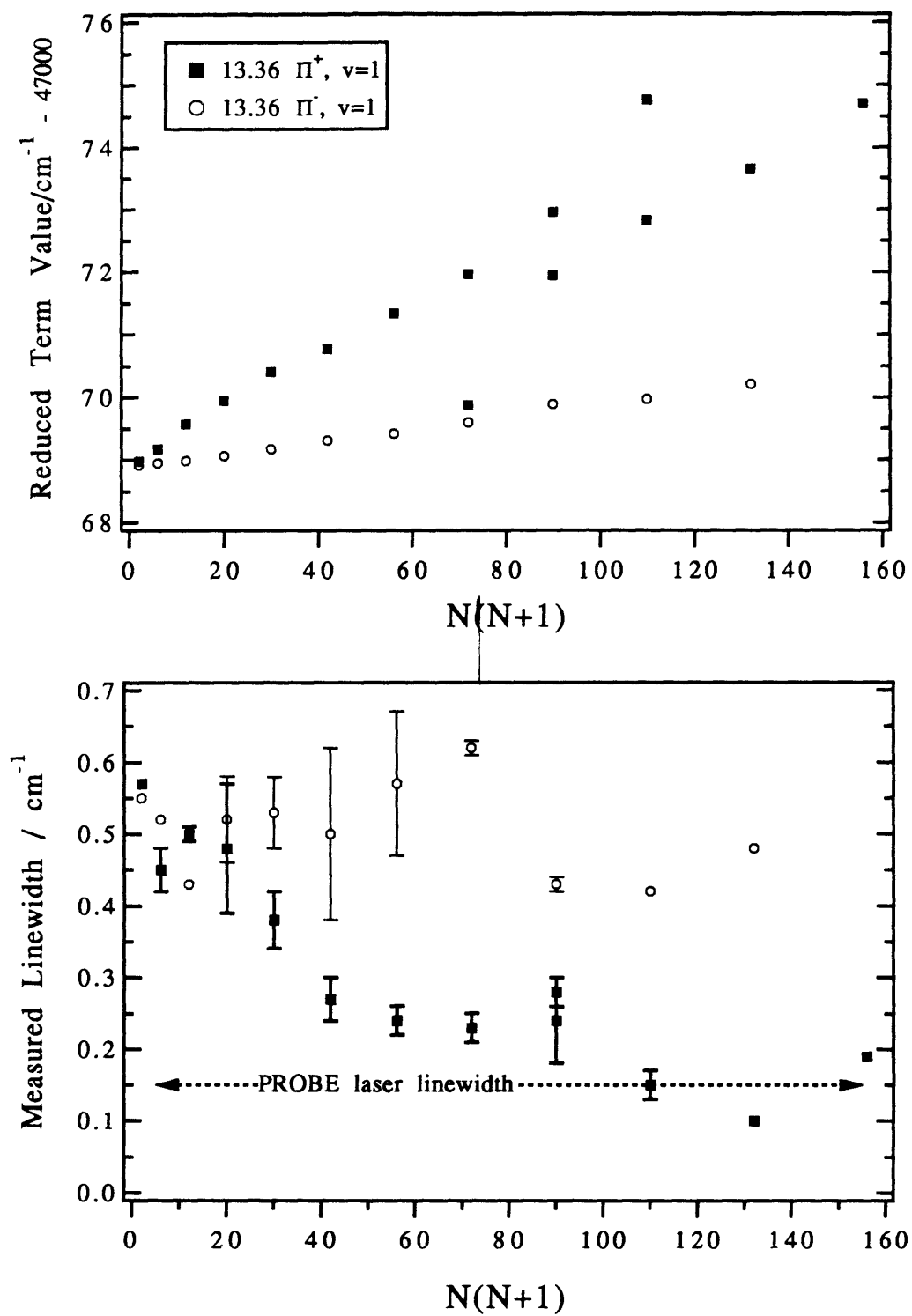


Figure 5.2. Reduction of 13.36  $\Pi$  vibrational autoionization rate by  $l$ -uncoupling. Top: Reduced term value plot. Bottom: Linewidths of rotational levels.

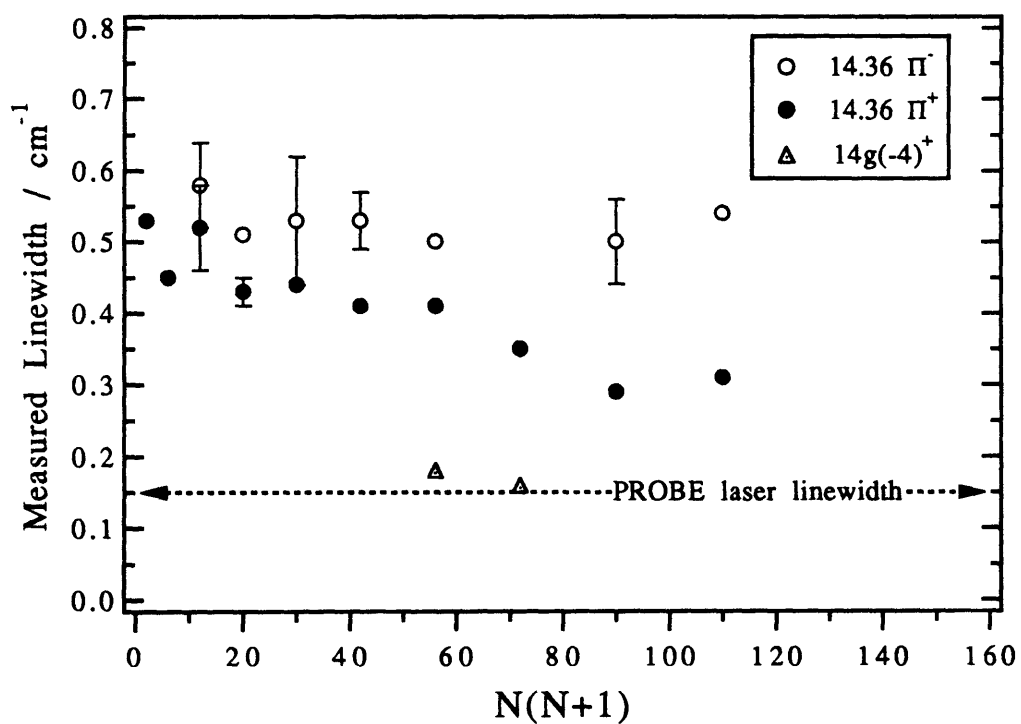
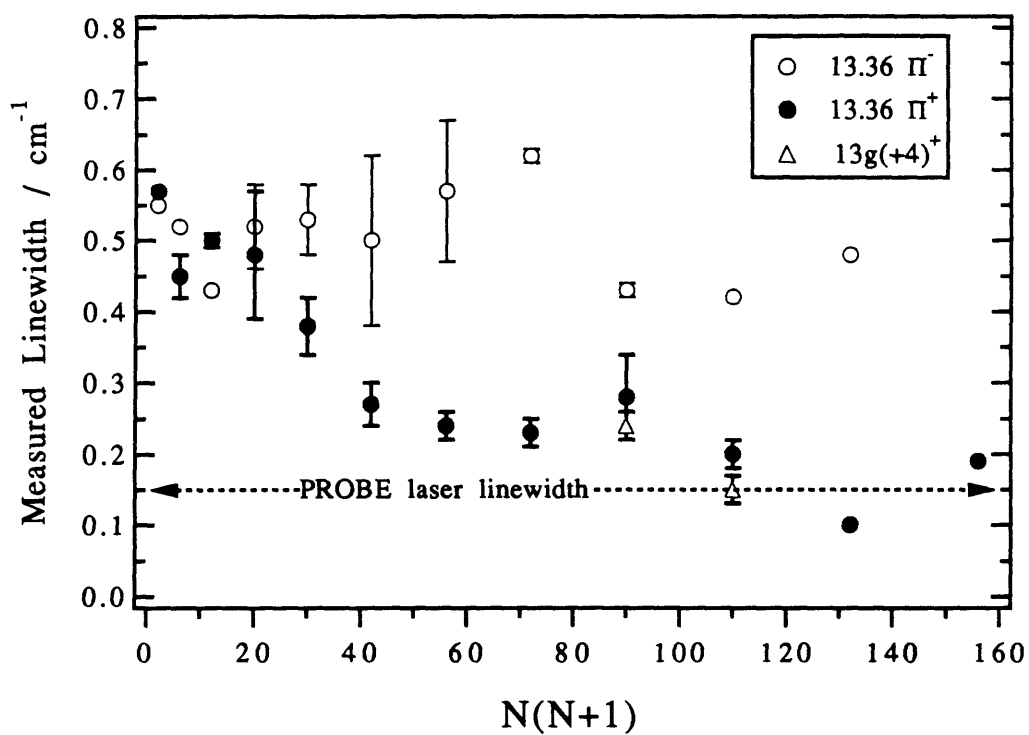


Figure 5.3. Measured linewidths in the 13.36  $\Pi$ ,  $v=1$  and 14.36  $\Pi$ ,  $v=1$  states. The error bars on points represent  $\sigma$  of multiple measurement. Points without error bars represent single measurements. The observed reduction in linewidth with increasing rotational quantum number is caused by a decrease in vibrational autoionization rate due to  $\ell$ -uncoupling.

understood qualitatively by constructing the effective Hamiltonian for an n\*-complex derived solely from a p-electron. A p-complex gives rise to a single negative Kronig-symmetry state, pΠ. The pΠ state retains 100% of its original pΠ character for all values of N. There are two positive symmetry states in a p-complex, pΣ<sup>+</sup> and pΠ<sup>+</sup>. The effective Hamiltonian for the positive Kronig symmetry states is:

$$\mathbf{H}^{\text{el}} + \mathbf{H}^{\text{rot}} = \begin{bmatrix} T_{\text{p}\Sigma^+} + \text{BN}(\text{N} + 1) & -2\text{B}\sqrt{\text{N}(\text{N} + 1)} \\ -2\text{B}\sqrt{\text{N}(\text{N} + 1)} & T_{\text{p}\Pi^+} + \text{BN}(\text{N} + 1) \end{bmatrix}. \quad (5.16)$$

The eigenvectors of Eq.(5.16) are:

$$|E_+, N\rangle = \cos\left(\frac{\theta}{2}\right)|\text{p}\Pi^+, N\rangle - \sin\left(\frac{\theta}{2}\right)|\text{p}\Sigma^+, N\rangle, \quad (5.17)$$

$$|E_-, N\rangle = \cos\left(\frac{\theta}{2}\right)|\text{p}\Sigma^+, N\rangle + \sin\left(\frac{\theta}{2}\right)|\text{p}\Pi^+, N\rangle, \quad (5.18)$$

where,

$$\tan \theta \equiv \frac{2\text{B}\sqrt{\text{N}(\text{N} + 1)}}{T_{\text{p}\Sigma^+} - T_{\text{p}\Pi^+}}. \quad (5.19)$$

In the limit of large N,  $\tan \theta = \infty$ ,  $\theta = \pi$ , and  $\cos\left(\frac{\theta}{2}\right) = \sqrt{\frac{1}{2}}$ . The positive symmetry eigenstates become 50/50 mixed as N tends toward infinity. If the autoionization rate of the pΣ<sup>+</sup> state is significantly slower than that of the pΠ state, the autoionization rate of the |E<sub>+</sub>, N>, nominally pΠ<sup>+</sup>, state will decrease and there will be a corresponding increase in the |E<sub>-</sub>, N>, nominally pΣ<sup>+</sup>, state's autoionization rate. (If the vibrational autoionization rate of the pΣ<sup>+</sup> state were zero, the linewidths of each of the positive Kronig-symmetry mixed states would tend towards  $\Gamma(\text{p}\Pi)/2$  in the limit of high N.) Because the 0.36 Π and 0.18 Σ<sup>+</sup> states have only fractional p-character (in Chapter 4 the 0.36 Π states were shown to possess only ~55% p-character), the analogy to a p-complex qualitative, not quantitative. The analogy does qualitatively explain the observed decrease in the linewidths of the positive Kronig-symmetry levels.

The analysis of linewidths in the 13.36 Π, v=1 and 14.36 Π, v=1 states supports Murphy's value of the quantum defect derivative determined by deperturbation of the 7.36 Π, v = 0 ~ 6.36 Π, v = 1 interaction at lower energy. Both the bound-bound interaction analyzed by Murphy and the bound-continuum interaction analyzed here involve the exchange of energy between the Rydberg electron and the CaF<sup>+</sup> cation. The rate of

exchange of vibrational and electronic energy in both cases is determined by the derivative of the quantum defect with respect to internuclear separation. Determination of the quantum defect derivative by the analysis of a single intrachannel perturbation or single autoionization rate measurement should allow one to make global predictions of the vibrational~electronic interaction between any two (or more) Rydberg states belonging to the same Rydberg series.

Table 5.2 Measured Linewidths of 13.36  $\Pi$  levels. ID-OODR transitions fit to Eq.(4.8);  $\sigma$  of multiple measurements in parentheses; no error bars listed for single measurement. Uncertainty in width for individual measurement typically  $0.02 \text{ cm}^{-1}$ .

N	13.36 $\Pi^-$	13.36 $\Pi^+$	13g(-4) <sup>+</sup>	9.18 $\Sigma^+$
0	-	-		0.25
1	0.55	0.57		
2	0.52	0.45(3)		
3	0.43	0.50(1)		0.19(4)
4	0.52(6)	0.48(9)		0.28(9)
5	0.53(5)	0.38(4)		0.27(1)
6	0.50(12)	0.27(3)		0.37(4)
7	0.57(10)	0.24(2)		0.37(2)
8	0.62(1)	0.23(2)		0.34
9	0.43(1)	0.28(2)*	0.24(6)*	0.29
10	0.42	0.15(2)	0.20*	0.30*
11	0.48	0.10		
12		0.19		

\* Perturbed

Table 5.3 Measured Linewidths of 14.36  $\Pi$  levels. ID-OODR transitions fit to Eq.(4.8);  $\sigma$  of multiple measurements in parentheses; no error bars listed for single measurement. Uncertainty in width for individual measurement typically  $0.05 \text{ cm}^{-1}$ .

N	14.36 $\Pi^-$	14.36 $\Pi^+$	14g(-4) <sup>+</sup>
1		0.53	
2		0.45	
3	0.58(6)	0.52(6)	
4	0.51	0.43(2)	
5	0.53(9)	0.44	
6	0.53(4)	0.41	
7	0.50	0.41*	0.18*
8		0.35*	0.16*
9	0.50(6)	0.29	
10	0.54	0.31	

\* Perturbed

## References

1. R.S. Berry, *J. Chem. Phys.*, v.45, 1228 (1966).
2. A. Russek, M.R. Patterson, R.L. Becker, *Phys. Rev.*, v.167, 17 (1968).
3. G. Herzberg and Ch. Jungen, *J. Mol. Spec.*, v.41, 425 (1972).
4. H. Lefebvre-Brion and R.W. Field, "Perturbations in the Spectra of Diatomic Molecules", p.399, Academic Press, 1986.
5. S. Rice, H. Martin, and R.W. Field, *J. Chem. Phys.*, v.82, 5023 (1985).
6. P. Bündgen, B. Engels, and S.D.Peyerimhoff, *Chem. Phys. Lett.*, v.176, 407 (1991).
7. W.E. Ernst and J. Kändler, *Phys. Rev. A*, v.39, 1575 (1989).
8. J.E. Murphy, J. M. Berg, A.J. Merer, N.A. Harris, and R.W.Field, *Phys. Rev. Lett.*, v.65, 1861 (1990).
9. R.S. Mulliken, *J. Am. Chem. Soc.*, v.91, 4615 (1969).
10. J. M. Berg, J.E. Murphy, N.A. Harris, and R.W.Field, *Phys. Rev. A*, v.48, 3012 (1993).
11. J.E. Murphy, Ph.D. thesis, MIT, 1992.

**Appendix I: Timing Diagram of ID-OODR Experiment**



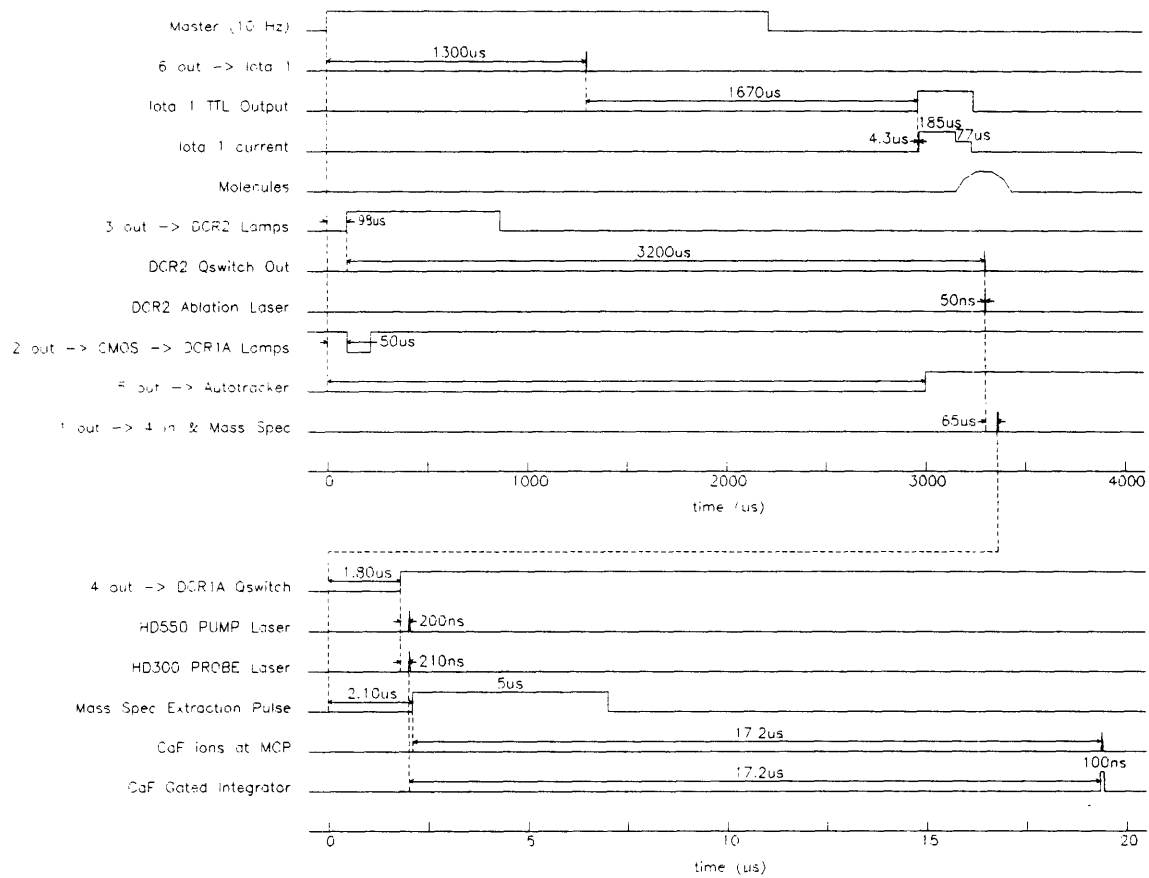


(Figure by Will Polik, 1995.)

**Appendix II: Price List for the Ablation Source Vacuum System  
and Time-of-Flight Mass Spectrometer**

<u>Item</u>	<u>Vendor</u>	<u>Model [Part Number]</u>	<u>Price (1992\$)</u>
Source Vacuum Chamber	MDC, Hayward CA	L1200-6 [custom modified]	\$ 4,950
Diffusion Pump (10" ASA)	Varian, Lexington MA	VHS-10 [0185-0426-308]	\$ 7,763
50 CFM Mechanical Pump	HK Equip., Burlington MA	Alcarel 2063 [rebuild]	\$ 2,600
Gate Valve (10" ASA)	VRC, Pittsburgh PA	LP Series [94578-101]	\$ 2,870
Liquid Nitrogen Trap	K.J.Lesker Co., Clairton PA	Cooke Vacuum [LNT-4210LL]	\$ 2,145
Ionization Gauge Controller	Duniway Skrm., Min. View CA	Granville-Phillips 271-004 [used]	\$ 800
Nude Ionization Gauges	Duniway Skrm., Min. View CA	[-075-P] (2)	\$ 152
Time-of-Flight Mass. Spec.	R.M.Jordan Co., Grass Valley CA	Lens Stack+Flight Tube [C-677]	\$ 3,145
		Shroud+Beam Skimmer [B-682]	\$ 2,100
		Ion Flight Tube Liner [D-679]	\$ 1,100
		AREF Power Supply [D-803]	\$ 4,750
		Dual MCP Detector [C-701]	\$ 2,075
		HV Pulser [D-1040]	\$ 850
		HV Pulser Power Supply [D-1003]	\$ 1,900
		Flight Tube Liner End Shield	\$ 250
		10" Adaptor Flange	\$ 100
		Reflector/Detector Flange	\$ 500
		AREF Flight Tube	\$ 1,050
		Flight Tube Side Port	\$ 535
		Ion Gauge Port	\$ 95
Source Chamber Flanges	R.M.Jordan Co., Grass Valley CA	L-1200B w/6" + 6x2.75" ICF (2)	\$ 1,600
(modified MDC L-1200B's)		L-1200B w/8" ICF (2)	\$ 1,070
		L-1200B w/6" ICF	\$ 455
		L-1200B w/2x2.75" ICFs + window	\$ 540
Vacuum Hardware	misc.		\$ 2,100
Chamber Table	Unistrut Northeast, Canton MA	misc.	\$ 566
	Fran-Dan Bolt, Cambridge MA	misc.	\$ 169
TOTAL			\$ 46,230



## Acknowledgments

Since last August, my grandmother and Andrew + Amy have shared their homes and good company. I am grateful for their hospitality and will miss them all very much. My friend Dave has been a source fun and support throughout my time at MIT. I think I came to take our hiking trips in the White Mountains and excursions to the beach for granted. I will miss him when I'm in California. Laura's e-mail notes over the past year have been the one bright spot on many dark days in the basement. I've enjoyed Marie's company and conversation over the past few years. After each of our conversations I feel I have new ideas to ponder and other perspectives to consider. Mary Ni is a great listener and I always enjoy talking with her, whether it is about the adjudication of fairness by the powers that be or less weighty issues.

Nicole Harris and I collaborated on quite a few experiments. Her initial assignments and renderings of the ID-ODDR spectra gave me a much clearer understanding of the data I was looking at. I couldn't have written Chapter 4 without her insights. George Adamson was a good friend for well over five years. I've missed his wit, social commentary, and technical expertise since he graduated last summer. I think it is fair to say that he is the most talented experimentalist I've had the privilege of working with. Kevin Cunningham put up with my surly attitude in lab for a number of months. I hope I didn't set too bad an example. It was great to work with someone who brought so much enthusiasm to the experiment. Will Polik's organizational skills never cease to impress me. His comments on my thesis chapters were much appreciated and I always enjoyed our conversations in the office. Laura, Dora, and Amy made 2-052 a much more enjoyable office to work in. Amy was a real stabilizing influence on the Superlab. It was always a joy to discuss *Harper's* articles, Leon B., politics, education, and careers with Laura.

The character of the Field group has changed a lot over the past six years. Lunches in Walker (ca.1989-90) with Dave Baldwin, Jim Murphy, Mike and Diane, and Foss were always interesting. I was also glad to know Jim Lundberg, Dave Jonas, and Dave Watt during those early years. More recently, I've enjoyed interacting with Zygmunt, Jon O'Brien, Stephani, Jon Bloch, Ma Hui, James, Bhavani, UROPs Don Lucas and Pete Mao, and the rest of the Field group. I owe Bob thanks for writing the REMPI system into grant proposals and for standing by the project even when it was progressing very slowly.

I will always remember the camping trip to the Pemigawasset (sp?) Wilderness Area with Jon, Amelia, George, Jody, and Dave. Next time someone tells me, "Hey Chris, there's a bear!", I'll believe them. Recreational activities have been few and far between,

but over the past six years I've enjoyed playing hockey with Cold Fusion and softball with the Rigid Rotors. Somehow I know this year will be the one they win the pennant.

I've been fortunate to work with a number of visiting scientists from Japan over my time here: Ken Onda, Ryuma Takashi, and Yoshi Torimoto. Jun Miyawaki and Ken were great hosts during my visit to Tokyo. Ryuma is the best defensive outfielder I've seen play. Every time I missed a catch for the Rotors last year I'd tell myself, "Ryuma would have had that." Yoshi was a lot of fun. His observations on American language and culture always generated a few hours (days) discussion.

I couldn't have put my experiment together without the help of the people in the shop: Murray, Tony, Johnny, and Ed. Tony did a lot of machining for me during my first two years at MIT. He always saw to it that I got the object I wanted, which was not always the one I had submitted on the shop plans. Ray Mariella of LLNL arranged for the loan of a pulsed YAG for the past five years. My experiments wouldn't have been possible without it.

I enjoyed working with the people on the Graduate Student Council: Roger, Susan, Stan, Joe Bambenek, David Cuthbert and many others. It is great to see it becoming a strong, representative student organization. The three people I worked most closely with were Yingying Li, Anand Mehta, and Caryl Brown. All three have been good friends. I enjoyed long discussions with Yingying both in the office and early Monday mornings on our drive in to Officers' meetings. Anand got the GSC off the ground back when it had only half a dozen active members and I have a lot of respect for that. Caryl changed my attitude towards networking and "Leadership Workshops". I hope the Republicans don't get their hands on him.

Above all, I thank my parents and the rest of my family for their generosity, love, and support over the past six and a half years. This wouldn't have been possible without them.



Room 14-0551  
77 Massachusetts Avenue  
Cambridge, MA 02139  
Ph: 617.253.5668 Fax: 617.253.1690  
Email: docs@mit.edu  
<http://libraries.mit.edu/docs>

## **DISCLAIMER OF QUALITY**

Due to the condition of the original material, there are unavoidable flaws in this reproduction. We have made every effort possible to provide you with the best copy available. If you are dissatisfied with this product and find it unusable, please contact Document Services as soon as possible.

Thank you.

**Some pages in the original document contain color pictures or graphics that will not scan or reproduce well.**